

**Characterizing hadronic phase in relativistic
hadronic and heavy-ion collisions and study of
muon puzzle in cosmic ray events with
GRAPES-3 experiment**

Ph.D. Thesis

By

GIRIJA SANKAR PRADHAN



DEPARTMENT OF PHYSICS

INDIAN INSTITUTE OF TECHNOLOGY INDORE

July 2024

Characterizing hadronic phase in relativistic
hadronic and heavy-ion collisions and study of
muon puzzle in cosmic ray events with
GRAPES–3 experiment

A THESIS

Submitted in partial fulfilment of the requirements

for the award of the degree

of

DOCTOR OF PHILOSOPHY

by

Girija Sankar Pradhan



DEPARTMENT OF PHYSICS

INDIAN INSTITUTE OF TECHNOLOGY INDORE

July 2024

Dedicated
to
My family, teachers, and the almighty



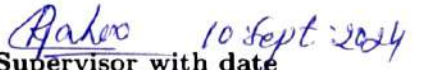
INDIAN INSTITUTE OF TECHNOLOGY INDORE

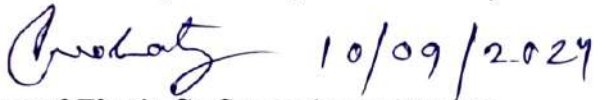
I hereby certify that the work which is being presented in the thesis entitled **Characterizing hadronic phase in relativistic hadronic and heavy-ion collisions and study of muon puzzle in cosmic ray events with GRAPES-3 experiment** in the partial fulfillment of the requirements for the award of the degree of **DOCTOR OF PHILOSOPHY** and submitted in the **DEPARTMENT OF PHYSICS, Indian Institute of Technology Indore**, is an authentic record of my own work carried out during the time period from July 2019 to July 2024 under the supervision of Prof. Raghunath Sahoo, Professor, Department of Physics, Indian Institute of Technology Indore and Dr. Pravata Kumar Mohanty, Reader, Department of High Energy Physics, Tata Institute of Fundamental Research, Mumbai.

The matter presented in this thesis has not been submitted by me for the award of any other degree of this or any other institute.

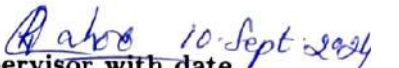

Signature of the student with date
(Girija Sankar Pradhan)

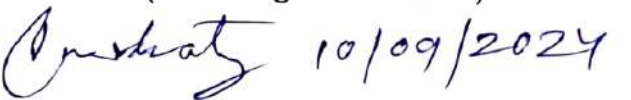
This is to certify that the above statement made by the candidate is correct to the best of my knowledge.


Signature of Thesis Supervisor with date
(Prof. Raghunath Sahoo)


Signature of Thesis Co-Supervisor with date
(Dr. Pravata Kumar Mohanty)

Mr. **Girija Sankar Pradhan** has successfully given his Ph.D. Oral Examination held on 10 Sept. 2024


Signature of Thesis Supervisor with date
(Prof. Raghunath Sahoo)


Signature of Thesis Co-Supervisor with date
(Dr. Pravata Kumar Mohanty)

ACKNOWLEDGEMENTS

Ph.D. is a long journey, and on this journey, I learned numerous new things from my mentor, teachers, collaborators, friends, family, and well-wishers, contributing to fulfilling my dream. I tried to remember everyone's contribution during my Ph.D. journey. Please accept my apologies if I forgot someone's contribution who deserved to be on this list.

First, I want to convey my most profound and sincere gratitude to my thesis supervisor, Prof. Raghunath Sahoo, for his invaluable guidance, supervision, consistent support, and encouragement throughout my Ph.D. journey. I enjoyed every moment of my PhD, primarily due to his constant support in and beyond academics. His dedicated supervision, advice, and constructive criticism helped me to achieve my goal, and it helped shape my life. He is always available to help me with physics discussions. I thank him for providing all the necessary resources and opportunities for my research work. My words are insufficient for his impact on me during my Ph.D. journey. His inspiring advice and suggestions will stay with me for a lifetime.

I sincerely thank my thesis co-supervisor, Dr. Pravata Kumar Mohanty, who mentored me during this journey. I admire his constant efforts, enthusiasm, and visions, which inspire me to pursue my research goals. I am very grateful to him for allowing me to work with him in person by inviting me to the Tata Institute of Fundamental Research and arranging all the facilities. I am thankful to him for allowing me to visit the GRAPES-3 experiment at Ooty and work with the GRAPES-3 group. I thank the entire GRAPES-3 family for their help and support.

I want to thank my PSPC committee members, Dr. Debajyoti Sarkar and Prof. Satyajit Chatterjee, for their support, motivation, and encouragement. I

thank my external examiner of JRF to the SRF conversion seminar, Prof. Tapan Kumar Nayak, for his constructive and encouraging comments. I am very grateful to the Department of Physics, IIT Indore, for providing me with all the required resources. I am sincerely thankful to one of the wonderful people in my Ph.D. career, Late Prof. Jean Cleymans. It was delightful to get engaged in work directly with a renowned physicist and joyful personality. I am thankful to the DST-INSPIRE program of Govt. of India for providing the fellowship throughout my Ph.D. tenure.

I am thankful to all my fellow lab-mates of the Experimental High Energy Physics lab at IIT Indore for constructive physics discussions and all the amusement throughout the last five years. Working with Dr. Sushanta Tripathy, Dr. Arvind Khuntia, Dr. Rutuparna Rath, Dr. Suman Deb, Dr. Captain Rituraj Singh, Dr. Jayanta Dey, Dushmanta, Neelkamal, Ronald, Suraj, Debadatta, Kshitish, Kamaljeet, Bhagyarathi, Kangkan, Aswathy, Purnima and Parul has been a privilege. Special appreciation to Neelkamal and Suraj for helping calculate the elliptic flow coefficient using the two-particle correlation method and Dr. Arvind Khuntia and Dr. Jayanta Dey for their help in cross-checking thermodynamic consistency calculation in Tsallis Statistics in an external magnetic field. Thanks to Dr. Captain Rituraj Singh and Bhagyarathi for helping me understand physics during our discussion. Also, I want to thank Dr. Pranaba Nayak, Dr. Hari Haran Balakrishnan, Dr. Meeran Zubery, Dr. Fahim Varsi, Mr. Dipti Ranjan Pattanaik, Mr. Kaviti Ramesh and Miss. Medha Chakraborty helped and supported me during this journey.

I thank Dr. Gayatri Sahu for her support and encouragement during my stay at IIT Indore. The blissful moments with Mamun and Papun are outstanding.

I thank my school, college, and university teachers for their guidance, which helped me reach this stage. I am thankful to my friends for their love and constant support. I thank my friends Subhrajit, Rajib, and Jitendra for their support during the bad times. I also thank Dhruv, Omkar, Bikash, and Kulbhushan for

making the time at IIT Indore eventful and pleasant.

Finally, I thank my parents for their endless love, support, blessings, and encouragement. They always believed in me and ensured I had access to a good education despite financial limitations. I thank my sisters Srabani, Priyanka, and Swati; my brothers Jagannatha, Gourishankar, Subash, Arun, and Kanha, Gouranga, Purnendu, Subhendu, and Ardhendu for their love and affection. I want to thank my beloved Late grandparents and Aai for their love and support. I also thank my aunties Lata, Trupti, Sumati, Arati, and uncles Gadadhara, Rabindra, Ajit, and Kamalakanta for their unconditional love and care. Without their love and support, this achievement would not have been achievable. Their selfless love and faith encouraged me to pursue my dreams. I will always uphold their love and support, no matter where life takes me. I thank the almighty God for the showers of blessings to complete the research work successfully.

(Girija Sankar Pradhan)

ABSTRACT

In high-energy nuclear physics, studying heavy ion collisions at the Relativistic Heavy Ion Collider (RHIC) and the Large Hadron Collider (LHC) shows a glance into the extreme conditions that existed a few microseconds after the Big Bang. These collisions, described by the collision of heavy atomic nuclei at ultra-relativistic velocities, aim to recreate and study the properties of quark-gluon plasma (QGP). QGP is a state of matter where quarks and gluons are freed from their usual confinement within hadrons and move freely within a volume larger than the hadrons. This plasma acts like a nearly perfect fluid in nature. Several signatures of experimental and theoretical analyses suggest the formation of QGP. Studies have observed strong collective flow in particle distributions, indicating the QGP's hydrodynamic behavior and rapid evolution and cooling phases. Likewise, phenomena such as strangeness enhancement, jet quenching, and suppression of quarkonia states act as an indirect probe into the dynamics and thermalization processes within the QGP medium. These signatures stress the complex interplay between partonic interactions and the evolution of matter under extreme temperatures and energy densities. Generally, proton-proton (pp) collisions are where one does not expect a QGP formation due to their smaller system size and lower energy densities than heavy ion collisions. However, recent observations at the LHC have challenged this concept. High-multiplicity pp collisions show features generally associated with heavy ion collisions, such as the enhanced production of strange particles and ridge-like structures in two-particle correlations. These results indicate the possibility of a QGP-like state forming in such small collision systems under extreme conditions of energy density and particle multiplicity.

This thesis works on several vital areas to understand these phenomena more in-depth, providing a comprehensive understanding of particle production mechanisms, the effect of magnetic fields in QCD matter, freeze-out processes in particle

collisions, and cosmic ray interactions. One significant focus uses the A Multi-phase Transport (AMPT) model to study the effects of nuclear deformation and hadron cascade time (τ_{HC}) on particle production and elliptic flow in Xe+Xe collisions at $\sqrt{s_{\text{NN}}} = 5.44$ TeV. By varying the hadronic cascade time from 5 to 25 fm/ c , we study the p_{T} -differential particle ratios and elliptic flow (v_2). Results indicate that longer hadron cascade times increase anisotropic flow, especially at very low and high- p_{T} . This analysis reveals a considerable dependence of identified particle ratios and elliptic flow on τ_{HC} . Explaining the interplay between scattering cross-sections, hadronic phase lifetime, and initial collision geometry provides a precise understanding of how these factors affect the results of heavy ion collisions. Building on QGP knowledge, we explore the influence of constant magnetic fields on hadron systems using non-extensive statistics within a hadron resonance gas model. This study focuses on the transient magnetic fields produced in heavy-ion collisions at RHIC and LHC energies and their effects on thermodynamic properties such as energy density (ϵ), pressure (P), entropy density (s), and magnetization (M). This work emphasizes transitions from diamagnetic to paramagnetic behavior under varying field strengths when the system is away from equilibrium. Further, the squared speed of sound (c_s^2) is studied, and we observed that the value of c_s^2 decreases with increasing magnetic field strength, that is the system is more interacting in the presence of a finite magnetic field. The impact of magnetic fields on the equation of state and phase diagram in heavy-ion collisions warrants deeper investigations of QCD matter under such extreme conditions.

Additionally, we study the charged-particle p_{T} -spectra measured by the ALICE collaboration for pp collisions at $\sqrt{s} = 7$ and 13 TeV using a thermodynamic consistent Tsallis non-extensive statistics. The Tsallis distribution function is fitted to the p_{T} -spectra. The results are analyzed as a function of final state charged-particle multiplicity for various light flavor and strange particles, such as π^\pm , K^\pm , $p + \bar{p}$, ϕ , $\Lambda + \bar{\Lambda}$, $\Xi + \bar{\Xi}$, $\Omega + \bar{\Omega}$. We use an alternative procedure that uses

parameter redundancy by introducing a finite chemical potential at the kinetic freeze-out stage. This work stresses the significance of the chemical potential (μ) of the system produced in pp collisions at the LHC energies using the Tsallis distribution function, which brings the system to a single freeze-out scenario.

Also, we attempt to address a longstanding puzzle in cosmic ray physics, the muon puzzle. The muon puzzle is the discrepancy between the predicted and observed muon multiplicities in cosmic ray events. However, current theoretical models must pay attention to the number of muons detected by experiments, showing a gap in our understanding of cosmic ray interactions involved in different hadronic interaction models. Addressing the puzzle is important for understanding astrophysical processes and improving the existing hadronic interaction models. In this work, extensive air shower (EAS) simulations are carried out using a Monte Carlo simulation package known as CORSIKA, which is widely used to simulate extensive air showers in the Earth's atmosphere for different primaries. Using extensive air shower simulation data and data from the GRAPES-3 experiment, we study the muon multiplicity, energy spectra, and angular distributions. We attempt to address this puzzle and extend our knowledge of cosmic ray phenomena using the GRAPES-3 experiment, which provides sensitive observations over a wide energy range. These works form the basis of the present thesis.

PUBLICATIONS

List of publications:

Publication included in this thesis:

1. “*Exploring the effect of hadron cascade-time on particle production in Xe+Xe collisions at $\sqrt{s_{NN}} = 5.44$ TeV using a multi-phase transport model*”, **G. S. Pradhan**, R. Rath, R. Scaria, and R. Sahoo, Phys. Rev. C **105**, 054905 (2022).
2. “*Hadron gas in the presence of a magnetic field using non-extensive statistics: A transition from diamagnetic to paramagnetic system*”, **G. S. Pradhan**, D. Sahu, S. Deb, and R. Sahoo, J. Phys. G: Nucl. Part. Phys. **50** 055104 (2023).
3. “*Role of chemical potential at kinetic freeze-out using Tsallis non-extensive statistics in proton-proton collisions at the Large Hadron Collider*”, **G. S. Pradhan**, D. Sahu, R. Rath, R. Sahoo, and J. Cleymans, Eur. Phys. J. A, **60**, 52 (2024).

Other publications:

1. “*Role of event multiplicity on hadronic phase lifetime and QCD phase boundary in ultrarelativistic collisions at energies available at the BNL Relativistic Heavy Ion Collider and CERN Large Hadron Collider*”, D. Sahu, S. Tripathy, **G. S. Pradhan**, and R. Sahoo, Phys. Rev. C **101**, 014902 (2020).
2. “*Evidence of a Hardening in the Cosmic Ray Proton Spectrum at around 166 TeV Observed by the GRAPES-3 Experiment*”, F. Varsi, ..., P. K. Mohanty, ..., **G. S. Pradhan**, ..., R. Sahoo, ..., *et al.* [GRAPES-3 Collaboration], Phys. Rev. Lett. **132**, 051002 (2024).

3. “*Small-scale Cosmic-Ray Anisotropy Observed by the GRAPES-3 Experiment at TeV Energies*”, M. Chakraborty, ..., P. K. Mohanty, ..., **G. S. Pradhan**, ..., R. Sahoo, ..., *et al.* [GRAPES-3 Collaboration], *Astrophys. J.* **961**, 87 (2024).
4. “*A GEANT4 based simulation framework for the large area muon telescope of the GRAPES-3 experiment*”, F. Varsi, ..., P. K. Mohanty, ..., **G. S. Pradhan**, ..., R. Sahoo, ..., *et al.* [GRAPES-3 Collaboration], *JINST* **18**, P03046 (2023).

Conference proceedings:

1. “*Probing the Effect of Hadron Cascade-Time on Particle Production and Elliptic Flow(v_2) in Xe+Xe Collisions at $\sqrt{s_{NN}} = 5.44$ TeV Using AMPT Model*”, **G. S. Pradhan**, R. Rath, R. Scaria, and R. Sahoo, *Springer Proc. Phys.* **304**, 795 (2024).
2. “*Magnetic Field Effects in Hadron Gas: Non-Extensive Insights*”, **G. S. Pradhan**, D. Sahu, S. Deb, and R. Sahoo, *DAE Symp. Nucl. Phys.* **67**, 1063 (2024).
3. “*Decoding Chemical Potential Effects at the Kinetic Freeze-Out through Tsallis Non-Extensive Statistics at the LHC*”, **G. S. Pradhan**, D. Sahu, R. Rath, R. Sahoo, and J. Cleymans, *DAE Symp. Nucl. Phys.* **67**, 1065 (2024).
4. “*Insight into the magnetic response of hadron gas using non-extensive statistics*”, **G. S. Pradhan**, D. Sahu, S. Deb, and R. Sahoo, *PoS LHCP2022*, 327 (2023).
5. “*Insight into the hadronic cascade-time effect on final state observables in Xe+Xe collisions at $\sqrt{s_{NN}} = 5.44$ TeV using AMPT model*”, **G. S. Prad-**

- han, R. Rath, R. Scaria, and R. Sahoo, DAE Symp. Nucl. Phys. **66**, 1012 (2023).
6. “*Investigation of Muon Puzzle with GRAPES-3 Experiment*”, **G. S. Pradhan**, ..., P. K. Mohanty, ..., R. Sahoo, ..., *et al.*, Springer Proc. Phys. **277**, 655 (2022).
 7. “*Dynamics of Hot QCD Matter – Current Status and Developments*”, S. K. Das, ..., **G. S. Pradhan**, *et al.* Int. J. Mod. Phys. E 31, 12 (2022).
 8. “*Hadronic Phase Lifetime and QCD Phase boundary in Ultra-relativistic Collisions at the RHIC and LHC: Collision System and Event Multiplicity Dependence*”, D. Sahu, S. Tripathy, **G. S. Pradhan**, and R. Sahoo, DAE Symp. Nucl. Phys. **64**, 754 (2019).
 9. Additional 22 conference proceedings in GRAPES-3 experiment.

Contents

1	Introduction	1
1.1	The Standard Model	2
1.2	Quantum Chromodynamics (QCD)	5
1.3	QCD phase transition and the Quark-Gluon Plasma	8
1.4	Ultra-relativistic heavy-ion collisions	12
1.4.1	Geometrical aspects of heavy-ion collisions	13
1.4.2	The time evolution of a heavy-ion collision	14
1.5	Signatures of QGP	18
1.5.1	Collective flow	18
1.5.2	Strangeness enhancement	20
1.5.3	Jet quenching	22
1.5.4	J/ψ suppression	24
1.6	Connection between the collider and cosmic ray physics	25
1.7	Cosmic rays and its origin	26
1.8	Cosmic rays energy spectrum	28
1.9	Composition of cosmic rays	31
1.10	Detection of cosmic rays	32
1.11	Extensive Air Showers	34
1.11.1	Electromagnetic showers	35
1.11.2	Hadronic showers	36
1.12	Thesis motivation	39

2	Effect of hadron cascade time on particle production in Xe+Xe collisions at $\sqrt{s_{\text{NN}}} = 5.44$ TeV using a multiphase transport model	43
2.1	A multiphase transport (AMPT) model	45
2.2	Results and Discussion	48
2.2.1	Identified p_{T} -differential particle ratios	51
2.2.2	Elliptic flow (v_2)	52
2.3	Summary	56
3	Effect of magnetic fields and non-extensive statistics in a hadron resonance gas	59
3.1	Effect of the magnetic field in heavy-ion collisions	60
3.2	Hadron resonance gas (HRG) model	62
3.3	Tsallis non-extensive statistics	63
3.4	Thermodynamic consistency of Tsallis distribution function in the presence of an external magnetic field	69
3.5	Thermodynamics of hadron gas in an external magnetic field . . .	74
3.5.1	Energy density and magnetization of hadron gas	75
3.5.2	Pressure of a magnetized hadron gas	76
3.5.3	Renormalization of vacuum pressure	77
3.5.4	The speed of sound in a magnetized hadron gas	82
3.6	Results and Discussion	85
3.7	Summary	95
4	Role of chemical potential at kinetic freeze-out using Tsallis non-extensive statistics in pp collisions at the Large Hadron Collider	97
4.1	Physical interpretation of q and connection with lQCD	99
4.2	Significance of chemical potential in relativistic collision	101
4.3	Formulation	102

4.4	Transverse momentum spectra of identified hadrons	106
4.5	Results and Discussion	115
4.6	Summary	123
5	The GRAPES-3 Experiment at Ooty	125
5.1	EAS array	127
5.1.1	Scintillation detector	129
5.1.2	Signal processing and data acquisition system	132
5.2	GRAPES-3 muon telescope	134
5.2.1	Proportional counter (PRC)	136
5.2.2	Signal processing and data acquisition system	140
5.3	Summary	141
6	Study of muon puzzle in cosmic ray events with GRAPES-3	
	Experiment	143
6.1	CORSIKA simulation	145
6.2	Results and Discussion	152
6.2.1	Muon multiplicity distribution	152
6.2.2	Muon energy spectra	154
6.2.3	Muon zenith angle distributions	155
6.3	Summary	156
7	Summary and Outlook	161

Figures

1.1	The schematic representation of the standard model [16].	3
1.2	Running coupling constant (α_s) as a function of energy transfer (Q). The markers represent measurements based on perturbative calculations, and the solid line corresponds to an analytical prediction [18] .	6
1.3	Normalized pressure, energy density, and entropy density as a function of the temperature from lattice QCD calculation of (2+1) flavor at zero baryon chemical potential ($\mu_B = 0$), as represented by different color bands. The solid lines represent the HRG model's predictions. The horizontal dash line at $95\pi^2/60$ represents the Stefan-Boltzman ideal gas limit for energy density, while the vertical band indicates the crossover region, $T_c = (154 \pm 9)$ MeV [20].	8
1.4	Schematic representation of the QCD phase diagram as a function of the temperature and the net baryonic density [22].	10
1.5	Schematic picture of ultra-relativistic heavy ion collisions [36].	13
1.6	Schematic diagram representing various stages of heavy-ion collisions as a function of time [37].	15
1.7	A schematic diagram of the space-time evolution of relativistic nucleus-nucleus collision [38].	16
1.8	A schematic representation of a non-central heavy-ion collision with an almond-shaped interaction volume [39].	19

1.9	Comparison of the charged particles p_T -differential elliptic flow for Pb–Pb collisions at $\sqrt{s_{NN}} = 2.76$ TeV in solid markers to Au–Au collisions at $\sqrt{s_{NN}} = 200$ GeV that represents in shaded regions. [42, 43].	20
1.10	Integrated strange hadron-to-pion ratios as a function of charged particle multiplicities in pp, p–Pb, and Pb–Pb collisions at LHC energies. Different lines represent predictions from different MC generators for pp collisions at $\sqrt{s} = 13$ TeV [46, 47].	21
1.11	$R_{AA}(p_T)$ for charged hadrons (h^\pm) and neutral pions (π^0) in central heavy-ion collisions at SPS, RHIC, and the LHC [50].	23
1.12	R_{AA} of J/ψ in Pb–Pb collisions at $\sqrt{s_{NN}} = 2.76$ TeV and Au–Au collisions at $\sqrt{s_{NN}} = 200$ GeV as a function of an average number of participant nucleons [52].	24
1.13	Results obtained by Victor Hess (left) and W. Kolhörster (right) during their balloon flights [59].	27
1.14	Cosmic rays energy spectrum measured by different direct and indirect experiments [67].	29
1.15	Cosmic ray elemental abundances compared to abundances in present-day solar system material. Abundances are normalized to Si = 10^3 [76].	31
1.16	Schematic of EAS development for a high energy γ -ray [99].	35
1.17	Schematic of EAS development for a cosmic ray primary [99].	36
2.1	p_T -differential particle ratios of K^\pm , $p(\bar{p})$, ϕ and $\Lambda(\bar{\Lambda})$ to π^\pm in Xe+Xe collisions at $\sqrt{s_{NN}} = 5.44$ TeV for (20–30)% centrality class. Different symbols show various hadron cascade times. The vertical lines on the data points are the statistical uncertainties [135].	49
2.2	p_T -differential particle ratios of K^\pm , $p(\bar{p})$, ϕ and $\Lambda(\bar{\Lambda})$ to π^\pm in Xe+Xe collisions at $\sqrt{s_{NN}} = 5.44$ TeV for (50–60)% centrality class. Different symbols show various hadron cascade times. The vertical lines on the data points are the statistical uncertainties [135].	50

2.3	<p>p_T-differential particle ratios of ϕ to p in Xe+Xe collisions at $\sqrt{s_{NN}} = 5.44$ TeV for (20–30)% (left) and (50–60)% (right) centrality classes. Different symbols show various hadron cascade times. The vertical lines in the data points are the statistical uncertainties [135].</p>	51
2.4	<p>p_T-differential elliptic flow of charged particles in Xe+Xe collisions at $\sqrt{s_{NN}} = 5.44$ TeV for (20-30)% and (50-60)% centrality classes. Different symbols show various hadron cascade times [135]. The results are compared with the ALICE data [105].</p>	53
2.5	<p>p_T-differential particle ratios of ϕ to p in Xe+Xe collisions at $\sqrt{s_{NN}} = 5.44$ TeV for (20–30)% (left) and (50–60)% (right) centrality classes. Different symbols show various hadron cascade times. The vertical lines in the data points are the statistical uncertainties [135].</p>	54
2.6	<p>p_T-integrated elliptic flow of the charged particles in Xe+Xe collisions at $\sqrt{s_{NN}} = 5.44$ TeV for (0-10)%, (10-20)%, (20-30)%, (30-40)%, (40-50)% and (50-60)% centrality classes. Different symbols show various hadron cascade times [135].</p>	55
3.1	<p>Fits the normalized differential yields of π^+ as measured by the ALICE Collaboration in pp collisions at $\sqrt{s} = 0.9$ TeV [170] fitted with the Tsallis (solid line) and Boltzmann distributions (dashed line). Additionally, variations of the Tsallis distribution were explored: a fit retaining terms to first order in $(q-1)$ is represented by the dash-dotted line, while a fit retaining term to second order in $(q-1)$ is shown as the dotted line. The bottom panel shows the difference between model (M) and experiment (E) normalized to the model (M) values [169]. .</p>	65

3.2	The energy density of a hadron gas as a function of temperature for near equilibrium, <i>i.e.</i> for $q = 1.001$, values of non-extensive parameters at a constant magnetic field $eB = 0 \text{ GeV}^2$ and $eB = 0.3 \text{ GeV}^2$ respectively [153]. The results are compared to the relevant HRG and lattice QCD data [155, 159].	86
3.3	The pressure of a hadron gas as a function of temperature for near equilibrium (for $q = 1.001$) at a constant magnetic field $eB = 0.3 \text{ GeV}^2$ [153]. The findings are compared to HRG and lattice QCD data [155, 159].	87
3.4	Total energy density of a hadron gas as a function of temperature for different values of the non-extensive parameter (q) at a constant magnetic field $eB = 15m_\pi^2$ [153].	88
3.5	Total energy density of a hadron gas as a function of temperature at different magnetic fields and different q values [153].	89
3.6	Magnetization of a hadron gas as a function of temperature for different values of the non-extensive parameter at a constant magnetic field $eB = 15m_\pi^2$ [153].	90
3.7	Magnetization of a hadron gas as a function of temperature at different magnetic fields and for different q -values [153].	91
3.8	Pressure as a function of temperature in a magnetized hadron gas for different q -values, respectively [153].	92
3.9	Entropy density as a function of temperature in a magnetized hadron gas for different q -values, respectively [153].	93
3.10	The squared speed of sound of a hadron gas as a function of temperature for different q -values for different magnetic field strengths [153].	94
4.1	Fitting of experimentally measured p_T -spectra of pion (π^\pm), kaon (K^\pm), proton ($p + \bar{p}$) and phi (ϕ) at zero chemical potential ($\mu = 0$) using Tsallis non-extensive statistical model for pp -collisions at $\sqrt{s} = 7 \text{ TeV}$	107

4.2	Fitting of experimentally measured p_T -spectra of lambda ($\Lambda + \bar{\Lambda}$), cascade ($\Xi + \bar{\Xi}$) and omega ($\Omega + \bar{\Omega}$) at zero chemical potential ($\mu = 0$) using Tsallis non-extensive statistical model for pp -collisions at $\sqrt{s} = 7$ TeV.	108
4.3	Fitting of experimentally measured p_T -spectra of pion (π^\pm), kaon (K^\pm), proton ($p+\bar{p}$) and phi (ϕ) at non-zero value of chemical potential ($\mu \neq 0$) using Tsallis non-extensive statistical model for pp -collisions at $\sqrt{s} = 7$ TeV.	109
4.4	Fitting of experimentally measured p_T -spectra of pion (π^\pm), kaon (K^\pm), proton ($p+\bar{p}$) and phi (ϕ) at non-zero value of chemical potential ($\mu \neq 0$) using Tsallis non-extensive statistical model for pp -collisions at $\sqrt{s} = 7$ TeV.	110
4.5	The non-extensive parameter (q) at ($\mu = 0$) as a function of q for ($\mu \neq 0$) for pp collisions at $\sqrt{s} = 7$ TeV (left panel) and 13 TeV (right panel) for different final state particles. The line represents the fit function, $y = mx + c$ [212].	115
4.6	Comparison of the non-extensive parameter (q) at ($\mu = 0$) and ($\mu \neq 0$) for pp collisions at $\sqrt{s} = 7$ TeV for different final state particles as a function of final state multiplicity. Shown in the bottom panel is the ratio of both cases, which indicates that q hardly depends on the chemical potential of the system [212].	116
4.7	Non-extensive parameter (q) as a function of charged-particle multiplicity for pp collisions at $\sqrt{s} = 7$ TeV (left panel) and 13 TeV (right panel) for different final state particles. The uncertainties in charged-particle multiplicity are the quadratic sum of statistical and systematic contributions, and the error in the value of q is statistical errors [212].	117

4.8	Temperature (T_0) as a function of charged-particle multiplicity for pp collisions at $\sqrt{s} = 7$ TeV (left panel) and 13 TeV (right panel) for different final state particles at zero chemical potential. The uncertainties in charged-particle multiplicity are the quadratic sum of statistical and systematic contributions, and the error in the value of T_0 are statistical errors [212].	118
4.9	Temperature (T) as a function of charged-particle multiplicity for pp collisions at $\sqrt{s} = 7$ TeV (left panel) and 13 TeV (right panel) for different final state particles at the non-zero chemical potential. The uncertainties in charged-particle multiplicity are the quadratic sum of statistical and systematic contributions, and the error in the value of T are statistical errors [212].	119
4.10	Radius of the system (R) as a function of charged-particle multiplicity for pp collisions at $\sqrt{s} = 7$ TeV (left panel) and 13 TeV (right panel) for different final state particles. The uncertainties in charged-particle multiplicity are the quadratic sum of statistical and systematic contributions, and the error in the value of R are statistical errors [212].	120
4.11	Chemical potential (μ) as a function of charged-particle multiplicity for pp collisions at $\sqrt{s} = 7$ TeV (left panel) and 13 TeV (right panel) for different final state particles. The uncertainties in charged-particle multiplicity are the quadratic sum of statistical and systematic contributions, and the error in the value of μ are statistical errors [212].	121
4.12	χ^2/ndf as a function of charged-particle multiplicity for pp collisions at $\sqrt{s} = 7$ TeV (left panel) and 13 TeV (right panel) for different final state particles [212].	122
5.1	A view of the GRAPES-3 extensive air shower array.	126

5.2	The schematic diagram of the GRAPES-3 experiment depicts single PMT scintillator detectors as blue triangles, double PMT scintillator detectors as red triangles, and G3MT modules as green open squares [255].	128
5.3	The schematic of a cone-type scintillator detector shows plastic scintillator blocks (blue) housed within a trapezoidal cone-shaped aluminum case (black line), with a PMT positioned at the top. A muon telescope under the detector is used for calibration.	130
5.4	Schematic of a double PMT fiber-type scintillator detector [247].	131
5.5	The schematic of the signal processing system for the scintillator detector shows the basic components of data acquisition and the propagation of signals to ADC and TDC, along with signals used for EAS trigger generating and rate monitoring [246].	133
5.6	Schematic of the shower trigger system for generating the Level-0 trigger using the basic 3-line coincidence [246].	134
5.7	Schematic representation of the G3MT for GRAPES-3 coordinates system. Red squares represent the muon modules (M00 \rightarrow M15), and the blue dashed squares represent supermodules (S ₀ \rightarrow S ₃).The direction of the PRC within each layer is indicated by the notation \Leftarrow . However, the arrangement of the proportional counters for each projection in a given module is shown explicitly. However, the placement of proportional counters in each projection inside a certain module is explicitly shown and denoted by the symbol 0 \rightarrow 57 [255]	135
5.8	A cross-section projection of a supermodule depicting two front modules with four layers of proportional counters and a concrete absorber [249].	136
5.9	A schematic of the PRC is used as the basic detector element in the GRAPES-3 tracking muon detector [256].	137
5.10	A typical pulse amplitude distribution for a proportional counter [256].	138

5.11	Schematics of two PRC pulses of amplitude A1 and A2, respectively, and corresponding discriminator output pulses of width W1 and W2, respectively [255].	139
5.12	A schematic of the signal processing system and DAQ for the G3MT showing the digital wave memory (DWM) card and DWM control card [249].	140
6.1	A comparison of the observed muon multiplicity distribution for shower size $10^{4.6}$ – $10^{4.8}$ with simulations for p, He, N, Al, and Fe for QGSJET-II-04.	147
6.2	A comparison of the observed muon multiplicity distribution for shower size $10^{4.6}$ – $10^{4.8}$ with simulations for p, He, N, Al, and Fe for EPOS-LHC.	148
6.3	Muon energy spectra with simulations for primary cosmic rays (p, He, N, Al, Fe) using the QGSJET-II-04 model.	150
6.4	Muon energy spectra with simulations for primary cosmic rays (p, He, N, Al, Fe) using the EPOS-LHC model.	151
6.5	Simulated muon zenith angle distributions for different primary cosmic rays primaries (p, He, N, Al, Fe) using the QGSJET-II-04 model. This figure demonstrates the variation in muon count with the zenith angle, showing the effects of different primary particles on air showers and muon production characteristics.	158
6.6	Simulated muon zenith angle distributions for different primary cosmic rays primaries (p, He, N, Al, Fe) using the EPOS-LHC model. This figure demonstrates the variation in muon count with the zenith angle, showing the effects of different primary particles on air showers and muon production characteristics.	159

Tables

3.1	List of hadrons and resonances taken into account in the HRG description.	64
4.1	Number of mean charged particle multiplicity density for all the particles at mid-rapidity corresponding to different event classes at $\sqrt{s} = 7$ TeV [239]. The uncertainties are the quadratic sum of statistical and systematic contributions.	106
4.2	Number of mean charged particle multiplicity density for π, K, p at mid-rapidity corresponding to different event classes at $\sqrt{s} = 13$ TeV [47]. The uncertainties are the quadratic sum of statistical and systematic contributions.	106
4.3	Number of mean charged particle multiplicity density for $\phi, \Lambda, \Xi, \Omega$ at mid-rapidity corresponding to different event classes at $\sqrt{s} = 13$ TeV [240, 241]. The uncertainties are the quadratic sum of statistical and systematic contributions.	106
4.4	Fit results at $\sqrt{s} = 7$ TeV [239], using data from the ALICE Collaboration using Eq. 4.5 and 4.7. The reason of merging bins Mul[1+2], Mul[3+4] etc for Ω is lack of statistics.	111
4.5	Fit results at $\sqrt{s} = 13$ TeV [47, 240, 241], using data from the ALICE Collaboration using Eq. 4.5 and 4.7. The reason of merging bins Mul[1+2], Mul[3+4] etc for Ω is lack of statistics.	112
4.6	Fit results at $\sqrt{s} = 7$ TeV [239], using data from the ALICE Collaboration with q from Table 4.4 following Eq. 4.2 and 4.6.	113

4.7 Fit results at $\sqrt{s} = 13$ TeV [47, 240, 241], using data from the ALICE Collaboration with q from Table 4.5 following Eq. 4.2 and 4.6.114

Chapter 1

Introduction

In high-energy theoretical and experimental physics, scientists are motivated by an ambitious desire to discover the unknown and solve the mysteries of the Universe. Their combined efforts are crucial to understanding the fundamental building block of matter that constitutes the entire Universe, as well as gaining an understanding of the Universe's possible beginnings and evolution.

The advancement of the scientific approach saw a resurgence of foundational concepts during the 19th and 20th centuries, with substantial contributions such as John Dalton's atomic theory and Joseph J. Thomson's discovery of the electron [1], the first identified subatomic particle, came to light in 1897. In 1911, Ernest Rutherford found the atomic nucleus through an experiment of scattering of alpha particles on a thin gold foil [2] and revealed that a positively charged nucleus surrounded by negatively charged electrons; this ground-breaking discovery fundamentally changed our understanding of atoms. The subsequent discovery of proton [3] and neutron [4] enhanced our knowledge of the nucleus and its fundamental nuclear properties. Significant discoveries occurred: the muon was identified in 1937 [5, 6]; pions [7] and kaons in cosmic rays were detected in 1947 [8, 9]; the Λ particle was revealed in 1950 [10], the anti-proton was discovered in 1955 [11], and the identification of electron and muon neutrinos occurred

in 1956 [12] and 1962 [13], respectively. Another significant development in our knowledge of particle physics was finding the Ω particle in 1964 [14]. By the early 1960s, more than 30 new particles had been discovered, making a mysterious particle zoo that baffled physicists for a decade. In the 1970s, thanks to the interplay between theory and experiment, the Standard Model of particle physics successfully explains the experimental results of elementary particles with high precision. Its ability to describe complex particle interactions incorporates fundamental forces.

1.1 The Standard Model

In the present state of the Universe, ordinary matter comprises atoms, each consisting of a nucleus composed of protons and neutrons (besides the hydrogen atom), surrounded by a cloud of electrons. The orthodox belief was that protons and neutrons within the atomic nucleus were the fundamental particles. In the next few decades, many new particles were proposed theoretically and discovered experimentally. Still, there was no classification of a vast number of particles. For the first time, Murray Gell-Mann introduced the Eight-fold way to classify the hadrons based on the electric charge and net strangeness content following Mendeleev's way of organizing elements, which resulted in the periodic table of elements. However, in 1964, the quark model superseded the Eight-fold way when Gell-Mann and George Zweig independently proposed that all the hadrons are composed of quarks [15]. Quarks and leptons are elementary or fundamental particles and lack substructures. The Standard Model of particle physics, formulated by Glashow, Salam, and Weinberg in the 1970s, successfully explains the experimental results of elementary particles with high precision and encapsulates the relationships among these particles and the first three forces: strong, electromagnetic, and weak. Quantum numbers like spin (S), electric charge (Q), baryon (B), lepton (L) numbers, etc are used to characterize elementary particles. Figure 1.1

1.1 The Standard Model

represents the standard model of particle physics.

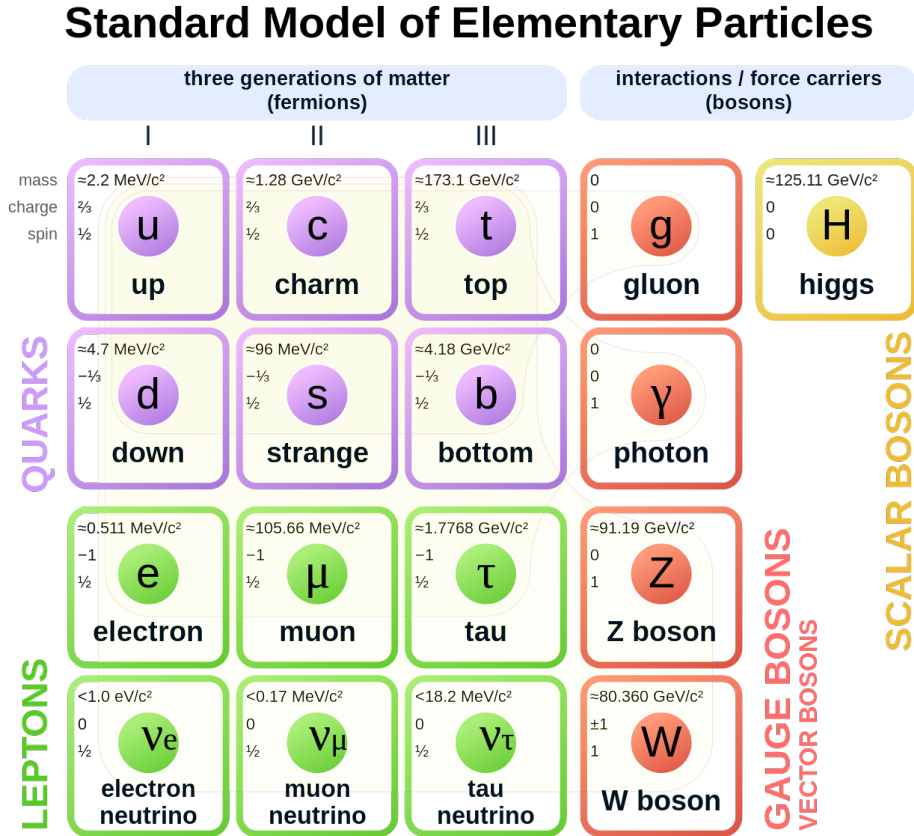


Figure 1.1: The schematic representation of the standard model [16].

According to the standard model of particle physics, all visible matter in the Universe comprises quarks, leptons, gauge bosons, and Higgs bosons, which are the fundamental particles classified into these groups by the standard model. Quarks and leptons are classified into three generations: up (u) and down (d) quarks are in the first generation, charm (c) and strange (s) quarks are in the second generation, and top (t) and bottom (b) quarks are in the third generation. Similarly, leptons are divided into three generations, each with a corresponding neutrino. These generations include electrons (e), muons (μ), and taus (τ). Particles that are lightest and most stable belong to the first generation, while the

second and third generations are heavier and less stable. The quarks and leptons are fermions and have a half-integral spin ($1/2$) quantum number, and they follow Fermi–Dirac statistics and Pauli’s exclusion principle. Hadrons are made of quarks. A meson is a hadron of a quark and an antiquark pair, and a baryon is a hadron of three quarks. Because of Pauli’s exclusion principle, no two quarks inside a baryon can have the same quantum number. Hence, a new quantum number known as the color charge was introduced for this reason. A fractional electric charge (either $+2/3 e$ or $-1/3 e$) and a distinct color charge (red (r), blue (b), or green (g)) are carried by each quark. Gauge bosons are the carriers of these fundamental forces present. There are four fundamental forces in nature: strong, electromagnetic, weak, and gravitational. Each fundamental force has its force carrier; the strong force is carried by the gluons (g), the W and Z^\pm bosons are responsible for the weak force, and the electromagnetic force is held by the photons (γ). Self-interacting gluons carry the color charge, which is crucial for strong interaction. After the discovery of the Higgs boson at the Large Hadron Collider (LHC), CERN, Geneva, responsible for mass generation in elementary particles, the Standard Model stands complete in its prescribed form. The gravitational force carrier, the Graviton, has yet to be discovered. Within the domain of quantum field theory (QFT), Quantum Electrodynamics (QED) governs electromagnetic interaction, offering profound insights into the behavior of charged particles and photons. Furthermore, the Electroweak (EW) theory unified the weak and electromagnetic forces, shedding light on phenomena ranging from radioactive decay to electromagnetism at the subatomic level. Diving deeper into Quantum Chromodynamics (QCD) emerges as the governing principle behind the strong interaction, which will be further explored in the subsequent section.

1.2 Quantum Chromodynamics (QCD)

Quantum Chromodynamics (QCD) describes the strong interactions between color-charged particles, namely partons (quarks and gluons), the fundamental constituents of matter. Nonetheless, hadrons, colorless composite particles, trap quarks and gluons, just as protons and neutrons do. Its foundation is the gauge symmetry group $SU(3)$, which imposes the conservation of color and has eight generators that produce eight massless gauge bosons known as gluons. The QCD potential, which characterizes the force between quarks mediated by gluons, encapsulates the dynamics of QCD. Understanding quark activity within hadrons mainly depends on the static quark-antiquark potential, which considers both short- and long-range interactions.

$$V_{QCD}(r) = -\frac{4}{3} \frac{\alpha_s}{r} + kr. \quad (1.1)$$

Here, α_s denotes the strong coupling constant, k is the color string tension constant, and r represents the distance between interacting partons (quarks or gluons) [17]. The Coulomb-like term in the QCD potential is similar to the one in QED, dominant at small distances, and the second term corresponds to an elastic spring-type force dominant at more considerable distances. Notably, the coupling constant (α_s) is not static but varies with four-momentum transfers, called the running coupling constant. It emerges from the vacuum polarization of gluon or quark pairs, similar to the electric charge polarization in QED. The running coupling constant as a function of momentum transfer (Q^2) is given as,

$$\alpha_s(Q^2) = \frac{12\pi}{(11n_c - 2n_f) \ln(Q^2/\Lambda_{QCD}^2)}. \quad (1.2)$$

Here, $n_c = 3$ colors, n_f is the number of quark flavors, and Λ_{QCD} is the non-perturbative QCD scale parameter. Figure 1.2 illustrates the behavior of the running coupling constant, α_s , as a function of the energy transfer Q . The

strong interaction weakens at large Q , corresponding to small distances (α_s small). Conversely, at small Q , corresponding to large distances, the coupling constant strengthens (α_s large), signifying a considerable variation in interaction strength.

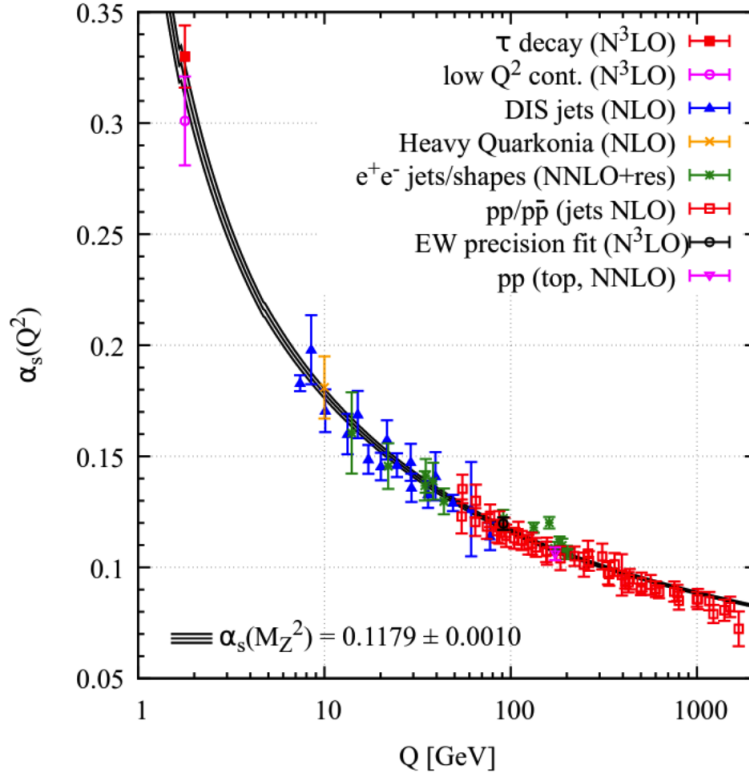


Figure 1.2: Running coupling constant (α_s) as a function of energy transfer (Q). The markers represent measurements based on perturbative calculations, and the solid line corresponds to an analytical prediction [18]

The characteristic energy scale Λ_{QCD} is estimated to be around 200 MeV. Above this scale, perturbative QCD (pQCD) becomes feasible as the contributions of high-order diagrams diminish rapidly. However, as the energy transfer decreases, the coupling constant increases, leading to diverging perturbative calculations, eventually becoming infinite at Λ_{QCD} . Below this scale, QCD is dominated by high-order diagrams and requires non-perturbative treatment.

At a small distance, $r \leq 0.1$ fm, the Coulomb-type term of Eq. 1.1 dominates,

1.2 Quantum Chromodynamics (QCD)

causing the interaction potential to diminish asymptotically as the distance decreases. Importantly, this decrease is not infinite, as α_s also varies. Consequently, quarks gradually interact less, approaching a quasi-free state. This phenomenon is known as asymptotic freedom. Notably, neither the electrostatic force between two charges nor the gravitational force between two masses exhibit such behavior. The interaction gets weaker as the distance increases between the two objects. Conversely, the second term of Eq. 1.1 takes the upper hand at $r \geq 1$ fm. The force increases linearly with the distance between the two quarks as if they stand connected by an elastic or spring made up of gluons. As the quarks move apart, the energy stored in the gluon spring builds until it approaches the threshold necessary to form a quark-antiquark pair. This process is repeated until every quark-antiquark has enough energy to unite to form a hadron. Note that a pair of gluons could replace the initial quark-antiquark pair, and the process will remain the same. Accordingly, any color-charged particle, quark or gluon, cannot live in isolation and must be confined within color-neutral objects, mesons, and baryons, known as color confinement.

These unique properties of QCD can give rise to an exciting phase of matter under extreme temperature and/or baryon density conditions. In such scenarios, typically at temperatures exceeding 100 MeV (equivalent to 10^{12} K), where quarks and gluons become relevant degrees of freedom instead of hadrons in such scenarios. It is conjectured that the Universe was filled with these fundamental particles just a few microseconds after the Big Bang. Unlike their usual confinement within hadrons, during this phase, they exist in a deconfined state, constituting a matter known as quark-gluon plasma (QGP). Understanding the QCD phase transition and the origins of the QGP phase provides insight into the early Universe. It reveals details about the underlying nature of matter under such circumstances. In the following section, we will go into greater detail about these notions.

1.3 QCD phase transition and the Quark-Gluon Plasma

To reproduce conditions similar to the early Universe, powerful accelerators collide massive ions head-on, smashing hundreds of protons and neutrons into each other at ultra-relativistic energies of a few trillion volts each. The lQCD calculation offers insights into the transition from a state where particles are confined within hadrons to one where they exist as quasi-free partons, occurring at a critical temperature (T_c) and lower baryon chemical potential (μ_B) [19].

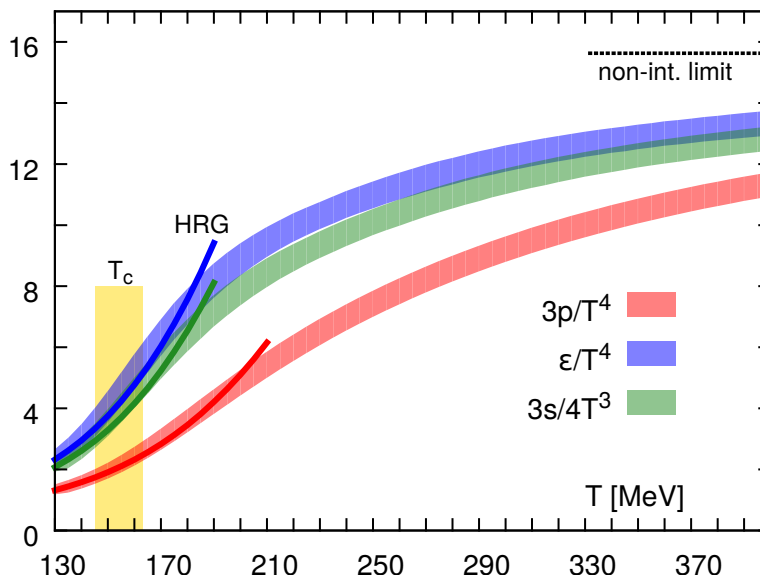


Figure 1.3: Normalized pressure, energy density, and entropy density as a function of the temperature from lattice QCD calculation of (2+1) flavor at zero baryon chemical potential ($\mu_B = 0$), as represented by different color bands. The solid lines represent the HRG model's predictions. The horizontal dash line at $95\pi^2/60$ represents the Stefan-Boltzmann ideal gas limit for energy density, while the vertical band indicates the crossover region, $T_c = (154 \pm 9)$ MeV [20].

Figure 1.3 compares energy density, pressure, and entropy calculated in a

1.3 QCD phase transition and the Quark-Gluon Plasma

hadron resonance gas (HRG) model with the lQCD prediction as a function of temperature. As one moves towards a higher temperature region, observe an abrupt change in the system's energy density, pressure, and entropy. Notably, significant changes occur as the temperature reaches $T_c = 154$ MeV, indicating the liberation of numerous degrees of freedom. Specifically, the partons, usually confined within hadrons, undergo a deconfinement transition, becoming quasi-free. Initially, it was thought to interact weakly, similar to a plasma. Later, it was realized through experimental measurements that they interact strongly. Thus, the QGP represents a phase of strongly interacting matter and is referred to as strongly interacting quark-gluon plasma. As the coupling between the partons decreases with the increasing momentum transfer and temperature, the energy density will eventually coincide with the ideal gas limit but at a considerably higher temperature. This observation offers a glimpse into the critical energy density and temperature associated with the QCD phase transition. Following its discovery, it became evident that this state of matter behaves as a perfect fluid exhibiting the lowest viscosity to entropy ratios (η/s) compared to any other fluid found in nature [21]. Consequently, numerous findings from heavy-ion experiments find adequate explanations through hydrodynamical models. These models operate under the assumption of local thermal equilibrium and utilize local conservation principles encompassing energy, momentum, and, sometimes, conserved charges or entropy. The system created in the pp collisions is often seen as too tiny to form a thermalized system or inadequate to form a non-hadronic medium, in contrast to the heavy-ion collisions. However, considering the similarity of some findings between the large and small systems at LHC energies, one could anticipate that at sufficiently high energy densities, the degrees of freedom in pp may permit a collective characterization of the system.

At significant momentum transfer or small distances, the coupling among partons weakens due to asymptotic freedom. This leads to a transition from the hadronic gas phase to the deconfined phase known as quark-gluon plasma

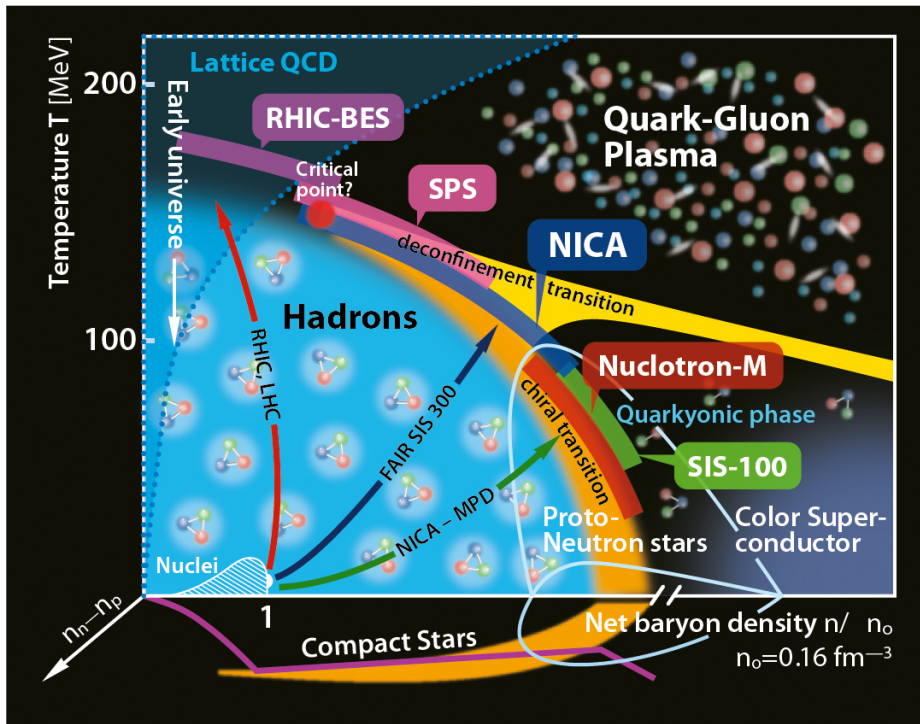


Figure 1.4: Schematic representation of the QCD phase diagram as a function of the temperature and the net baryonic density [22].

(QGP). This is similar to the state of matter produced a few microseconds after the Big Bang. The initial outline of the QCD phase diagram was proposed by N. Cabibbo and G. Parisi in 1975 [23]. However, our insight into the phase diagram of quark matter needs to be improved theoretically and experimentally. The phase transition of strongly interacting matter is governed by temperature and net baryonic chemical potential (μ_B). Varying beam energy in experiments allows for exploration across this phase diagram. At low temperatures and baryon chemical potentials, strongly interacting matter exists in a normal state as atomic nuclei. Enhancing the energy density can induce a transition from a hadronic gas to a deconfined phase of partons. This transformation can be achieved by increasing the temperature, the baryon-chemical potential, or a combination of both.

1.3 QCD phase transition and the Quark-Gluon Plasma

Lattice QCD calculations estimate a critical temperature (T_c) for the transition to QGP, approximately in the range of 140-170 MeV, corresponding to an energy density (ϵ_c) of around 1GeV/fm³. Different models predict different natures of this transition. QCD-inspired models suggest a first-order transition at high net baryon densities. In contrast, lattice QCD predicts a crossover at zero net baryon density, implying the existence of a critical point. This critical phenomenon resembles the phase diagram of water. The simultaneous phases between water and vapor become less distinctive as it approaches the critical point. The complete QCD phase diagram, depicted in Fig. 1.4, illustrates two primary ways to form QGP: increasing temperature or net baryonic density by compressing the hadronic matter. The transition shown in Fig. 1.3 corresponds to the former, where heating a system with almost zero net baryon density transforms ordinary nuclear matter into a hadron gas and then toward QGP. On the other hand, hadronic matter compressed at low temperatures leads to an increase in baryonic density and eventually a transition to QGP, which is similar to the conditions seen in the cores of neutron stars [24] and may show color superconductor characteristics [25]. Fig. 1.4 shows the smooth transition from high-temperature regions to high baryon densities, indicating a second-order or crossover phase transition [26]. In contrast, transitions driven by high baryon density are expected to be abrupt, similar to ice melting into water, representing a first-order transition. This suggests the presence of a critical point bridging first and second (or crossover) phase transitions [27]. However, its precise location remains unknown. No singularities have been observed to date.

Having explored the QCD phase transition and the emergence of QGP, we now pivot to ultra-relativistic heavy-ion collisions. Similar to the early Universe, these collisions provide insights into the properties and behavior of QGP. Let us explore how these collisions shed light on the principles of cosmic evolution and fundamental physics.

1.4 Ultra-relativistic heavy-ion collisions

Each field of research has a pioneer, and the study of quark-gluon plasma is no exception. Rolf Hagedorn used statistical physics to explore particle production using the statistical bootstrap model (SBM) in 1964. The statistical bootstrap model considers a gas of interacting hadrons in a thermal bath, which includes all possible particles and their resonances. Many massive resonances were observed then, and this model successfully explained how these particles were produced. Thus, the hadron gas can be considered a gas of fireballs that can become a fireball upon compression. This framework provided a comprehensive explanation for the mass spectrum of hadronic states. However, Johann Rafelski managed to transform the SBM into a model that could accommodate quarks, which was an outstanding achievement [28, 29]. It was recognized that hadrons melt at a specific temperature, giving rise to the QGP phase. However, this concept has already been intuited by several physicists before. Still, the connection between the QGP and relativistic heavy-ion collisions was first suggested by Chaplin and Kerman, with subsequent quantitative analyses by Siu A. Chin [30] and James D. Bjorken in 1983 [31]. Bjorken's analytical solution for relativistic hydrodynamics in heavy-ion collisions and his description of the space-time evolution of the QGP, known as the Bjorken scenario, laid the foundation for research programs at CERN.

Experimental efforts to investigate the QGP strengthened with the operation of the Relativistic Heavy Ion Collider (RHIC) at BNL, which started in the early 2000s. The confirmation of a new state of matter, similar to the QGP, was revealed by CERN in February 2000, following experiments with heavy-ion collisions at the Super Proton Synchrotron (SPS) [32], and became turning point in the theoretical concept of partonic matter, became empirically validated. Our understanding of the properties of QGP is validated by subsequent experiments of

1.4 Ultra-relativistic heavy-ion collisions

RHIC such as BRAHMS [33], PHOBOS [34], PHENIX [35], and STAR [21]. The focus of QGP research expanded with the commissioning of the Large Hadron Collider (LHC) at CERN in 2009. It consists of four primary experiments: ALICE, CMS, ATLAS, and LHCb. Among its four main experiments, ALICE stands out for its dedicated study of the QGP. By colliding lead nuclei at unprecedented energies, the LHC, particularly ALICE, aims to explore the QCD phase diagram and characterize the QGP in greater detail at much higher energies than RHIC. For comparison, the LHC delivers Pb-Pb collisions at a center-of-mass energy per nucleon $\sqrt{s_{NN}} = 2.76$ and 5.02 TeV, and Xe-Xe collisions at $\sqrt{s_{NN}} = 5.44$ TeV. This is about 14 to 25 times more energetic than the top RHIC energies.

1.4.1 Geometrical aspects of heavy-ion collisions

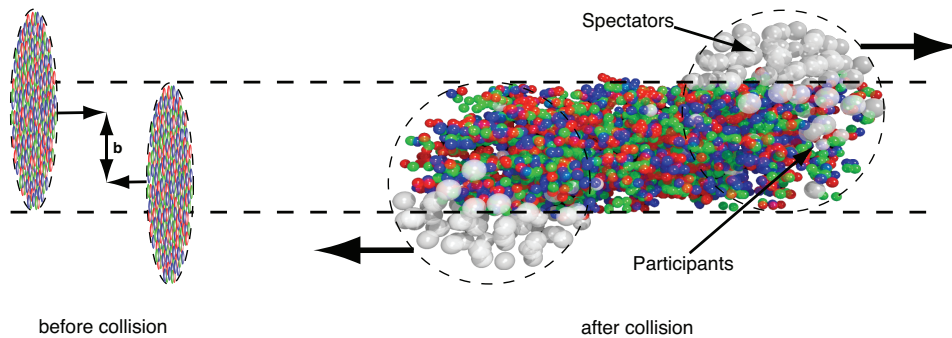


Figure 1.5: Schematic picture of ultra-relativistic heavy ion collisions [36].

A geometric representation of the collision of two symmetric heavy ions is depicted in Fig. 1.5. At ultra-relativistic energy, the projectile and target beams are Lorentz contracted along the direction of motion (generally taken as the z -axis). The distance between the centers of the colliding nuclei perpendicular to their motion is termed the impact parameter (b), determining the collision's centrality. The nucleons colliding in the overlap region are called participant nucleons (N_{part}). Nucleons that do not participate in collisions are spectators

($N_{\text{spectator}} = 2A - N_{\text{part}}$, where A is the nucleus' mass number). Impact parameter values range from 0 fm (representing head-on collisions) to approximately twice the nucleus's radius (characterizing peripheral collisions). The impact parameter (b) cannot be directly measured experimentally. However, the number of charged particles produced in collisions determines collision geometry, also known as centrality or multiplicity. Central collisions involve many participating nucleons, small impact parameters, or a high count of produced charged particles. Conversely, peripheral collisions have fewer participating nucleons, a more significant impact parameter value, or fewer final charged particles produced. A transient substantial magnetic field is produced at the RHIC and the LHC energies due to spectator protons in non-central heavy ion collisions. The order of magnetic field $eB \sim (m_\pi^2) \sim 10^{18}\text{G}$ at RHIC and $eB \sim (15m_\pi^2)$ at the LHC, respectively where m_π is the mass of a pion have been observed. The transient magnetic field generated in such collisions represents the strongest observed magnetic field. It stresses the importance of investigating its effects on hot and dense matter formed in hadronic and non-central heavy-ion collisions. Not only temperature (T) and μ_B but also magnetic fields (B) can affect the equation of state (EoS), which plays an essential role in understanding the phase diagram. We have a detailed discussion on this in chapter 3.

1.4.2 The time evolution of a heavy-ion collision

In the high-energy collision experiment, two Lorentz contracted extremely boosted nuclei approach towards each other at ultra-relativistic speed. The collision takes place at proper time $\tau = 0$ and $z = 0$. The overlapping region determines the impact parameter of the colliding nuclei at the interaction point. The system generated in heavy-ion collisions goes through multiple stages of transition, as Fig. 1.6 and Fig. 1.7 illustrate, from a quark-gluon plasma state to a hadron gas state.

1.4 Ultra-relativistic heavy-ion collisions

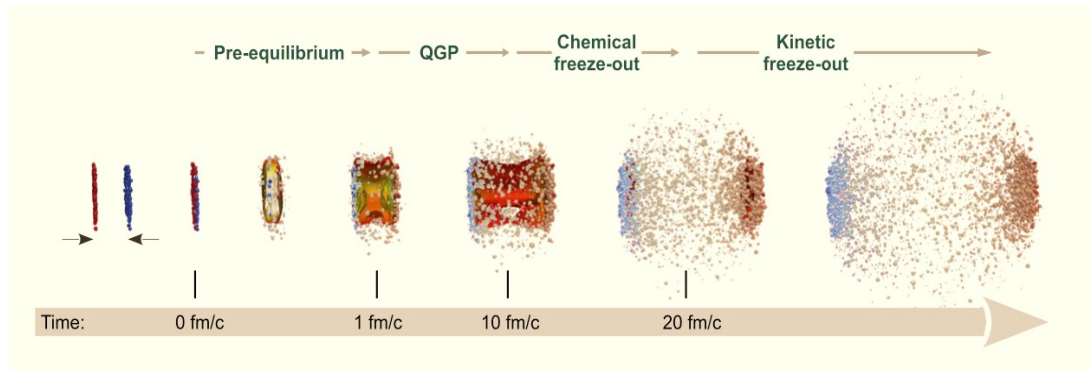


Figure 1.6: Schematic diagram representing various stages of heavy-ion collisions as a function of time [37].

- **Pre-equilibrium stage:** Following the collision, a significant amount of kinetic energy is deposited in the overlap region between the two colliding nuclei within a small volume and over a short time interval. Each nucleus's partons start interacting either through hard processes, which are characterized by large momentum transfers and give rise to massive quarks such as charm, bottom, or even top quarks, or through soft processes, which are characterized by small momentum transfers and control the early stages of the collision. As the number of parton-parton interactions increases, the system's energy density becomes sufficiently high, creating quarks and gluons from the vacuum. However, this dense state of matter where partons are strongly coupled but not yet thermalized at timescales less than 1fm/c.
- **QGP evolution:** A Quark-Gluon Plasma (QGP) is formed when the fireball reaches the critical temperature and energy density, and a local equilib-

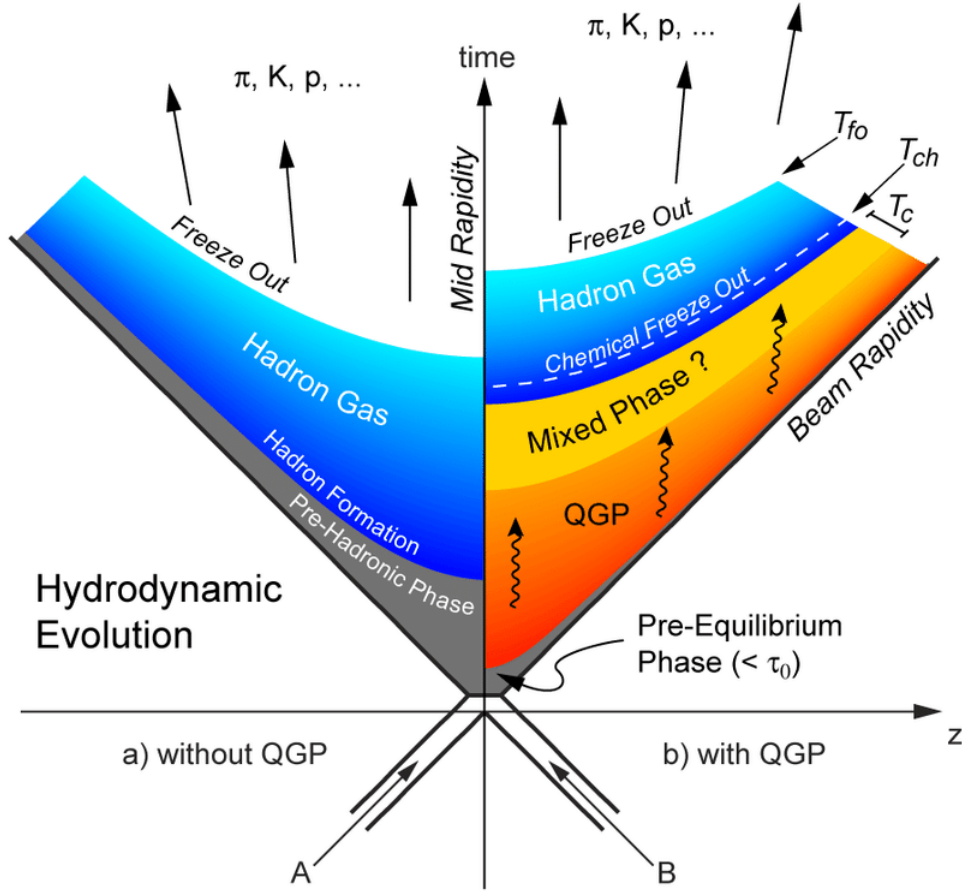


Figure 1.7: A schematic diagram of the space-time evolution of relativistic nucleus-nucleus collision [38].

rium is formed. QGP is produced when the critical energy density is more than $1 \text{ GeV}/\text{fm}^3$ or when the critical temperature (T_c) is exceeded, according to lattice QCD calculations. Within the QGP, elastic and inelastic interactions among quarks and gluons lead to a thermalization phase. These inelastic interactions alter the flavor composition of the system's partons. Due to the high internal pressure and temperature, the system undergoes rapid expansion. The mixed phase starts when the QGP cools down and changes into a hadron gas.

1.4 Ultra-relativistic heavy-ion collisions

- **Hadron gas phase and freeze-out** There are two main mechanisms of hadronization from QGP: fragmentation and coalescence. At high energies, fragmentation predominates, leading to the fragmentation of a high transverse momentum (p_T) parton into lesser p_T hadrons. On the other hand, coalescence involves lower momentum partons combining to form higher p_T hadrons. Following hadronization, hadrons interact through elastic and inelastic interactions until freeze-out occurs. Chemical freeze-out is reached when inelastic collisions cease, where the stable particle ratios are fixed. The corresponding temperature is known as the chemical freeze-out temperature (T_{ch}). Elastic collisions still occur during this phase. Kinetic or thermal freeze-out occurs when the mean free path becomes sufficiently large, causing elastic collisions among hadrons to cease and the temperature known as the kinetic freeze-out temperature (T_{fo}). At this stage, the particles' transverse momentum spectral shape becomes fixed. Following the freeze-out, all the particles fly toward the detector and are detected. However, in scenarios where the matter produced in heavy-ion or hadronic collisions does not reach the high temperature or energy density required, a different space-time evolution is possible, as shown on the left side of Fig. 1.7. In such circumstances, the system has only hadronic degrees of freedom. A pre-hadronic phase is created immediately after the collisions, during which nucleons can recombine into new hadrons. The produced hadrons can then be detected following the freeze-out of the hadron gas phase.

Next, we will examine the vital observables that could provide insights into the formation of QGP droplets in small systems and QGP in nuclear collisions. These observables are essential for identifying and understanding the signatures of QGP.

1.5 Signatures of QGP

Due to the small lifespan of the QGP, which is only a few femtoseconds, direct observation of its detection is not feasible, unlike ordinary electromagnetic plasma. When the QGP medium forms, it undergoes expansion, cooling, and hadronization, eventually producing a final state of hadrons. Observing each stage separately in experiments is not possible. Instead, we measure time-integrated final state quantities such as charged particle multiplicities, photon or lepton multiplicities, particle transverse momentum spectra, energy, and anisotropic flow. The various processes during the fireball's time evolution leave footprints on these final state observables, preserving some temporal information. Different signatures telling of QGP formation include collective flow, strangeness enhancement, jet quenching, J/ψ suppression, etc., discussed below.

1.5.1 Collective flow

QGP is a nearly perfect liquid with constituents that have a tiny mean-free path. During heavy-ion collisions, the pressure gradient creates a collective flow that develops mainly at the partonic stage, which can be described using ultra-relativistic hydrodynamic models. This flow is investigated through measurements sensitive to both radial/isotropic and anisotropic components, where low- p_T hadrons are boosted to higher p_T , with heavier hadrons receiving a more significant boost. The collective motion of partons can also be observed through the long-range particle correlations in rapidity.

In non-central heavy-ion collisions, the overlap region takes an almond shape, leading to a maximum pressure gradient along the minor axis and a minimum along the major axis, as shown in Fig. 1.8. The initial spatial anisotropy created in non-central heavy-ion collision reflects in the momentum anisotropy to the final state particles, which is characterized by the elliptic flow (v_2). v_2 is the second

1.5 Signatures of QGP

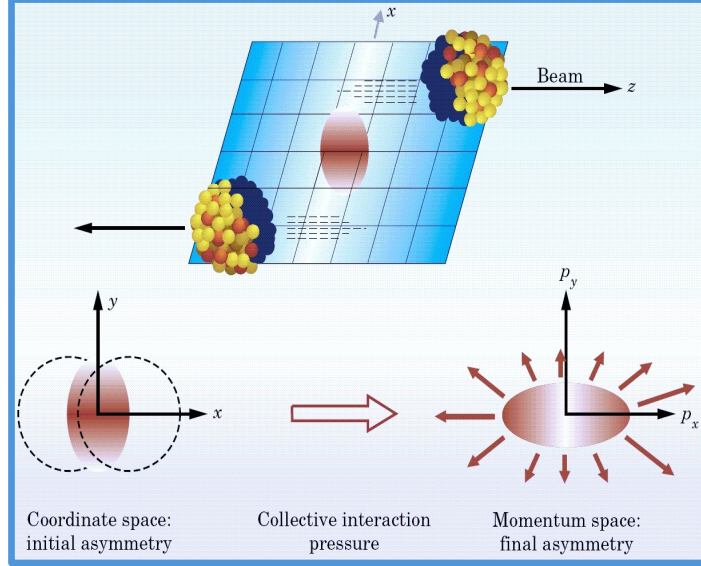


Figure 1.8: A schematic representation of a non-central heavy-ion collision with an almond-shaped interaction volume [39].

harmonics coefficient of Fourier expansion of the azimuthal distribution of emitted particles and is very important to understand the system's initial conditions and collective dynamics. The expression for this Fourier expansion is [40–43]:

$$E \frac{d^3 N}{dp^3} = \frac{d^2 N}{2\pi p_T dp_T dy} \left[1 + 2 \sum_{n=1}^{\infty} v_n \cos[n(\varphi - \psi_n)] \right]. \quad (1.3)$$

Here v_2 is the elliptic flow coefficient. φ represents the azimuthal angle and ψ_R is the reaction plane angle, the angle between the impact parameter and beam axis in heavy ion collisions. With Pb–Pb collisions at the LHC, a partonic phase with a relatively larger lifetime is expected to be produced compared to Au–Au collisions at RHIC energies. Consequently, this leads to a lower hadronic contribution to the elliptic flow. Figure 1.9 illustrates the p_T -differential elliptic flow for Pb–Pb and Au–Au collisions at $\sqrt{s_{NN}} = 2.76$ TeV and 200 GeV, respectively,

across various centrality classes. Despite the differences in systems and energies, the p_T -differential elliptic flow displays a similar trend for both collision types.

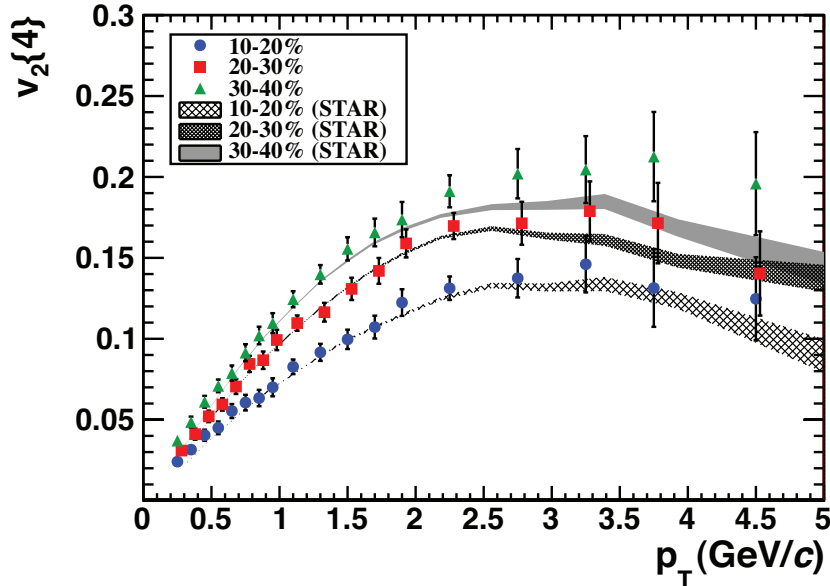


Figure 1.9: Comparison of the charged particles p_T -differential elliptic flow for Pb–Pb collisions at $\sqrt{s_{NN}} = 2.76$ TeV in solid markers to Au–Au collisions at $\sqrt{s_{NN}} = 200$ GeV that represents in shaded regions. [42, 43].

1.5.2 Strangeness enhancement

J. Rafelski and B. Muller proposed that the enhanced production of strange particles in heavy-ion collisions could be a signature of QGP formation, as the colliding matter initially contains no strange quantum numbers [44, 45]. Strange particles' production rate and mechanism in the QGP medium differ significantly from those in a hadron gas. One can gain insights into strangeness enhancement by comparing the abundance of strange particle production in the hadronic and QGP phases. In the QGP medium, strange quarks are produced through processes like flavor creation ($gg \rightarrow s\bar{s}$, $q\bar{q} \rightarrow s\bar{s}$), flavor excitation ($gs \rightarrow gs$, $qs \rightarrow qs$), and gluon splitting ($g \rightarrow s\bar{s}$). Due to the high gluon density in the

1.5 Signatures of QGP

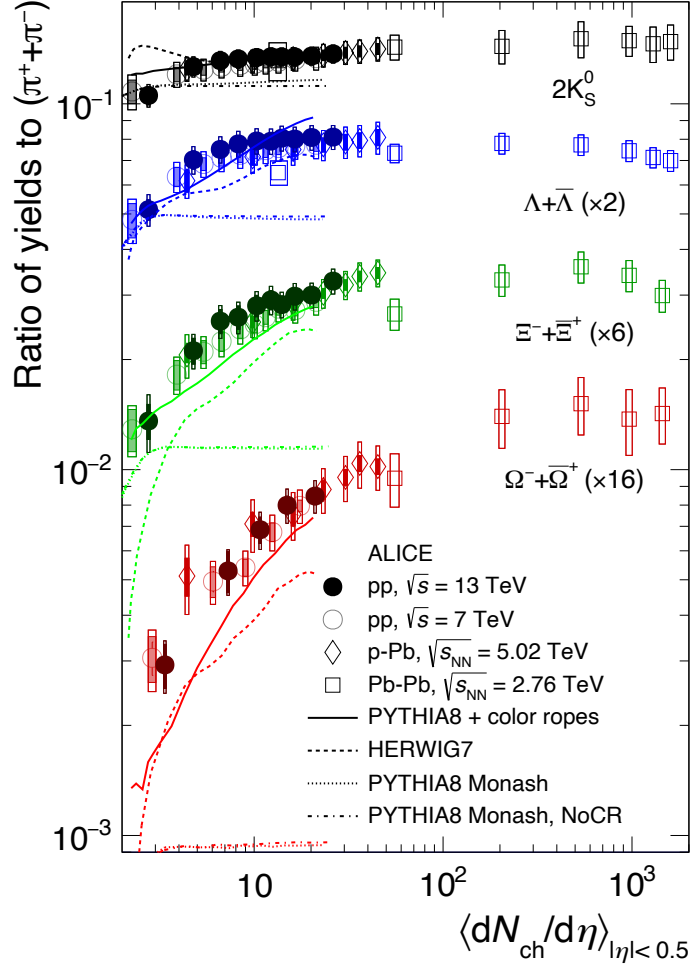


Figure 1.10: Integrated strange hadron-to-pion ratios as a function of charged particle multiplicities in pp, p-Pb, and Pb-Pb collisions at LHC energies. Different lines represent predictions from different MC generators for pp collisions at $\sqrt{s} = 13$ TeV [46, 47].

QGP, the $s\bar{s}$ pairs formed via the $g\bar{g} \rightarrow s\bar{s}$ channel dominate over those from the $q\bar{q} \rightarrow s\bar{s}$ channel. Conversely, in pp collisions, where QGP formation is not usually expected, the primary mechanism for producing strange quarks is the annihilation of light quarks into strange quarks. This difference is quantified by

the enhancement factor, defined as:

$$\text{Enhancement factor} = \frac{2}{\langle N_{part} \rangle} \frac{\text{Yield}_{AA}}{\text{Yield}_{pp}} \Big|_{y=0}. \quad (1.4)$$

Here, $\langle N_{part} \rangle$ represents the average number of participants. An enhancement factor value greater than unity indicates an enhancement in strangeness production. Interestingly, recent observations have shown that strangeness enhancement is not limited to heavy-ion collisions; it has also been detected in high-multiplicity pp collisions. The ALICE experiment reported an increase in the production of strange and multi-strange particles relative to pions in this high-multiplicity pp collisions [46, 47], as illustrated in Fig. 1.10. This phenomenon is considered one of the signatures of the possible formation of QGP droplets in high-energy hadronic collisions.

1.5.3 Jet quenching

The discovery of suppression in producing high- p_T mesons is one of the significant results from RHIC, providing a hint of QGP medium formation. In relativistic heavy-ion collisions, partons with very high- p_T are created, which travel in all directions from the collision points and eventually fragment into narrow cones of hadrons, known as jets. These highly energetic secondary parton showers are referred to as jets. When these jets penetrate the thermalized QGP medium, they interact with the particles, losing energy and momentum before hadronizing. This results in suppression observed in nucleus-nucleus collisions compared to corresponding data from pp collisions scaled by the number of binary collisions [48, 49]. This phenomenon is known as jet quenching. The suppression of high- p_T particles is typically expressed in terms of the nuclear modification factor (R_{AA}):

$$R_{AA}(p_T) = \frac{1}{\langle N_{coll} \rangle} \frac{\text{Yield}_{AA}}{\text{Yield}_{pp}}. \quad (1.5)$$

1.5 Signatures of QGP

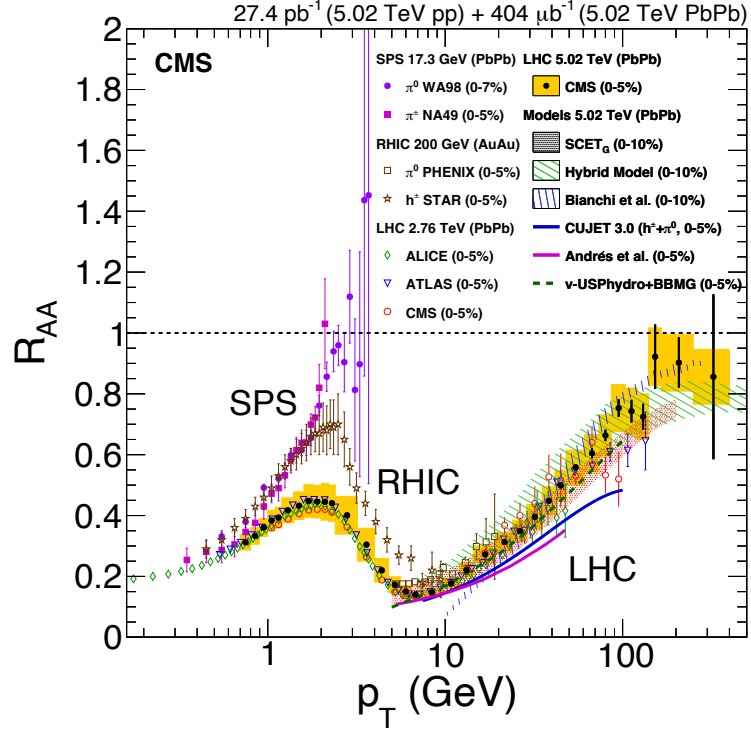


Figure 1.11: $R_{AA}(p_T)$ for charged hadrons (h^\pm) and neutral pions (π^0) in central heavy-ion collisions at SPS, RHIC, and the LHC [50].

Here, $\langle N_{coll} \rangle$ represents the average number of binary collisions in a single nucleus-nucleus collision. R_{AA} value of 1 suggests that heavy-ion collisions are merely a linear superposition of pp collisions, indicating no QGP medium formation. However, observations show that $R_{AA} < 1$ for identified particles in Pb–Pb or Au–Au collisions [43]. This indicates that the QGP medium causes high- p_T particles to lose energy through multiple interactions as they traverse it. Fig. 1.11 presents the R_{AA} results for charged particles and neutral pions, as measured by various experiments. An apparent suppression of hadrons is observed at both LHC and RHIC, reinforcing the presence of jet quenching in these collisions [50].

1.5.4 J/ψ suppression

The J/ψ is a bound state of a charm, and an anti-charm quark ($c\bar{c}$) is produced early in heavy-ion collisions through hard scatterings. Since J/ψ are generated in the initial stages of these collisions, they experience the entire evolution of the produced system, making them valuable probes for studying the dynamics of the medium formed in such collisions. Theoretical models predict that the production of J/ψ in heavy-ion collisions will be suppressed compared to pp collisions [51].

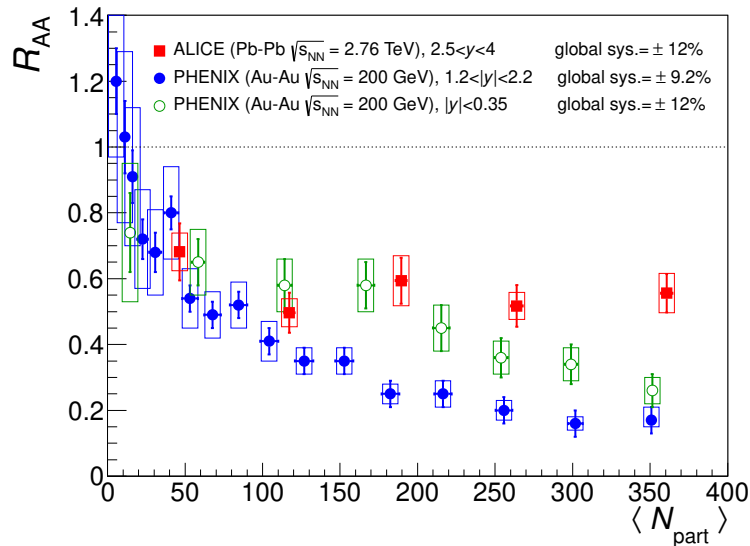


Figure 1.12: R_{AA} of J/ψ in Pb–Pb collisions at $\sqrt{s_{NN}} = 2.76$ TeV and Au–Au collisions at $\sqrt{s_{NN}} = 200$ GeV as a function of an average number of participant nucleons [52].

This suppression is attributed to color Debye screening in the QGP medium, where the presence of quarks and gluons hinders the formation of a bound state between a charm and an anti-charm quark. Thus, J/ψ suppression is considered a signature of QGP. Experimentally, this suppression was first observed at the SPS [53] and later at RHIC [54, 55], confirming the formation of QGP. The nuclear modification factor (R_{AA}) of J/ψ as a function of centrality at RHIC and LHC

1.6 Connection between the collider and cosmic ray physics

energies is shown in Fig 1.12. It is observed that J/ψ is more suppressed in RHIC energy. On the other hand, this suppression can be counter-balanced at the LHC energy by regenerating the quarkonium states because of the availability of higher energy phase space.

Let us pivot our discussion from the complex dynamics of ultra-relativistic heavy-ion collisions, where we've examined the different phases of their evolution and the various signatures of QGP, to a fascinating intersection between collider physics and cosmic ray phenomena. Here, we will explore how the knowledge gathered from particle collisions within accelerators can elucidate our understanding of cosmic rays, providing valuable insights into fundamental processes that shape the Universe.

1.6 Connection between the collider and cosmic ray physics

The primary goal of the collider and cosmic ray physics experiments is to study and explore the unknown mystery of fundamental particles and their interactions. The LHC is one of the collider experiments that replicate similar conditions that are experienced in the cosmic ray air shower collisions in the Earth's atmosphere. Accordingly, it is helpful for researchers to investigate the behavior of these particles under such a controlled environment. Using these experiments, one can examine the properties of particles like proton, pion, kaon, and Higgs boson and understand the dynamics of their interactions. The different theoretical models which are used to understand the cosmic ray sources, propagation, and acceleration in the atmosphere, can be refined using the collider experiment data. On the other hand, the energy of cosmic rays is much higher than that achievable in a collider experiment, allowing us to test various theoretical models (primarily hadronic interaction models). Observations of cosmic rays, particularly at ultra-

high energies, challenge our understanding and push the boundaries of current particle physics theories.

Further, the data produced by the secondary particles of cosmic rays in the Earth's atmosphere gives us very useful informations that complements the collider experiment like the LHC. Ground-based detectors collect extensive information regarding the secondary particles produced, which enriches our understanding of these ultra-high energetic particles in a natural environment. This synergy between the collider and cosmic ray physics motivates us to take a broad approach to studying the Universe's most energetic phenomenon at the highest energy level. Once we combine colliders and cosmic ray physics, one can gather knowledge on particles and the fundamental forces that govern them, which will eventually enhance our understanding of high-energy particle and astroparticle physics.

In the following section, let us explore the cosmic rays, their origins, energy spectrum, and composition in detail.

1.7 Cosmic rays and its origin

High-energy charged particles traveling at relativistic speeds, known as Cosmic Rays (CRs), continuously bombard the Earth's surface from outer space. These particles arrive in an almost isotropic manner and exhibit a broad range of energies, from approximately 10^8 eV to nearly 10^{20} eV. The existence of cosmic rays was first inferred from observations of increased ionization in the atmosphere, which known radiation sources could not explain. In 1912, Victor Hess conducted a series of balloon flights to measure ionizing radiation at various altitudes. His crucial discovery came on August 7, 1912, during his final flight when he carried three electroscopes to an altitude of 5350 meters. Hess observed a decrease in ionization levels up to 1400 meters, followed by a significant increase to nearly four times the level at the ground. This crucial observation led Hess to conclude

1.7 Cosmic rays and its origin

that the radiation had an extraterrestrial origin [56]. To further investigate, Hess conducted measurements during a solar eclipse to rule out the sun as the source of this radiation. Hess was awarded the Nobel Prize in 1936 for his groundbreaking work in discovering cosmic rays. His findings were later corroborated by Werner Kolhörster, who conducted observations at even higher altitudes, reaching 6200 meters in 1913 [57] and 9300 meters in 1914 [58]. Fig. 1.13 illustrates the result obtained by V. Hess and W. Kolhörster.

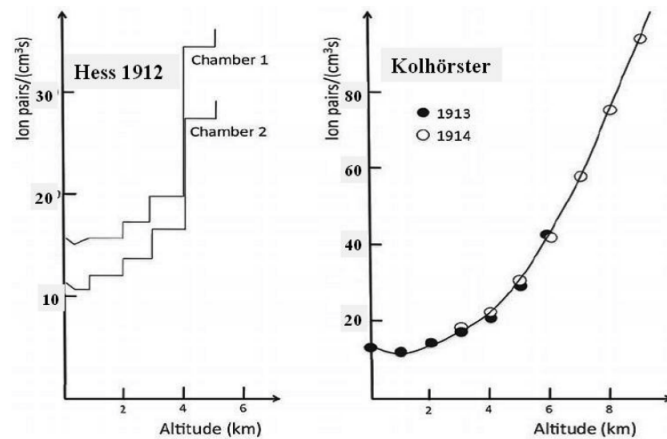


Figure 1.13: Results obtained by Victor Hess (left) and W. Kolhörster (right) during their balloon flights [59].

Throughout the 20th century, extensive research provided more profound insights into the nature and origin of cosmic rays. Scientists discovered that cosmic rays consist primarily of high-energy protons and atomic nuclei, originating from various astrophysical sources such as the Sun, distant stars, supernovae, and active galactic nuclei. Approximately 98% of cosmic rays are composed of atomic nuclei, while the remaining 2% are electrons. Among these nuclei, over 87% are protons, 12% are helium nuclei, and the remaining 1% are other heavy nuclei [60].

Cosmic rays originate from different sources depending on their energy levels. Those with energies around 10^9 eV are typically attributed to the Sun. Cosmic rays with energies up to nearly 10^{17} eV are believed to come from within

our galaxy, while higher-energy cosmic rays may originate from extra-galactic sources. Potential sources include Supernova Remnants (SNRs) [61, 62], Gamma-Ray Bursts (GRBs) [63, 64], and Active Galactic Nuclei (AGNs) [65, 66]. Electrically neutral particles such as γ -rays and neutrinos are unaffected by the interstellar magnetic field (IMF), allowing them to indicate their sources directly. In contrast, cosmic ray protons diffuse in the IMF with a lifespan of nearly 10^6 years, causing them to lose directional information about their origins. As a result, even after a century of research, the exact sources of cosmic rays still need to be discovered.

The broad energy range of cosmic rays presents significant challenges for single experiments to explore the entire spectrum. Consequently, numerous experiments are conducted to detect cosmic rays across various energy ranges. There are two main types of cosmic ray detection: direct and indirect. Direct detection experiments use satellites or high-altitude balloons to observe cosmic rays above or in the upper atmosphere. Indirect detection experiments sample the secondary particles of extensive air showers using various detection systems on or below the ground, which will be discussed in detail in the 1.10.

1.8 Cosmic rays energy spectrum

The cosmic ray energy spectrum is crucial for understanding cosmic rays' origin, acceleration, and propagation. By analyzing spectral features, researchers gain insights into the confinement of cosmic rays in the galaxy, the transition from galactic to extra-galactic origins, the maximum energy of cosmic rays, and changes in the spectrum during propagation. The cosmic ray energy spectrum depicts the relationship between cosmic ray flux (F) and energy, defined as:

$$F = \frac{dN}{dA d\Omega dt} m^{-2} sr^{-1} s^{-1}. \quad (1.6)$$

1.8 Cosmic rays energy spectrum

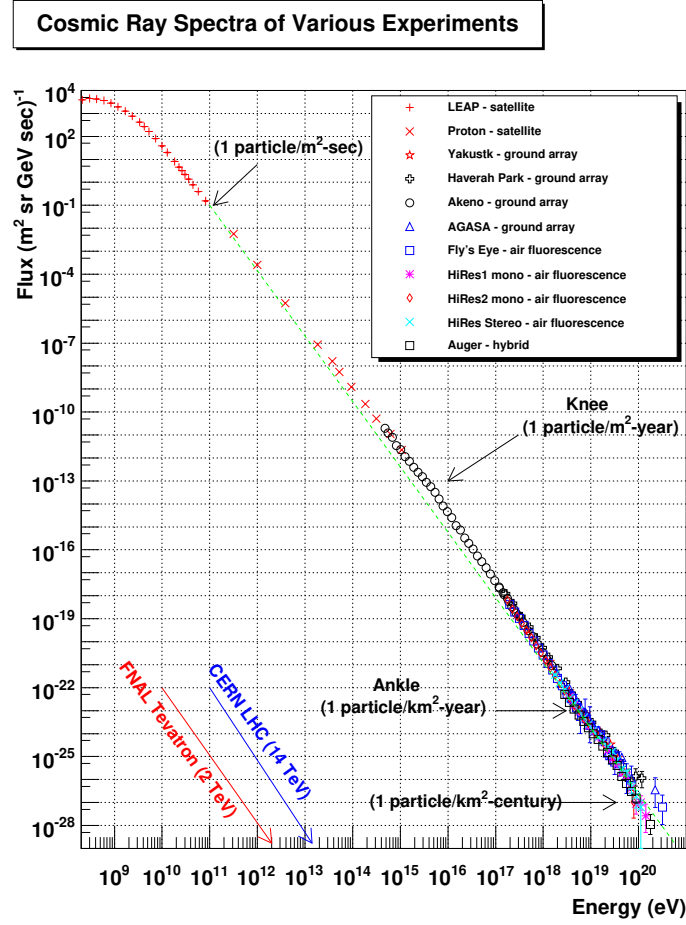


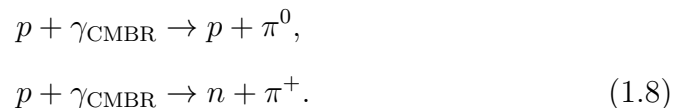
Figure 1.14: Cosmic rays energy spectrum measured by different direct and indirect experiments [67].

dN is the number of cosmic rays recorded, dA is the effective area, $d\Omega$ is the viewing solid angle, and dt is the observation time. Fig. 1.14 depicts the measured energy spectrum by various experiments, with the differential flux ($\Phi = \frac{dF}{dE}$) plotted against energy on a log-log scale. The flux, Φ , shifts by about 32 orders of magnitude over 12 orders of magnitude in energy, following a non-thermal inverse power law:

$$\Phi = kE^{-\gamma} m^{-2} sr^{-1} s^{-1} eV^{-1}. \quad (1.7)$$

k is the normalization constant, and γ is the spectral slope, ranging from 2.5 to 3.2. Fig. 1.14 indicates the value of Φ decreases rapidly with increasing energy. For instance, at 10^{11} eV, there is about one cosmic ray particle $\text{m}^{-2}\text{s}^{-1}$, which decreases to approximately one particle $\text{m}^{-2}\text{yr}^{-1}$ at 10^{16} eV, and one particle $\text{km}^{-2}\text{century}^{-1}$ at 10^{20} eV. The magnetized solar plasma affects the spectrum below 10^{10} eV and is known as solar modulation. Key features in the all-particle energy spectrum include:

- **Knee:** Around 3×10^{15} eV, the spectral slope γ changes from 2.7 to 3.1, first observed by Kulikov and Khrisriansen in 1958 [68]. Various models explain the knee, linking it to the maximum acceleration within diffusive shocks in galactic supernova remnants [69–71], leakage from galactic magnetic confinement [72, 73], or particle acceleration in shock waves [74].
- **Ankle:** Around 5×10^{18} eV, where the spectrum hardens, changing γ from 3.1 to 2.75, marking the transition from galactic to extra-galactic cosmic rays [75, 76], confirmed by Telescope Array (TA) [77] and Auger [78, 79].
- **Greisen-Zatsepin-Kuzmin (GZK) cutoff:** Around 5×10^{19} eV, Greisen, Zatsepin, and Kuzmin [80, 81] predicted that cosmic ray protons interact with the cosmic microwave background radiation, leading to energy losses through reactions such as [82]:



These interactions impose an upper energy limit on cosmic ray protons. The HiRes experiment [83] first confirmed the GZK cutoff and was later confirmed by Auger [84] and TA [85].

1.9 Composition of cosmic rays

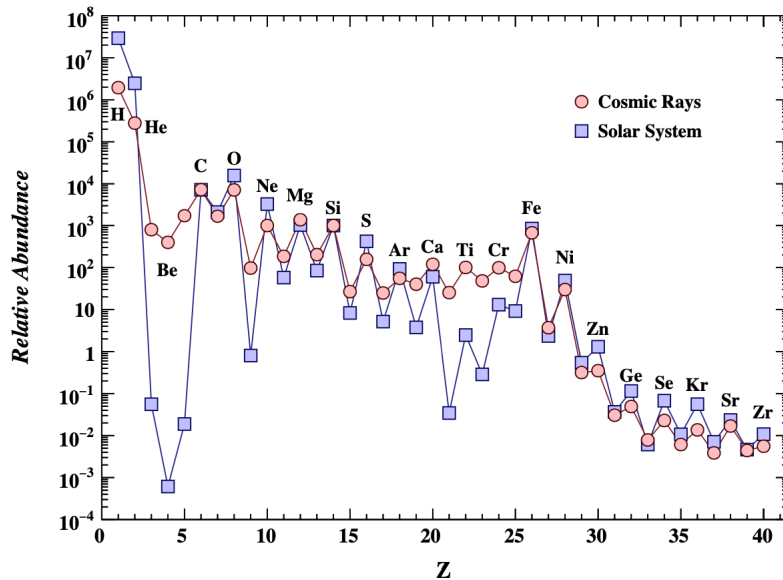


Figure 1.15: Cosmic ray elemental abundances compared to abundances in present-day solar system material. Abundances are normalized to $\text{Si} = 10^3$ [76].

The mass composition of cosmic rays provides valuable insights into their sources and propagation. We can deduce crucial information by comparing cosmic ray compositions with those of various astrophysical sources. Figure 1.15 compares cosmic ray elemental abundances and present-day solar system material at energies around 10^9 eV/nucleon [76]. Using silicon as the reference point with a relative abundance of 1000, both compositions show good agreement and exhibit the even-odd effect, indicating the stability of nuclei with even numbers of protons. This similarity suggests a common origin with stellar nucleosynthesis. However, there are notable differences:

- **Lower H and He abundance:** Cosmic rays have a lower relative composition of hydrogen and helium than solar composition, potentially due to

different source compositions or constraints in particle acceleration related to their higher ionization potentials. However, the precise cause of this difference has yet to be understood entirely.

- **Higher abundance of lighter and heavier groups:** The relative composition of lighter elements (Li, Be, B) and heavier elements (Sc, Ti, V, Cr, Mn) is higher in cosmic rays than in solar material. This is due to the spallation of C and O into lighter elements and Fe into heavier elements during cosmic rays' propagation through the interstellar medium (ISM). Analyzing this difference alongside spallation cross-sections helps understand cosmic ray propagation and confinement within the galaxy.

Precise mass composition measurements have been obtained through direct experiments, but extrapolating these results to higher energies is challenging due to potential differences in elemental energy spectra profiles. Ground-based experiments such as GRAPES-3 [86, 87], KASCADE [88], IceTop [89], TA [90], and Auger [91] have estimated mass compositions, but their results show systematic discrepancies. Additionally, hadronic interaction models in Monte Carlo (MC) simulations introduce significant systematic uncertainties.

Having thoroughly explored the origins, energy spectrum, and composition of cosmic rays, let us now explore the techniques used for their detection.

1.10 Detection of cosmic rays

Due to atmospheric absorption, extensive air showers (EAS) generated by primary cosmic rays (PCR) with energies around the GeV range cannot reach sea level effectively. However, their significantly higher flux permits direct detection in the upper atmosphere or above using detectors on satellites (about 400 km altitude) or balloon flights (about 40 km altitude). These direct experiments offer good

1.10 Detection of cosmic rays

energy and charge resolution but face two main limitations. The first limitation is related to the detector's configuration, including the magnetic field strength, detector volume, and tracking system resolution, which collectively determine the highest energy that can be detected. Secondly, the rapid decline in cosmic ray flux with increasing energy limits the number of detectable events. As a result, at energies above 100 TeV, the smaller flux and limited exposure (a product of the detector's geometric acceptance and total live time) necessitate better statistics for direct observations.

Magnetic spectrometers AMS [92, 93] and PAMELA [94] provide high-precision energy measurements but are limited to detecting cosmic ray proton and helium spectra up to TeV/nucleon energies due to their limited exposure. Calorimetric detectors such as JACEE [95] and RUNJOB [96] can record cosmic rays up to nearly 100 TeV but have lower energy resolution due to event-to-event fluctuations. Hybrid detectors like CREAM-III [97] and DAMPE [98] offer precise measurements with substantial exposure up to or above 100 TeV. Large ground-based detectors, spanning ~ 0.1 kilometer to thousands of square kilometers and operating for years, indirectly detect cosmic rays above 100 TeV by sampling secondary particles from extensive air showers. These include a scintillator detector (SD), water Cherenkov detector (WCD), and resistive plate chamber (RPC), which sample the lateral distribution of extensive air shower particles and model shower parameters. Though they have a 100% duty cycle, their energy resolution is limited by shower-to-shower fluctuations. Cherenkov and fluorescence telescopes, capturing the longitudinal profile of extensive air showers, offer excellent energy resolution but have a 10% duty cycle restricted to clear, moonless nights.

Currently, many indirect experiments operate with varying energy ranges, resolutions, and sensitivity to mass composition, influenced by elements such as detector array coverage, geometrical deployment, detector spacing, and observation site altitude. The lower energy threshold relies on the array's compactness, as low-energy extensive air showers have a smaller lateral spread of secondary

particles, demanding tighter detector placement to generate triggers and record sufficient particles. Conversely, higher energy extensive air showers spread over kilometers, necessitating a larger detector array to record effectively, defining the experiment's upper threshold. The following section will delve into a detailed discussion of extensive air showers.

1.11 Extensive Air Showers

Ground-based detectors with extensive coverage and operating for extended periods can measure cosmic rays with energies surpassing 100 TeV. When primary cosmic ray particles or high-energy γ -rays enter the atmosphere, they collide with air molecule nuclei (primarily nitrogen), producing secondary particles that move toward the primary particle's momentum. The first interaction's depth depends on the interaction cross-section of the incident primaries and the atmospheric density. Thus, the interaction cross-section distribution affects the depth of the initial interaction, leading to shower-to-shower fluctuations. The secondary particles generated in this initial collision either continue interacting with air nuclei or decay, depending on atmospheric density and their lifespans, creating more secondary particles and initiating the EAS cascade. As the EAS develops, the average energy of secondary particles decreases until it falls below the critical energy. At this point, the production of new secondary particles stops. The EAS is then attenuated through absorption or scattering by the atmosphere. The shower maximum is the point at which the particles' energy equals the critical energy. EAS development can be categorized into two types based on the nature of the incident primary: electromagnetic (EM) showers and hadronic showers.

1.11 Extensive Air Showers

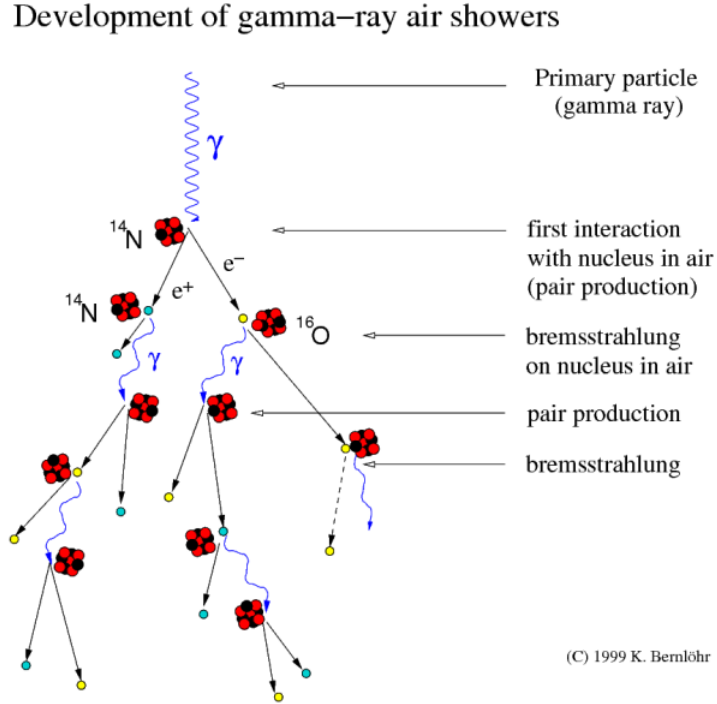


Figure 1.16: Schematic of EAS development for a high energy γ -ray [99].

1.11.1 Electromagnetic showers

Cosmic ray e^-/e^+ or γ -rays interact exclusively through electromagnetic interactions. When high-energy γ -rays traverse the atmosphere, they produce $e^- - e^+$ pairs via pair production, facilitated by the strong electric field of an air nucleus (X):

$$\gamma + X \rightarrow e^- + e^+ + X. \quad (1.9)$$

The contribution of μ^\pm pair production is negligible. The e^\pm particles subsequently generate γ -rays near the air nucleus (X) through the bremsstrahlung process:

$$e^\pm + X \rightarrow e^\pm + \gamma + X. \quad (1.10)$$

These processes repeat, creating a cascade of electromagnetic interactions. The development of an EAS for a high-energy γ -ray is illustrated in Fig.1.10.

Due to the low muon content in EM showers, observed muon data can help differentiate EM showers from hadronic showers.

Heitler's model [100] provides insight into the development of electromagnetic showers along their axis. According to this model, when e^\pm undergo bremsstrahlung, they split their energy with a resulting γ -ray. Similarly, the γ -ray produces an $e^- - e^+$ pair of equal energy after each radiation length ($\lambda_r \approx 37, \text{g/cm}^2$ for air). The number of secondary particles doubles after each λ_r , continuing until $E = E_c^{em}$ ($E_c^{em} = 80 \text{ GeV}$ in the air). At this point, the EAS reaches its maximum number of secondary particles.

1.11.2 Hadronic showers

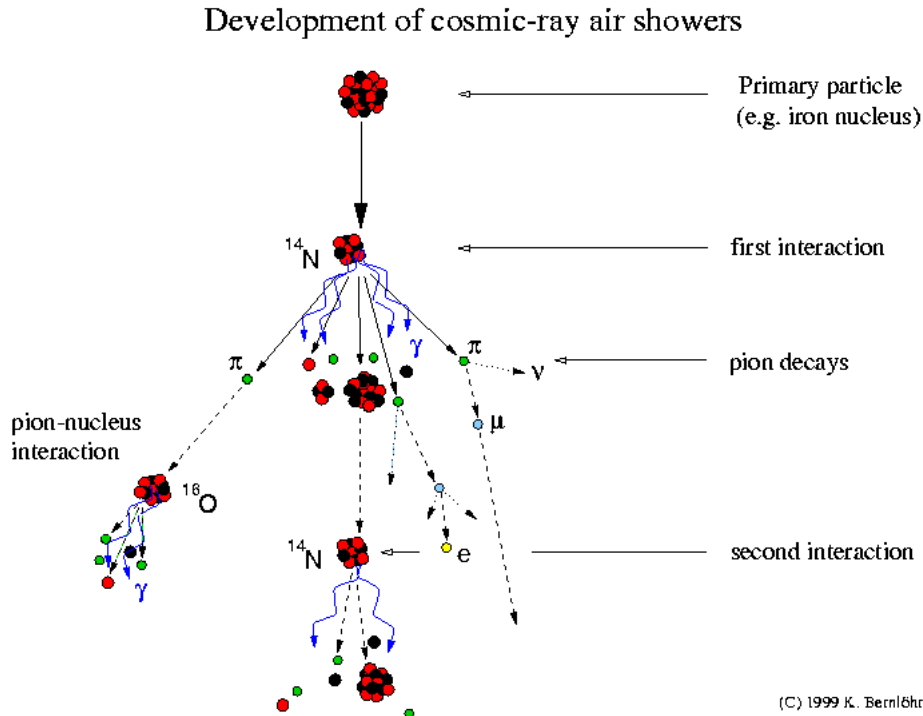


Figure 1.17: Schematic of EAS development for a cosmic ray primary [99].

1.11 Extensive Air Showers

When a primary cosmic ray, such as a proton, collides with the nuclei of an air molecule (denoted as X), it initiates a cascade of particle interactions, as depicted in Fig. 1.17. This interaction yields various charged and neutral particles, including pions (π^\pm , π^0), nucleons (represented as A), and kaons (K^\pm) as illustrated in Eq. 1.11.

$$p + X \rightarrow N_1 A + N_{\text{ch}} \pi^\pm + N_{\text{ch}} \pi^0 + N_2 K^\pm. \quad (1.11)$$

where N_{ch} is the number of π^\pm and N_1 and N_2 are the numbers of A and K^\pm , respectively. The nucleons and other particles produced continue along the shower axis, interacting with other air nuclei. However, the neutral pion (π^0) has a very short lifetime and promptly decays into two photons, as shown in Eq. 1.12. These photons initiate electromagnetic sub-showers under the influence of surrounding air nuclei, contributing to the development of the overall cascade.

$$\pi^0 \rightarrow \gamma + \gamma. \quad (1.12)$$

Each π^0 generated during this cascade process adds energy to the electromagnetic sub-showers. As a result, a multitude of secondary photons and electron-positron pairs (e^\pm) are produced at the observational level, constituting the majority of secondary particles within the EAS.

If the interaction length (λ_{π^\pm}) of charged pions (π^\pm) is shorter than their decay length (λ_{π^\pm}), they will further interact with air nuclei. Otherwise, they decay into muons (μ^- , μ^+) and the corresponding muon-neutrinos (ν_μ , $\bar{\nu}_\mu$), as described in Eq. 1.13.

$$\pi^-(\pi^+) \rightarrow \mu^-(\mu^+) + \nu_\mu(\bar{\nu}_\mu). \quad (1.13)$$

Similarly, charged kaons (K^\pm) decay into muons, pions, and neutrinos through

specific decay modes, as outlined in Eq. 1.14.

$$\begin{aligned} K^-(K^+) &\rightarrow \mu^-(\mu^+) + \nu_\mu(\bar{\nu}_\mu), \\ K^\pm &\rightarrow \pi^\pm + \pi^0. \end{aligned} \quad (1.14)$$

The probability of decay for charged pions and kaons is higher in the upper atmosphere, while their probability of interaction increases with depth due to the increase in atmospheric density. Consequently, numerous muons are produced in the upper atmosphere, offering valuable insights into the early stages of EAS development. These secondary muons possess greater penetration power and primarily lose energy through ionization, enabling them to reach the observational level with minimal attenuation. Muons may further decay into electrons or positrons (e^- , e^+) and corresponding neutrinos with a lifetime of approximately $2.2, \mu s$, as shown in Eq. 1.15.

$$\mu^-(\mu^+) \rightarrow e^-(e^+) + \nu_e(\bar{\nu}_e) + \nu_\mu(\bar{\nu}_\mu). \quad (1.15)$$

An extensive array of secondary particles is present at the observational level, including photons, electrons, muons, neutrinos, charged and neutral pions, protons, neutrons, and other hadrons. The longitudinal development of the hadronic shower can be effectively modeled using established formalisms. Each nucleon interacts independently for heavier primary cosmic rays with a mass number A , carrying an energy of E_0/A . Consequently, the interaction of a heavier primary, such as iron, with air nuclei can be understood as a superposition of interactions of its constituent nucleons. Most ground-based experiments observe extensive air showers beyond the point of maximum shower development. It is found that, in comparison to lighter primaries of equal energies, heavier primaries display a greater surface depth of shower maximum. Consequently, the attenuation of the number of electrons (N_e) is more pronounced for showers initiated by heavier primaries, resulting in relatively smaller N_e at the observational level compared to lighter primaries.

1.12 Thesis motivation

The formation of matter in an extreme condition similar to those produced in the early Universe is an important area of research and analysis in the contemporary physics domain. The theoretical aspects for gathering knowledge and understanding the matter in the region of high energy density and high temperature are provided by Quantum Chromodynamics (QCD). In this respect, studying interactions between quarks and gluons and the constituents of hadrons, such as protons and neutrons, during high-energy collisions is important. These collisions at particle accelerators offer a glimpse into the conditions prevailing shortly after the Big Bang, potentially leading to the formation of the QGP, a hypothesized state of matter. In this thesis, we examine a broad spectrum of topics to improve our knowledge of QCD matter and its consequences for the origin of the Universe. It explores the complex dynamics of heavy-ion collisions with the goal of reproducing QGP in controlled conditions. Analyzing various signatures such as collective flow, strangeness enhancement, and J/ψ suppression develops our understanding of the formation of the QGP. Also, we explore the origin of cosmic rays and their energy spectra. After that, we discuss the composition and detection techniques using direct and indirect methods.

Furthermore, this thesis explores the effects of nuclear deformation and hadron cascade time (τ_{HC}) on particle production and elliptic flow in Xe+Xe collisions at $\sqrt{s_{\text{NN}}} = 5.44$ TeV using A Multiphase Transport (AMPT) model. This work examines how nuclear deformation and cascade time influence the final state observables' particle production and elliptic flow. We analyze the impact of hadronic cascade time on p_{T} -differential particle ratios and elliptic flow, varying the cascade time from 5 to 25 fm/ c . Results show longer hadron cascade times increase anisotropic flow, especially at very low and high p_{T} .

Moreover, we explore the impact of magnetic fields usually generated in a

non-central heavy ion collision, influencing the QCD matter. This study uses the non-extensive Tsallis statistics within a hadron resonance gas model. This study investigates a hadron gas under an external static magnetic field using a non-extensive Tsallis distribution function. We examine energy density (ϵ), entropy density (s), pressure (P), and speed of sound (c_s), and explore magnetization (M) to understand diamagnetic and paramagnetic effects under varying magnetic fields. By analyzing the non-extensive parameter (q), we assess the impact of initial magnetic fields on final state observables in non-central heavy-ion collisions, where the Tsallis distribution better describes particle transverse momentum spectra.

Additionally, we explore the effect of chemical potential at the kinetic freeze-out boundary in pp collision, offering an alternative perspective to look at the freeze-out boundary and particle production. In this work, the charged-particle transverse momentum spectra (p_T -spectra) for pp collisions at $\sqrt{s} = 7$ and 13 TeV have been analyzed using a thermodynamically consistent Tsallis non-extensive distribution. The Tsallis function is fitted to p_T -spectra, examining final state charged-particle multiplicity for various particles: π^\pm , K^\pm , $p+\bar{p}$, ϕ , $\Lambda+\bar{\Lambda}$, $\Xi+\bar{\Xi}$, $\Omega+\bar{\Omega}$. This study highlights the role of chemical potential in pp collisions at LHC energies, suggesting a single freeze-out scenario using the Tsallis distribution.

Lastly, the thesis addresses a longstanding puzzle in cosmic ray physics, the muon puzzle. The muon puzzle refers to a mysterious discrepancy between the predicted and observed numbers of muons in cosmic ray events. However, current theoretical models often need to pay more attention to the quantity of muons detected by experiments, indicating a gap in our understanding of cosmic ray interactions. The muon puzzle is one of the most important problems in cosmic ray physics for understanding the composition and astrophysical processes and improving the cosmic ray hadronic interaction model. In this analysis, we simulate the EAS using the CORSIKA simulation program, a widely used air shower simulator of EAS for different primary particles in the Earth's atmosphere. We

1.12 Thesis motivation

attempt to address this puzzle and advance our understanding of cosmic ray phenomena using the GRAPES-3 experiment, which provides sensitive observations over a wide energy range. These works form the basis of the present thesis.

The thesis is organized as follows: This chapter covers the theoretical framework of QCD and the strong force governing quark and gluon interactions. It introduces the QGP and discusses its formation in heavy-ion collisions and its various signatures. Additionally, it explores cosmic rays' origin and energy spectra, followed by an overview of detection techniques using direct and indirect methods. In chapter 2, we discuss and examine the influence of nuclear deformation and hadron cascade time in Xe+Xe collisions, shedding light on how these factors shape particle ratios and flow patterns. In chapter 3, the impact of external magnetic fields and non-extensive statistics on hadron gas properties, providing insights into the interplay between magnetic effects and thermodynamic behavior in heavy-ion collisions. In chapter 4, we explore the role of chemical potential at kinetic freeze-out in pp collisions, proposing an alternative perspective on freeze-out dynamics and its implications for particle production. In chapter 5, we discuss the GRAPES-3 detectors used for our data analysis. In chapter 6, we present the study of muons puzzle in cosmic ray events with the GRAPES-3 experiment. In the end, in chapter 7, the results are summarised with essential findings.

Chapter 2

Effect of hadron cascade time on particle production in Xe+Xe collisions at $\sqrt{s_{\text{NN}}} = 5.44$ TeV using a multiphase transport model

Heavy-ion collisions at ultra-relativistic energies create extreme conditions of energy density and temperature, producing a deconfined state of quarks and gluons known as quark-gluon plasma (QGP). This research investigates the effects of nuclear deformation and hadron cascade time on particle production and elliptic flow using the multiphase transport (AMPT) model in Xe+Xe collisions at $\sqrt{s_{\text{NN}}} = 5.44$ TeV. The study examines how varying the hadronic cascade time between 5 and 25 fm/c influences identified particle production and elliptic flow, revealing that extended hadron cascade times enhance anisotropic flow at both low and high transverse momentum p_{T} .

Facilities such as the Relativistic Heavy-ion Collider (RHIC) at BNL, USA,

and the Large Hadron Collider (LHC) at CERN, Switzerland, are designed to create and study QGP under these extreme conditions. These collisions generate significant initial energy density and pressure, driving the system's expansion through various complex processes. Quarks and gluons interact during this expansion, potentially forming a thermalized system that undergoes collective expansion and hadronization into composite hadrons. The final-state particles retain information about the initial-state conditions, with the initial geometry influencing the spatial anisotropy, which translates into momentum anisotropy in non-central collisions. This anisotropic flow, quantified by flow coefficients (v_n), is a crucial signature of QGP and is described by the Fourier expansion of the momentum distribution of final-state particles:

$$E \frac{d^3N}{dp^3} = \frac{d^2N}{2\pi p_T dp_T dy} \left[1 + 2 \sum_{n=1}^{\infty} v_n \cos[n(\varphi - \psi_n)] \right]. \quad (2.1)$$

Here φ is the azimuthal angle of particle emission, and ψ_n is the angle relative to the reaction plane. The second-order Fourier coefficient of the anisotropic flow is called elliptic flow (v_2) and is sensitive to the equation of state (EoS) and transport properties [101]. Extensive studies of v_2 have been conducted using various colliding systems (e.g., Au+Au, Cu+Cu, U+U, Xe+Xe, Pb+Pb) at different energies, revealing that the shape of the colliding nuclei affects the initial geometry and subsequent elliptic flow [102–104].

A comparison of v_2 between spherical nuclei and a deformed one in the central collisions can establish the origin of elliptic flow due to the initial state effect. Recently, LHC has collided with intrinsically deformed nuclei Xenon (Xe) at $\sqrt{s_{NN}} = 5.44$ TeV, which also bridges the final state charged particle multiplicity gap between the smaller systems (p+p and p+Pb) and larger system (Pb+Pb). For the most central collisions (0–5%), the v_2 is found to be $\sim 35\%$ higher in Xe+Xe as compared to Pb+Pb [105]. Further, the violation of quark participant scaling of identified particle v_2 is also observed for the Xe+Xe system, like other colliding

2.1 A multiphase transport (AMPT) model

systems having spherical nuclei [106, 107]. The system produced in heavy-ion collisions evolves through different stages, with the hadronic phase occurring between chemical and kinetic freeze-out boundaries. During this phase, elastic collisions continue until kinetic freeze-out, potentially altering final-state hadrons' momentum distribution and anisotropy. This effect, influenced by the hadronic phase lifetime and the collision energy, can be explored using models like AMPT. Previous studies have examined the impact of the hadronic phase on v_2 and resonance production using spherical nuclei [108], but analyzing these effects with deformed nuclei like Xe provides new insights. Particle production mechanisms in heavy-ion collisions can be understood by analyzing p_T -differential particle ratios, which reflect different production processes at various p_T scales [109]. At low p_T , identified particle spectra are influenced by radial flow, as observed in central heavy-ion collisions at the LHC and explained by hydrodynamic models [110, 111]. Radial flow shifts heavier particles to higher p_T , enhancing heavier-to-lighter particle ratios. At intermediate p_T , baryon-to-meson ratios, such as p/π , are enhanced due to coalescence mechanisms and radial flow. At the same time, high- p_T regions are dominated by jet fragmentation and perturbative QCD processes. Interactions during the hadronic phase, influenced by phase lifetime and cross-sections, can further modify these ratios. In this study, we thoroughly examine the impact of the hadronic phase lifetime (also known as the hadronic cascade time) on p_T -differential particle ratios, as well as on p_T -differential and integrated elliptic flow. We utilize the AMPT model (string melting version) to generate events with hadronic phase times ranging from 5 to 25 fm/ c . Let's discuss the AMPT model in more detail in the following section 2.1.

2.1 A multiphase transport (AMPT) model

This study employs the multiphase transport (AMPT) hybrid model [112–114], which includes four key components: the heavy-ion jet interaction generator (HI-

JING) for collision initialization [115], Zhang’s parton cascade model (ZPC) for parton transport post-initialization, the Lund string fragmentation or quark coalescence model for hadronization, and a relativistic transport (ART) model for hadron transport. The differential cross-section of the produced min-ijet particles in p+p collisions is calculated in the HIJING model, which is given by:

$$\frac{d\sigma}{dp_T^2 dy_1 dy_2} = K \sum_{a,b} x_1 f_a(x_1, p_{T1}^2) x_2 f_b(x_2, p_{T2}^2) \times \frac{d\hat{\sigma}_{ab}}{d\hat{t}}. \quad (2.2)$$

Where σ and \hat{t} are the produced particles’ cross-section and the momentum transfer during partonic interactions in p+p collisions, respectively. x_i ’s and $f(x, p_T^2)$ ’s represent the momentum fraction of the mother protons which are carried by interacting partons and the parton density functions (PDF) accordingly. HIJING integrates a Glauber model’s shadowing and nuclear overlap functions to transform parton interactions from p+p to A+A and p+A collisions. Nucleon distributions in spherical nuclei like Au and Pb are modeled using the Woods-Saxon (WS) distribution [116], while deformed nuclei like Xenon utilize a modified WS (MWS) distribution with deformation parameters β_n and spherical harmonics $Y_{nl}(\theta)$ [117–119].

The nucleon density in a nucleus follows a three-parameter Fermi distribution [120]:

$$\rho(r) = \rho_0 \left[\frac{1 + w(r/R)^2}{1 + \exp[(r - R)/a]} \right]. \quad (2.3)$$

Here, ρ_0 is the nuclear matter density in the center of the nucleus, w adjusts for surface deviations, a is the surface thickness, R is the nuclear radius, and r is the radial distance. Hence, the reduced nucleonic density function [121] for a spherical nucleus can be written as,

$$\rho(r) = \frac{\rho_0}{1 + \exp[(r - R)/a]}. \quad (2.4)$$

The radius parameter, R , can be modified for an axially symmetric deformed

2.1 A multiphase transport (AMPT) model

nucleus like Xe. The modified Woods-Saxon nuclear radius [122] is given by:

$$R_{A\Theta} = R[1 + \beta_2 Y_{20}(\theta) + \beta_4 Y_{40}(\theta)]. \quad (2.5)$$

Here, the β_i 's are deformation parameters. In case of Xenon nucleus, the deformation parameters, $\beta_2 = 0.162$ and $\beta_4 = -0.003$, which are taken from Ref. [123, 124]. The spherical harmonics, Y_{20} , and Y_{40} are given by [125]:

$$\begin{aligned} Y_{20}(\theta) &= \frac{1}{4} \sqrt{\frac{5}{\pi}} (3 \cos^2 \theta - 1), \\ Y_{40}(\theta) &= \frac{3}{16\sqrt{\pi}} (35 \cos^4 \theta - 30 \cos^2 \theta + 3). \end{aligned} \quad (2.6)$$

The positions of nucleons within the distribution, $\rho(r)$, are illustrated using the volume element $r^2 \sin \theta \, dr \, d\theta \, d\phi$ [126]. For random orientation of nuclei, position configurations are measured using both polar angle (angle between major axis and beam axis) Θ in $[0, \pi]$ and azimuthal angle (angle between major axis and impact parameter) Φ within limits $[0, 2\pi]$. Both target and projectile nuclei are rotated event-by-event in Θ and Φ space. In this paper, calculations have been done only with random orientation, which means unpolarized and averaged value over random Θ and Φ [127]. The ZPC model [128] transports quarks and gluons using the Boltzmann transport equation:

$$p^\mu \partial_\mu f(x, p, t) = C[f]. \quad (2.7)$$

The leading order equation showing interactions among partons is approximately given by

$$\frac{d\hat{\sigma}_{gg}}{d\hat{t}} \approx \frac{9\pi\alpha_s^2}{2(\hat{t} - \mu^2)^2}. \quad (2.8)$$

Where σ_{gg} is the gluon scattering cross-section and α_s is the strong coupling constant. Here, μ^2 is the cutoff used to avoid infrared divergences that may occur if the momentum transfer, \hat{t} , goes to zero during scattering. In the AMPT-SM version, colored strings melt into low momentum partons which take place at the start of the ZPC and are calculated using the Lund FRITIOF model of HIJING.

These resulting partons undergo multiple scattering when any two partons are within minimum separation that is given by $d \leq \sqrt{\sigma/\pi}$, where σ is the scattering cross-section of the partons. The hadronization occurs via coalescence [129, 130], followed by hadronic evolution in the ART model where interactions occur among meson-meson, baryon-baryon, and meson-baryon before we get the final state hadrons [131, 132]. This study uses AMPT version 2.26t7, setting the partonic cross-section (σ_{gg}) to 10 mb, and the Lund string fragmentation parameters $a = 2.2$ and $b = 0.5/\text{GeV}^2$. Note that we have kept the hadron level decay flagged as off for ϕ and K_s^0 to study these particles in the final state. The hadron cascade time is controlled by the parameters named NTMAX and DT. By varying DT, we have generated the data in the AMPT-SM for the hadron cascade times from 5 to 25 fm/c within a time interval of 5 fm/c. Since the hadronic phase lifetime for the default version of the AMPT is 30 fm and the lower limit obtained from the study of re-scattering effect using resonances with experimental data is $\sim 2\text{--}4$ fm [133, 134], we have taken such an interval of hadron cascade-time for our studies.

After comprehensively examining the AMPT model, we now transition to the results and discussion section. In this section, we analyze our findings offering a complete study and interpretation of the data.

2.2 Results and Discussion

In this work [135], we have investigated the p_T -differential particle ratios, as well as p_T -differential and p_T -integrated elliptic flow for both identified and charged particles across various centralities. The study focuses on Xe+Xe collisions at $\sqrt{s_{\text{NN}}} = 5.44$ TeV, using events generated by the AMPT-SM model, which incorporates the deformation effect of Xe nuclei. Events were generated over a range of hadronic cascade times from 5 to 25 fm/c in 5 fm/c intervals. We analyzed the p_T -differential identified particle ratios with respect to $(\pi^+ + \pi^-)$ and

2.2 Results and Discussion

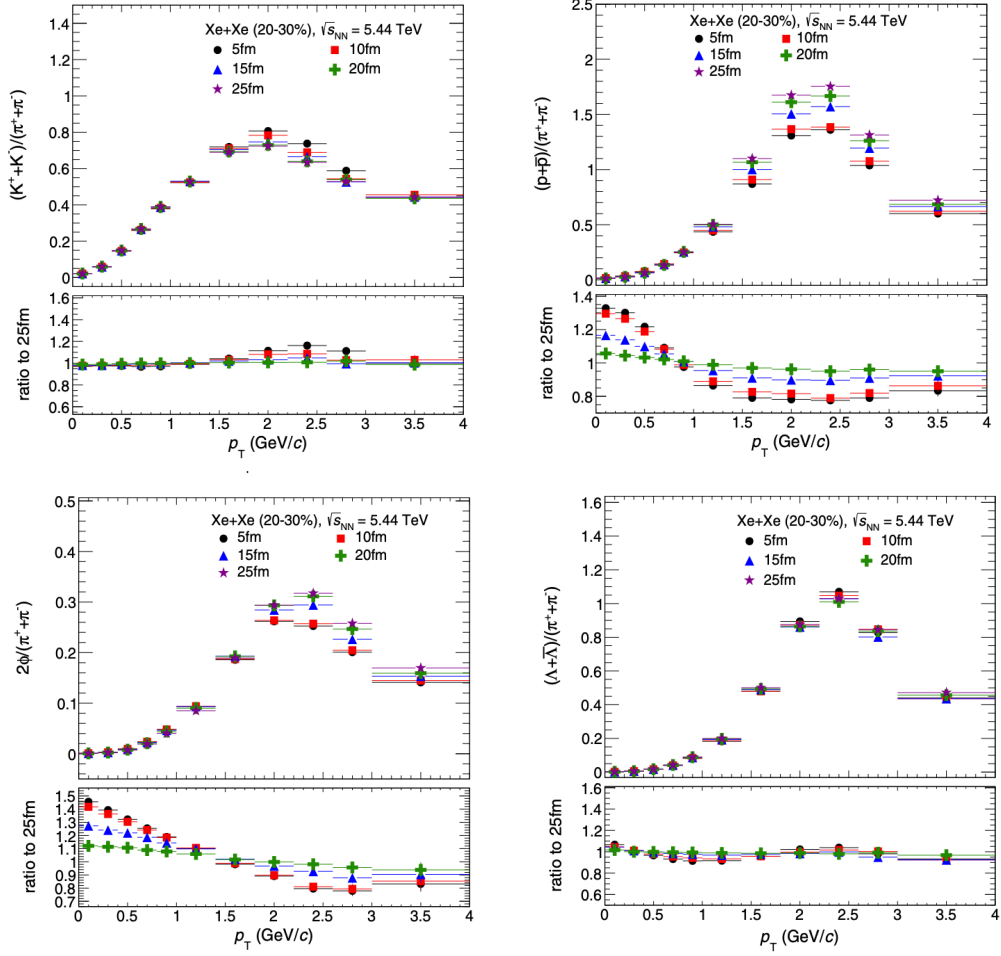


Figure 2.1: p_T -differential particle ratios of K^\pm , $p(\bar{p})$, ϕ and $\Lambda(\bar{\Lambda})$ to π^\pm in Xe+Xe collisions at $\sqrt{s_{\text{NN}}} = 5.44$ TeV for (20–30)% centrality class. Different symbols show various hadron cascade times. The vertical lines on the data points are the statistical uncertainties [135].

$(p+\bar{p})$. Additionally, we examined the quark participant scaled elliptic flow for identified particles such as $(\pi^+ + \pi^-)$, $(K^+ + K^-)$, $(p+\bar{p})$, ϕ , and $(\Lambda + \bar{\Lambda})$. The p_T -differential identified particle ratios are influenced by the hadronic cascade time, depending on the particles' scattering cross-sections in the hadronic phase and the duration of this phase. Further, the multiple scattering of the final state particles may modify their azimuthal direction and transverse momentum, which

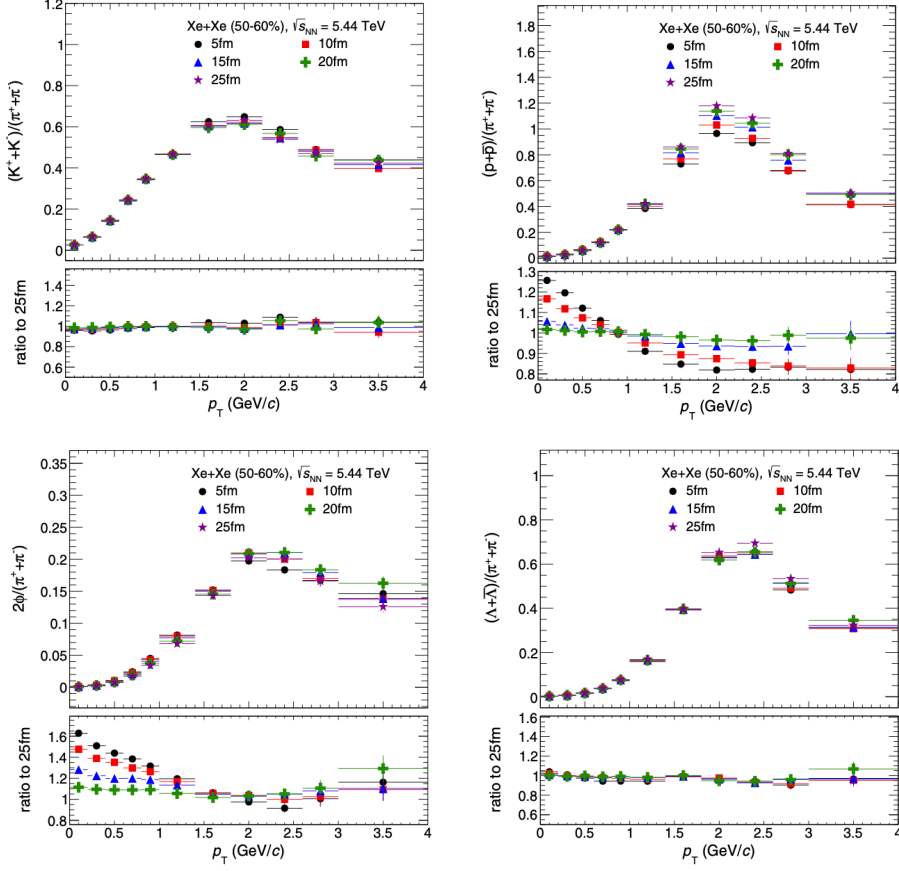


Figure 2.2: p_T -differential particle ratios of K^\pm , $p(\bar{p})$, ϕ and $\Lambda(\bar{\Lambda})$ to π^\pm in Xe+Xe collisions at $\sqrt{s_{NN}} = 5.44$ TeV for (50–60)% centrality class. Different symbols show various hadron cascade times. The vertical lines on the data points are the statistical uncertainties [135].

will be reflected on the p_T -differential and p_T -integrated elliptic flow. Our main objective is to quantify the effect of hadronic cascade time (τ_{HC}) on observables like p_T -differential particle ratios and elliptic flow in the Xe+Xe collision system. This research aims to enhance our understanding of particle production dynamics and the influence of hadronic cascade time, considering the finite hadronic phase lifetime at LHC energies, even in smaller collision systems.

2.2 Results and Discussion

2.2.1 Identified p_T -differential particle ratios

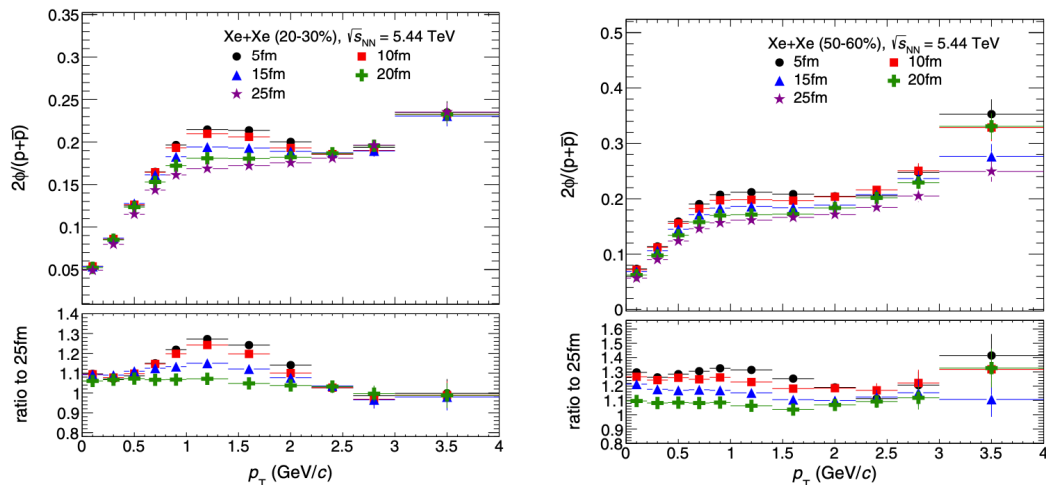


Figure 2.3: p_T -differential particle ratios of ϕ to p in Xe+Xe collisions at $\sqrt{s_{\text{NN}}} = 5.44$ TeV for (20–30)% (left) and (50–60)% (right) centrality classes. Different symbols show various hadron cascade times. The vertical lines in the data points are the statistical uncertainties [135].

Figures 2.1 and 2.2 show the ratios of $K^+ + K^-$, $p+\bar{p}$, ϕ , and $\Lambda + \bar{\Lambda}$ to pions as functions of transverse momentum for centrality classes of (20–30)% and (50–60)%. These ratios are presented for different hadronic cascade times. The production rate of these identified particles relative to pions increases with p_T , attains a maximum value in the intermediate p_T range (2–3 GeV/ c). This trend is consistent across all hadronic cascade times. At lower transverse momentum ($p_T < 1$ GeV/ c), there is a notable impact of hadronic cascade time on ϕ/π and p/π ratios, with a maximum deviation of about 40% for $\tau_{\text{HC}} = 5$ fm/ c compared to 25 fm/ c . However, this trend reverses for $p_T > 1$ GeV/ c . Additionally, the hadronic cascade time has a smaller effect on strange particle ratios like K/π and Λ/π . In the (50–60)% centrality class, the deviation in the ϕ/π ratio is more pronounced at lower p_T compared to the (20–30)% centrality class.

Furthermore, we explored the effect of hadronic cascade time on the ϕ/p p_T -differential ratio, as these particles have nearly similar masses. Figure 2.3 shows the ϕ/p ratio as a function of p_T in (20–30)% and (50–60)% centrality classes for various hadronic cascade times. The ratio increases with p_T and begins to saturate after $p_T = 1$ GeV/ c in both centrality classes, with further enhancement at higher p_T . A similar trend holds for all hadronic cascade times. The lower panels of the figures reveal a clear dependence on τ_{HC} , especially in the (50–60)% centrality class, where the ratio increases as τ_{HC} decreases, showing a maximum deviation of about 30% for $\tau_{HC} = 5$ fm/ c compared to 25 fm/ c .

This study underscores the importance of various processes in the hadronic phase and their impact on p_T -differential identified particle ratios. This insight prompts further investigation into the effect of hadronic cascade time on another crucial observable elliptic flow, which will be discussed in the next section, 2.2.2.

2.2.2 Elliptic flow (v_2)

To be in line with the experimental procedure for estimating elliptic flow, this study employs the two-particle correlation method to compare AMPT data directly. Details of this method can be found elsewhere [136]. The two-particle correlation method offers the advantage of incorporating a proper pseudorapidity cut, effectively reducing significant residual non-flow effects in elliptic flow. Non-flow effects refer to azimuthal correlations arising from jets and resonance decays unrelated to the symmetry planes. Figure 2.4 shows the charged particle elliptic flow as a function of p_T for both (20–30)% and (50–60)% centrality classes. Here, we have compared the p_T -differential elliptic flow generated for the two extreme cases, $\tau_{HC} = 5$ fm/ c and 25 fm/ c for both the centrality classes. The elliptic flow increases with p_T , reaching a maximum at around 2–2.5 GeV/ c . Higher v_2 values are observed for peripheral collisions ((50–60)%) compared to semi-central collisions ((20–30)%). These results are also compared with the p_T -differential elliptic

2.2 Results and Discussion

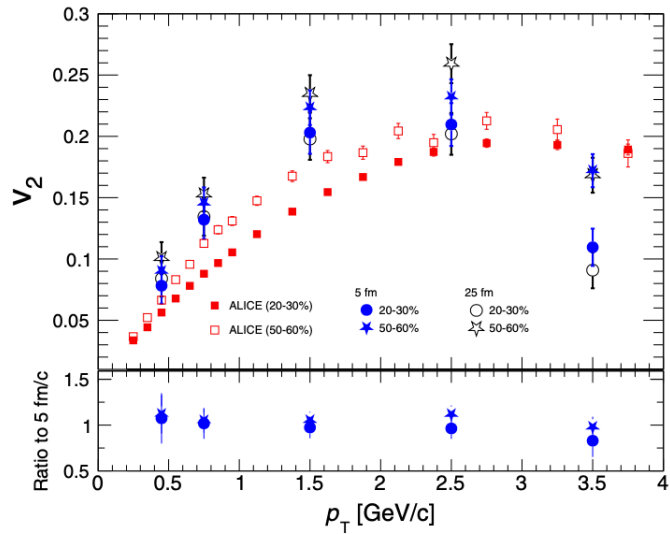


Figure 2.4: p_T -differential elliptic flow of charged particles in Xe+Xe collisions at $\sqrt{s_{\text{NN}}} = 5.44$ TeV for (20-30)% and (50-60)% centrality classes. Different symbols show various hadron cascade times [135]. The results are compared with the ALICE data [105].

flow of charged particles measured by ALICE for both centrality classes. The observed trends qualitatively match the ALICE data, showing a higher elliptic flow for the (50–60)% centrality class, consistent with experimental observations.

This can be attributed to the initial momentum anisotropy due to the geometry of the overlapping region formed after collisions, which is more pronounced in peripheral collisions. When considering different hadronic cascade times, the p_T -differential elliptic flow exhibits similar behavior in both (20–30)% and (50–60)% centrality classes. A higher cascade time for both centralities results in a more anisotropic azimuthal distribution of final state particles in the high- and very low- p_T regions. However, the intermediate- p_T region appears less affected by the hadronic cascade time.

The particle production via quark coalescence can be validated by examining the elliptic flow of baryons and mesons at intermediate p_T , after scaling both p_T

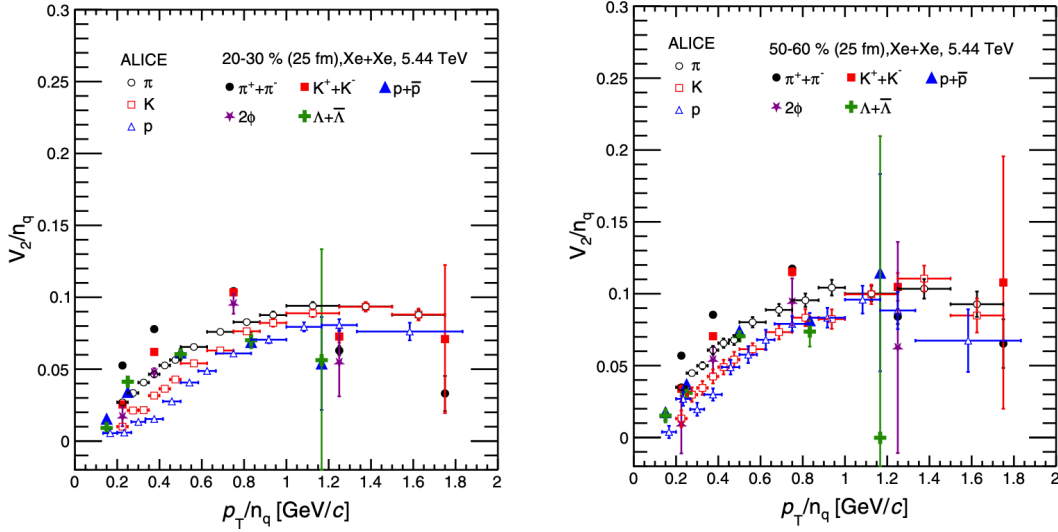


Figure 2.5: p_T -differential particle ratios of ϕ to p in Xe+Xe collisions at $\sqrt{s_{NN}} = 5.44$ TeV for (20–30)% (left) and (50–60)% (right) centrality classes. Different symbols show various hadron cascade times. The vertical lines in the data points are the statistical uncertainties [135].

and v_2 by the number of constituent quarks n_q . In the AMPT model with string melting mode, mesons and baryons form when a quark-antiquark pair and three quarks come close together in phase space. Under these conditions, the elliptic flow for baryons is higher than that for mesons at intermediate p_T due to the recombination effect. Figure 2.5 represents the constituent quark-scaled v_2 as a function of p_T/n_q . For this analysis, both the elliptic flow and p_T are scaled by 2 for mesons (such as pions, kaons, and ϕ) and by 3 for baryons (such as protons and Λ). We can clearly see the violation of the scaling behavior in both (20–30)% and (50–60)% centrality classes at $\tau_{HC} = 25$ fm/c, which are in line with the deviations that are already reported in ALICE [137] and several experimental studies performed at LHC energies [138]. We have explicitly checked that this violation is also observed for $\tau_{HC} = 5$ fm/c, indicating that hadron cascade-time has no role in the quark-participant scaling violation in the elliptic flow.

2.2 Results and Discussion

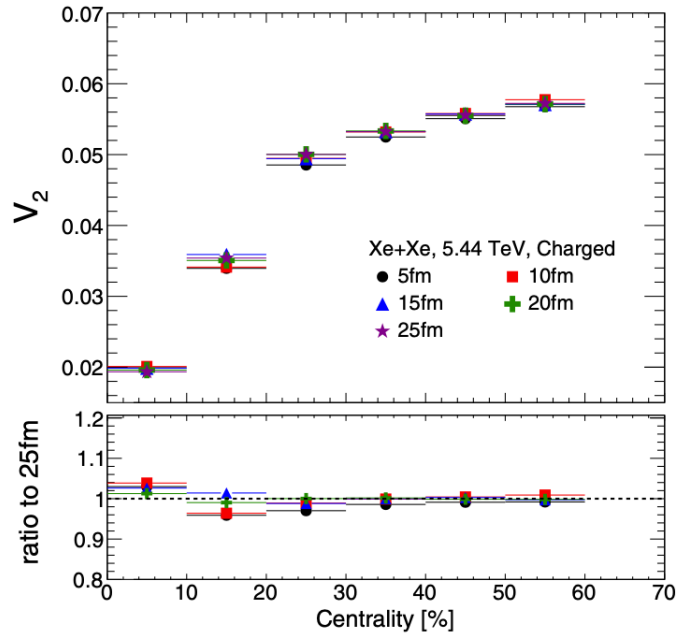


Figure 2.6: p_T -integrated elliptic flow of the charged particles in Xe+Xe collisions at $\sqrt{s_{NN}} = 5.44$ TeV for (0-10)%, (10-20)%, (20-30)%, (30-40)%, (40-50)% and (50-60)% centrality classes. Different symbols show various hadron cascade times [135].

Additionally, to explore the impact of hadronic cascade time on the bulk part of the system with respect to centrality, we examined the p_T -integrated elliptic flow of charged particles. Inspired by the ALICE kinematic acceptance, we have considered the charged tracks with p_T lying between 0.2 to 3 GeV/ c . Figure 2.6 shows the p_T -integrated elliptic flow as a function of centrality for different τ_{HC} values. Moving from central to peripheral collisions, the p_T -integrated v_2 increases for all hadronic cascade times. To quantify the dependence on hadronic cascade time, the lower panel of Fig. 2.6 shows the ratio relative to 25 fm/ c . We do not observe a significant dependence of the p_T -integrated v_2 on the hadronic cascade time, though we see a clear dependence on hadronic cascade time in the case of the p_T -differential v_2 .

2.3 Summary

In this analysis, we have explored the effect of hadronic cascade-time (τ_{HC}) on the p_{T} -differential identified particle ratios, p_{T} -differential and p_{T} -integrated elliptic flow in Xe+Xe collision at $\sqrt{s_{\text{NN}}} = 5.44$ TeV using the data generated from the AMPT-SM version. In the AMPT-SM, the participation of soft partons originating from the string melting process in partonic scatterings results in an increased elliptic flow compared to the default AMPT. In addition, it allows for modifying the final state hadronic phase lifetime by varying the number of time steps in a hadron cascade and/or the length of the time step. The significance of the hadronic cascade time on particle production depends on the scattering cross-section among the final state particles and the duration of the hadronic phase. This study is more significant in looking into the larger hadronic phase lifetime at the LHC energies. We see a considerable dependence of identified particle ratios and elliptic flow on the τ_{HC} when studied as a function of p_{T} and centrality. The essential findings of this study are summarised below:

- Significant dependence of p_{T} -differential particle ratios for ϕ/π and p/π on τ_{HC} is observed at low p_{T} , which is higher for ϕ/π ratio. With higher τ_{HC} , the low p_{T} particles shift towards intermediate and higher p_{T} region due to more interactions which are reflected in the particle ratios.
- To cancel out the mass dependence on τ_{HC} , we have looked into the ϕ/p p_{T} -differential particle ratio. We see a scaling of this ratio for 50-60% centrality class with τ_{HC} . However, we see a significant dependence of τ_{HC} on ϕ/p ratio at intermediate p_{T} region for mid-central collisions.
- The p_{T} -differential charged particle elliptic flow is higher for $\tau_{\text{HC}} = 25$ fm/ c compared to 5 fm/ c at very low and high- p_{T} region. This indicates that added anisotropy in the azimuthal distribution of the charged particles

2.3 Summary

might originate from multiple scattering in the hadronic phase with higher τ_{HC} .

- In line with the experimental results obtained at the LHC energies, we do not observe any scaling behavior with the number of constituent quarks (n_q) on elliptic flow. The hadron cascade time has no effect on the quark-participant scaling violation in the elliptic flow is supposed to be an initial state effect in contrast to the hadronic rescattering, which is a final state effect.
- To see the effect of hadronic cascade-time over the bulk of the medium, we have estimated the p_T -integrated charged particle elliptic flow in different centrality classes. We found the p_T -integrated charged particle elliptic flow is almost independent of the hadronic cascade time. This might be due to the compensation of anisotropy over different p_T regions.

More precisely, we observe the effect of hadron cascade time on p_T -differential identified particle ratios, p_T -differential, and integrated charged particle elliptic flow. We see an interplay of different hadronic phase effects, such as scattering cross-sections, hadronic phase lifetime, and momentum anisotropy inherited from initial collision geometry on these observables.

Chapter 3

Effect of magnetic fields and non-extensive statistics in a hadron resonance gas

Non-central collisions of heavy ions at ultra-relativistic energies represent a unique scenario in creating magnetic fields of significant strength in the laboratory. Such magnetic fields emerge during the initial stages of collision, potentially affecting the properties of Quantum Chromodynamics (QCD) matter formed in relativistic heavy-ion collisions. The transient nature of the magnetic fields leaves its reminiscence, significantly affecting the final state dynamics *i.e.* thermodynamic and transport properties. In this study, we explore the thermodynamic properties of a hadron gas under the influence of an external static magnetic field, employing a thermodynamically consistent non-extensive Tsallis distribution function.

The thermodynamic observables, including energy density (ϵ), pressure (P), entropy density (s), and square speed of sound (c_s^2), are the main focus of the study. Furthermore, a study of magnetization (M) highlights the complex interaction between the paramagnetic and diamagnetic characteristics of the system under varying magnetic field intensities. In addition, to understand the system's

behavior near and far from equilibrium, we study the effect of the non-extensive parameter (q) on the observables noted above. The aim of this study is to analyze the impact of the initial magnetic field on final state observables in an away-from-equilibrium scenario specific to non-central heavy-ion collisions, in which the non-extensive Tsallis statistical distribution function better describes particle transverse momentum spectra. The following section will examine the impact of heavy-ion collisions in magnetic fields.

3.1 Effect of the magnetic field in heavy-ion collisions

The Biot-Savart law, the fundamental law of electromagnetism, elucidates how moving electric charges can produce magnetic fields (B). Analogously, in relativistic colliders, the fast and oppositely directed motion of spectator protons in peripheral heavy-ion collisions generate magnetic fields of considerable strength as the colliding beams carry a large positive electric charge [139–141]. These colliders afford a unique tool to probe and comprehend the QCD phase diagram across a broad spectrum of temperatures (T) and baryon-chemical potentials (μ_B). These parameters are vital in understanding the equation of state (EoS) governing the evolution of systems formed in such collider experiments. Notably, in experiments like STAR at the Relativistic Heavy Ion Collider (RHIC) and ALICE at the Large Hadron Collider (LHC), where heavy ions collide to explore resulting QCD matter, magnetic fields of the order $eB \sim (m_\pi^2) \sim 10^{18}\text{G}$ [142] and $eB \sim (15m_\pi^2)$, respectively where m_π is the mass of a pion have been observed [143, 144]. These values are astronomically more prominent than the strongest man-made steady magnetic field in the laboratory. Such strong magnetic fields are anticipated in dense neutron stars [145, 146] and might have influenced the electroweak transition during the early universe [147, 148]. Moreover, the magnetic field created on

3.1 Effect of the magnetic field in heavy-ion collisions

Earth in the form of an electromagnetic shock wave is $\sim 10^7$ G, and the calculated value of the magnetic field inside a neutron star is $10^{10} - 10^{13}$ G [149, 150]. For a physical comparison, the magnitude of Earth's magnetic field at its surface is around 0.25 - 0.65 G. Studying the effects of the transitory magnetic field produced in a heavy-ion collision on hot and dense matter formed in such collisions is important since it may be the strongest magnetic field yet measured in nature. Hence, apart from T and μ_B , the parameter B can affect the EoS, and therefore, it can have a crucial role in understanding the phase diagram.

Despite the immense strength of the electromagnetic field generated in heavy-ion collisions, its duration is concise. For instance, in Au + Au collisions at $\sqrt{s_{\text{NN}}} = 200$ GeV, the maximum electromagnetic field strength is of the order $5m_\pi^2$, lasting only about 0.3 fm/c [141, 144]. Although the initially produced magnetic field almost decays with the evolution of matter created in the off-central collisions, the initially produced magnetic field is practically not observed in the final state. However, as mentioned earlier, the strength of the initially produced magnetic field is so enormous that it can affect the EOS of the matter produced in the collisions and whose effect should be observed in the final state observables. Furthermore, the existence of electrical conductivity will delay the decay of this transient magnetic field significantly, which might mean that even in the hadronic phase, a relatively small magnetic field can be present. We choose a static magnetic field for simplicity and focus on a final state hadronic system, as the magnetic field is transitory and difficult to include in early pre-equilibrium phases within theoretical models. Analogous to away-from-equilibrium systems observed in non-central heavy-ion collisions, we adopt a non-extensive statistical distribution function with a magnetic field to analyze various thermodynamic properties. In the following section, we discuss the hadron resonance gas (HRG) as we implement the effect of magnetic field and non-extensive statistics.

3.2 Hadron resonance gas (HRG) model

A prominent phenomenological model for explaining the thermodynamics of hadronic matter, especially in heavy-ion collisions and the Quark-Gluon Plasma (QGP), is the Hadron Resonance Gas (HRG) model. The HRG model is a statistical bootstrap model suggested by Rolf Hagedorn. A gas of free hadrons and resonances can describe the thermodynamics of a system composed of hadrons. The fundamental concept is that the interaction among hadrons can effectively include higher mass resonances in the thermodynamic ensemble [151]. The model treats these resonances as non-interacting particles, simplifying the partition function estimation. As the partition function is the crucial component of the system's thermodynamics, it encodes all the information regarding the system. In the HRG model, the partition function is calculated by adding all the hadron states, including the resonances. In general, the HRG model considered interactions among hadron. To account for the attractive and repulsive forces between hadrons and their finite size, Van der Waals interactions are one such extension. The Excluded Volume HRG model [151] is the name of this expanded model. The HRG model has successfully described the equation of the state of QCD matter at temperatures below the deconfinement transition temperature. It has been used to fit experimental data from the heavy-ion collisions, such as particle yield and fluctuations, and compare with the lattice QCD results [152]. The HRG model investigates the QCD phase diagram as its most fascinating feature. The many phases of quark matter are plotted against temperature and baryon chemical potential on the QCD phase diagram. Understanding the hadronic phase and the transition to the QGP is aided by the HRG model. Quantum statistics have been incorporated into the HRG model, and their implications for the critical point of QCD are being examined. A first-order phase transition is thought to occur at the critical point, a hypothetical position on the QCD phase diagram, as opposed

3.3 Tsallis non-extensive statistics

to a smooth crossover [151].

The dispersion relation of a particle moving in a nonzero magnetic field is expressed as [153–161]

$$E = \sqrt{p_z^2 + m^2 + 2|e|(k - s_z + \frac{1}{2})B}. \quad (3.1)$$

Where k is any positive integer corresponding to allowed Landau levels, e is the charge of the particle under consideration, s_z is the component of spin along the z-direction, and B is the magnetic field strength. Here p_z is the momentum of the particle along the z-direction, and m is its corresponding mass.

Thus, the energy for neutral (n) and charged particles (c) in the presence of an external magnetic field are respectively given by,

$$E_{i,n} = \sqrt{p^2 + m_i^2}. \quad (3.2)$$

$$E_{i,c}(p_z, k, s_z) = \sqrt{p_z^2 + m_i^2 + 2|e_i|B(k + 1/2 - s_z)}. \quad (3.3)$$

In the current investigation, the hadrons taken into account extend from pions up to the baryon mass of 1.2 GeV, as listed in the particle data book [162], and are tabulated in table 3.1. In this approach, we have taken the spin of the hadrons for $s = 0, 1/2$, and 1, respectively. Moreover, the simple formula 3.3 adequately describes the dispersion relation of a spin-3/2 particle and is therefore not obvious. In fact, unlike other spin, the $s = 3/2$ would negatively contribute to the system's pressure for any nonzero magnetic field, marking an instability in the theory [155]. For this reason, we do not consider resonances with $s = 3/2$ or higher in the model.

3.3 Tsallis non-extensive statistics

In literature, several studies have examined the effect of external magnetic fields on hadron gas [154–157]. Unlike previous works, the present study investigates

Table 3.1: List of hadrons and resonances taken into account in the HRG description.

Hadron	$m(\text{GeV})$	$ e $	Spin	Deg.	Hadron	$m(\text{GeV})$	$ e $	Spin	Deg.
π^\pm	0.135	1	0	2	p	0.938	1	1/2	2
π^0	0.135	0	0	1	n	0.938	0	1/2	2
K^\pm	0.495	1	0	2	η'	0.958	0	0	1
K^0	0.495	0	0	2	f_0	0.980	0	0	1
η	0.548	0	0	1	a_0	0.980	0	1	1
ρ^\pm	0.776	1	1	2	ϕ	1.020	0	1	1
ρ	0.776	0	1	1	Λ	1.116	0	1/2	1
ω	0.782	0	1	1	h_1	1.170	0	1	1
$K^{*\pm}$	0.892	1	1	2	Σ^\pm	1.189	1	1/2	2
K^{*0}	0.892	0	1	2	Σ^0	1.189	0	1/2	1

the hadron gas system away from equilibrium and under the influence of the external magnetic fields. It is observed at RHIC [163, 164] and LHC [165–169] energies that the transverse momentum spectra of particles produced in pp and peripheral heavy-ion collisions deviate from the standard Boltzmann-Gibbs (BG) distribution. Fig. 3.1 depicts a comparative analysis between the distributions proposed by Tsallis and Boltzmann, as measured by the ALICE Collaboration in pp collisions at $\sqrt{s} = 0.9$ TeV [170]. The experimental transverse momentum distributions were subjected to fitting procedures employing the Boltzmann distribution, the Tsallis distribution, and expansions of the Tsallis distribution up to the first and second order of $(q-1)$. Notably, the Tsallis fits show excellent agreement with the data from pp collisions [169].

The BG distribution accurately describes the low- p_T part of the spectra, while a power-law type distribution fits the high- p_T region. Traditionally, two distribution functions described the entire p_T range. However, the Tsallis non-extensive

3.3 Tsallis non-extensive statistics

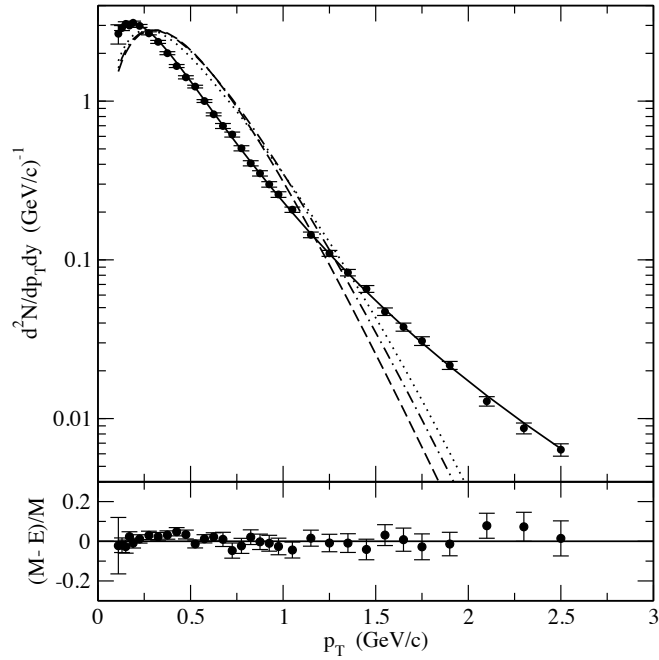


Figure 3.1: Fits the normalized differential yields of π^+ as measured by the ALICE Collaboration in pp collisions at $\sqrt{s} = 0.9$ TeV [170] fitted with the Tsallis (solid line) and Boltzmann distributions (dashed line). Additionally, variations of the Tsallis distribution were explored: a fit retaining terms to first order in $(q-1)$ is represented by the dash-dotted line, while a fit retaining term to second order in $(q-1)$ is shown as the dotted line. The bottom panel shows the difference between model (M) and experiment (E) normalized to the model (M) values [169].

distribution has been shown to effectively explain the p_T spectra across the entire range. This has motivated us to use a thermodynamically consistent form of the Tsallis distribution function for the present work. Such a distribution function has been used extensively to study the thermodynamical properties of the systems formed in heavy-ion collisions [171–173]. The Tsallis distribution introduces a parameter known as the non-extensive parameter (q), which measures the degree of deviation from equilibrium. A q value of 1 indicates an equilibrium state (BG scenario), while values between 1 and 11/9 [174] reflect the system’s deviation from equilibrium. Given that the systems formed in pp and peripheral heavy-ion collisions are typically out of equilibrium, it is appropriate to consider the non-extensive parameter in the current study.

A generalized statistical approach must address the systems under consideration so that, within an appropriate limit, the generalized statistics are reduced to the BG statistics. Tsallis statistics, which generalize BG statistics, have successfully described systems with long-range correlations using generalized entropy given by,

$$S_q \equiv k \frac{1 - \sum_{i=1}^W p_i^q}{q - 1}, \quad \text{with} \quad (q \in \mathbb{R}; \sum_{i=1}^W p_i = 1). \quad (3.4)$$

where, S_q is the Tsallis entropy, k is the Boltzmann constant, p_i is the probability of the system being in the i^{th} microstate, W is the total number of microstates, and q is the non-extensive parameter. It is immediately verified that, when $q \rightarrow 1$, S_q approaches the Boltzmann entropy (S_B), given by,

$$S_B = \lim_{q \rightarrow 1} S_q = -k \sum_{i=1}^W p_i \ln p_i. \quad (3.5)$$

The non-extensivity parameter, q , describes the deviation of thermodynamic systems from an equilibrium distribution. The physical interpretation of the non-extensive parameter has become crucial in Tsallis statistics and its applications to high-energy physics. The name non-extensivity arises from the non-additive (often anointed as pseudo-additive) nature of the entropy, which is shown below,

3.3 Tsallis non-extensive statistics

$$S_q(A + B) = S_q(A) + S_q(B) + (1 - q)S_q(A)S_q(B). \quad (3.6)$$

Here, A and B are two independent systems in that the probabilities of the microstates of A+B factorize into those of A and B. The additive nature of the entropy can be restored when $q \rightarrow 1$, which is the case for the BG statistics. Further, we introduce the thermodynamically consistent Tsallis distribution function as [175–179],

$$f(E, q, T, \mu) = \frac{1}{\exp_q\left(\frac{E-\mu}{T}\right)}. \quad (3.7)$$

Where the q -exponential function is expressed as:

$$\exp_q(x) \equiv \begin{cases} [1 + (q - 1)x]^{\frac{1}{q-1}} & \text{if } x > 0, \\ [1 + (1 - q)x]^{\frac{1}{1-q}} & \text{if } x \leq 0, \end{cases} \quad (3.8)$$

where, $x = (E - \mu)/T$. Here, E , μ , T , and q are the energy, chemical potential, temperature, and the non-extensive parameter, respectively. It is worth noting that in the limit, $q \rightarrow 1$, the standard q -exponential function reduces to,

$$\lim_{q \rightarrow 1} \exp_q(x) = \exp(x). \quad (3.9)$$

To achieve thermodynamic consistency, an extra power of q is required in the distribution function:

$$f^q(E, q, T, \mu) = \frac{1}{[1 + (q - 1)\frac{E-\mu}{T}]^{\frac{q}{q-1}}}. \quad (3.10)$$

Numerically, the difference between Eq. 3.7 and Eq. 3.10 is insignificant as the value of q is always close to 1 for hadronic and nuclear collisions at relativistic energies. Since 2012, this modified form of the Tsallis distribution function (Eq. 3.10) has been widely used in the community and is popularly termed a thermodynamically consistent Tsallis distribution function. The thermodynamical quantities such as number density (n), energy density (ϵ), pressure (P), and

entropy density (s) in non-extensive statistics, can be obtained from the following relations:

$$n = g \int \frac{d^3p}{(2\pi)^3} \left[1 + (q-1) \frac{E-\mu}{T} \right]^{\frac{-q}{q-1}}, \quad (3.11)$$

$$\epsilon = g \int \frac{d^3p}{(2\pi)^3} E \left[1 + (q-1) \frac{E-\mu}{T} \right]^{\frac{-q}{q-1}}, \quad (3.12)$$

$$P = g \int \frac{d^3p}{(2\pi)^3} \frac{p^2}{3E} \left[1 + (q-1) \frac{E-\mu}{T} \right]^{\frac{-q}{q-1}}, \quad (3.13)$$

$$s = -g \int \frac{d^3p}{(2\pi)^3} \left[\frac{f-f^q}{1-q} - f \right], \quad (3.14)$$

where g is the degeneracy factor. The first and second laws of thermodynamics are described by the following two differential relations [180]:

$$d\epsilon = Tds + \mu dn, \quad (3.15)$$

$$dP = sdT + nd\mu. \quad (3.16)$$

Thermodynamic consistency demands that the subsequent relations be satisfied.

$$T = \left. \frac{\partial \epsilon}{\partial s} \right|_n, \quad (3.17)$$

$$n = \left. \frac{\partial P}{\partial \mu} \right|_T, \quad (3.18)$$

$$s = \left. \frac{\partial P}{\partial T} \right|_\mu, \quad (3.19)$$

$$\mu = \left. \frac{\partial \epsilon}{\partial n} \right|_s. \quad (3.20)$$

It is to be emphasized that Eq. 3.17 shows the variable T appearing in Eq. 3.10 obeys the thermodynamic relation and hence, the parameter T can be called

3.4 Thermodynamic consistency of Tsallis distribution function in the presence of an external magnetic field

a temperature, albeit for a system obeying Tsallis and not Boltzmann–Gibbs statistics. The detailed derivation is presented in [177, 178]. This work further demonstrates the thermodynamic consistency of these observables in the presence of an external magnetic field, as detailed in the following section.

3.4 Thermodynamic consistency of Tsallis distribution function in the presence of an external magnetic field

Before calculating the thermodynamic observables in this study, it is imperative to assess the thermodynamic consistency of Tsallis statistics under the influence of an external magnetic field. The specific form of distribution function given by Eq. 3.10 is employed in this investigation. Now, one can show its thermodynamic consistency as follows [153].

Note that one of the relevant constraints is given by the average number of particles, *i.e.*

$$\sum_i f_i^q = N. \quad (3.21)$$

Correspondingly, the energy of the system gives a constraint,

$$\sum_i f_i^q E_i = E. \quad (3.22)$$

Here, E_i stands for both $E_{i,n}$ and $E_{i,c}(p_z, k, s_z)$ and f_i stands for $f(E, q, T, \mu)$, which are defined in the formulation part. The first and second laws of thermodynamics follow the modified differential relations in the presence of an external magnetic field,

$$d\epsilon = Tds + \mu dn + (eB)dM, \quad (3.23)$$

$$dP = sdT + nd\mu + Md(eB). \quad (3.24)$$

Here, $\epsilon = E/V$, $s = S/V$, $n = N/V$, and $M = \mathcal{M}/V$ are the energy, entropy, particle, and magnetization density, respectively. Thermodynamic consistency demands that the subsequent relations be satisfied.

$$T = \left. \frac{\partial \epsilon}{\partial s} \right|_{n, M}, \quad (3.25)$$

$$n = \left. \frac{\partial P}{\partial \mu} \right|_{T, eB}, \quad (3.26)$$

$$s = \left. \frac{\partial P}{\partial T} \right|_{\mu, eB}, \quad (3.27)$$

$$\mu = \left. \frac{\partial \epsilon}{\partial n} \right|_{s, M}, \quad (3.28)$$

$$eB = \left. \frac{\partial \epsilon}{\partial M} \right|_{n, s}, \quad (3.29)$$

$$M = \left. \frac{\partial P}{\partial (eB)} \right|_{T, \mu}. \quad (3.30)$$

Now one proceeds to calculate Eq. 3.25, which can be explicitly written as,

$$\begin{aligned} \left. \frac{\partial E}{\partial S} \right|_{n, M} &= \frac{\frac{\partial E}{\partial T} dT + \frac{\partial E}{\partial \mu} d\mu + \frac{\partial E}{\partial (eB)} d(eB)}{\frac{\partial S}{\partial T} dT + \frac{\partial S}{\partial \mu} d\mu + \frac{\partial S}{\partial (eB)} d(eB)} \\ &= \frac{\frac{\partial E}{\partial T} + \frac{\partial E}{\partial \mu} \frac{d\mu}{dT} + \frac{\partial E}{\partial (eB)} \frac{d(eB)}{dT}}{\frac{\partial S}{\partial T} + \frac{\partial S}{\partial \mu} \frac{d\mu}{dT} + \frac{\partial S}{\partial (eB)} \frac{d(eB)}{dT}}. \end{aligned} \quad (3.31)$$

One of the additional constraint is that n is kept fixed, which leads to,

$$\begin{aligned} dn &= \frac{\partial n}{\partial T} dT + \frac{\partial n}{\partial \mu} d\mu + \frac{\partial n}{\partial (eB)} d(eB) = 0 \\ \Rightarrow \frac{d\mu}{dT} &= - \left[\frac{\frac{\partial n}{\partial T} + \frac{\partial n}{\partial (eB)} \frac{d(eB)}{dT}}{\frac{\partial n}{\partial \mu}} \right]. \end{aligned} \quad (3.32)$$

Now we calculate each term of Eq. 3.31, which can be explicitly written as follows:

$$\frac{\partial E}{\partial T} = \sum_i q E_i f_i^{q-1} \frac{\partial f_i}{\partial T}, \quad (3.33)$$

3.4 Thermodynamic consistency of Tsallis distribution function in the presence of an external magnetic field

$$\frac{\partial E}{\partial \mu} = \sum_i q E_i f_i^{q-1} \frac{\partial f_i}{\partial \mu}, \quad (3.34)$$

$$\frac{\partial n}{\partial T} = \frac{1}{V} \left[\sum_i q f_i^{q-1} \frac{\partial f_i}{\partial T} \right], \quad (3.35)$$

$$\frac{\partial n}{\partial \mu} = \frac{1}{V} \left[\sum_i q f_i^{q-1} \frac{\partial f_i}{\partial \mu} \right], \quad (3.36)$$

$$\frac{\partial S}{\partial T} = \sum_i q \left[\frac{-f_i^{q-1} + (1-f_i)^{q-1}}{q-1} \right] \frac{\partial f_i}{\partial T}, \quad (3.37)$$

$$\frac{\partial S}{\partial \mu} = \sum_i q \left[\frac{-f_i^{q-1} + (1-f_i)^{q-1}}{q-1} \right] \frac{\partial f_i}{\partial \mu}, \quad (3.38)$$

$$\frac{\partial E}{\partial(eB)} = \sum_i q E_i f_i^{q-1} \frac{\partial f_i}{\partial(eB)}, \quad (3.39)$$

$$\frac{\partial n}{\partial(eB)} = \frac{1}{V} \left[\sum_i q f_i^{q-1} \frac{\partial f_i}{\partial(eB)} \right], \quad (3.40)$$

$$\frac{\partial S}{\partial(eB)} = \sum_i q \left[\frac{-f_i^{q-1} + (1-f_i)^{q-1}}{q-1} \right] \frac{\partial f_i}{\partial(eB)}, \quad (3.41)$$

Where,

$$(1-f_i)^{q-1} = f_i^{q-1} \left[1 + \frac{(q-1)(E_i - \mu)}{T} \right]. \quad (3.42)$$

With these substitutions, the numerator of Eq. 3.31 becomes,

$$\begin{aligned}
 & \frac{\partial E}{\partial T} + \frac{\partial E}{\partial \mu} \frac{d\mu}{dT} + \frac{\partial E}{\partial(eB)} \frac{d(eB)}{dT} \\
 &= \sum_i q E_i f_i^{q-1} \frac{\partial f_i}{\partial T} - \sum_i q E_i f_i^{q-1} \frac{\partial f_i}{\partial \mu} \left[\frac{\frac{\partial n}{\partial T} + \frac{\partial n}{\partial(eB)} \frac{d(eB)}{dT}}{\frac{\partial n}{\partial \mu}} \right] \\
 &+ \sum_k q E_k f_k^{q-1} \frac{\partial f_k}{\partial(eB)} \frac{d(eB)}{dT} \\
 &= \sum_i q E_i f_i^{q-1} \frac{\partial f_i}{\partial T} - \frac{\sum_j q E_j f_j^{q-1} \frac{\partial f_j}{\partial \mu} \sum_i q f_i^{q-1} \frac{\partial f_i}{\partial T}}{\sum_j q f_j^{q-1} \frac{\partial f_j}{\partial \mu}} \\
 &- \frac{\sum_j q E_j f_j^{q-1} \frac{\partial f_j}{\partial \mu} \sum_k q f_k^{q-1} \frac{\partial f_k}{\partial(eB)} \frac{d(eB)}{dT}}{\sum_j q f_j^{q-1} \frac{\partial f_j}{\partial \mu}} + \sum_k q E_k f_k^{q-1} \frac{\partial f_k}{\partial(eB)} \frac{d(eB)}{dT} \\
 &= \frac{q \left[\sum_{i,j} E_i C_{ij} + \sum_{j,k} E_j D_{jk} \frac{d(eB)}{dT} \right]}{\sum_j f_j^{q-1} \frac{\partial f_j}{\partial \mu}}. \tag{3.43}
 \end{aligned}$$

Here,

$$C_{ij} \equiv (f_i f_j)^{q-1} \left[\frac{\partial f_i}{\partial T} \frac{\partial f_j}{\partial \mu} - \frac{\partial f_j}{\partial T} \frac{\partial f_i}{\partial \mu} \right], \tag{3.44}$$

$$D_{jk} \equiv (f_j f_k)^{q-1} \left[\frac{\partial f_j}{\partial \mu} \frac{\partial f_k}{\partial(eB)} - \frac{\partial f_k}{\partial \mu} \frac{\partial f_j}{\partial(eB)} \right]. \tag{3.45}$$

Similarly, the denominator of Eq. 3.31 is,

$$\begin{aligned}
 & \frac{\partial S}{\partial T} + \frac{\partial S}{\partial \mu} \frac{d\mu}{dT} + \frac{\partial S}{\partial(eB)} \frac{d(eB)}{dT} = \frac{\partial S}{\partial T} - \frac{\partial S}{\partial \mu} \left[\frac{\frac{\partial n}{\partial T} + \frac{\partial n}{\partial(eB)} \frac{d(eB)}{dT}}{\frac{\partial n}{\partial \mu}} \right] + \frac{\partial S}{\partial(eB)} \frac{d(eB)}{dT} \\
 &= \sum_i q \left[\frac{-f_i^{q-1} + (1-f_i)^{q-1}}{q-1} \right] \frac{\partial f_i}{\partial T} - \frac{\sum_j q \left[\frac{-f_j^{q-1} + (1-f_j)^{q-1}}{q-1} \right] \frac{\partial f_j}{\partial \mu} \sum_i q f_i^{q-1} \frac{\partial f_i}{\partial T}}{\sum_j q f_j^{q-1} \frac{\partial f_j}{\partial \mu}} \\
 &- \frac{\sum_j q \left[\frac{-f_j^{q-1} + (1-f_j)^{q-1}}{q-1} \right] \frac{\partial f_j}{\partial \mu} \sum_k q f_k^{q-1} \frac{\partial f_k}{\partial(eB)} \frac{d(eB)}{dT}}{\sum_j q f_j^{q-1} \frac{\partial f_j}{\partial \mu}} \\
 &+ \sum_k q \left[\frac{-f_k^{q-1} + (1-f_k)^{q-1}}{q-1} \right] \frac{\partial f_k}{\partial(eB)} \frac{d(eB)}{dT} \\
 &= \frac{q \left[\sum_{i,j} (E_i - \mu) C_{i,j} + \sum_{j,k} (E_j - \mu) D_{j,k} \frac{d(eB)}{dT} \right]}{T \sum_j f_j^{q-1} \frac{\partial f_j}{\partial \mu}}. \tag{3.46}
 \end{aligned}$$

3.4 Thermodynamic consistency of Tsallis distribution function in the presence of an external magnetic field

Where,

$$\frac{-f_i^{q-1} + (1-f_i)^{q-1}}{q-1} = \frac{(E_i - \mu)}{T} f_i^{q-1}. \quad (3.47)$$

Now, by substituting Eq. 3.43 and Eq. 3.46 in Eq. 3.31 one obtain,

$$\left. \frac{\partial E}{\partial S} \right|_{n,M} = T \left[\frac{\sum_{i,j} E_i C_{ij} + \sum_{j,k} E_j D_{jk} \frac{d(eB)}{dT}}{\sum_{i,j} (E_i - \mu) C_{ij} + \sum_{j,k} (E_j - \mu) D_{jk} \frac{d(eB)}{dT}} \right]. \quad (3.48)$$

Since, $\sum_{i,j} C_{ij} = 0$ and $\sum_{j,k} D_{jk} = 0$ it eventually leads to the desired result

$$\left. \frac{\partial E}{\partial S} \right|_{n,M} = T. \quad (3.49)$$

Another thermodynamic quantity is the number density n and partial derivative concerning μ to check for thermodynamic consistency. From the law of thermodynamics, it is known that,

$$P = \frac{-E_{\text{total}} + TS + \mu N + eB\mathcal{M}}{V} = \frac{-E + TS + \mu N}{V}, \quad (3.50)$$

where, $E_{\text{total}} = E + eB\mathcal{M}$.

$$\begin{aligned} \left. \frac{\partial P}{\partial \mu} \right|_{T,eB} &= \frac{1}{V} \left[-\frac{\partial E}{\partial \mu} + T \frac{\partial S}{\partial \mu} + N + \mu \frac{\partial N}{\partial \mu} \right] \\ &= \frac{1}{V} \left[N - \frac{\partial E}{\partial \mu} + \frac{\partial E}{\partial \mu} \right]. \end{aligned} \quad (3.51)$$

Where,

$$T \frac{\partial S}{\partial \mu} + \mu \frac{\partial N}{\partial \mu} = \frac{\partial E}{\partial \mu}. \quad (3.52)$$

Hence, one obtains,

$$\left. \frac{\partial P}{\partial \mu} \right|_{T,eB} = n. \quad (3.53)$$

Similarly, one can define,

$$\mathcal{M} = MV = \sum_i f_i^q \left(\frac{E_{\text{total}} - E_i}{eB} \right), \quad (3.54)$$

$$\frac{\partial E_{\text{total}}}{\partial(eB)} = \sum_i q E_{\text{total}} f_i^{q-1} \frac{\partial f_i}{\partial(eB)}, \quad (3.55)$$

$$\frac{\partial \mathcal{M}}{\partial(eB)} = \sum_i q \left(\frac{E_{\text{total}} - E_i}{eB} \right) f_i^{q-1} \frac{\partial f_i}{\partial(eB)}. \quad (3.56)$$

$$\begin{aligned} \left. \frac{\partial P}{\partial(eB)} \right|_{T,\mu} &= \frac{1}{V} \left[-\frac{\partial E_{\text{total}}}{\partial(eB)} + T \frac{\partial S}{\partial(eB)} + \mu \frac{\partial N}{\partial(eB)} + \mathcal{M} + eB \frac{\partial \mathcal{M}}{\partial(eB)} \right] \\ &= \frac{1}{V} \left[\mathcal{M} - \frac{\partial E_{\text{total}}}{\partial(eB)} + \frac{\partial E_{\text{total}}}{\partial(eB)} \right]. \end{aligned} \quad (3.57)$$

Where,

$$T \frac{\partial S}{\partial(eB)} + \mu \frac{\partial N}{\partial(eB)} + eB \frac{\partial \mathcal{M}}{\partial(eB)} = \frac{\partial E_{\text{total}}}{\partial(eB)}. \quad (3.58)$$

Hence, to obtain the desired result,

$$\left. \frac{\partial P}{\partial(eB)} \right|_{T,\mu} = M. \quad (3.59)$$

Hence, it establishes that the definitions of temperature, pressure, and magnetization density within the Tsallis non-extensive statistics used in this work are consistent with thermodynamics' first and second laws. The remaining relations can be verified similarly. In the following section, we estimate the thermodynamical observables of hadron gas in the presence of an external magnetic field.

3.5 Thermodynamics of hadron gas in an external magnetic field

In quantum mechanics, when a charged particle moves in a magnetic field, its energy associated with circular motion in the plane perpendicular to the field is

3.5 Thermodynamics of hadron gas in an external magnetic field

quantized. In contrast, motion along the direction parallel to the field remains continuous. Integrating over the momentum components p_x and p_y representing motion in the plane perpendicular to the magnetic field - effectively sums over quantized momentum states, yielding the density of states in the $x - y$ plane per unit area. Thus, in the presence of a finite magnetic field, the phase-space integral is expressed as a one-dimensional integral, $\frac{1}{(2\pi)^2} \iint dp_x dp_y = \frac{|e_i|B}{2\pi}$ [160, 161].

Now, one can rewrite Eq. 3.11 for charged and neutral particles in the presence of a strong magnetic field for chemical potential, $\mu = 0$ as follows,

$$n_c = \sum_i \sum_k \sum_{s_z} \frac{g_i |e_i| B}{(2\pi)^2} \int dp_z \left[1 + (q-1) \frac{E_{i,c}}{T} \right]^{\frac{-q}{q-1}}; \quad (e_i \neq 0). \quad (3.60)$$

$$n_n = \sum_i g_i \int \frac{d^3p}{(2\pi)^3} \left[1 + (q-1) \frac{E_{i,n}}{T} \right]^{\frac{-q}{q-1}}; \quad (e_i = 0). \quad (3.61)$$

Here, summations over i, k, s_z refer to all the hadrons up to the mass of 1.2 GeV, Landau levels, and spin along the z-direction, respectively.

3.5.1 Energy density and magnetization of hadron gas

The Eq. 3.12 can be rewritten for charged and neutral particles in the presence of a strong magnetic field for chemical potential, $\mu = 0$ as follows,

$$\epsilon_c = \sum_i \sum_k \sum_{s_z} \frac{g_i |e_i| B}{(2\pi)^2} \int dp_z E_{i,c} \left[1 + (q-1) \frac{E_{i,c}}{T} \right]^{\frac{-q}{q-1}}; \quad (e_i \neq 0). \quad (3.62)$$

$$\epsilon_n = \sum_i g_i \int \frac{d^3p}{(2\pi)^3} E_{i,n} \left[1 + (q-1) \frac{E_{i,n}}{T} \right]^{\frac{-q}{q-1}}; \quad (e_i = 0). \quad (3.63)$$

Further, the Helmholtz free energy is written as,

$$f_H = \epsilon - Ts. \quad (3.64)$$

In the presence of constant external magnetic field B , the modified energy density and Helmholtz free energy become,

$$\epsilon_{\text{total}} = \epsilon_c + \epsilon_n + eB(M + \Delta M_{\text{vac}}) = \epsilon + eBM_{\text{total}}. \quad (3.65)$$

Where, $\epsilon = \epsilon_c + \epsilon_n$ and $M_{\text{total}} = M + \Delta M_{\text{vac}}$, and M_{total} is the total magnetization of the system due to external magnetic field. Furthermore, ΔM_{vac} is the vacuum magnetization term in the presence of an external magnetic field at $T=0$. The vacuum magnetization of the system is given by,

$$\Delta M_{\text{vac}} = \frac{\partial(\Delta P_{\text{vac}})}{\partial(eB)}. \quad (3.66)$$

$$f_{\text{H}} = \epsilon_{\text{total}} - Ts - eBM_{\text{total}}. \quad (3.67)$$

At the thermodynamical limit, $V \rightarrow \infty$, we can assume $f_{\text{H}} = -P$ [154, 155]. So, from Eq. 3.67 we have,

$$eBM_{\text{total}} = \epsilon_{\text{total}} - Ts + P. \quad (3.68)$$

$$M_{\text{total}} = \frac{\epsilon_{\text{total}} - (Ts - P)}{eB}. \quad (3.69)$$

$$M_{\text{total}} = \frac{\epsilon_{\text{total}} - \epsilon}{eB}, \quad \text{where, } \epsilon = (Ts - P). \quad (3.70)$$

3.5.2 Pressure of a magnetized hardon gas

Furthermore, Eq. 3.13 can be rewritten for charged and neutral particles in the presence of a strong magnetic field for chemical potential, $\mu = 0$ as follows,

$$P_c = \sum_i \sum_k \sum_{s_z} \frac{g_i |e_i| B}{(2\pi)^2} \int dp_z \frac{p^2}{3E_{i,c}} \left[1 + (q-1) \frac{E_{i,c}}{T} \right]^{\frac{-q}{q-1}}; \quad (e_i \neq 0). \quad (3.71)$$

$$P_n = \sum_i g_i \int \frac{d^3p}{(2\pi)^3} \frac{p^2}{3E_{i,n}} \left[1 + (q-1) \frac{E_{i,n}}{T} \right]^{\frac{-q}{q-1}}; \quad (e_i = 0). \quad (3.72)$$

Thus, the total pressure(P) of the system is obtained by adding the thermal part of the pressure to the vacuum part (ΔP_{vac}).

$$P = P_c + P_n + \Delta P_{\text{vac}}. \quad (3.73)$$

3.5 Thermodynamics of hadron gas in an external magnetic field

The following section will calculate the renormalized vacuum pressure at a finite magnetic field.

3.5.3 Renormalization of vacuum pressure

In the prior section, we calculated the thermal component of the thermodynamic observables. Now, let's shift our focus to the vacuum contribution of these observables in the presence of an external magnetic field, utilizing a regularization technique. The magnetic field induces a vacuum contribution to most observables, ensuring that, for instance, the pressure does not vanish at $T = 0$. However, the vacuum pressure term diverges and demands suitable regularization. Unphysical results can arise, especially when employing magnetic field-dependent regularization methods. Therefore, it is crucial to distinctly separate the magnetic field-dependent and independent components using an appropriate regularization technique.

In the presence of an external magnetic field, the vacuum pressure for spin- $\frac{1}{2}$ charged-particles is shown below [154–156],

$$P_{\text{vac}}(S = 1/2, B) = \frac{1}{2} \sum_{k=0}^{\infty} g_k \frac{eB}{2\pi} \int_{-\infty}^{\infty} \frac{dp_z}{2\pi} E_{p,k}(B), \quad (3.74)$$

where $g_k = 2 - \delta_{k0}$ is the degeneracy of k^{th} Landau level. Now, adding and subtracting the lowest Landau level contribution term (i.e., $k = 0$) from the overhead equation, one obtains,

$$P_{\text{vac}}(S = 1/2, B) = \frac{1}{2} \sum_{k=0}^{\infty} 2 \frac{eB}{2\pi} \int_{-\infty}^{\infty} \frac{dp_z}{2\pi} \left[E_{p,k}(B) - \frac{E_{p,0}(B)}{2} \right]. \quad (3.75)$$

The divergence can be regularized using the dimensional regularization approach [181]. When employing a $d - \epsilon$ dimension Eq. 3.75 can be reformulated as follow:

$$P_{\text{vac}}(S = 1/2, B) = \sum_{k=0}^{\infty} \frac{eB}{2\pi} \mu^\epsilon \int_{-\infty}^{\infty} \frac{d^{1-\epsilon} p_z}{(2\pi)^{1-\epsilon}} \left[\sqrt{p_z^2 + m^2 - 2eBk} - \sqrt{p_z^2 + m^2} \right]. \quad (3.76)$$

In the above expression, μ fixes the dimension to one. Integration is performed utilizing conventional d -dimensional formula [181, 182].

$$\int_{-\infty}^{\infty} \frac{d^d p}{(2\pi)^d} \left[p^2 + m^2 \right]^{-A} = \frac{\Gamma[A - \frac{d}{2}]}{(4\pi)^{d/2} \Gamma[A] (M^2)^{(A - \frac{d}{2})}}. \quad (3.77)$$

The first term in Eq. 3.76 is integrated as:

$$\begin{aligned} I_1 &= \sum_{k=0}^{\infty} \frac{eB}{2\pi} \mu^\epsilon \int_{-\infty}^{\infty} \frac{d^{1-\epsilon} p_z}{(2\pi)^{1-\epsilon}} \left[p_z^2 + m^2 - 2eBk \right]^{\frac{1}{2}} \\ &= -\frac{(eB)^2}{4\pi^2} \left(\frac{2eB}{4\pi\mu} \right)^{-\frac{\epsilon}{2}} \Gamma \left[-1 + \frac{\epsilon}{2} \right] \zeta \left[-1 + \frac{\epsilon}{2}, x \right]. \end{aligned} \quad (3.78)$$

Here, $x \equiv \frac{m^2}{2eB}$. The Landau infinite sum has been depicted in terms of the Riemann-Hurwitz ζ -function

$$\zeta[z, x] = \sum_{k=0}^{\infty} \frac{1}{[x+k]^z}, \quad (3.79)$$

with the expansion

$$\zeta \left[-1 + \frac{\epsilon}{2}, x \right] \approx -\frac{1}{12} - \frac{x^2}{2} + \frac{x}{2} + \frac{\epsilon}{2} \zeta'(-1, x) + \mathcal{O}(\epsilon^2), \quad (3.80)$$

and the asymptotic behavior of the derivative [183, 184],

$$\zeta'(-1, x) = \frac{1}{12} - \frac{x^2}{4} + \left(\frac{1}{12} - \frac{x}{2} + \frac{x^2}{2} \right) \ln(x) + \mathcal{O}(x^{-2}). \quad (3.81)$$

The expansion of the Γ -function around negative integers is given by

$$\Gamma \left[-1 + \frac{\epsilon}{2} \right] = -\frac{2}{\epsilon} + \gamma - 1 + \mathcal{O}(\epsilon), \quad (3.82)$$

3.5 Thermodynamics of hadron gas in an external magnetic field

and

$$\Gamma\left[-2 + \frac{\epsilon}{2}\right] = \frac{1}{\epsilon} - \frac{\gamma}{2} + \frac{3}{4} + \mathcal{O}(\epsilon), \quad (3.83)$$

Here γ is the Euler constant. The limiting expression for natural logarithm,

$$\lim_{\epsilon \rightarrow 0} a^{-\epsilon/2} \approx 1 - \frac{\epsilon}{2} \ln(a). \quad (3.84)$$

By employing the expansion of both the ζ and Γ functions, it is possible to express Eq. 3.78 as:

$$I_1 = -\frac{(eB)^2}{4\pi^2} \left[-\frac{2}{\epsilon} + \gamma - 1 + \ln\left(\frac{2eB}{4\pi\mu^2}\right) \right] \left[-\frac{1}{12} - \frac{x^2}{2} + \frac{x}{2} + \frac{\epsilon}{2} \zeta'(-1, x) + \mathcal{O}(\epsilon^2) \right] \quad (3.85)$$

The second term in Eq. 3.76 can be simplified similarly. One obtains

$$\begin{aligned} I_2 &= \sum_{k=0}^{\infty} \frac{eB}{2\pi} \mu^\epsilon \int_{-\infty}^{\infty} \frac{d^{1-\epsilon} p_z}{(2\pi)^{1-\epsilon}} \left[p_z^2 + m^2 \right]^{\frac{1}{2}} \\ &= \frac{(eB)^2}{4\pi^2} \left[-\frac{x}{\epsilon} - \frac{(1-\gamma)}{2} x + \frac{x}{2} \ln\left(\frac{2eB}{4\pi\mu^2}\right) + \frac{x}{2} \ln(x) \right]. \end{aligned} \quad (3.86)$$

Hence, the vacuum pressure in the presence of an external magnetic field becomes

$$\begin{aligned} P_{\text{vac}}(S = 1/2, B) &= \frac{(eB)^2}{4\pi^2} \left[\zeta'(-1, x) - \frac{2}{12\epsilon} - \frac{(1-\gamma)}{12} - \frac{x^2}{\epsilon} - \frac{(1-\gamma)}{2} x^2 \right. \\ &\quad \left. + \frac{x}{2} \ln(x) + \frac{x^2}{2} \ln\left(\frac{2eB}{4\pi\mu^2}\right) + \frac{1}{12} \ln\left(\frac{2eB}{4\pi\mu^2}\right) \right]. \end{aligned} \quad (3.87)$$

There is still divergence in the expression mentioned above. As a result, we add and subtract the $B = 0$ contribution. To execute the renormalization of the $B > 0$ pressure, it is essential to determine the $B = 0$ contribution. The vacuum pressure at $B = 0$ in $d = 3 - \epsilon$ dimensions is expressed as follows.

$$\begin{aligned} P_{\text{vac}}(S = 1/2, B = 0) &= \mu^\epsilon \int \frac{d^{3-\epsilon} p}{(2\pi)^{3-\epsilon}} (p^2 + m^2)^{\frac{1}{2}} \\ &= \frac{(eB)^2}{4\pi^2} \left(\frac{2eB}{4\pi\mu^2} \right)^{-\frac{\epsilon}{2}} \Gamma\left(-2 + \frac{\epsilon}{2}\right) x^{2-\frac{\epsilon}{2}}. \end{aligned} \quad (3.88)$$

The Γ -function expansion in Eq. 3.83 can further simplify the above Eq. 3.88 as:

$$P_{\text{vac}}(S = 1/2, B = 0) = -\frac{(eB)^2}{4\pi^2} x^2 \left[\frac{1}{\epsilon} + \frac{3}{4} - \frac{\gamma}{2} - \frac{1}{2} \ln \left(\frac{2eB}{4\pi\mu^2} \right) - \frac{1}{2} \ln(x) \right]. \quad (3.89)$$

Now, we obtain the regularized pressure with the vacuum component and the magnetic field-dependent part separated as follows by adding and subtracting Eq. 3.89 from Eq. 3.87,

$$P_{\text{vac}}(S = 1/2, B) = P_{\text{vac}}(1/2, B = 0) + \Delta P_{\text{vac}}(1/2, B), \quad (3.90)$$

where,

$$\begin{aligned} \Delta P_{\text{vac}}(S = 1/2, B) = & \frac{(eB)^2}{4\pi^2} \left[-\frac{2}{12\epsilon} + \frac{\gamma}{12} + \frac{1}{12} \ln \left(\frac{m^2}{4\pi\mu^2} \right) + \frac{x}{2} \ln(x) \right. \\ & \left. - \frac{x^2}{2} \ln(x) + \frac{x^2}{4} - \frac{\ln(x) + 1}{12} + \zeta'(-1, x) \right]. \end{aligned} \quad (3.91)$$

However, due to the existence of the magnetic field dependent term $\frac{B^2}{\epsilon}$ [185–187], the field contribution provided by Eq. 3.91 is divergent. This divergence can be eliminated by redefining the field-dependent pressure contribution to include the magnetic field component.

$$\Delta P_{\text{vac}}^r = \Delta P_{\text{vac}}(B) - \frac{B^2}{2}. \quad (3.92)$$

The divergences are absorbed into the renormalization of the electric charge and the magnetic field strength [155],

$$B^2 = Z_e B_r^2; \quad e^2 = Z_e^{-1} e_r^2; \quad e_r B_r = eB. \quad (3.93)$$

Where the renormalization constant for electric charge is

$$Z_e \left(S = \frac{1}{2} \right) = 1 + \frac{1}{2} e_r^2 \left[-\frac{2}{12\epsilon} + \frac{\gamma}{12} + \frac{1}{12} \ln \left(\frac{m_*}{4\pi\mu^2} \right) \right], \quad (3.94)$$

3.5 Thermodynamics of hadron gas in an external magnetic field

where $m_* = m$, *i.e.*, is fixed to the particle's physical mass. Consequently, the field-dependent pressure that is renormalized without the contribution of pure magnetic field ($\frac{B^2}{2}$) is,

$$\Delta P_{\text{vac}}^r(S = 1/2, B) = \frac{(eB)^2}{4\pi^2} \left[\zeta'(-1, x) + \frac{x}{2} \ln(x) - \frac{x^2}{2} \ln(x) + \frac{x^2}{4} - \frac{\ln(x) + 1}{12} \right]. \quad (3.95)$$

The technique formerly described can be used to illustrate the renormalized magnetic field (B) dependent pressure for spin-zero and spin-one particles. These terms play a significant role in finding the magnetization of the hadronic matter. We observed that the charge, mass, spin, etc., affect the vacuum pressure. Therefore, the total vacuum pressure of hadron gas is estimated by summing the vacuum pressure of all the particles considered in this work.

For spin-zero particles, the regularized vacuum pressure is

$$\Delta P_{\text{vac}}^r(s = 0, B) = -\frac{(eB)^2}{8\pi^2} \left[\zeta'(-1, x + 1/2) - \frac{x^2}{2} \ln(x) + \frac{x^2}{4} + \frac{\ln(x) + 1}{24} \right]. \quad (3.96)$$

Similarly, for spin-one particles,

$$\begin{aligned} \Delta P_{\text{vac}}^r(s = 1, B) &= -\frac{3(eB)^2}{8\pi^2} \left[\zeta'(-1, x - 1/2) + \frac{(x + 1/2)}{3} \ln(x + 1/2) \right. \\ &\quad \left. + \frac{2}{3}(x - 1/2) \ln(x - 1/2) - \frac{x^2}{2} \ln(x) + \frac{x^2}{4} - \frac{7}{24}(\ln(x) + 1) \right]. \end{aligned} \quad (3.97)$$

So, the total magnetic field-dependent vacuum pressure becomes

$$\Delta P_{\text{vac}} = \Delta P_{\text{vac}}^r(s = 0, B) + \Delta P_{\text{vac}}^r(S = 1/2, B) + \Delta P_{\text{vac}}^r(s = 1, B). \quad (3.98)$$

3.5.4 The speed of sound in a magnetized hadron gas

The speed of sound is essential in hydrodynamics for describing the equation of state and, consequently, the associated phase transition [188–190]

$$c_s^2(T, \mu, eB) = \left(\frac{\partial P}{\partial \epsilon} \right) \Big|_{\frac{s}{n}}. \quad (3.99)$$

This can be rewritten using T , μ , and eB as variables.

$$c_s^2(T, \mu, eB) = \frac{\partial P}{\partial \epsilon} = \frac{\frac{\partial P}{\partial T} + \frac{\partial P}{\partial \mu} \frac{d\mu}{dT} + \frac{\partial P}{\partial(eB)} \frac{d(eB)}{dT}}{\frac{\partial \epsilon}{\partial T} + \frac{\partial \epsilon}{\partial \mu} \frac{d\mu}{dT} + \frac{\partial \epsilon}{\partial(eB)} \frac{d(eB)}{dT}}. \quad (3.100)$$

The number density (n) and entropy density (s) of a system depend on (T, μ, eB) . The first condition is keeping the ratio (s/n) constant. From the derivative, one gets

$$d\left(\frac{s}{n}\right) = 0, \quad (3.101)$$

which implies:

$$nds = sdn. \quad (3.102)$$

Divide both sides by dT so that the above Eq. 3.102 can be modified as:

$$n\left(\frac{ds}{dT}\right) = s\left(\frac{dn}{dT}\right). \quad (3.103)$$

One can write $n(T, \mu, eB)$ and $s(T, \mu, eB)$ in the form of differential as:

$$dn = \frac{\partial n}{\partial T} dT + \frac{\partial n}{\partial \mu} d\mu + \frac{\partial n}{\partial(eB)} d(eB). \quad (3.104)$$

Hence, we obtained the following result by dividing both sides of Eq. 3.104 by dT .

$$\frac{dn}{dT} = \frac{\partial n}{\partial T} + \frac{\partial n}{\partial \mu} \frac{d\mu}{dT} + \frac{\partial n}{\partial(eB)} \frac{d(eB)}{dT}. \quad (3.105)$$

Likewise for $s(T, \mu, eB)$ we can write,

$$ds = \frac{\partial s}{\partial T} dT + \frac{\partial s}{\partial \mu} d\mu + \frac{\partial s}{\partial(eB)} d(eB). \quad (3.106)$$

3.5 Thermodynamics of hadron gas in an external magnetic field

$$\frac{ds}{dT} = \frac{\partial s}{\partial T} + \frac{\partial s}{\partial \mu} \frac{d\mu}{dT} + \frac{\partial s}{\partial(eB)} \frac{d(eB)}{dT}. \quad (3.107)$$

Substituting Eq. 3.105 and Eq. 3.107 in Eq. 3.103 we get,

$$n \left(\frac{\partial s}{\partial T} + \frac{\partial s}{\partial \mu} \frac{d\mu}{dT} + \frac{\partial s}{\partial(eB)} \frac{d(eB)}{dT} \right) = s \left(\frac{\partial n}{\partial T} + \frac{\partial n}{\partial \mu} \frac{d\mu}{dT} + \frac{\partial n}{\partial(eB)} \frac{d(eB)}{dT} \right). \quad (3.108)$$

Now, one can rearrange the coefficient and obtain the following relation

$$\begin{aligned} \frac{d\mu}{dT} \left(n \frac{\partial s}{\partial \mu} - s \frac{\partial n}{\partial \mu} \right) &= s \left(\frac{\partial n}{\partial T} + \frac{\partial n}{\partial(eB)} \frac{d(eB)}{dT} \right) - n \left(\frac{\partial s}{\partial T} + \frac{\partial s}{\partial(eB)} \frac{d(eB)}{dT} \right) \\ \Rightarrow \frac{d\mu}{dT} &= \frac{\left(s \frac{\partial n}{\partial T} - n \frac{\partial s}{\partial T} \right) + \left(s \frac{\partial n}{\partial(eB)} - n \frac{\partial s}{\partial(eB)} \right) \frac{d(eB)}{dT}}{n \frac{\partial s}{\partial \mu} - s \frac{\partial n}{\partial \mu}}. \end{aligned} \quad (3.109)$$

Similarly, one can evaluate $\frac{d(eB)}{dT}$ from Eq. 3.108 as follows,

$$\frac{d(eB)}{dT} = \frac{\left(s \frac{\partial n}{\partial T} - n \frac{\partial s}{\partial T} \right) + \left(s \frac{\partial n}{\partial \mu} - n \frac{\partial s}{\partial \mu} \right) \frac{d\mu}{dT}}{n \frac{\partial s}{\partial(eB)} - s \frac{\partial n}{\partial(eB)}}. \quad (3.110)$$

For a finite baryon chemical potential and finite external magnetic field, the above two transcendental equations can be solved numerically to find the speed of sound of the system. However, in this work, we have done our calculation at vanishing baryon chemical potential, which leads to $c_s^2(T, eB)$ as follows:

$$c_s^2(T, eB) = \frac{\frac{\partial P}{\partial T} + \frac{\partial P}{\partial(eB)} \frac{d(eB)}{dT}}{\frac{\partial \epsilon}{\partial T} + \frac{\partial \epsilon}{\partial(eB)} \frac{d(eB)}{dT}}. \quad (3.111)$$

Where,

$$\frac{d(eB)}{dT} = \frac{s \frac{\partial n}{\partial T} - n \frac{\partial s}{\partial T}}{n \frac{\partial s}{\partial(eB)} - s \frac{\partial n}{\partial(eB)}}, \quad (3.112)$$

$$\begin{aligned} \frac{\partial P}{\partial T} &= \frac{\partial P_c}{\partial T} + \frac{\partial P_n}{\partial T} = \sum_i \sum_k \sum_{s_z} \frac{g_i eB}{12\pi^2} \int dp_z \frac{p^2 q}{T^2} \left[1 + (q-1) \frac{E_{i,c}}{T} \right]^{\frac{1-2q}{q-1}} \\ &+ \sum_i \frac{g_i}{6\pi^2} \int dp \frac{p^4 q}{T^2} \left[1 + (q-1) \frac{E_{i,n}}{T} \right]^{\frac{1-2q}{q-1}}, \end{aligned} \quad (3.113)$$

$$\begin{aligned} \frac{\partial \epsilon}{\partial T} = \frac{\partial \epsilon_c}{\partial T} + \frac{\partial \epsilon_n}{\partial T} &= \sum_i \sum_k \sum_{s_z} \frac{g_i e B}{4\pi^2} \int dp_z \frac{q E_{i,c}^2}{T^2} \left[1 + (q-1) \frac{E_{i,c}}{T} \right]^{\frac{1-2q}{q-1}} \\ &+ \sum_i \frac{g_i}{2\pi^2} \int dp \frac{p^2 q E_{i,n}^2}{T^2} \left[1 + (q-1) \frac{E_{i,n}}{T} \right]^{\frac{1-2q}{q-1}}, \end{aligned} \quad (3.114)$$

$$\begin{aligned} \frac{\partial P}{\partial(eB)} = \frac{\partial P_c}{\partial(eB)} &= \sum_i \sum_k \sum_{s_z} \frac{g_i}{12\pi^2} \int dp_z p^2 \left[\frac{1}{E_{i,c}} \left(1 + (q-1) \frac{E_{i,c}}{T} \right)^{\frac{-q}{q-1}} \right. \\ &- \frac{eB(k+1/2-s_z)}{E_{i,c}^3} \left(1 + (q-1) \frac{E_{i,c}}{T} \right)^{\frac{-q}{q-1}} \\ &\left. - \frac{eB(k+1/2-s_z)q}{T E_{i,c}^2} \left(1 + (q-1) \frac{E_{i,c}}{T} \right)^{\frac{1-2q}{q-1}} \right], \end{aligned} \quad (3.115)$$

$$\begin{aligned} \frac{\partial \epsilon}{\partial(eB)} = \frac{\partial \epsilon_c}{\partial(eB)} &= \sum_i \sum_k \sum_{s_z} \frac{g_i}{4\pi^2} \int dp_z \left[E_{i,c} \left(1 + (q-1) \frac{E_{i,c}}{T} \right)^{\frac{-q}{q-1}} \right. \\ &+ \frac{eB(k+1/2-s_z)}{E_{i,c}} \left(1 + (q-1) \frac{E_{i,c}}{T} \right)^{\frac{-q}{q-1}} \\ &\left. - \frac{eB(k+1/2-s_z)q}{T} \left(1 + (q-1) \frac{E_{i,c}}{T} \right)^{\frac{1-2q}{q-1}} \right], \end{aligned} \quad (3.116)$$

$$\begin{aligned} \frac{\partial n}{\partial T} = \frac{\partial n_c}{\partial T} + \frac{\partial n_n}{\partial T} &= \sum_i \sum_k \sum_{s_z} \frac{g_i e B}{4\pi^2} \int dp_z \frac{q E_{i,c}}{T^2} \left(1 + (q-1) \frac{E_{i,c}}{T} \right)^{\frac{1-2q}{q-1}} \\ &+ \sum_i \frac{g_i}{2\pi^2} \int dp \frac{p^2 q E_{i,n}}{T^2} \left(1 + (q-1) \frac{E_{i,n}}{T} \right)^{\frac{1-2q}{q-1}}, \end{aligned} \quad (3.117)$$

$$\begin{aligned} \frac{\partial n}{\partial(eB)} = \frac{\partial n_c}{\partial(eB)} &= \sum_i \sum_k \sum_{s_z} \frac{g_i}{4\pi^2} \int dp_z \left[\left(1 + (q-1) \frac{E_{i,c}}{T} \right)^{\frac{-q}{q-1}} \right. \\ &\left. - \frac{eB(k+1/2-s_z)q}{E_{i,c} T} \left(1 + (q-1) \frac{E_{i,c}}{T} \right)^{\frac{1-2q}{q-1}} \right]. \end{aligned} \quad (3.118)$$

3.6 Results and Discussion

In the case of neutral particles, the contribution from $\frac{\partial P_e}{\partial(eB)}$, $\frac{\partial \epsilon_n}{\partial(eB)}$, and $\frac{\partial n_n}{\partial(eB)} = 0$ is absent due to the absence of the magnetic field term. When there are no external magnetic fields, the system's speed of sound drops to $c_s^2 = (\frac{\partial P}{\partial \epsilon})$. Note that, regardless of whether the system is extensive or non-extensive, the speed of sound can be determined from Euler's law as applied to a continuous medium without the need for thermodynamics [188].

With the above-detailed formalism, we discuss the results in the next section.

3.6 Results and Discussion

Enriching our exploration of a hadron gas, we have elegantly integrated the impact of an external magnetic field into the Tsallis distribution function. Our detailed calculations of the system's thermodynamic observables reflect the depth of our analysis. To illustrate the robustness of our findings, we have compared our findings with established results deriving from the Hadron Resonance Gas (HRG) model and the lattice Quantum Chromodynamics (QCD) model. This agreeable convergence of theoretical perspectives enhances our work's aesthetic appeal and strengthens our contributions' credibility within the hadronic physics [155, 159].

Figure. 3.2 depicts the variation of the total energy density of a hadron gas as a function of temperature for near equilibrium ($q = 1.001$), values of non-extensive parameters at a constant magnetic field $eB = 0 \text{ GeV}^2$ and $eB = 0.3 \text{ GeV}^2$, respectively. The behavior of the total energy density in the hadron gas system is paramount for understanding its thermodynamic properties, especially under the influence of an external magnetic field. We compare our results to those of the existing HRG and lattice QCD results. For $eB = 0 \text{ GeV}^2$, our results are consistent with HRG results [155] up to $T \sim 150 \text{ MeV}$. For $eB = 0.3 \text{ GeV}^2$, the total energy density values are consistent with HRG results up to $T \sim 110 \text{ MeV}$. Moreover, our results for an external magnetic field $eB = 0.3 \text{ GeV}^2$ are comparable to lattice QCD results [159]. This comprehensive analysis aids in

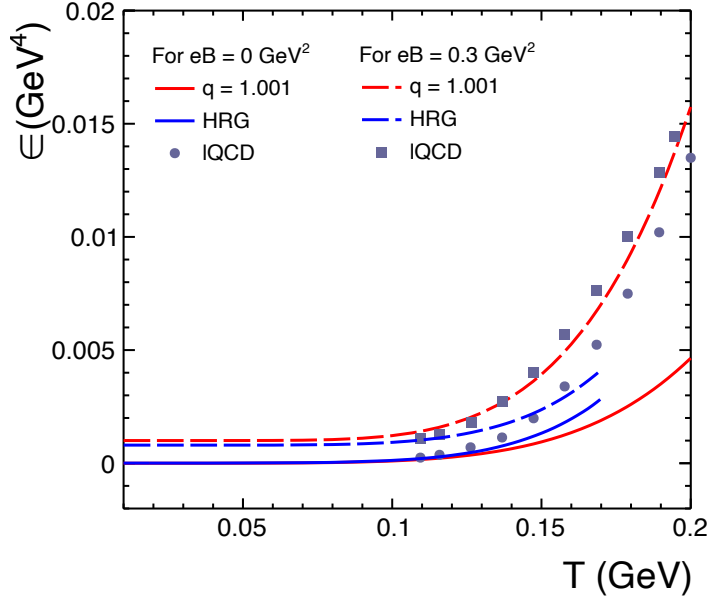


Figure 3.2: The energy density of a hadron gas as a function of temperature for near equilibrium, *i.e.* for $q = 1.001$, values of non-extensive parameters at a constant magnetic field $eB = 0 \text{ GeV}^2$ and $eB = 0.3 \text{ GeV}^2$ respectively [153]. The results are compared to the relevant HRG and lattice QCD data [155, 159].

refining our understanding of the intricate interplay between temperature, magnetic fields, and the thermodynamic behavior of hadronic matter, shedding light on phenomena occurring in extreme environments, such as those encountered in heavy-ion collisions.

The investigation into the total pressure of a hadron gas under the influence of a magnetic field provides additional insight into its thermodynamic behavior. Figure 3.3 demonstrates this variation, showing the total pressure as a function of temperature for $q = 1.001$ under a constant magnetic field of $eB = 0.3 \text{ GeV}^2$. Our estimated total pressure aligns closely with existing HRG predictions, indicating consistency within this theoretical framework. However, as the temperature increases, deviations between our estimations and the lattice QCD results become

3.6 Results and Discussion

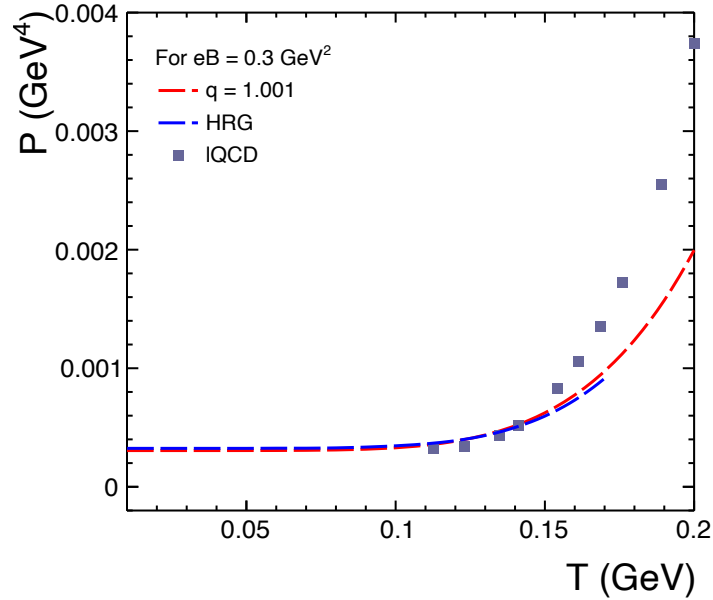


Figure 3.3: The pressure of a hadron gas as a function of temperature for near equilibrium (for $q = 1.001$) at a constant magnetic field $eB = 0.3 \text{ GeV}^2$ [153]. The findings are compared to HRG and lattice QCD data [155, 159].

apparent. This deviation underscores the complex nature of the system, hinting at the limitations of specific theoretical approaches and the necessity for further improvement to fully capture the thermodynamic intricacies of hadronic matter under extreme conditions. Such comparisons offer invaluable guidance for advancing our understanding of the behavior of strongly interacting matter.

After aligning our findings for the total energy density and the pressure of a magnetized hadron gas taking near equilibrium scenario ($q = 1.001$) with those from both the HRG model and lattice QCD, we now delve into a comprehensive investigation of thermodynamic observables under constant magnetic fields generated at RHIC (m_π^2) and LHC ($15m_\pi^2$) energies for both near and away from equilibrium using the non-extensive Tsallis statistics.

Figure 3.4 presents our investigation into the total energy density of a hadron

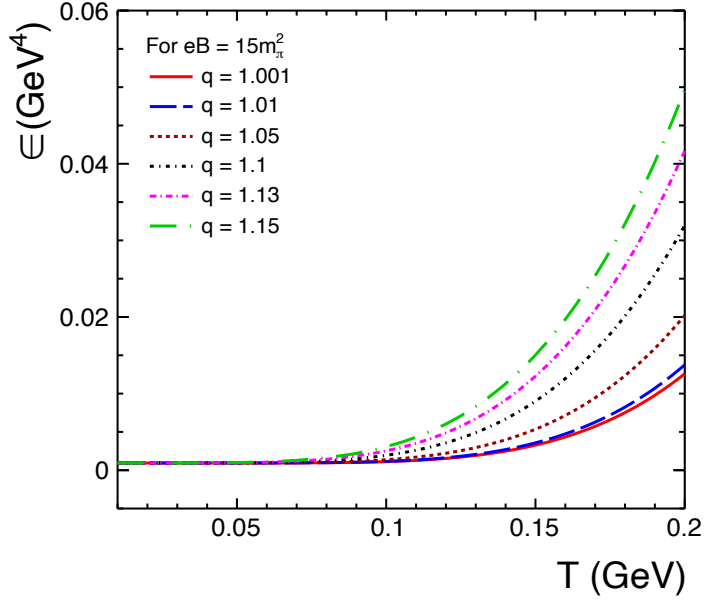


Figure 3.4: Total energy density of a hadron gas as a function of temperature for different values of the non-extensive parameter (q) at a constant magnetic field $eB = 15m_\pi^2$ [153].

gas, analyzing its behavior across a range of non-extensive parameter values under the influence of a fixed external magnetic field of $eB = 15m_\pi^2$. This magnetic field strength typically corresponds to the one usually created in non-central heavy-ion collisions at the LHC energies. Our observations reveal that energy density monotonically increases with an increase in temperature across all q -values. Notably, the system with the lowest q -value, indicating near equilibrium, consistently exhibits the lowest energy density across all temperatures. Conversely, the energy density rises as the system moves away from equilibrium, characterized by increasing q values. Notably, the system away from equilibrium, with the maximum q -value, consistently demonstrates the highest energy density across all temperature ranges. It's worth noting that at lower temperatures, a finite energy density exists attributable to vacuum contributions.

3.6 Results and Discussion

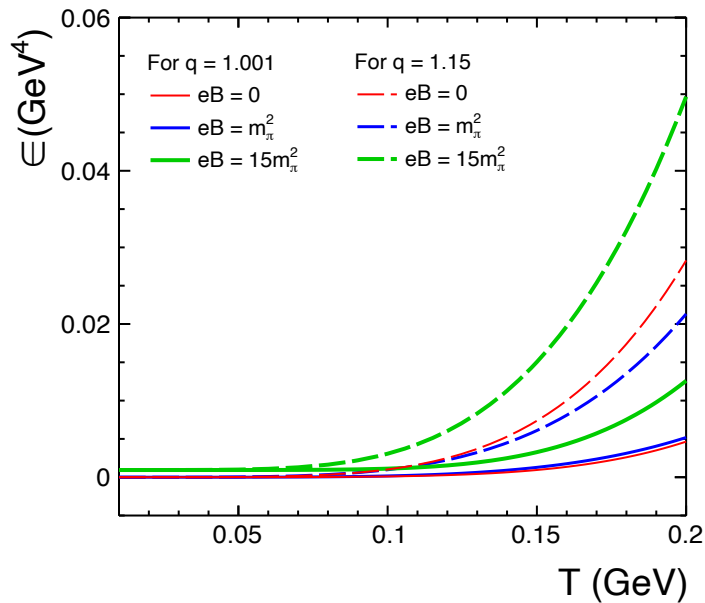


Figure 3.5: Total energy density of a hadron gas as a function of temperature at different magnetic fields and different q values [153].

Following the observation of a strong non-extensive parameter dependence of the system's energy density in the presence of an external magnetic field, we now investigate the competing effects of the non-extensive parameter and the external magnetic field by taking two extreme values of q . The Fig. 3.5 illustrates this. The two extreme values of q are $q = 1.001$, which corresponds to a near-equilibrium system, and $q = 1.15$, which corresponds to a system away from equilibrium. The former corresponds to central heavy-ion collisions in a realistic heavy-ion collision scenario, creating an equilibrated system. In contrast, the latter corresponds to mostly non-central heavy-ion or hadronic collisions. The energy density increases as the magnetic field increases for both the equilibrated system and the system that is out of equilibrium. For the scenario of the highest magnetic field taken into consideration in this study, as well as for the system primarily out of equilibrium, we see an enhanced energy density. When a system

is considered away from equilibrium ($q = 1.15$), we find that the energy density of the system increases with an increase in an external magnetic field at a lower temperature regime. However, the system with an external magnetic field $eB = m_\pi^2$ has a lower energy density at a higher temperature regime than the system without an external magnetic field. This result is fascinating, considering that this behavior is observed at high q -values when the system is away from equilibrium. However, this is not observed in the case of the equilibrated system $q = 1.001$.

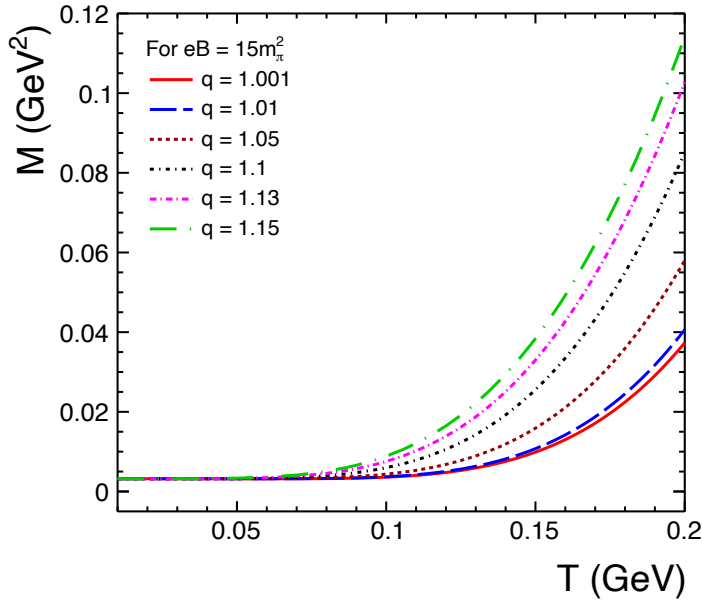


Figure 3.6: Magnetization of a hadron gas as a function of temperature for different values of the non-extensive parameter at a constant magnetic field $eB = 15m_\pi^2$ [153].

Figure 3.6 depicts the interpretation of magnetization of a hadron gas with temperature across various values of the non-extensive parameter, under a constant magnetic field strength of $eB = 15m_\pi^2$. It is evident that with the increase in temperature, the magnetization increases across all q -values. At lower temperatures, finite magnetization is attributed to the vacuum contribution, which

3.6 Results and Discussion

progressively increases with an increase in temperature. When the system approaches near equilibrium, denoted by lower q -values, the magnetization of the system is relatively lower. However, as the q value increases, indicating that it is away from equilibrium conditions, the magnetization of the system increases at all temperatures. Notably, the magnetization is higher for a given system temperature when away from equilibrium.

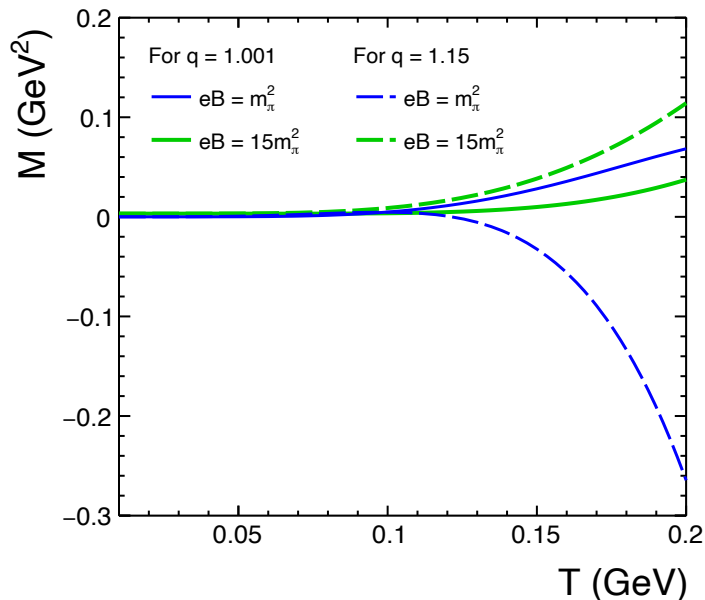


Figure 3.7: Magnetization of a hadron gas as a function of temperature at different magnetic fields and for different q -values [153].

Figure 3.7 shows the variation of magnetization at different magnetic fields for systems near and away from equilibrium. For $q = 1.001$ values, when the system is near equilibrium, the magnetization of the system with a lower external magnetic field is higher for all temperatures up to $T \sim 200$ MeV. However, exciting phenomena appear for $q=1.15$, indicating an away from equilibrium conditions. The magnetization of the system with external magnetic field $eB = m_{\pi}^2$ is observed to be negative. This indicates the system produced in high-energy

collisions under such an external magnetic field has diamagnetic properties. On the other hand, as the external magnetic field strength increases for the system away from equilibrium to $eB = 15m_\pi^2$, the system exhibits a positive magnetization, suggesting a paramagnetic behavior. This observation is fascinating as the produced magnetic field increases with the center-of-mass energy of the system from RHIC to the LHC, and the system undergoes a shift from diamagnetic to paramagnetic for peripheral heavy-ion collisions. Remember that, as discussed in the previous studies Ref. [155], a positive magnetization at a temperature of around 150 MeV has been regarded as resulting from the development of a paramagnetic substance. Similar observations are also found in Ref. [157]. However, the detailed dynamics of such a transition are beyond the scope of the current study and warrant further investigation.

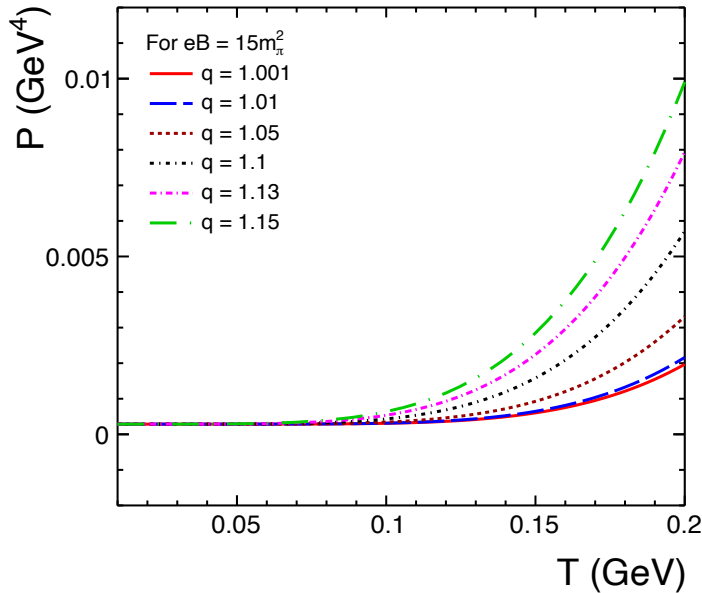


Figure 3.8: Pressure as a function of temperature in a magnetized hadron gas for different q -values, respectively [153].

Fig. 3.8 illustrates the variation of pressure of a magnetized hadron gas as a

3.6 Results and Discussion

function of temperature for different q -values. The system's pressure increases as the temperature increases for all q -values at a constant magnetic field $eB = 15m_\pi^2$. When the system is near equilibrium, *i.e.* for $q = 1.001$, the system's pressure is the lowest, and with increasing q values, the system's pressure rises for all temperatures. This implies that non-extensive parameters influence the pressure of the system. The vacuum contribution makes total pressure finite even at zero temperature.

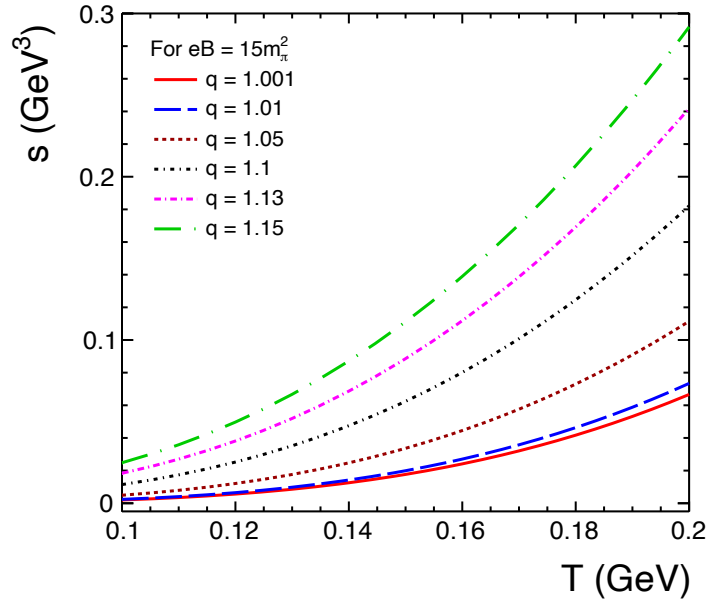


Figure 3.9: Entropy density as a function of temperature in a magnetized hadron gas for different q -values, respectively [153].

Fig. 3.9 depicts the entropy density of a hadron gas system as a function of temperature, influenced by an external magnetic field at various q -values. As the temperature increases, the entropy density of the system increases, which holds across all q -values. At $q = 1.001$, when the system approaches near equilibrium, the entropy density reaches its minimum value. Further, as we move away from equilibrium, the entropy density increases for all temperatures. This behavior

aligns with our intuitive understanding.

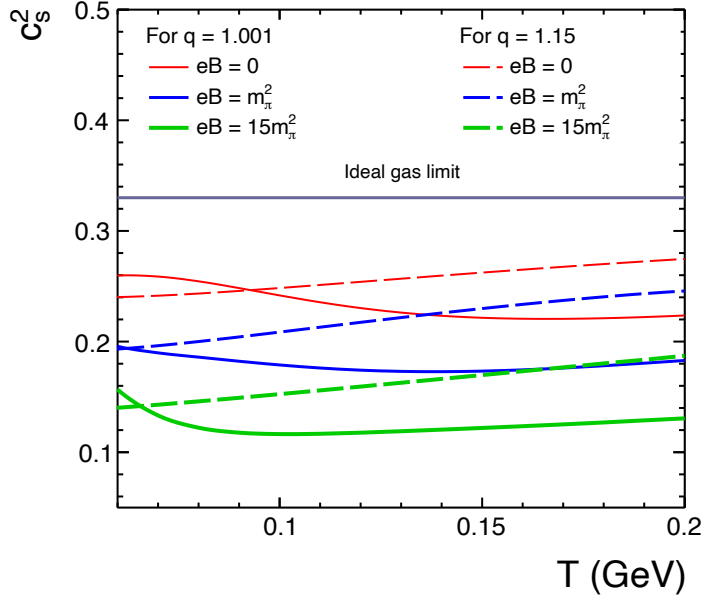


Figure 3.10: The squared speed of sound of a hadron gas as a function of temperature for different q -values for different magnetic field strengths [153].

To grasp the hydrodynamical evolution of the matter formed in relativistic heavy-ion collisions, one of the most essential thermodynamical observables is the speed of sound, denoted as c_s . To investigate this, in Fig. 3.10, we have estimated the squared speed of sound, (c_s^2) , for a hadron gas as a function of temperature for different q -values under varying strengths of external magnetic field ($eB = 0, m_\pi^2$ and $15m_\pi^2$). The squared speed of sound of the system decreases with increasing temperature for all external magnetic fields when the system is in near equilibrium, *i.e.*, for $q = 1.001$. The speed of sound is the highest in the absence of the external magnetic field in the case of a system near equilibrium. Conversely, when the system is away from equilibrium, especially at $q = 1.15$, we observed a consistent increase in the squared speed of sound with temperature across nearly all observed cases of external magnetic fields. An external magnetic field in the

3.7 Summary

system seems to reduce the speed of sound in the medium at all temperatures. This suggests that the system is more interactive in nature under an external magnetic field than a system without a magnetic field. The magnetic field seems to set in additional interactions between charged particles in the system, altering its behavior and taking it away from an ideal gas behavior.

3.7 Summary

In this analysis, we have used non-extensive Tsallis statistics to study a hadron gas formed in peripheral heavy-ion collisions, for which the transverse momentum spectra are usually described by non-extensive statistics. Such collisions generate a strong external magnetic field, whose effect can be observed in the final state when we study various thermodynamic properties of the hadron gas.

- The strength of the produced magnetic field is found to increase with the collision energy of the system, making it the highest one being produced at the LHC
- We observe that when the system is away from equilibrium, it has higher values of energy density, pressure, and entropy density
- We observed that under a strong magnetic field ($eB = 15m_\pi^2$), the system maintains positive magnetization across all q values while deviating from equilibrium ($q = 1.15$), resulting in diamagnetic behavior under a weaker magnetic field ($eB = m_\pi^2$), transitioning to paramagnetic behavior as magnetic field strength increases.
- We observed that under a strong magnetic field ($eB = 15m_\pi^2$), the system maintains positive magnetization across all q values while deviating from equilibrium ($q = 1.15$), resulting in diamagnetic behavior under a weaker

magnetic field ($eB = m_\pi^2$), transitioning to paramagnetic behavior as magnetic field strength increases.

- An interesting result that may require extensive research is a diamagnetic to paramagnetic transition for non-central heavy-ion collisions for a system away from equilibrium as one advances from RHIC to the LHC energies.
- In addition, the squared speed of sound c_s^2 of hadron gas in the presence of an external magnetic field asymptotically decreases with increasing magnetic field strength, suggesting that the system is more interacting in the presence of a finite magnetic field.
- This analysis highlights the interplay of non-extensive parameters (q) and magnetic fields and thermodynamic properties on non-central heavy-ion collisions, stressing further research to understand these phenomena completely.

Chapter 4

Role of chemical potential at kinetic freeze-out using Tsallis non-extensive statistics in pp collisions at the Large Hadron Collider

Ultrarelativistic hadron and heavy-ion collision use particle colliders such as the RHIC and LHC to understand matter formed in extreme conditions of high temperature and/or energy density, resulting in a system of deconfined quarks and gluons [191–193]. The produced fireball goes through rapid expansion and cooling during its space-time evolution, where quarks and gluons combine to form the confined hadrons. The chemical freeze-out temperature is the temperature at which stable particle yields are preserved. Finally, the final-state particle momentum is fixed at the kinetic freeze-out boundary, allowing the free streaming of particles to be detected in the detectors surrounding the collision point. The chemical freeze-out stage is well understood and supported by various ex-

perimental evidences [194, 195], including experimental observations, theoretical frameworks such as Lattice Quantum Chromodynamics (lQCD), and hydrodynamic simulations [196, 197]. The kinetic freeze-out stage remains a subject of intense investigation. Numerous studies have explored this stage by analyzing the final state-identified charged-particle transverse momentum spectra (p_T -spectra). The complexity of the kinetic freeze-out phenomenon is evident from the diverse range of proposed scenarios. Some studies advocate for a single kinetic freeze-out scenario [198], while others suggest double [199–201] or multiple kinetic freeze-out scenarios [202–204]. Recently, a study has even proposed a triple kinetic freeze-out scenario [205], highlighting the intricate dynamics involved, particularly regarding the freeze-out times of different particle species. Despite numerous studies on kinetic freeze-out scenarios, consensus remains elusive within the high-energy physics community. The most appropriate freeze-out scenario remains an open and actively debated topic, emphasizing the ongoing quest for a deeper understanding of the underlying processes in extreme conditions.

The transverse momentum (p_T) spectra measured at LHC energies can reveal information about the kinetic freeze-out stage of the collision. To extract relevant information, one typically fits a Boltzmann-type distribution function to the p_T -spectra. However, the Boltzmann distribution function can only account for the spectra's low- p_T region. High-energy hadronic collisions have yielded transverse momenta in the hundreds of GeV range. This indicates that the high- p_T regime is essential for understanding the system generated in such collisions and should not be ignored. Power-law distribution functions can accurately describe and adequately characterize the high- p_T component of the spectra, resulting from perturbative QCD. To completely understand the system, a unique distribution function is required to explain both the low- and high- p_T spectra. The thermodynamically consistent Tsallis distribution function is often employed for this purpose [163–170, 175–179, 206–210]. The charged-particle p_T -spectra measured by the ALICE collaboration for pp collisions at $\sqrt{s} = 7$ and 13 TeV have been

4.1 Physical interpretation of q and connection with IQCD

investigated using a thermodynamically consistent form of Tsallis non-extensive statistics. The p_T spectra are fitted with the Tsallis distribution function.

The results are investigated as a function of final state charged-particle multiplicity for various light flavor and strange particles, such as π^\pm , K^\pm , $p + \bar{p}$, ϕ , $\Lambda + \bar{\Lambda}$, $\Xi + \bar{\Xi}$, $\Omega + \bar{\Omega}$. Furthermore, studies show that finite radial flow [47] and collective effects such as long-range correlations [211] have been observed in high-energy pp collisions. These phenomena are often attributed to the underlying partonic structure of the colliding protons rather than radial flow. Thus, this work [212] presents an alternative technique to the single freeze-out scenario that does not account for the radial flow effect. We employ an alternative method that takes advantage of parameter redundancy by providing a finite chemical potential during the kinetic freeze-out stage.

In chapter 3, we had a detailed discussion on the Tsallis non-extensive statistic and its thermodynamic consistency. In the following section, we aim to elucidate the physical significance of the Tsallis non-extensive parameter (q) and its relationship with Lattice Quantum Chromodynamics (lQCD).

4.1 Physical interpretation of q and connection with IQCD

In high-energy nuclear collisions, multiplicity fluctuation is attributed to intrinsic fluctuations in the temperature of the hadronizing system formed in such processes. These fluctuations are quantified using the non-extensivity parameter q , where $|q - 1|$ directly measures the fluctuation [213–217]. When fluctuations vanish, $q \rightarrow 1$, Tsallis statistics becomes the conventional Boltzmann-Gibbs one, and the power-like Tsallis q exponents become the usual exponential distribution. The non-extensive parameter q is specifically related to the event-by-event temperature fluctuation of a system and expressed as $q = 1 + Var(1/T)/\langle 1/T \rangle^2$. To

analyze the evolution of temperature fluctuation in a system approaching thermodynamic equilibrium, the Boltzmann transport equation in Tsallis non-extensive statistics is also used [218]. As mentioned in Ref. [218], the QCD deconfinement transition and the possible location of a critical point in the QCD phase diagram manifest with large-scale observable fluctuations, which should be reflected in the fluctuations in q -values. In addition, the non-extensivity of a physical system created in high-energy hadronic and heavy-ion collisions is also linked to temperature fluctuation and, hence, the system's heat capacity/specific heat.

Furthermore, the connections between the Tsallis and Boltzmann statistics proposed so far are related to thermodynamical aspects of the system but not directly related to the microscopic aspects of hadronic matter and QCD interaction. A comparison of results from the non-extensive self-consistent thermodynamics IQCD has been conducted [219–222] revealing a reasonable agreement between the two approaches. Notably, recent investigation [220] introduces a thermofractal system characterized by a fractal structure in its thermodynamic functions. It shows that the Tsallis statistics more naturally describes its behavior than Boltzmann statistics. This investigation establishes a relationship between the fractal dimension and the entropic index (q), indicating that the ratio of Tsallis temperature (τ) to Boltzmann temperature (T) is influenced by the entropic index (q) and the number of subsystems. It shows that while τ governs the system's overall energy, T regulates the fraction of total energy accumulated as internal energy within subsystems. This finding enables a connection between the entropic index and fundamental aspects of constituent interactions while also establishing constraints on the S-matrix necessary for the emergence of non-extensivity in the system under consideration.

Also, chemical potential plays an important role in relativistic pp and heavy-ion collisions, affecting the thermodynamic characteristics and particle composition of the system. The statistical description of the system becomes more complex due to the presence of chemical potential, which makes a detailed un-

4.2 Significance of chemical potential in relativistic collision

derstanding of its interaction with non-extensivity and temperature changes imperative. Let us examine its importance in the following section.

4.2 Significance of chemical potential in relativistic collision

According to the first law of thermodynamics, the chemical potential of a system is defined as the change in internal energy of the system when one more particle is added in such a way that the volume (V) and entropy (S) are constant, expressed as ($\mu = \frac{\partial U}{\partial N}|_{S,V}$) [223]. However, maintaining constant entropy is a tricky part. In a system, the entropy increases with the increasing number of particles and the increasing energy of the system. To define the system's chemical potential, one wishes to increase the number of particles while maintaining a constant entropy. To do this, the system's energy must be reduced to compensate for the increasing effect on entropy as the number of particles increases. The system of fermions and bosons behaves like a classical system at very high temperatures. To sum up, increasing the number of particles in a classical gas requires changing the system's energy by a negative amount while keeping the entropy unchanged. This change in energy represents the chemical potential of a system. The chemical potential can take on different values depending on the system under consideration. In some scenarios, the chemical potential of a particle may be positive, signifying that adding more particles demands energy input. Conversely, a negative chemical potential suggests adding more particles to the system releases energy.

In recent years, numerous investigations in lattice QCD have successfully studied high temperatures and scenarios with vanishing chemical potential. However, exploring the phase structure of QCD under non-zero chemical potential is one of the most exciting problems in modern physics [224–228]. Notably, the theoretical side suggests the existence of color superconducting and superfluid phases at high

baryon densities [229]. Hence, exploring the QCD phase transition utilizing lattice gauge theory simulations at the non-zero chemical potential is necessary. As mentioned in Ref. [196], a consequence of the vanishing baryon-chemical potential leads to the vanishing of the strangeness chemical potential μ_s , which implies that the strange quantum number is no longer relevant for particle production. The abundance of strange and multi-strange mesons and baryons within the fireball is solely determined by their mass (m), spin degeneracy (g), and temperature (T). At the LHC energies, the baryochemical potential is expected to be zero at chemical freeze-out due to equal production of particles and antiparticles, assuming the same condition at kinetic freeze-out temperature is not straightforward. Hence, there could be a finite total chemical potential at the kinetic freeze-out stage, and its consequences cannot be ignored.

Applying Tsallis statistics, we explored the concept of a finite chemical potential at the kinetic freeze-out boundary. In the following section, we will discuss the technique in further detail.

4.3 Formulation

The Tsallis distribution function that satisfies the thermodynamic consistency relations [163–170, 175–179, 206–210]

$$E \frac{d^3 N}{dp^3} = gV E \frac{1}{(2\pi)^3} \left[1 + (q-1) \frac{E-\mu}{T} \right]^{-\frac{q}{q-1}}. \quad (4.1)$$

Here, E represents the energy of the particle, $d^3 N$ is the invariant yield, V is the volume of the system, g is the degeneracy factor, q is the non-extensive parameter, T is the temperature, p denotes the momentum, and μ is the total chemical potential defined as $\mu = B\mu_B + S\mu_S + Q\mu_Q$, where B , S , and Q represent the baryon number, strangeness quantum number, and electric charge respectively, and μ_B , μ_S , and μ_Q are the chemical potentials for baryons, strangeness, and

4.3 Formulation

electric charge.

At mid-rapidity ($y = 0$), Eq. 4.1 can be expressed in terms of transverse momentum, p_T , and transverse mass, $m_T = \sqrt{p_T^2 + m^2}$, where $E = m_T \cosh y$, as:

$$\left. \frac{d^2 N}{dp_T dy} \right|_{y=0} = gV \frac{p_T m_T}{(2\pi)^2} \left[1 + (q-1) \frac{m_T - \mu}{T} \right]^{-\frac{q}{q-1}}. \quad (4.2)$$

To extract the Tsallis parameters for identified non-strange, strange, and multi-strange particles, we use Eq. 4.2. Here, the degeneracy factor $g = 2 \times (2s+1)$ is considered to be 2, 2, 4, 3, 8, 4, and 8 for π^\pm , K^\pm , $p + \bar{p}$, ϕ , $\Lambda + \bar{\Lambda}$, $\Xi + \bar{\Xi}$, $\Omega + \bar{\Omega}$, respectively, where s represents the particle's spin, and the factor of 2 accounts for antiparticles. The indistinguishability of Σ^0 and Λ implies a degeneracy factor of 8 for the Λ particle. It's worth mentioning that the four parameters T , V , q , and μ in Eq. 4.2 exhibit redundancy for $\mu \neq 0$ [230–233]. Specifically, for fixed values of q , let $T = T_0$ and $V = V_0$ at $\mu = 0$. Comparing Eq. 4.2 for $\mu = 0$ and for a finite value of μ one obtains the following transformation relations [230–233].

$$T_0 = T \left[1 - (q-1) \frac{\mu}{T} \right], \text{ with } \mu \leq \frac{T}{q-1}, \quad (4.3)$$

$$V_0 = V \left[1 - (q-1) \frac{\mu}{T} \right]^{\frac{q}{1-q}}. \quad (4.4)$$

Thus, the variables T and V are functions of μ at fixed values of q , and they can be estimated if the parameters (T_0, V_0) , and q are known. This redundancy does not exist when $\mu = 0$. In that case, the transverse momentum distribution can be expressed in terms of these modified variables as,

$$\frac{d^2 N}{dp_T dy} = gV_0 \frac{p_T m_T}{(2\pi)^2} \left[1 + (q-1) \frac{m_T}{T_0} \right]^{-\frac{q}{q-1}}, \quad (4.5)$$

where the system's chemical potential (μ) does not appear explicitly. Analogous to the volumes V and V_0 defined in Eq. 4.1 and 4.4, one can introduce the corresponding radii R and R_0 , assuming a spherically symmetric system [234, 235].

$$V = \frac{4\pi}{3}R^3, \quad (4.6)$$

$$V_0 = \frac{4\pi}{3}R_0^3. \quad (4.7)$$

The two-particle interferometry analysis (often called HBT) utilizes a novel Bose-Einstein correlations experimental technique to estimate the sizes and lifetimes of particle sources in high-energy and nuclear physics. The parameter R does not necessarily correspond to the size of the system as determined from an HBT analysis [234–237]; however, it serves to fix the normalization of the distribution Eq. 4.2. An important suggestion was made to determine the chemical potential in [233]. The observation was that the radius R_0 given in Table 4.4 and V are more significant than those obtained from a femtoscopy analysis [238] by a factor κ , approximately 3.5, expressed as,

$$R_{\text{Femto}} \approx \frac{1}{\kappa}R_0. \quad (4.8)$$

Thus, in [233], a suggestion is made to identify the corresponding volume V_{Femto} with the volume V appearing in Eq. 4.1.

Hence

$$V_0 \approx V \cdot \kappa^3. \quad (4.9)$$

Combining this with Eq. 4.6 and 4.7 can derive the chemical potential, which is given by,

$$\mu = \frac{T_0}{q-1} (\kappa^{3(q-1)/q} - 1), \quad (4.10)$$

With this proposal, knowing T_0 would determine μ . However, our study [212] comparing the values of the chemical potential μ using this proposal [233] to those derived from the technique mentioned above, starting with Eq. 4.2, indicates significantly different results. Therefore, our findings do not support this assumption, suggesting that the volume V in Eq. 4.2 cannot be equated with the

4.3 Formulation

volume estimated by femtoscopy. Instead, V must be considered specific to the Tsallis distribution, as with all other variables used in this study.

At chemical equilibrium, $\mu = 0$ for all quantum numbers, as particles and antiparticles are equal. However, the equality of particle-antiparticle numbers at kinetic freeze-out implies equal chemical potentials, but it is not necessarily zero. Importantly, we stress that Eq. 4.2 and 4.5 have distinct interpretations, with neither T_0 equal to T nor V_0 equaling V . Notably, Eq. 4.5 does not include μ . Our objective is to address this discrepancy by employing the following technique:

1. To determine the three parameters T_0 , q , and V_0 , we use Eq. 4.5 to fit the transverse momentum distribution, keeping all the parameters free.
2. Fix the value of parameter q , which is obtained from the previous step.
3. Then perform the fit to the transverse momentum distributions using Eq. 4.2, keeping q fixed as determined in the previous step, which determines the parameters T , V and the chemical potential μ .
4. We show that the choice of q , which is particle species dependent, appears to be independent of the chemical potential of the system for all particles.
5. At last, check the consistency with Eq. 4.6 and 4.7.

Each step of the fitting procedure includes only three parameters to describe the transverse momentum distributions. Ref. [231, 232] introduce this technique. The current work conveys that the chemical potential at kinetic freeze-out differs from that at chemical freeze-out. The chemical potentials are considered zero at chemical freeze-out, where thermal and chemical equilibrium has been established. At kinetic freeze-out, we observed a finite chemical potential for both particle and antiparticle. However, they do not have to be zero due to the absence of chemical equilibrium at kinetic freeze-out. The only limitation is that they should be equal for particles and antiparticles.

The transverse momentum spectra of the identified particles for various multiplicity classes in pp collisions at $\sqrt{s} = 7$ TeV and $\sqrt{s} = 13$ TeV were then examined in detail. The spectra will be analyzed for two distinct scenarios, namely zero μ and finite μ .

4.4 Transverse momentum spectra of identified hadrons

Table 4.1: Number of mean charged particle multiplicity density for all the particles at mid-rapidity corresponding to different event classes at $\sqrt{s} = 7$ TeV [239]. The uncertainties are the quadratic sum of statistical and systematic contributions.

Multiplicityclass	Mul1	Mul2	Mul3	Mul4	Mul5	Mul6	Mul7	Mul8	Mul9	Mul10
$\langle \frac{dN_{ch}}{d\eta} \rangle$	21.3±0.6	16.5±0.5	13.5±0.4	11.5±0.3	10.1±0.3	8.45±0.25	6.72±0.21	5.40±0.17	3.90±0.14	2.26±0.12

Table 4.2: Number of mean charged particle multiplicity density for π, K, p at mid-rapidity corresponding to different event classes at $\sqrt{s} = 13$ TeV [47]. The uncertainties are the quadratic sum of statistical and systematic contributions.

Multiplicityclass	Mul1	Mul2	Mul3	Mul4	Mul5	Mul6	Mul7	Mul8	Mul9	Mul10
$\langle \frac{dN_{ch}}{d\eta} \rangle$	26.02±0.35	20.02±0.27	16.17±0.22	13.77±0.19	12.04±0.17	10.02±0.14	7.95±0.11	6.32±0.09	4.50±0.07	2.55 ±0.04

Table 4.3: Number of mean charged particle multiplicity density for $\phi, \Lambda, \Xi, \Omega$ at mid-rapidity corresponding to different event classes at $\sqrt{s} = 13$ TeV [240, 241]. The uncertainties are the quadratic sum of statistical and systematic contributions.

Multiplicityclass	Mul1	Mul2	Mul3	Mul4	Mul5	Mul6	Mul7	Mul8	Mul9	Mul10
$\langle \frac{dN_{ch}}{d\eta} \rangle$	25.75±0.40	19.83±0.30	16.12±0.24	13.76±0.21	12.06±0.18	10.11±0.15	8.07±0.12	6.48±0.10	4.64±0.07	2.52 ±0.04

4.4 Transverse momentum spectra of identified hadrons

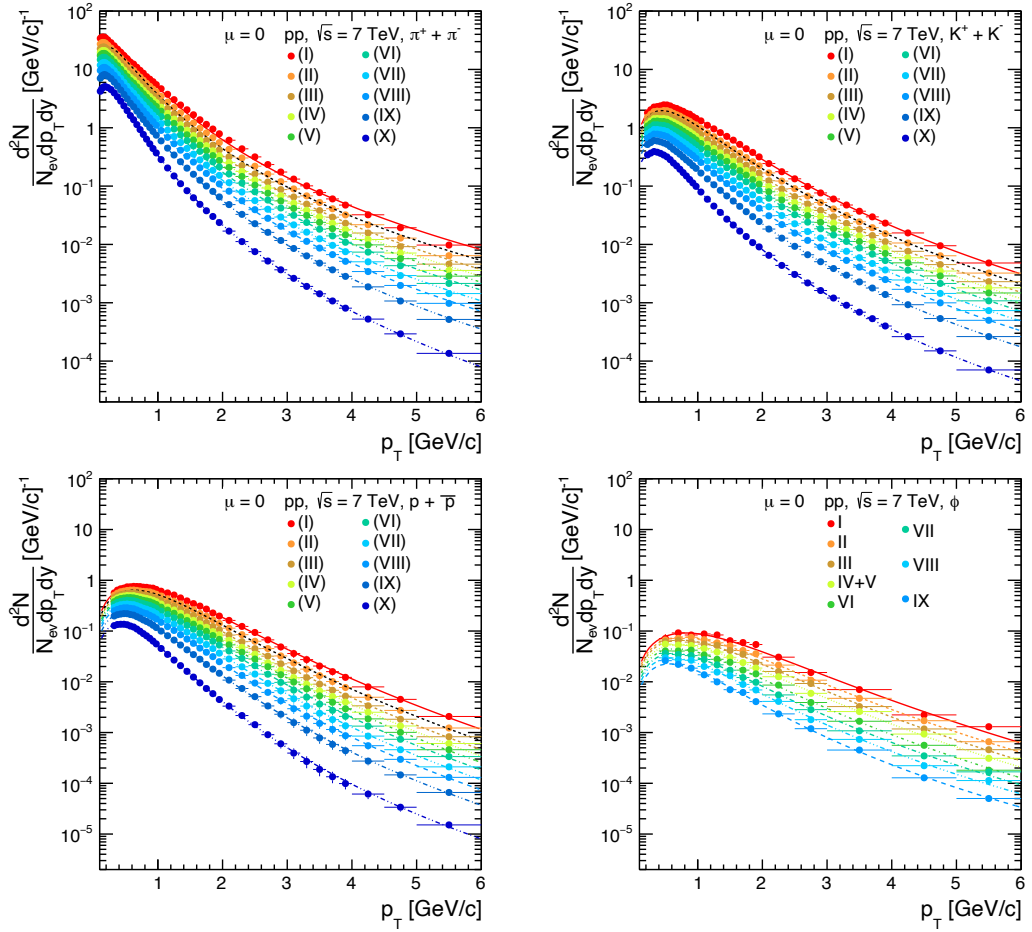


Figure 4.1: Fitting of experimentally measured p_T -spectra of pion (π^\pm), kaon (K^\pm), proton ($p + \bar{p}$) and phi (ϕ) at zero chemical potential ($\mu = 0$) using Tsallis non-extensive statistical model for pp -collisions at $\sqrt{s} = 7$ TeV.

The p_T spectra of various particle species, including non-strange, strange, and multi-strange particles such as π^\pm , K^\pm , $p + \bar{p}$, ϕ , $\Lambda + \bar{\Lambda}$, $\Xi + \bar{\Xi}$, and $\Omega + \bar{\Omega}$, are analyzed through a Tsallis distribution function for pp collisions at both $\sqrt{s} = 7$ TeV and $\sqrt{s} = 13$ TeV for different multiplicity classes at the LHC, as measured by ALICE [47, 239–241]. Initially, the parameters of the Tsallis distribution, namely the non-extensive parameter (q), temperature parameter (T_0), and radius parameter (R_0) at zero chemical potential ($\mu = 0$), are determined using Eq. 4.5.

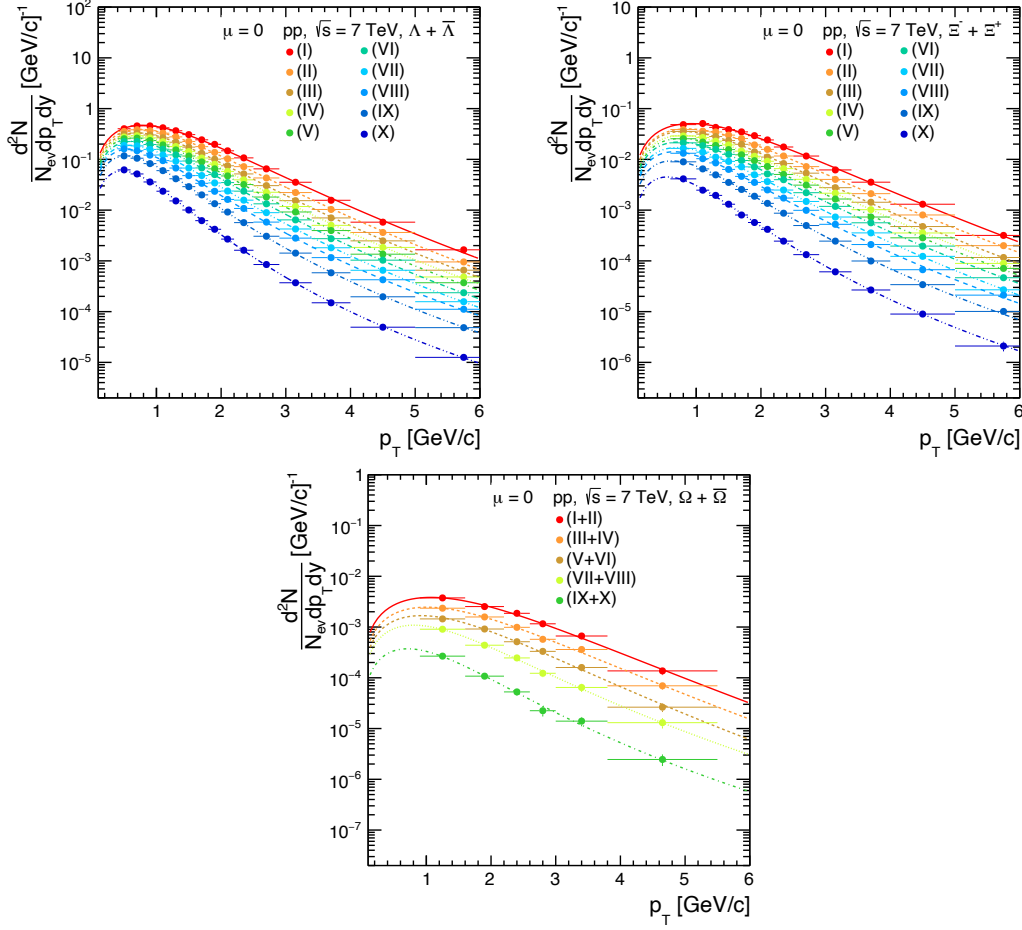


Figure 4.2: Fitting of experimentally measured p_T -spectra of lambda ($\Lambda + \bar{\Lambda}$), cascade ($\Xi + \bar{\Xi}$) and omega ($\Omega + \bar{\Omega}$) at zero chemical potential ($\mu = 0$) using Tsallis non-extensive statistical model for pp -collisions at $\sqrt{s} = 7$ TeV.

Fig. 4.1 and 4.2 illustrate the fittings for $\sqrt{s} = 7$ TeV, while similar results can be shown for $\sqrt{s} = 13$ TeV. The obtained parameter values and the corresponding χ^2/ndf are presented in Tables 4.4 and 4.5 for both centre-of-mass energy $\sqrt{s} = 7$ TeV and $\sqrt{s} = 13$ TeV, respectively.

Subsequently, fixing the non-extensive parameter obtained from the previous step, Eq. 4.2 is employed to extract all fitting parameters, including temperature (T), system radius (R), and chemical potential (μ). Fittings are shown in Fig. 4.3

4.4 Transverse momentum spectra of identified hadrons

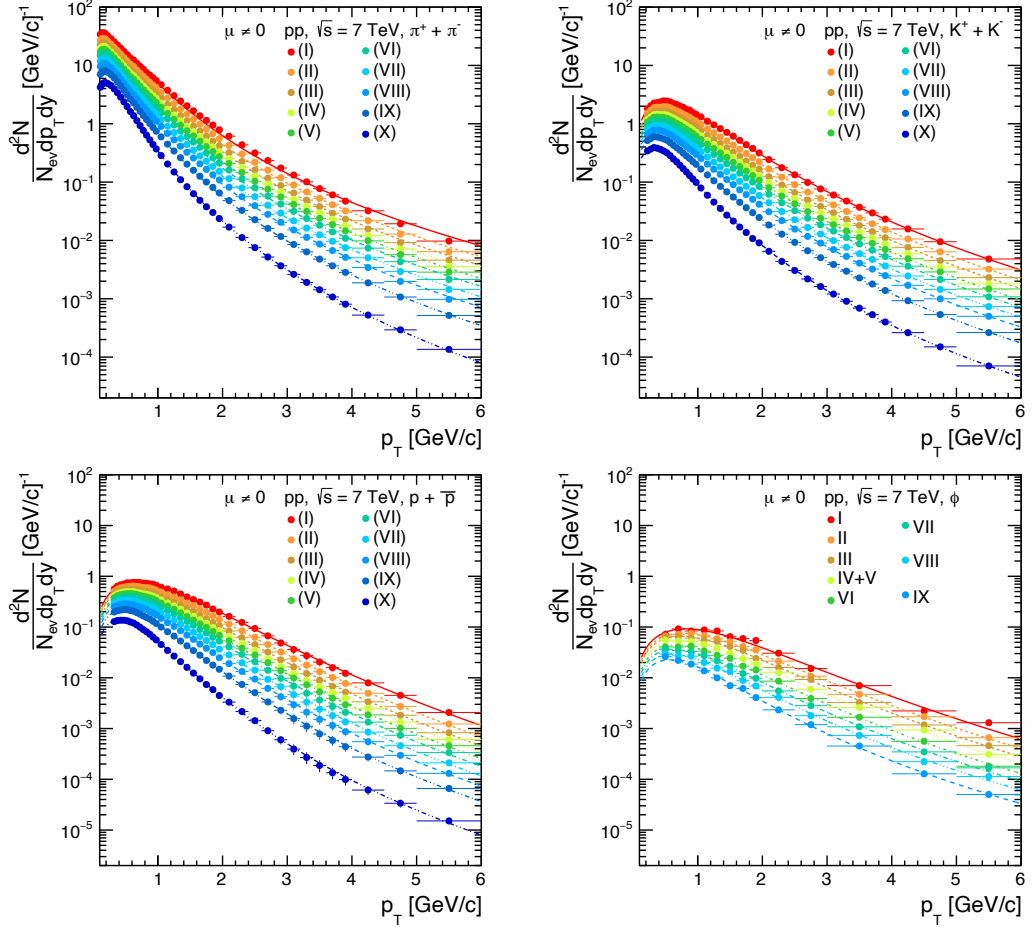


Figure 4.3: Fitting of experimentally measured p_T -spectra of pion (π^\pm), kaon (K^\pm), proton ($p + \bar{p}$) and phi (ϕ) at non-zero value of chemical potential ($\mu \neq 0$) using Tsallis non-extensive statistical model for pp -collisions at $\sqrt{s} = 7$ TeV.

and 4.4, for $\sqrt{s} = 7$ TeV, while similar results can be shown for $\sqrt{s} = 13$ TeV, and the resultant parameter values and χ^2/ndf are tabulated in Tables 4.6 and 4.7 for for $\sqrt{s} = 7$ TeV and $\sqrt{s} = 13$ TeV, respectively. The fitting procedure utilizes the TMinuit class from the ROOT library, keeping all three parameters free [242], employing a chi-squared fitting approach. The reduced- χ^2 values in the tables gauge the goodness of fit, indicating that the non-extensive distribution function well describes the spectra. However, the reduced- χ^2 values for pions are

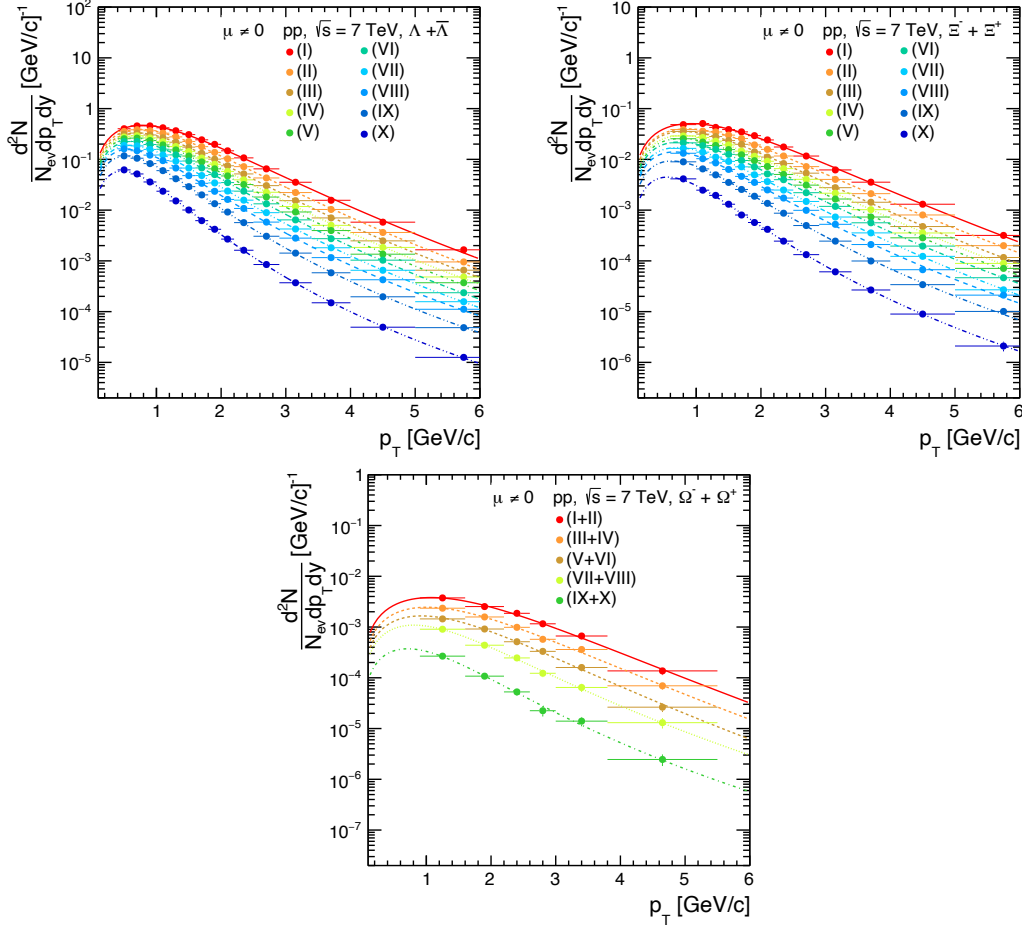


Figure 4.4: Fitting of experimentally measured p_T -spectra of pion (π^\pm), kaon (K^\pm), proton ($p + \bar{p}$) and phi (ϕ) at non-zero value of chemical potential ($\mu \neq 0$) using Tsallis non-extensive statistical model for pp -collisions at $\sqrt{s} = 7$ TeV.

comparatively bad for pions in contrast to other particle species considered in this analysis, possibly due to the contribution from resonance decay.

After completing fitting transverse momentum spectra and extracting parameters for different particle species in pp collisions at various energies, we now focus on the results and discussion section. We will analyze and compare the extracted values for different collision energies and multiplicity classes, understanding particles produced in high-energy collisions.

4.4 Transverse momentum spectra of identified hadrons

Table 4.4: Fit results at $\sqrt{s} = 7$ TeV [239], using data from the ALICE Collaboration using Eq. 4.5 and 4.7. The reason of merging bins Mul[1+2], Mul[3+4] etc for Ω is lack of statistics.

Particles		Multiplicity class									
		Mul1	Mul2	Mul3	Mul4	Mul5	Mul6	Mul7	Mul8	Mul9	Mul10
$\pi^+ + \pi^-$	T_0 (GeV)	0.086±0.001	0.083±0.001	0.081±0.001	0.080±0.001	0.079±0.001	0.077±0.001	0.076±0.001	0.073±0.001	0.073±0.001	0.070±0.001
	R_0 (fm)	6.878±0.008	6.583±0.083	6.354±0.006	6.188±0.094	6.042±0.066	5.855±0.007	5.596±0.077	5.454±0.010	5.021±0.083	4.553±0.090
	q	1.170±0.001	1.168±0.001	1.167±0.001	1.165±0.001	1.164±0.001	1.162±0.001	1.160±0.001	1.158±0.001	1.151±0.001	1.139±0.001
	χ^2/ndf	6.923	7.184	6.383	5.587	4.981	4.117	2.980	1.967	0.583	0.117
$K^+ + K^-$	T_0 (GeV)	0.154±0.004	0.140±0.004	0.130±0.003	0.122±0.003	0.116±0.003	0.109±0.003	0.100±0.003	0.092±0.003	0.080±0.003	0.061±0.003
	R_0 (fm)	2.394±0.072	2.467±0.076	2.523±0.082	2.577±0.088	2.645±0.096	2.687±0.101	2.795±0.113	2.933±0.129	3.181±0.168	4.144±0.323
	q	1.137±0.003	1.141±0.002	1.143±0.002	1.145±0.002	1.147±0.002	1.148±0.002	1.150±0.002	1.151±0.002	1.152±0.002	1.149±0.002
	χ^2/ndf	0.087	0.077	0.081	0.085	0.081	0.078	0.053	0.048	0.038	0.114
$p + \bar{p}$	T_0 (fm)	0.205±0.008	0.183±0.008	0.163±0.007	0.146±0.007	0.137±0.007	0.121±0.006	0.104±0.006	0.086±0.006	0.064±0.006	0.026±0.006
	R_0 (fm)	1.339±0.070	1.472±0.082	1.643±0.102	1.845±0.128	1.973±0.145	2.271±0.186	2.737±0.275	3.600±0.003	5.699±0.009	32.505±0.010
	q	1.097±0.004	1.100±0.004	1.104±0.004	1.108±0.004	1.109±0.004	1.112±0.004	1.116±0.004	1.120±0.004	1.124±0.004	1.129±0.004
	χ^2/ndf	0.079	0.079	0.078	0.085	0.085	0.100	0.092	0.090	0.074	0.114
$\Lambda + \bar{\Lambda}$	T_0 (GeV)	0.253±0.005	0.217±0.004	0.186±0.004	0.165±0.003	0.151±0.008	0.137±0.001	0.107±0.003	0.079±0.002	0.054±0.006	0.014±0.001
	R_0 (fm)	0.790±0.008	0.906±0.005	1.058±0.006	1.201±0.003	1.334±0.005	1.480±0.007	2.068±0.004	3.330±0.008	6.245±0.007	100.545±7.691
	q	1.081±0.004	1.089±0.005	1.097±0.002	1.102±0.004	1.104±0.004	1.106±0.001	1.115±0.006	1.124±0.001	1.128±0.005	1.136±0.001
	χ^2/ndf	0.419	0.184	0.161	0.176	0.197	0.121	0.053	0.129	0.120	0.091
$\Xi^- + \bar{\Xi}^+$	T_0 (GeV)	0.315±0.004	0.267±0.010	0.224±0.007	0.211±0.005	0.185±0.003	0.164±0.007	0.146±0.003	0.103±0.001	0.073±0.002	0.021±0.007
	R_0 (fm)	0.405±0.004	0.463±0.010	0.569±0.007	0.582±0.083	0.675±0.008	0.775±0.007	0.868±0.024	1.470±0.013	2.511±0.392	32.494±1.897
	q	1.067±0.006	1.078±0.002	1.086±0.003	1.088±0.002	1.096±0.005	1.100±0.007	1.102±0.005	1.115±0.001	1.121±0.004	1.132±0.002
	χ^2/ndf	0.418	0.402	0.298	0.114	0.149	0.196	0.201	0.571	0.267	0.168
ϕ		Mul1	Mul2	Mul3	Mul[4+5]		Mul6	Mul7	Mul8	Mul9	Mul10
	T_0 (GeV)	0.270±0.002	0.236±0.004	0.216±0.006	0.192±0.001		0.159±0.001	0.135±0.001	0.112±0.006	0.082±0.001	0.025±0.008
	R_0 (fm)	0.540±0.009	0.591±0.007	0.630±0.007	0.680±0.005		0.817±0.006	0.955±0.007	1.173±0.004	1.740±0.010	15.414±0.069
	q	1.103±0.004	1.109±0.005	1.112±0.002	0.119±0.003		1.126±0.002	1.134±0.004	1.140±0.002	1.146±0.002	1.155±0.002
χ^2/ndf	1.046	0.318	0.429	0.280		0.585	0.335	0.525	0.543	0.220	
$\Omega^- + \bar{\Omega}^+$		Mul[1+2]		Mul[3+4]		Mul[5+6]		Mul[7+8]		Mul[9+10]	
	T_0 (GeV)	0.360±0.006		0.309±0.007		0.242±0.010		0.122±0.007		0.036±0.001	
	R_0 (fm)	0.137±0.006		0.145±0.006		0.188±0.005		0.503±0.009		4.696±0.009	
	q	1.056±0.009		1.065±0.001		1.076±0.005		1.110±0.009		1.130±0.007	
χ^2/ndf	0.362		0.450		0.411		0.236		0.580		

Table 4.5: Fit results at $\sqrt{s} = 13$ TeV [47, 240, 241], using data from the ALICE Collaboration using Eq. 4.5 and 4.7. The reason of merging bins Mul[1+2], Mul[3+4] etc for Ω is lack of statistics.

Particles		Multiplicity class									
		Mul1	Mul2	Mul3	Mul4	Mul5	Mul6	Mul7	Mul8	Mul9	Mul10
$\pi^+ + \pi^-$	T_0 (GeV)	0.089±0.001	0.087±0.001	0.084±0.001	0.083±0.001	0.081±0.001	0.079±0.001	0.078±0.001	0.076±0.001	0.074±0.001	0.070±0.001
	R_0 (fm)	6.989±0.006	6.652±0.006	6.422±0.005	6.250±0.003	6.105±0.006	5.922±0.006	5.671±0.006	5.431±0.006	5.068±0.006	4.585±0.008
	q	1.176±0.001	1.173±0.001	1.171±0.001	1.170±0.001	1.169±0.001	1.167±0.001	1.165±0.001	1.162±0.001	1.157±0.001	1.145±0.0
	χ^2/ndf	7.959	7.130	6.254	5.563	5.006	4.158	3.199	2.217	1.034	0.504
$K^+ + K^-$	T_0 (GeV)	0.161±0.001	0.145±0.003	0.134±0.003	0.126±0.003	0.120±0.003	0.113±0.003	0.103±0.003	0.095±0.003	0.082±0.002	0.055±0.0
	R_0 (fm)	2.328±0.007	2.462±0.070	2.515±0.075	2.569±0.080	2.609±0.085	2.666±0.092	2.775±0.104	2.858±0.114	3.126±0.139	4.815±0.014
	q	1.145±0.001	1.149±0.002	1.151±0.002	1.152±0.002	1.154±0.002	1.155±0.002	1.156±0.002	1.157±0.002	1.158±0.002	1.160±0.001
	χ^2/ndf	0.585	0.154	0.143	0.153	0.201	0.199	0.156	0.204	0.136	0.559
$p + \bar{p}$	T_0 (fm)	0.228±0.007	0.197±0.007	0.172±0.007	0.153±0.007	0.140±0.007	0.123±0.007	0.104±0.006	0.084±0.007	0.059±0.001	0.017±0.001
	R_0 (fm)	1.227±0.006	1.348±0.013	1.563±0.098	1.768±0.124	1.935±0.148	2.250±0.198	2.785±0.075	3.700±0.488	6.499±1.333	79.389±0.006
	q	1.098±0.004	1.104±0.004	1.109±0.004	1.114±0.004	1.116±0.004	1.120±0.004	1.123±0.004	1.128±0.004	1.133±0.004	1.139±0.004
	χ^2/ndf	0.170	0.151	0.168	0.152	0.137	0.158	0.142	0.119	0.166	0.192
ϕ	T_0 (fm)	0.310±0.003	0.266±0.005	0.251±0.002	0.224±0.005	0.205±0.013	0.182±0.004	0.155±0.006	0.140±0.006	0.108±0.001	0.049±0.001
	R_0 (fm)	0.481±0.006	0.533±0.003	0.535±0.006	0.570±0.010	0.618±0.006	0.691±0.005	0.796±0.007	0.832±0.004	1.108±0.007	3.505±0.009
	q	1.097±0.004	1.105±0.006	1.108±0.003	1.119±0.006	1.124±0.002	1.126±0.005	1.135±0.005	1.140±0.005	1.146±0.002	1.154±0.006
	χ^2/ndf	0.721	0.491	0.396	0.584	0.432	0.371	0.497	0.215	0.510	0.763
$\Lambda + \bar{\Lambda}$	T_0 (GeV)	0.286±0.005	0.246±0.006	0.218±0.006	0.187±0.004	0.176±0.006	0.152±0.003	0.121±0.002	0.101±0.006	0.069±0.004	0.018±0.005
	R_0 (fm)	0.705±0.005	0.800±0.007	0.889±0.005	1.050±0.003	1.098±0.008	1.308±0.150	1.740±0.005	2.204±0.007	4.019±0.008	6.184±0.255
	q	1.081±0.007	1.088±0.007	1.093±0.004	1.102±0.007	1.103±0.007	1.109±0.007	1.117±0.001	1.122±0.007	1.128±0.002	1.138±0.001
	χ^2/ndf	0.560	0.355	0.373	0.433	0.338	0.230	0.333	0.178	0.229	0.260
$\Xi^- + \Xi^+$	T_0 (GeV)	0.347±0.007	0.309±0.002	0.253±0.007	0.237±0.006	0.199±0.006	0.176±0.001	0.158±0.005	0.127±0.001	0.102±0.005	0.026±0.001
	R_0 (fm)	0.383±0.008	0.405±0.005	0.495±0.006	0.515±0.007	0.630±0.008	0.722±0.008	0.796±0.003	1.079±0.005	1.330±0.007	1.784±0.040
	q	1.068±0.009	1.074±0.005	1.089±0.008	1.091±0.007	1.103±0.007	1.106±0.002	1.108±0.005	1.113±0.002	1.120±0.006	1.137±0.002
	χ^2/ndf	0.430	0.229	0.434	0.450	0.527	0.232	0.380	0.535	0.305	0.305
$\Omega^- + \bar{\Omega}^+$		Mul[1+2]		Mul[3+4]		Mul[5+6]		Mul[7+8]		Mul[9+10]	
	T_0 (GeV)	0.402±0.007		0.311±0.002		0.265±0.005		0.198±0.007		0.130±0.009	
	R_0 (fm)	0.626±0.030		0.826±0.005		0.847±0.006		1.107±0.005		1.671±0.006	
	q	1.057±0.009		1.065±0.010		1.085±0.011		1.097±0.006		1.106±0.005	
	χ^2/ndf	0.048		1.625		0.430		1.525		0.729	

4.4 Transverse momentum spectra of identified hadrons

Table 4.6: Fit results at $\sqrt{s} = 7$ TeV [239], using data from the ALICE Collaboration with q from Table 4.4 following Eq. 4.2 and 4.6.

Particles		Multiplicity class									
		Mul1	Mul2	Mul3	Mul4	Mul5	Mul6	Mul7	Mul8	Mul9	Mul10
$\pi^+ + \pi^-$	T (GeV)	0.196±0.006	0.193±0.003	0.189±0.007	0.186±0.007	0.182±0.008	0.175±0.002	0.169±0.008	0.163±0.005	0.153±0.001	0.134±0.007
	R (fm)	1.060±0.008	0.959±0.007	0.900±0.007	0.861±0.006	0.851±0.005	0.848±0.008	0.811±0.004	0.788±0.006	0.787±0.007	0.785±0.005
	μ	0.642±0.002	0.649±0.007	0.644±0.005	0.640±0.007	0.624±0.006	0.599±0.005	0.584±0.008	0.564±0.005	0.523±0.009	0.459±0.005
	χ^2/ndf	6.928	7.194	6.383	5.597	4.984	4.130	2.980	1.953	0.595	0.117
$K^+ + K^-$	T (GeV)	0.197±0.009	0.193±0.005	0.189±0.006	0.186±0.006	0.182±0.009	0.175±0.005	0.169±0.009	0.164±0.009	0.149±0.007	0.124±0.009
	R (fm)	1.227±0.005	1.046±0.005	0.941±0.005	0.871±0.007	0.821±0.005	0.802±0.008	0.736±0.007	0.675±0.006	0.672±0.006	0.671±0.006
	μ	0.308±0.005	0.372±0.007	0.407±0.007	0.430±0.006	0.447±0.005	0.441±0.007	0.459±0.007	0.476±0.006	0.451±0.007	0.423±0.005
	χ^2/ndf	0.087	0.077	0.082	0.087	0.083	0.080	0.053	0.050	0.038	0.115
$p + \bar{p}$	T (fm)	0.198±0.001	0.193±0.006	0.189±0.006	0.187±0.005	0.183±0.006	0.176±0.005	0.169±0.006	0.163±0.007	0.149±0.007	0.117±0.006
	R (fm)	1.546±0.005	1.214±0.005	0.984±0.006	0.794±0.008	0.739±0.005	0.676±0.007	0.578±0.005	0.491±0.006	0.448±0.008	0.446±0.007
	μ	-0.082±0.008	0.096±0.005	0.242±0.006	0.377±0.005	0.421±0.006	0.477±0.007	0.562±0.005	0.642±0.008	0.681±0.005	0.696±0.005
	χ^2/ndf	0.079	0.080	0.079	0.085	0.085	0.101	0.092	0.090	0.074	0.114
$\Lambda + \bar{\Lambda}$	T (GeV)	0.201±0.007	0.196±0.008	0.191±0.006	0.187±0.006	0.184±0.005	0.180±0.007	0.171±0.007	0.163±0.007	0.153±0.009	0.119±0.009
	R (fm)	2.226±0.005	1.380±0.008	0.964±0.007	0.772±0.008	0.675±0.007	0.586±0.006	0.466±0.005	0.378±0.006	0.309±0.007	0.299±0.007
	μ	-0.653±0.006	-0.239±0.007	0.046±0.005	0.211±0.007	0.303±0.006	0.393±0.007	0.584±0.005	0.671±0.007	0.763±0.009	0.770±0.005
	χ^2/ndf	0.419	0.184	0.162	0.176	0.199	0.124	0.053	0.131	0.116	0.091
$\Xi^- + \Xi^+$	T (GeV)	0.202±0.005	0.197±0.002	0.194±0.007	0.188±0.007	0.185±0.006	0.179±0.007	0.171±0.007	0.164±0.007	0.156±0.008	0.122±0.007
	R (fm)	4.307±0.005	1.907±0.005	1.040±0.008	0.954±0.007	0.678±0.007	0.564±0.005	0.488±0.007	0.332±0.006	0.249±0.006	0.222±0.007
	μ	-1.698±0.006	-0.916±0.005	-0.353±0.006	-0.276±0.006	-0.005±0.005	0.146±0.005	0.249±0.007	0.521±0.005	0.670±0.007	0.757±0.009
	χ^2/ndf	0.418	0.409	0.299	0.115	0.149	0.196	0.201	0.562	0.268	0.168
		Mul1	Mul2	Mul3	Mul[4+5]	Mul6	Mul7	Mul8	Mul9	Mul10	
ϕ	T (GeV)	0.198±0.007	0.193±0.007	0.189±0.005	0.183±0.005	0.175±0.005	0.171±0.006	0.163±0.005	0.149±0.005	0.118±0.001	
	R (fm)	1.610±0.005	1.186±0.005	0.980±0.007	0.797±0.006	0.631±0.005	0.491±0.005	0.421±0.005	0.375±0.006	0.333±0.008	
	μ	-0.687±0.005	-0.410±0.005	-0.241±0.007	-0.080±0.010	0.101±0.007	0.266±0.007	0.365±0.006	0.450±0.006	0.596±0.009	
	χ^2/ndf	1.046	0.318	0.429	0.281	0.550	0.342	0.527	0.549	0.233	
		Mul[1+2]		Mul[3+4]		Mul[5+6]		Mul[7+8]		Mul[9+10]	
$\Omega^- + \Omega^+$	T (GeV)	0.204±0.008		0.199±0.007		0.189±0.005		0.165±0.006		0.134±0.005	
	R (fm)	5.023±0.005		1.650±0.008		0.608±0.005		0.186±0.007		0.107±0.006	
	μ	-2.838±0.006		-1.729±0.009		-0.721±0.008		0.382±0.005		0.752±0.005	
	χ^2/ndf	0.354		0.450		0.400		0.237		0.580	

Table 4.7: Fit results at $\sqrt{s} = 13$ TeV [47, 240, 241], using data from the ALICE Collaboration with q from Table 4.5 following Eq. 4.2 and 4.6.

Particles		Multiplicity class									
		Mul1	Mul2	Mul3	Mul4	Mul5	Mul6	Mul7	Mul8	Mul9	Mul10
$\pi^+ + \pi^-$	T (GeV)	0.200±0.007	0.194±0.003	0.190±0.007	0.186±0.002	0.182±0.007	0.177±0.007	0.170±0.006	0.162±0.007	0.150±0.003	0.131±0.007
	R (fm)	1.175±0.005	1.093±0.006	1.028±0.006	0.984±0.008	0.961±0.006	0.932±0.007	0.907±0.006	0.897±0.006	0.892±0.007	0.887±0.008
	μ	0.626±0.005	0.617±0.005	0.612±0.007	0.606±0.005	0.595±0.005	0.581±0.005	0.557±0.007	0.529±0.007	0.486±0.006	0.419±0.007
	χ^2/ndf	7.960	7.134	6.264	5.566	5.007	4.165	3.200	2.220	1.035	0.505
$K^+ + K^-$	T (GeV)	0.200±0.008	0.194±0.005	0.190±0.006	0.186±0.006	0.182±0.007	0.177±0.009	0.170±0.007	0.162±0.006	0.151±0.007	0.131±0.005
	R (fm)	1.310±0.007	1.174±0.007	1.043±0.005	0.982±0.006	0.934±0.005	0.879±0.008	0.817±0.005	0.778±0.008	0.722±0.005	0.609±0.006
	μ	0.274±0.005	0.326±0.007	0.369±0.006	0.384±0.007	0.398±0.008	0.410±0.006	0.423±0.006	0.425±0.007	0.430±0.006	0.462±0.005
	χ^2/ndf	0.585	0.154	0.143	0.157	0.201	0.201	0.160	0.204	0.138	0.424
$p + \bar{p}$	T (fm)	0.202±0.006	0.196±0.003	0.192±0.007	0.188±0.007	0.183±0.007	0.178±0.007	0.171±0.007	0.163±0.005	0.150±0.006	0.130±0.005
	R (fm)	1.981±0.006	1.413±0.005	1.107±0.005	0.917±0.005	0.840±0.008	0.718±0.006	0.620±0.006	0.534±0.006	0.457±0.006	0.331±0.005
	μ	-0.286±0.007	-0.148±0.005	0.164±0.006	0.299±0.005	0.358±0.006	0.455±0.005	0.537±0.008	0.616±0.006	0.685±0.005	0.804±0.005
	χ^2/ndf	0.170	0.151	0.169	0.152	0.138	0.159	0.144	0.119	0.167	0.193
ϕ	T (fm)	0.203±0.003	0.196±0.007	0.193±0.007	0.188±0.007	0.183±0.005	0.178±0.006	0.173±0.006	0.164±0.008	0.152±0.007	0.126±0.009
	R (fm)	2.385±0.006	1.578±0.005	1.314±0.008	0.978±0.006	0.867±0.005	0.739±0.005	0.587±0.007	0.531±0.006	0.451±0.005	0.342±0.006
	μ	-1.113±0.006	-0.679±0.008	-0.540±0.006	-0.291±0.006	-0.173±0.007	-0.032±0.006	0.129±0.006	0.183±0.005	0.307±0.005	0.505±0.006
	χ^2/ndf	0.721	0.491	0.395	0.578	0.434	0.371	0.497	0.213	0.507	0.750
$\Lambda + \bar{\Lambda}$	T (GeV)	0.205±0.007	0.198±0.007	0.194±0.004	0.190±0.007	0.185±0.005	0.180±0.005	0.175±0.006	0.166±0.005	0.154±0.006	0.135±0.009
	R (fm)	3.070±0.005	1.976±0.006	1.403±0.007	0.998±0.006	0.934±0.006	0.740±0.006	0.554±0.006	0.486±0.006	0.394±0.007	0.274±0.006
	μ	-0.998±0.006	-0.557±0.006	-0.261±0.007	0.022±0.005	0.072±0.005	0.252±0.007	0.445±0.005	0.530±0.006	0.649±0.005	0.844±0.006
	χ^2/ndf	0.560	0.356	0.373	0.434	0.340	0.231	0.335	0.178	0.231	0.260
$\Xi^- + \Xi^+$	T (GeV)	0.206±0.002	0.200±0.007	0.196±0.006	0.192±0.006	0.187±0.005	0.181±0.005	0.173±0.007	0.168±0.006	0.155±0.006	0.135±0.007
	R (fm)	5.823±0.009	3.384±0.006	1.402±0.005	1.118±0.006	0.796±0.007	0.656±0.005	0.581±0.006	0.438±0.006	0.467±0.006	0.195±0.006
	μ	-2.067±0.006	-1.501±0.005	-0.647±0.005	-0.498±0.008	-0.123±0.006	0.040±0.006	0.140±0.005	0.351±0.005	0.439±0.005	0.785±0.009
	χ^2/ndf	0.430	0.226	0.434	0.455	0.527	0.233	0.380	0.535	0.305	0.305
$\Omega^- + \Omega^+$			Mul[1+2]	Mul[3+4]	Mul[5+6]	Mul[7+8]	Mul[9+10]				
	T (GeV)		0.207±0.007	0.203±0.006	0.192±0.006	0.166±0.006	0.138±0.007				
	R (fm)		6.186±0.005	1.637±0.007	0.648±0.005	0.413±0.006	0.274±0.005				
	μ		-3.141±0.006	-1.642±0.005	-0.845±0.006	-0.306±0.008	0.050±0.008				
	χ^2/ndf		0.106	1.624	0.433	1.524	0.723				

4.5 Results and Discussion

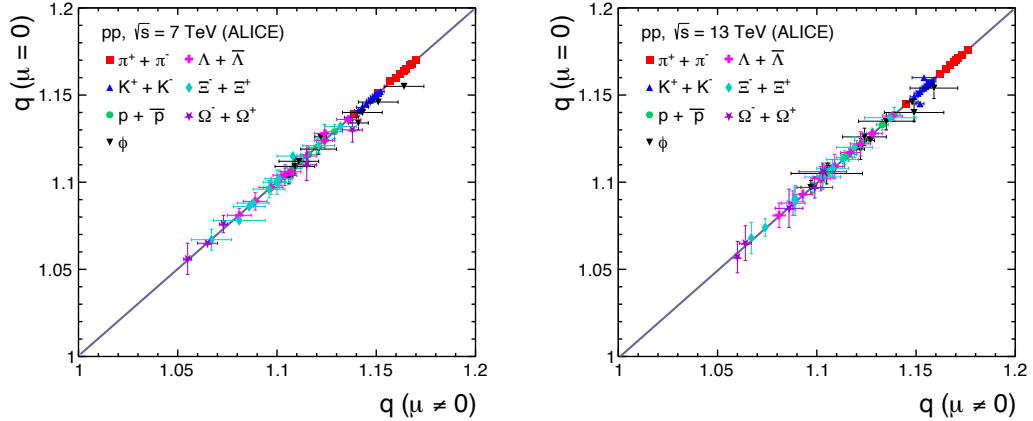


Figure 4.5: The non-extensive parameter (q) at ($\mu = 0$) as a function of q for ($\mu \neq 0$) for pp collisions at $\sqrt{s} = 7$ TeV (left panel) and 13 TeV (right panel) for different final state particles. The line represents the fit function, $y = mx + c$ [212].

Figure 4.5 depicts the variation of the non-extensive parameter at ($\mu = 0$) and ($\mu \neq 0$) for pp collisions at $\sqrt{s} = 7$ TeV (left panel) and 13 TeV (right panel) for various final state particles. It is mentioned in section 4.3 of the article that the value of the non-extensive parameter q is kept fixed, and parameters like T , V , and μ are determined by fitting transverse momentum distributions. So, to ensure the validity of our method, we have plotted the value of q for both the cases *i.e.* ($\mu = 0$) and ($\mu \neq 0$). The results suggest that the value of q remains independent irrespective of the value of μ . The contribution of μ is taken care of by T_0 and V_0 as mentioned in Eq. 4.3 and 4.4. For both the center-of-mass energies, *i.e.* $\sqrt{s} = 7$ and 13 TeV, we fitted the spectrum using $y = mx + c$. For $\sqrt{s} = 7$ TeV, the slope is $m = 0.998 \pm 0.019$, and the intercept is $c = 0.002 \pm 0.022$. In the same way, for $\sqrt{s} = 13$ TeV, $m = 1.004 \pm 0.018$ and $c = -0.005 \pm 0.021$. Moving one step further, the variation of the q -parameter is plotted for both $\mu = 0$ and $\mu \neq 0$

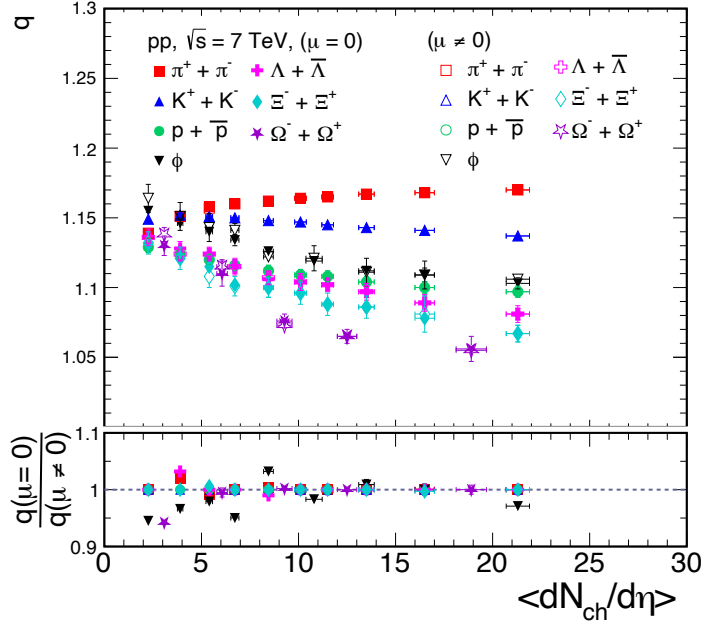


Figure 4.6: Comparison of the non-extensive parameter (q) at ($\mu = 0$) and ($\mu \neq 0$) for pp collisions at $\sqrt{s} = 7$ TeV for different final state particles as a function of final state multiplicity. Shown in the bottom panel is the ratio of both cases, which indicates that q hardly depends on the chemical potential of the system [212].

cases across all considered particle species as a function of final state-charged particle multiplicity for $\sqrt{s} = 7$ TeV, as depicted in Fig. 4.6. The bottom panel of this figure presents a ratio indicating the near-independence of the q -parameter on the system's chemical potential. This analysis provides additional support for the approach mentioned in the above section.

In Fig. 4.7, we utilize Eq. 4.5 to fit the transverse momentum spectra of various identified particles observed experimentally across different multiplicity classes at $\sqrt{s} = 7$ TeV and $\sqrt{s} = 13$ TeV. It illustrates the variation of the non-extensive parameter (q) as a function of charged-particle multiplicity, with the left panel representing $\sqrt{s} = 7$ TeV and the right panel representing $\sqrt{s} = 13$ TeV, for various final state particles. It is observed that the value of q decreases monotonically

4.5 Results and Discussion

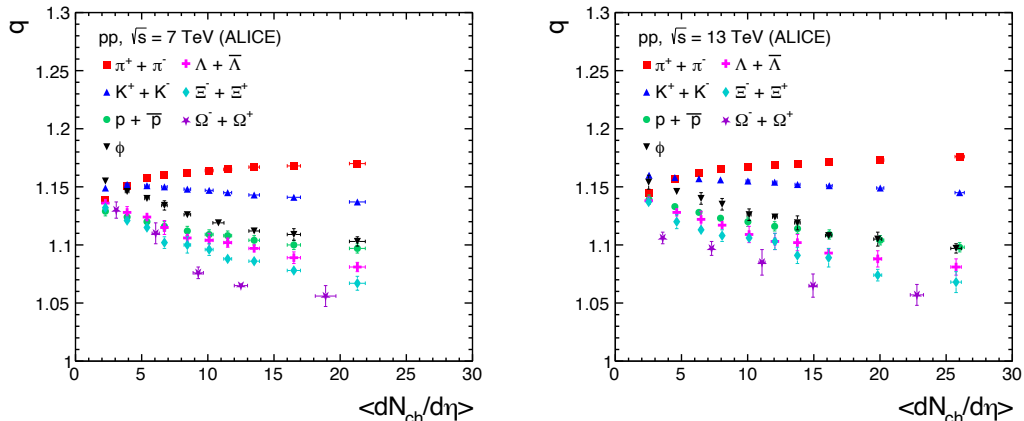


Figure 4.7: Non-extensive parameter (q) as a function of charged-particle multiplicity for pp collisions at $\sqrt{s} = 7$ TeV (left panel) and 13 TeV (right panel) for different final state particles. The uncertainties in charged-particle multiplicity are the quadratic sum of statistical and systematic contributions, and the error in the value of q is statistical errors [212].

with an increase in charged-particle multiplicity for all the particles except for pions, suggesting that the system created in higher multiplicity classes is close to thermal equilibrium. The more important thing is that q approaches 1 for high multiplicities. The decrease in q -values towards one is an important observation as it infers that the hot and dense system created in higher multiplicities is approaching a thermalized Boltzmann description of the system. However, it can be observed that the value of q monotonically increases for pions with charged-particle multiplicity. This suggests that the system deviates further from thermal equilibrium as the multiplicity of charged particles increases, which could be attributed to the contribution of resonance decay. With higher multiplicities, more resonances are likely involved, introducing additional non-equilibrium effects that impact the value of q .

Further, in Fig. 4.8, the temperature parameter (T_0) extracted from the fitting

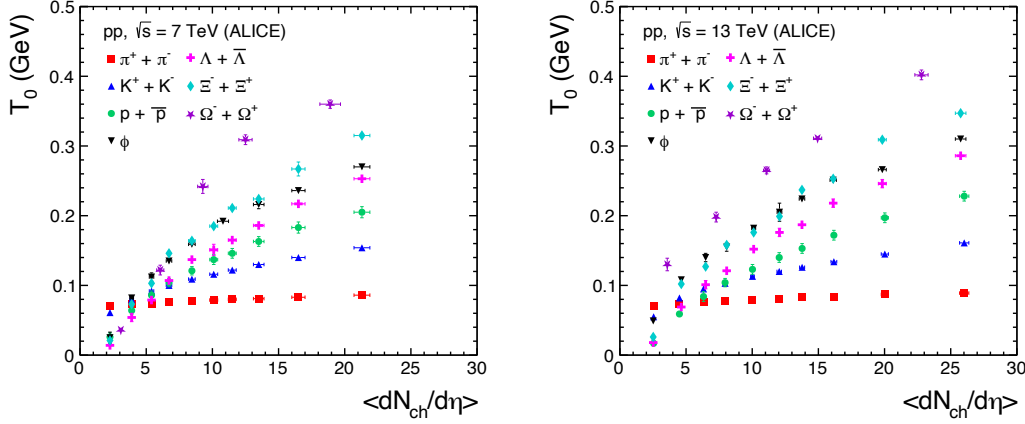


Figure 4.8: Temperature (T_0) as a function of charged-particle multiplicity for pp collisions at $\sqrt{s} = 7$ TeV (left panel) and 13 TeV (right panel) for different final state particles at zero chemical potential. The uncertainties in charged-particle multiplicity are the quadratic sum of statistical and systematic contributions, and the error in the value of T_0 are statistical errors [212].

is depicted as a function of charged-particle multiplicity for pp collisions at $\sqrt{s} = 7$ TeV (left panel) and 13 TeV (right panel), considering various final state particles at zero chemical potential. It is observed that as the charged-particle multiplicity increases, the temperature rises for all hadrons. A mass-ordering trend is observed in the figures, with heavier mass particles exhibiting a higher temperature than lighter mass particles across all charged-particle multiplicities. Similar findings are reported in Ref. [243]. This corresponds to a mass-dependent differential freeze-out scenario, where particles freeze out at different times, corresponding to different volumes and temperatures for different particle species.

In Fig. 4.9, we utilize the q -values obtained from the first set of fits as fixed parameters for the subsequent fits, where the parameters change from T_0 and R_0 to T and R , and the chemical potential remains a free parameter. The figure illustrates the temperature (T) at non-zero chemical potential as a function of

4.5 Results and Discussion

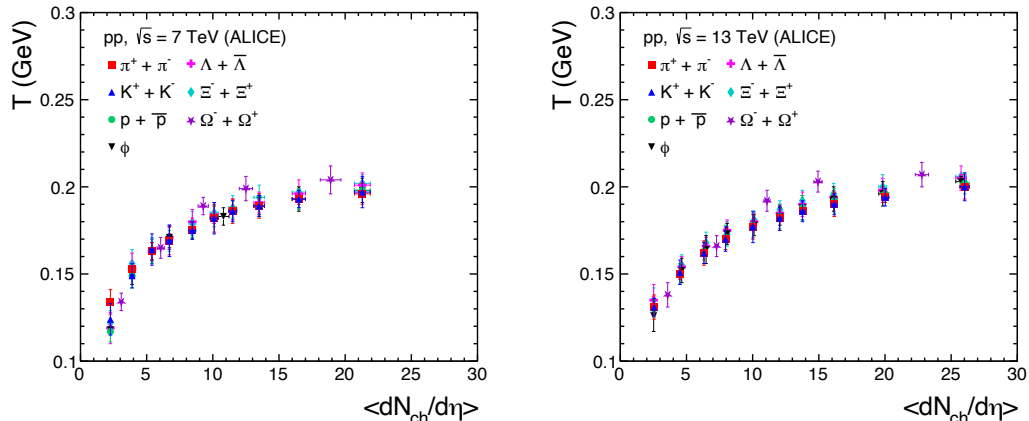


Figure 4.9: Temperature (T) as a function of charged-particle multiplicity for pp collisions at $\sqrt{s} = 7$ TeV (left panel) and 13 TeV (right panel) for different final state particles at the non-zero chemical potential. The uncertainties in charged-particle multiplicity are the quadratic sum of statistical and systematic contributions, and the error in the value of T are statistical errors [212].

charged-particle multiplicity for pp collisions at $\sqrt{s} = 7$ TeV (left panel) and 13 TeV (right panel) across various final state particles. As we proceed towards higher charged multiplicity, the temperature of all hadrons increases monotonically. Considering a given charged-particle multiplicity, the temperature exhibits a weak particle species dependency in pp collisions at both center-of-mass energies. This observation suggests that all the particles have the same kinetic freeze-out temperature for a given charged-particle multiplicity when a finite μ is allowed for the system. Furthermore, a finite chemical potential is observed at kinetic freeze-out, indicating the absence of chemical equilibrium. However, this chemical potential does not necessarily have to be zero, highlighting the complexity of the freeze-out process and the dynamics governing particle production in high-energy collisions.

Figure 4.10 depicts the radius of the system (R) as a function of charged-

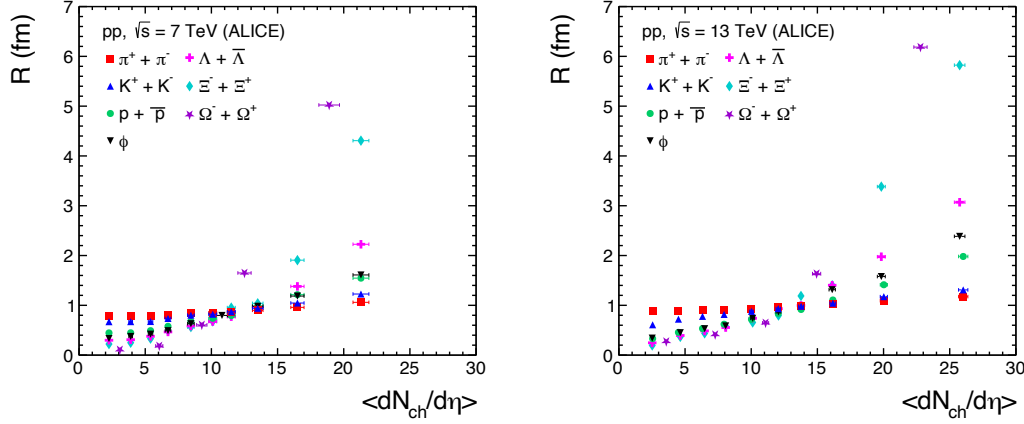


Figure 4.10: Radius of the system (R) as a function of charged-particle multiplicity for pp collisions at $\sqrt{s} = 7$ TeV (left panel) and 13 TeV (right panel) for different final state particles. The uncertainties in charged-particle multiplicity are the quadratic sum of statistical and systematic contributions, and the error in the value of R are statistical errors [212].

particle multiplicity for pp collisions at $\sqrt{s} = 7$ TeV (left panel) and 13 TeV (right panel) across different final state particles non-zero μ . The value of R increases with an increase in charged particle multiplicity, indicating that as the number of charged particles created in the collision increases, so does the size of the particle production region also increase. It suggests that increased charged particle multiplicities are often associated with more particle interactions and larger system sizes. Particle species dependency is observed in both low and high-multiplicity regions. However, an interesting finding is that the system's radius for all considered hadrons remains almost identical within the range of $\langle dN_{ch}/d\eta \rangle \simeq 8 - 14$. Beyond this range, we observe a particle species dependency in the value of R as the charged-particle multiplicity increases further.

Figure 4.11 illustrates chemical potential (μ) as a function of charged-particle multiplicity for pp collisions at $\sqrt{s} = 7$ (left panel) and 13 TeV (right panel) for

4.5 Results and Discussion

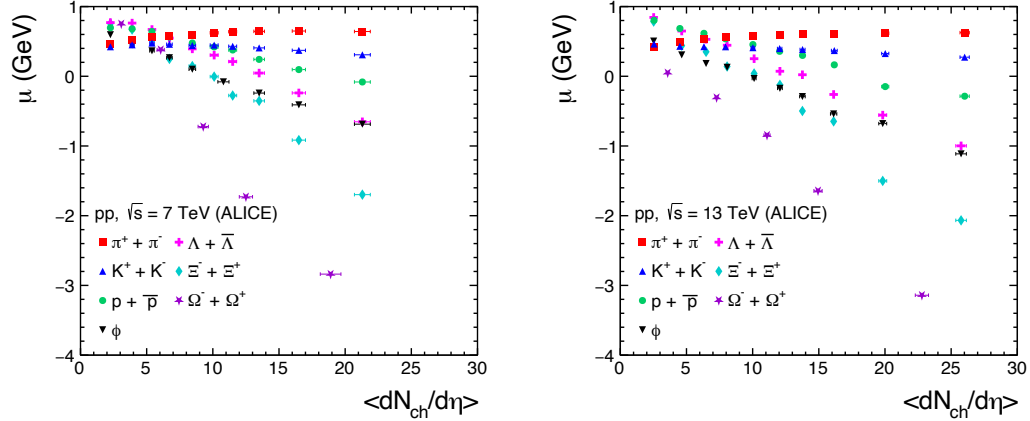


Figure 4.11: Chemical potential (μ) as a function of charged-particle multiplicity for pp collisions at $\sqrt{s} = 7$ TeV (left panel) and 13 TeV (right panel) for different final state particles. The uncertainties in charged-particle multiplicity are the quadratic sum of statistical and systematic contributions, and the error in the value of μ are statistical errors [212].

different final state particles at a fixed value of non-extensive parameters. A non-zero value of the chemical potential at kinetic freeze-out temperature is observed for all considered particle species. Moreover, a particle species dependency exists in the chemical potential values for both LHC center-of-mass energies. Notably, the chemical potentials become negative as we move towards more massive particles. However, lighter particles such as π , K , and p exhibit positive chemical potentials across all charged-particle multiplicities. The observed μ values vary considerably for different particle types. Particularly for baryons and other massive particles, the chemical potential can shift from positive to negative as the rate of change in particle multiplicity with respect to pseudorapidity increases. This transition towards negative values suggests that the production of heavier particles becomes less favorable.

It's worth noting that the chemical potentials obtained are absolute values

since we consider the combined experimental spectra of particles and their antiparticle counterparts. This approach allows us to infer QGP-like signals in the high-multiplicity class of pp events at LHC energies. One assumes a quark-antiquark system at the ground state when connecting the hadron chemical potential to constituent quarks. Given the chemical potential of a hadron, one can obtain the constituent quark chemical potentials by solving the following equation for a set of identified particles: $\mu^h = \sum_i \mu_i^q$, where i runs from 1 to the number of constituent quarks of a hadron, *i.e.*, 2 for a meson and 3 for a baryon. Here, μ^h is the chemical potential of a hadron, and μ^q is the chemical potential of a quark/antiquark [244].

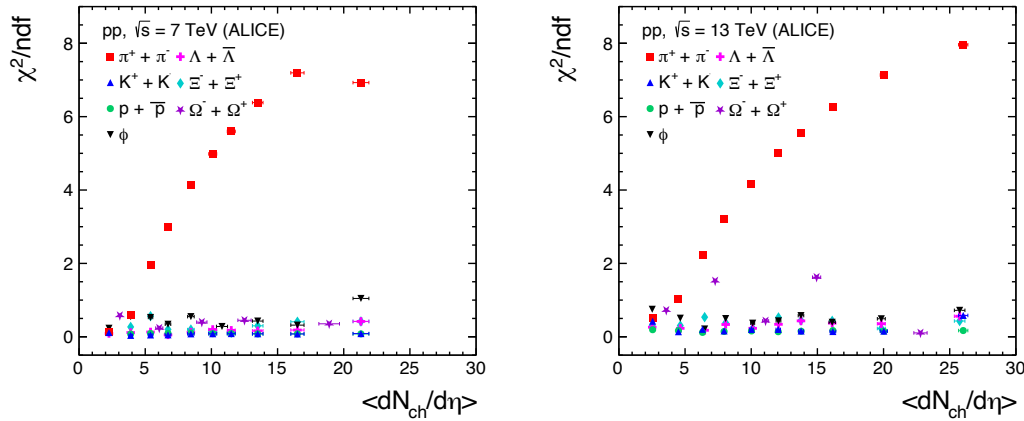


Figure 4.12: χ^2/ndf as a function of charged-particle multiplicity for pp collisions at $\sqrt{s} = 7$ TeV (left panel) and 13 TeV (right panel) for different final state particles [212].

Figure 4.12 depicts χ^2/ndf as a function of charged-particle multiplicity for pp collisions at $\sqrt{s} = 7$ TeV (left panel) and 13 TeV (right panel) across various final state particles under non-zero chemical potential conditions. The reduced χ^2 indicates the quality of fits, with values closer to one indicating a better agreement between the data and the fit function. This shows that the spectra are

4.6 Summary

well described by the thermodynamically consistent form of Tsallis distribution. Notably, the fit quality remains excellent up to p_T of 6 GeV, with χ^2/ndf consistently less than one, except for pions. Additionally, a p -value test of the fitting yielded p -values equal to 1 for all cases, further confirming the robustness of the fits and the compatibility of the Tsallis distribution with the observed data at the LHC.

4.6 Summary

This work examines another prospect to explain the kinetic freeze-out stage amidst significant chemical potential, especially in describing the final state particles of the system produced in pp collisions. A detailed investigation is presented, considering the chemical potential in the Tsallis distribution Eqn. 4.1 following a two-step procedure. We have utilized the redundancy present in the variables T , V , q , and μ expressed in Eqns. 4.3 and 4.4 and performed all fit using Eqn. 4.1, that is effectively establishing the chemical potential equal to zero. This study reviewed a comparison of T and T_0 values for both the center-of-mass energies. This result confirms that the variables T , V , q , and μ in the Tsallis distribution function Eqn. 4.1 have a redundancy for $\mu \neq 0$.

- Transverse momentum spectra of various particle species in pp collisions at $\sqrt{s} = 7$ TeV and 13 TeV were analyzed using the Tsallis non-extensive statistical model. The experimental data are fitted for different final-state particles, showing a good agreement between data and model.
- We determine the non-extensive parameter (q), temperature parameter (T_0), and radius parameter (R_0) at zero chemical potential ($\mu = 0$) using the Tsallis distribution.
- The non-extensive parameter (q) is unaffected by the system's chemical potential, indicating that T_0 and R_0 are responsible for the contribution. Also,

the q -value decreases with increasing charged-particle multiplicity, suggesting that the system approaches thermal equilibrium at higher multiplicities, except for pions, indicating an increasing trend due to contributions from resonance decay.

- A mass-ordering trend can be observed for Temperature (T_0) with heavier mass particles having a higher temperature than lighter mass particles across all charged-particle multiplicity, suggesting a differential freeze-out scenario.
- The Temperature (T) at non-zero chemical potential increases monotonically with the increase in charged-particle multiplicity, suggesting the absence of chemical equilibrium and a weak particle species dependency.
- The value of R increases with an increase in charged particle multiplicity, and we observe particle species dependencies in both low and high-charged-multiplicity regions.
- Chemical potential (μ) varies by particle species and shifts from positive to negative values for heavier particles as charged particle multiplicity increases.
- The χ^2/ndf values show the goodness of the fit, with values consistently less than one, indicating the robustness of the Tsallis distribution in explaining the ALICE experimental data.

Chapter 5

The GRAPES-3 Experiment at Ooty

The Gamma Ray Astronomy at PeV Energies-phase 3 (GRAPES-3) experiment is one of the world's major cosmic ray research facilities located at Ooty in Tamil Nadu, India. The experimental facility is situated at an altitude of 2200 m above mean sea level and latitude 11.4° N, longitude 76.7° E. It is a ground-based extensive air shower (EAS) experiment designed to study cosmic rays and γ -ray astronomy. The scientific objectives of GRAPES-3 experiment are as follows [245]:

1. Understanding the origin, acceleration, and propagation of galactic and extra-galactic cosmic rays ($> 10^{13}$ eV) by analyzing the energy spectra and mass composition of the muon.
2. Investigate the knee's existence in cosmic rays' energy spectrum.
3. Understanding the production and acceleration of the highest energy of high-energy cosmic rays ($\sim 10^{20}$ eV) through the investigation of the diffuse γ -rays of energy $> 10^{12}$ eV.

4. Exploring γ -ray astronomy at multi-TeV energies from supernova remnants and other compact objects.
5. Analyze the solar and atmospheric phenomena by exploring the directional information of muons.



Figure 5.1: A view of the GRAPES-3 extensive air shower array.

The GRAPES-3 experiment has been designed to fulfill the above-mentioned scientific objectives with a compact high-density array of ~ 400 plastic scintillator detectors, called the EAS array [246–248]. The experiment also includes a large area muon telescope, the GRAPES-3 muon telescope (G3MT) [249]. It consists of 3712 proportional counters (PRCs). The EAS array’s compactness results in a lowered energy threshold of nearly TeV, providing a significant overlap with space-based direct observations from balloon flights and satellite experiments, such as JACEE [95], RUNJOB [96], CREAM [97], DAMPE [98], ISS-CREAM [250] and

5.1 EAS array

NUCLEON [251]. The EAS muons data recorded by the G3MT is sensitive to the nature of primary and accurately estimates the mass composition of cosmic rays using Monte Carlo (MC) simulations. Similarly, the muon data is utilized to distinguish γ -ray showers from an overwhelming background of cosmic rays for γ -ray points and diffuse sources. Furthermore, the G3MT records muon directional data continuously, allowing the GRAPES-3 experiment to investigate various solar and atmospheric events. Due to the G3MT's sensitivity, even minimal fluctuations in muon intensity, ground-breaking discoveries such as giga-volt thunderstorm potentials [252] and temporary weakening of the Earth's magnetic field [253, 254] have been made. The GRAPES-3 experiment operates 24/7, collecting approximately 3×10^6 extensive air showers daily in the TeV–PeV energy range. The plastic scintillator detectors, proportional counters, and associated electronics used in the GRAPES-3 experiment were developed and produced in-house. The performance of scintillator detectors and proportional counters is regularly monitored. Figure 5.1 depicts the GRAPES-3 experimental site.

The GRAPES-3 experiment offers crucial insights into high-energy cosmic rays and their interactions with Earth's atmosphere. The extensive air showers produced when cosmic rays impact molecules in the atmosphere provide information about these particles' composition, energy, and behavior. The study of extensive air showers helps us to understand and explain astronomical events and cosmic ray (CR) physics. The following section will discuss the details of The GRAPES-3 EAS array, the corresponding signal processing unit, and the data acquisition (QAQ) systems.

5.1 EAS array

Each scintillator detector in the GRAPES-3 array is of an area of 1 m^2 . The EAS array spans a total physical area of 25000 m^2 . These scintillator detectors are arranged in a hexagonal pattern with a separation of 8 m between them.

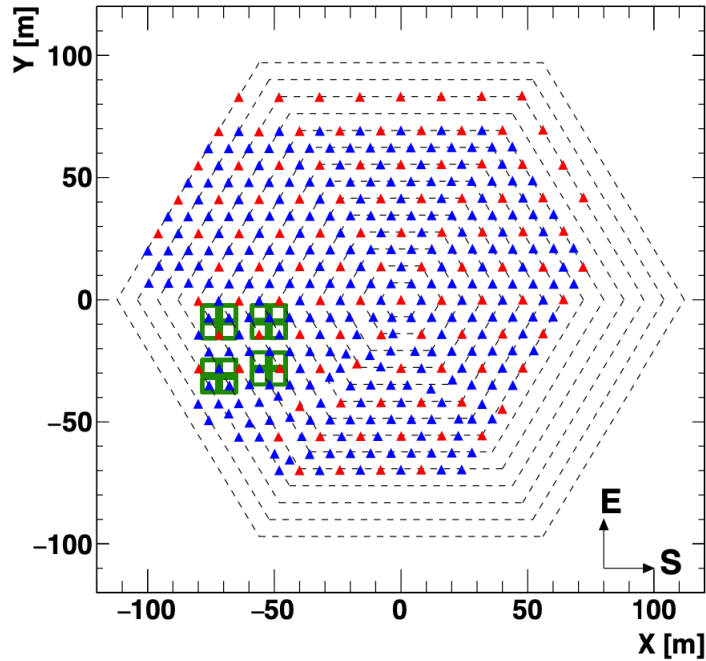


Figure 5.2: The schematic diagram of the GRAPES-3 experiment depicts single PMT scintillator detectors as blue triangles, double PMT scintillator detectors as red triangles, and G3MT modules as green open squares [255].

This configuration is designed to sample the EAS secondary particles across the entire array uniformly. Presently, the EAS array operates with two different scintillator detector designs, cone and fiber detectors. These detectors use individual methods for collecting scintillation photons. The cone detector has a single photo-multiplier tube (PMT). However, the fiber detectors have two different readout systems: a single PMT and a double PMT configuration. The double PMT scintillator detectors are strategically positioned uniformly, forming a subarray with hexagonal geometry and an inter-detector spacing of 16 m. The schematic diagram of the GRAPES-3 experiment detector system is depicted in Fig. 5.2. Blue and red triangles represent the single and double PMT scintillator detectors, respectively, while open green squares denote the G3MT modules. The EAS array records both the energy deposited and the arrival time (t) of the EAS

5.1 EAS array

secondary particles, which are expressed as analog-to-digital converter (ADC) and time-to-digital converter (TDC) counts, respectively. The deposited energy is converted into particle density (ρ) through calibration, the details of which are provided in [246]. The particle density data is then utilized to determine EAS trigger and shower parameters, such as shower cores (X_c, Y_c), size (N_e), and age parameter (s). Arrival time data is utilized for reconstructing the shower arrival direction (θ, ϕ).

5.1.1 Scintillation detector

The EAS array constitutes individual plastic scintillator detectors, each covering an area of 1 m². These detectors are designed to measure EAS particles' density and relative arrival time. Each cone-type detector consists of four identical blocks of plastic scintillators, each measuring 50 cm \times 50 cm in area and 5 cm in thickness. These blocks are enclosed within light-tight aluminum containers with a trapezoidal shape. The plastic scintillators are fabricated from polystyrene doped with 1% p-terphenyl and 0.03% POPOP. When charged particles traverse the scintillator block, a portion of their energy is deposited, which excites the polystyrene molecules. This excitation energy is promptly and efficiently transferred to p-terphenyl, which emits ultra-violet photons during the subsequent de-excitation process, with a decay time of a few nanoseconds. To compensate for the higher attenuation of UV photons within the plastic scintillator block than blue photons, POPOP is included in the composition. The POPOP absorbs ultraviolet photons and reemits blue photons, increasing total photon detection efficiency. Figure 5.3 shows a schematic of the cone detector. A photomultiplier tube (PMT) is positioned 60 cm above the plastic scintillators to collect scintillating photons from the blocks. The operational voltage for each PMT is around 1800 V. The inner surface of the detector is coated with super white TiO₂ paint to increase the reflectivity, which increases the photo-collection efficiency of

the PMT. Thus, the scintillation photons originating from the plastic scintillator blocks are guided toward the PMT through multiple reflections from the inner surface of the detector. Subsequently, the PMT converts the photons collected by the PMT into an electrical pulse with a rise time of nearly three ns and an amplitude of ~ -100 mV.

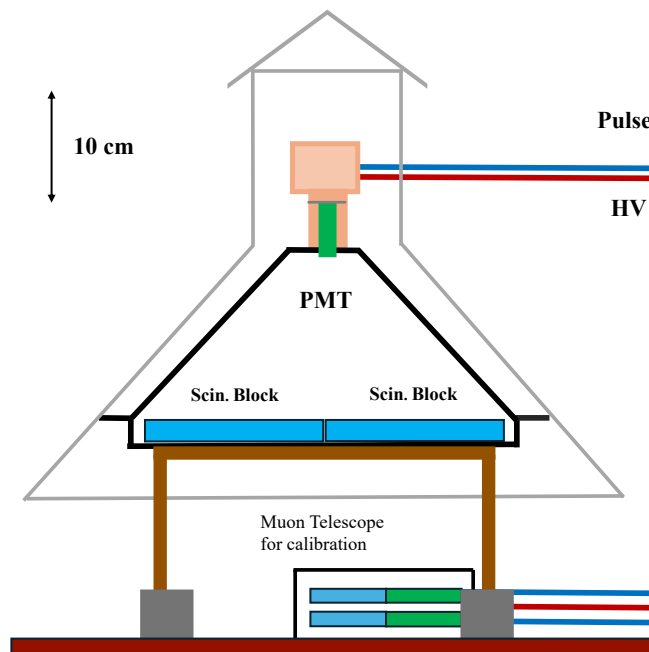


Figure 5.3: The schematic of a cone-type scintillator detector shows plastic scintillator blocks (blue) housed within a trapezoidal cone-shaped aluminum case (black line), with a PMT positioned at the top. A muon telescope under the detector is used for calibration.

An accurate measurement of an EAS requires a detector with enough sensitivity to identify individual particles going through it. Furthermore, the detector should provide signals unique enough to identify from background noise easily. The cone detectors often exhibit lower photo-collection efficiency (~ 5 photo-electrons) and non-uniform response ($\sim 30\%$) across the detector surface [247].

5.1 EAS array

These effects arise due to absorption and significant propagation delay of scintillator photons induced by multiple reflections from the inner surface of the detector. The introduction of wavelength shifting (WLS) fibers for guiding scintillator photons to the PMT has significantly enhanced the photo-collection efficiency (~ 20 photo-electrons) and reduced non-uniformity ($\sim 3\%$) [247]. Each plastic scintillator block features 12 parallel grooves carved on its surface, separating 4 cm between grooves. WLS fibers with a diameter of 1 mm are uniformly placed within these grooves. Unlike conventional optical fibers, which only accept light from their ends, WLS fibers can absorb blue scintillation photons from their surface and emit green photons. A fraction of these emitted green photons, with angles exceeding the critical angle, become trapped inside the WLS fiber and subsequently reach the PMT through multiple total internal reflections. Additionally, Tyvek sheets cover the plastic scintillator blocks, which increases photo-collection efficiency by reflecting scintillation photons into the blocks. It's worth noting that plastic scintillation blocks ranging in thickness from 2 cm to 2.4 cm have been shown to increase efficiency. This comprehensive technique improves detection sensitivity and homogeneity throughout the detector surface, critical for accurate measurements of EAS properties.

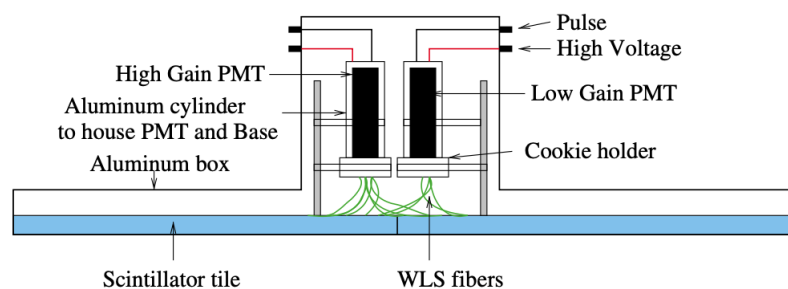


Figure 5.4: Schematic of a double PMT fiber-type scintillator detector [247].

The entire setup is enclosed within a more compact, light-tight aluminum

enclosure. Two distinct configurations of WLS fiber readout are employed: a single PMT and a double PMT setup. A high-gain PMT is utilized in the single PMT fiber detector, whereas the double PMT detector includes an additional low-gain PMT. Fig. 5.4 illustrates a double PMT fiber-type scintillator detector. Each plastic scintillator block contains 24 WLS fibers, with 2 in each groove. Among these 24 fibers, 6 positioned in alternate grooves direct the photons to low-gain PMT, while the remaining 18 guides the photons to high-gain PMT.

Both cone and fiber detectors are elevated on 60 cm tall stands and shielded by an external aluminum casing to safeguard against rain and harsh weather conditions. Initially, the GRAPES-3 experiment commenced with 257 cone detectors. However, as time progressed, some cone detectors were replaced with fiber detectors, and additional fiber detectors were deployed. Presently, the GRAPES-3 experiment operates with a nearly equal quantity of cone and fiber detectors. Among the fiber detectors, 105 are configured as double PMT scintillator detectors.

5.1.2 Signal processing and data acquisition system

The data acquisition mechanism for the EAS array's scintillator detectors ensures that signal pulses are precisely captured and processed. The anode pulse travels via a 230-meter coaxial cable with a 50Ω resistance, with low temporal delays due to equal cable length. After the arrival of signals, signals undergo passive splitting: one pulse is attenuated by 3% and sent to the ADC module via an 80-meter coaxial delay cable for charge integration, while the other is amplified by a factor of 10, passed through a discriminator, and converted into fixed-width digital pulses. Then, these digital pulses are used for different purposes, including recording signal arrival times and monitoring detector rates for EAS trigger generation. Fig. 5.5 shows the data acquisition system and signal processing used in the EAS array.

5.1 EAS array

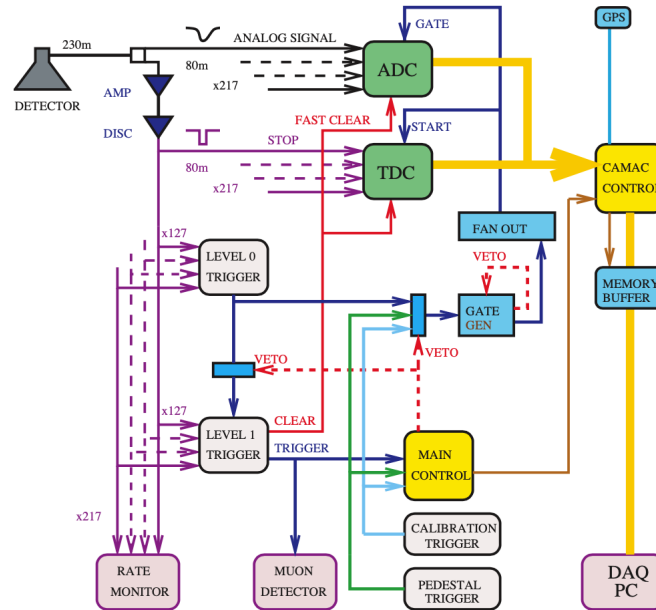


Figure 5.5: The schematic of the signal processing system for the scintillator detector shows the basic components of data acquisition and the propagation of signals to ADC and TDC, along with signals used for EAS trigger generating and rate monitoring [246].

When three adjacent lines coincide within 100 ns, this trigger gets triggered. As shown in Fig. 5.6, the lines were created by taking a logical OR of detectors in a north-south direction. After the Level-0 trigger is generated, the ADC and TDC record the integrated charge and arrival time. If a Level-1 trigger is not triggered in 2.5 milliseconds, the ADC and TDC outputs are reset. To produce the Level-1 trigger, a GATE signal is needed for data recording, and ten detectors are required. The data is captured using a real-time clock with a precision of 100 ns, synchronized every second with a GPS signal from satellites. The DAQ system has a dead time of approximately 3.5 ms [246]. The data is captured using a real-time clock with a precision of 100 ns, synchronized every second with a GPS signal from satellites. The DAQ system has a dead time of approximately 3.5 ms [246].

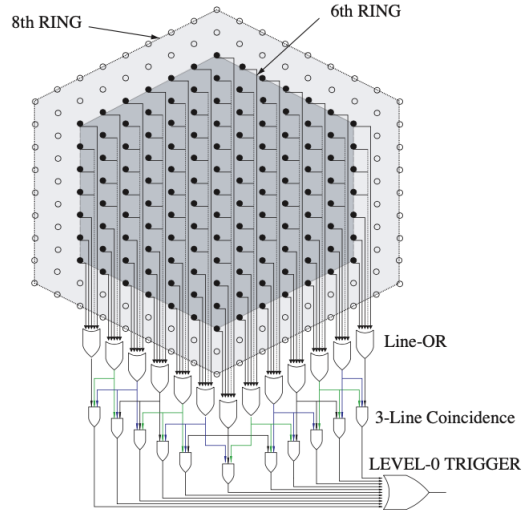


Figure 5.6: Schematic of the shower trigger system for generating the Level-0 trigger using the basic 3-line coincidence [246].

In the subsequent section, we will discuss the essential components of the GRAPES-3 muon telescope (G3MT) in great detail, how proportional counters are made and used, and the DAQ and signal processing techniques used for G3MT.

5.2 GRAPES-3 muon telescope

The GRAPES-3 experiment uses the G3MT (GRAPES-3 Muon Telescope), a detector system spanning 560 m^2 , explicitly designed to capture the muon component of extensive air showers. Each G3MT consists of 16 independent modules with a detection area of 35 m^2 . The proportional counter (PRC) is the primary detection unit in each module and has 232 proportional counters per module for a total of 3712 PRCs for the G3MT. The supermodules (blue dashed squares, S_0 to S_3) that house four adjacent modules each are formed by the arrangement of the muon modules, which are represented as red squares in Fig. 5.7. For efficient

5.2 GRAPES-3 muon telescope

muon track reconstruction, each module has four separate layers of proportional counters, designated Layer-0 to Layer-3, placed orthogonally.

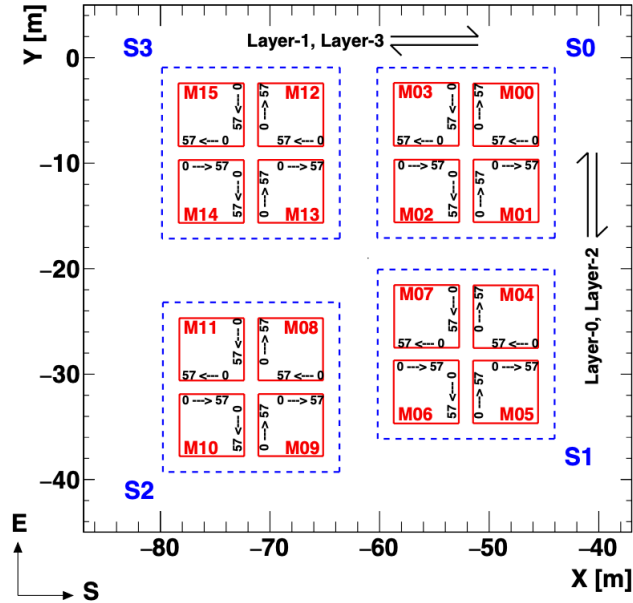


Figure 5.7: Schematic representation of the G3MT for GRAPES-3 coordinates system. Red squares represent the muon modules (M00 \rightarrow M15), and the blue dashed squares represent supermodules (S₀ \rightarrow S₃). The direction of the PRC within each layer is indicated by the notation \leftrightarrow . However, the arrangement of the proportional counters for each projection in a given module is shown explicitly. However, the placement of proportional counters in each projection inside a certain module is explicitly shown and denoted by the symbol $0 \rightarrow 57$ [255]

Fig. 5.7 illustrates the proportional counter structure for each module, which enables reconstruction in the Y-Z and X-Z projections. In the Y-Z projection, muon track reconstruction is primarily handled by Layers 0 and 2, whereas in the X-Z projection, reconstruction is handled by Layers 1 and 3. The direction of the muon can be confirmed by merging the tracks from these two projection planes. There are 58 proportional counters in each layer, from 0 to 57, in consecutive order. The gaps between successive layers are filled with concrete blocks, 60 cm

$\times 60 \text{ cm} \times 15 \text{ cm}$, which help reconstruct the muon track with an accuracy of 6° . In addition, 13 layers of 2 m thick concrete blocks are used to absorb the low-energy hadronic and electromagnetic components.

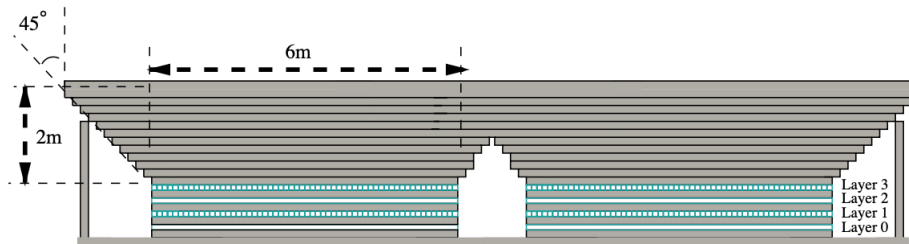


Figure 5.8: A cross-section projection of a supermodule depicting two front modules with four layers of proportional counters and a concrete absorber [249].

Figure 5.8 provides a cross-sectional projection of a supermodule, showing the arrangement of proportional counters and concrete absorbers. These concrete blocks serve as absorbers for the electromagnetic (EM) component and the low-energy hadronic component of the EAS. To achieve an energy threshold of 1 GeV for vertically incident muons and to absorb the electromagnetic component, a total thickness of 550 g/cm^2 in the form of concrete blocks was employed as an absorber. The supermodules' thick walls provide thermal insulation and keep the inside temperature at about 22°C . Dehumidifiers keep the humidity below 50%. The muon station's external temperature varies between 10°C and 20°C , but it varies less inside the supermodules. With this configuration, the proportional counters operate at their best and last longer in various environmental circumstances.

5.2.1 Proportional counter (PRC)

Proportional counters are constructed using a zinc-coated mild steel tube, 600 cm long with a cross-sectional area of $10 \text{ cm} \times 10 \text{ cm}$, as illustrated in Fig. 5.9. The tube's wall thickness is 2.3 mm. High-quality welding techniques seal both

5.2 GRAPES-3 muon telescope

ends of the tube with flat mild steel plates, each 6 mm thick, to prevent leaks. Inside the proportional counter, a gold-coated tungsten wire, 100 μm in diameter, acts as the anode, while the PRC tube is the cathode. This wire is positioned along the axis of the tube and is mounted through small openings at the center of both end plates. The anode wire operates at an approximate potential of 3000 V and is securely attached to the end plates using a glass-to-metal airtight seal, ensuring electrical insulation. One end plate of the proportional counter features a needle valve through which the counter is evacuated to a vacuum level of 10^{-3} mbar before being filled with P-10 gas. P-10 gas is a mixture of 90% argon (Ar) and 10% methane (CH_4), pressurized to about 35% above the local atmospheric pressure.

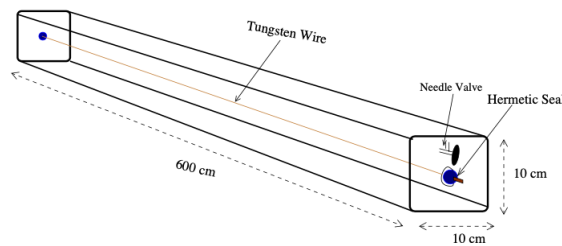


Figure 5.9: A schematic of the PRC is used as the basic detector element in the GRAPES-3 tracking muon detector [256].

When a high voltage is applied across the anode wire, a radial electric field is created inside the counter. Ionization events result in the production of electron-ion pairs as charged particles travel through the gas medium. When subjected to the electric field, ions drift toward the cathode and electrons toward the anode. Electrons travel faster than ions because of their higher mobility in the strong electric field, due to this they gain enough energy for further ionization, triggering the avalanche effect. A negative pulse travels along the anode wire as a result of the ensuing electron cloud, creating a localized positive charge close to it. The energy released by the charged particle in the gas is correlated with the signal's

magnitude [257]. UV photons are released from the gas as a result of atoms being excited by charged particles moving through it. As a quencher, CH_4 efficiently absorbs the UV photons and prevents them from causing unrelated avalanches within the proportional counters.

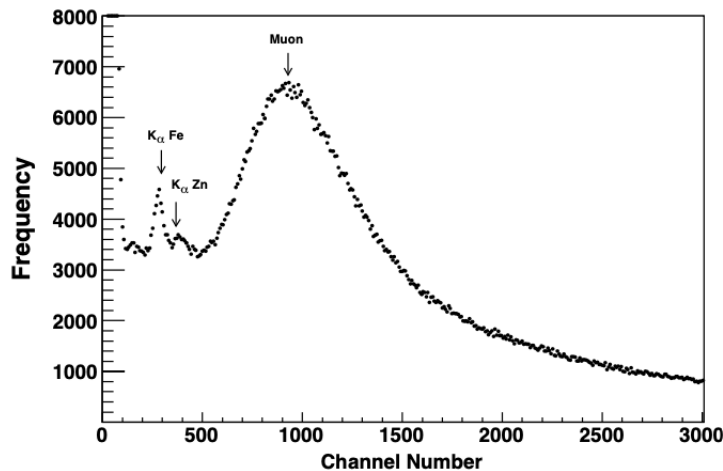


Figure 5.10: A typical pulse amplitude distribution for a proportional counter [256].

The amplitude distribution of PRC output pulses, as determined by a multi-channel analyzer, is shown in Fig. 5.10. The emission of fluorescent K_α X-rays from Fe and Zn is responsible for the first two small peaks. It is important to remember that proportional counters are made of zinc-coated iron tubes, which prevent rust. On the other hand, the notable peak is associated with muons from cosmic rays passing through the detector. To keep an eye on the proportional counters' health, one of the most essential parameters is the profile of its amplitude distribution. Any malfunction could cause the distribution to change shape and require the implementation of the necessary corrective actions to get it back to working order.

An amplifier with a gain value of 83 amplifies the PRC's output pulse. It

5.2 GRAPES-3 muon telescope

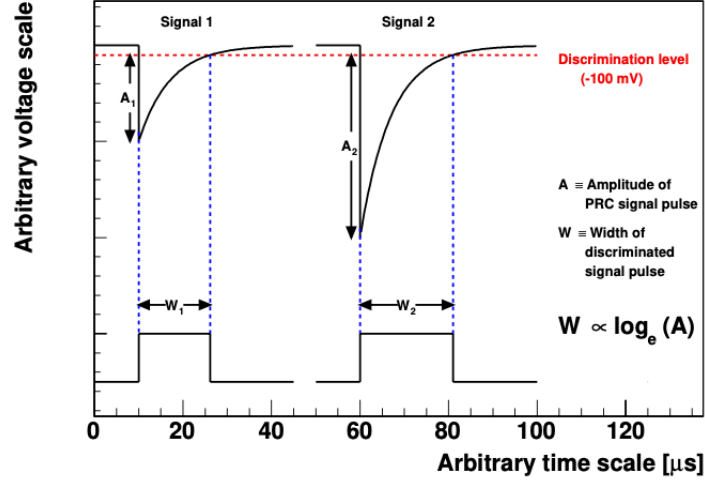


Figure 5.11: Schematics of two PRC pulses of amplitude A_1 and A_2 , respectively, and corresponding discriminator output pulses of width W_1 and W_2 , respectively [255].

is then formed into an exponential waveform with a $7\mu\text{s}$ decay time. Following shaping and amplification, the pulse travels via a discriminator with a threshold of -100 mV , or 20% of the energy of the least ionizing particle. The pulses that are above this threshold are digitalized by the discriminator. As seen in Fig. 5.11, the discriminator pulse width is directly proportional to the logarithm of the amplifier pulse magnitude because of the amplified pulse's exponential structure. The estimated number of muons (N_μ) passing through a proportional counter for a particular EAS is found as follows:

$$N_\mu = \exp\left(\frac{W_n - W_0}{\tau}\right) \quad (5.1)$$

W_n is the observed pulse width for EAS, W_0 is the pulse width corresponding to the minimum ionizing particle, and τ is the decay constant. Thus, the pulse width information helps estimate the number of muons passing through a given PRC for high-energy EAS.

5.2.2 Signal processing and data acquisition system

The PRC hits status, pulse width, and pulse arrival time information are captured when an output pulse exceeds the discriminator threshold. The G3MT records data in two modes: MuMain data, which records data for each EAS trigger, and MuAngle data, which records data independently of EAS triggers. Details of the MuMain DAQ are provided here, while MuAngle DAQ specifics can be found elsewhere [249].

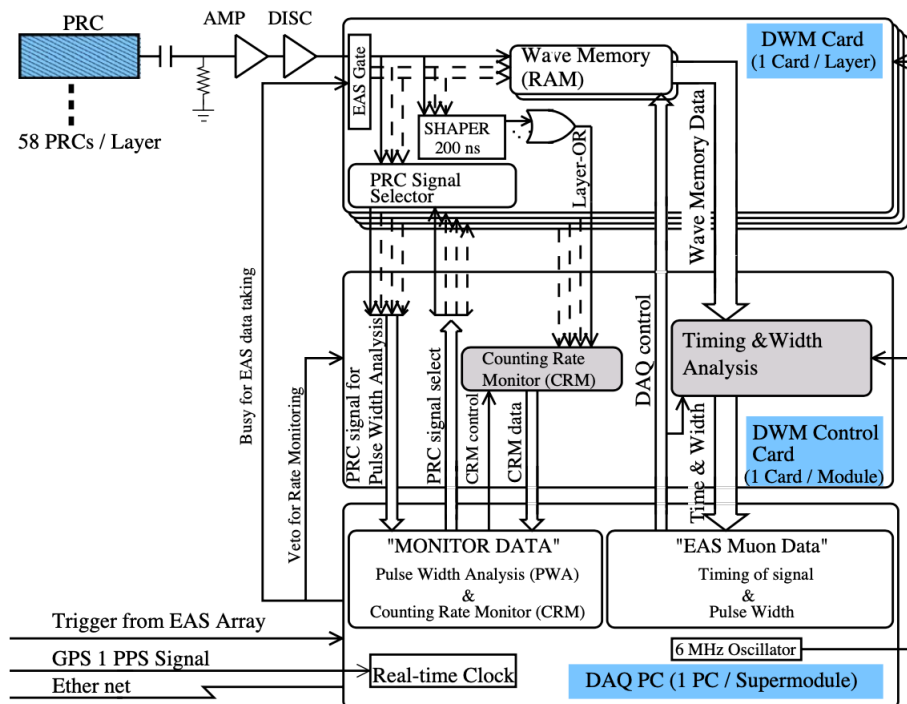


Figure 5.12: A schematic of the signal processing system and DAQ for the G3MT showing the digital wave memory (DWM) card and DWM control card [249].

Muon data is collected by four distinct DAQ systems, each dedicated to a super module. Fig. 5.12 illustrates the signal processing and DAQ setup. All DAQ systems trigger simultaneously on receiving an EAS trigger. Each layer's 58 proportional counters are linked to a standard digital wave memory (DWM)

5.3 Summary

card, which samples discriminator output pulses. The DWM card checks pulse status with 167 ns resolution, marking RAM with 1 for presence and 0 for absence. Consecutive 167 ns intervals with RAM determine pulse width (W) is set to 1. Sampling occurs 6 μ s pre-trigger, allowing for the ~ 2 μ s trigger generation post-shower passage. Each super module features a dedicated DAQ-PC managing four DWM control cards. When receiving an EAS trigger, the DAQ-PC instructs all DWM control cards to retrieve corresponding module data. This data, including PRC hits status, pulse arrival time, and pulse-width info, is stored on a hard disk with real-time clock (RTC) timestamps at 1 μ s precision. RTC synchronizes with a GPS receiver via a pulse-per-second signal every second. Muon and EAS DAQ systems operate independently; muon data timestamps align with EAS data during analysis. Each discriminator output pulse is reshaped into a 200 ns width digital pulse. A logic OR combines reshaped pulses per layer, generating Layer-OR. PRC performance is monitored by counting Layer-OR rates per layer and coincidences among Layer-OR signals facilitated by DWM control cards.

5.3 Summary

The GRAPES-3 experiment is one of the world's major cosmic ray research facilities located at Ooty in Tamil Nadu, India, mainly focusing on gamma-ray astronomy and extensive air shower analysis. The following are the essential aspects of its infrastructure and research capacity.

- The experiment features a dense array of approximately 400 plastic scintillator detectors and a large area muon telescope consisting of 3712 proportional counters, giving us to study the cosmic ray origins, energy spectra, gamma-ray astronomy, and analyzing solar and atmospheric phenomena.
- To effectively detect the EAS's secondary particles, cone and fiber scintillator detectors are arranged in a hexagonal pattern.

- The muon component of EAS is captured by PRCs in the G3MT, which are arranged into supermodules with four layers of counters for efficient reconstruction of the muon track.
- Study of muon data is made possible by the signal processing and data acquisition (DAQ) systems that capture PRC hits status, pulse width, and arrival time data.
- The experiment uses robust signal processing and data acquisition systems to constantly record and study muon data, contributing significantly to our understanding of cosmic ray physics and astrophysical phenomena.

Chapter 6

Study of muon puzzle in cosmic ray events with GRAPES-3

Experiment

The study of cosmic rays, mainly the high-energy interactions and propagation of particles within extensive air showers, has fascinated scientists and researchers in astroparticle physics. The muon puzzle is one of the most persistent challenges in cosmic ray physics. The discrepancy between the number of muons observed in the cosmic ray events and predicted by the theoretical model is known as the muon puzzle. Major experiments such as the Pierre Auger Observatory and the Telescope Array [258–261] highlighted this discrepancy in very high-energy. Additionally, the experiments at the CERN revealed an unexpected excess of muon bundles, with multiplicities reaching up to about 100 particles, exceeding expected levels even under assumptions of purely iron primary in cosmic rays [262, 263]. However, these experiments could have provided an understanding of the energy dependence of this excess. Addressing this, the NEVOD-DECOR experiment focused on an inclined extensive air shower, connecting different zenith angles with varying intervals of primary particle energies to analyze local muon den-

sity spectra [264, 265]. This analysis presents excess muon bundles produced, which vary with the energy of the primary particles. Though advanced hadronic interaction models like QGSJET, SIBYLL, and EPOS-LHC, observed muon multiplicities, especially at higher energy scales, still need to be predicted. However, this discrepancy indicates notable gaps in our understanding of high-energy interactions and cosmic ray propagation, necessitating modifications to these models to incorporate essential factors. In spite of the advancement in the field of high-energy hadronic interaction models like QGSJET, EPOS-LHC, and SIBYLL, the discrepancy observed between the experimental observations and the model's predictions show significant gaps in our understanding of the propagation of cosmic rays and the need to incorporate these important factors in these models.

To understand the discrepancy of muon multiplicity between the experimental observation and theoretical models, the extensive air shower simulator CORSIKA (Cosmic Ray SIMulations for KAscade), a widely used Monte Carlo simulator, is used to induce extensive air showers on the Earth's atmosphere for various primary particles [266]. In this analysis uses the data from the GRAPES-3 observatory to compare with the simulation data generated using the QGSJET-II-04 and the EPOS-LHC model. GRAPES-3 provides extensive observational data over a wide range of energies to compare the results of simulations with experimental data. In this study, we aim to understand this discrepancy to provide an underlying cause behind it by analyzing the muon multiplicity distribution, energy spectra, and zenith angle distribution. Hence, it can help us to refine the existing theoretical models. We used CORSIKA version 7.69 with the QGSJET-II-04 and EPOS-LHC models to generate extensive air showers to understand this puzzle. We attempt to address this longstanding puzzle in cosmic ray physics by analyzing the fundamental process that manages the Universe with the help of this analysis.

Extensive air shower (EAS) simulations are crucial in achieving these objectives. These simulations model hadronic and electromagnetic interactions result-

6.1 CORSIKA simulation

ing in thousands to millions of secondary particles. Given the complexity and randomness inherent in these interactions, a probabilistic approach is essential. This is where the Monte Carlo (MC) methods come into play.

6.1 CORSIKA simulation

Monte Carlo methods, which use random sampling to model complex phenomena, are integral to simulating extensive air showers (EAS). These methods rely on interaction cross-section data to simulate the distribution of secondary particles. CORSIKA (COsmic Ray SIMulations for KASCADE) is a leading Monte Carlo simulation software for EAS, developed by the KASCADE experiment group at the Karlsruhe Institute of Technology in Germany. CORSIKA can simulate particles such as photons, protons, and light nuclei up to iron within an energy range of 10^9 to 10^{20} eV. The simulation parameters in CORSIKA are set through an input steering file, which includes specifications for particle ID, energy, zenith angle, atmospheric model, altitude, and magnetic components at the observational level. CORSIKA tracks each particle through the atmosphere until it reaches an interaction point or the observational level. Various physical phenomena, such as energy loss, multiple scattering, deflection in the magnetic field, and Cherenkov light, are accounted for during the tracking. At a given interaction point, the particles may either interact with the nucleus of the air molecules or decay if the particle is unstable, as guided by hadronic and electromagnetic (EM) models. Secondary particles below a critical energy threshold are not further processed, while others are stored for further simulation. Due to the energy limitations of particle accelerators, high-energy hadronic interactions in cosmic ray events still need to be fully understood, requiring theoretical extrapolations. Hadronic interaction models are divided into low-energy models (e.g., GHEISHA [267], FLUKA [268], UrQMD [269]) for energies $\leq 8 \times 10^{10}$ eV and high-energy models (e.g., DPMJET [270], EPOS-LHC [271], NEXUS [272], QGSJET 01C [273], QGSJET-II-

04 [274], SIBYLL 2.1 [275]) for energies $> 8 \times 10^{10}$ eV. Electromagnetic interactions are described by the EGS4 [276] model and the Nishimura-Kamata-Greisen (NKG) formula [277, 278], with EGS4 explaining the photoproduction of muon pairs and hadrons, which is essential for muon production in γ -initiated extensive air showers.

In this study, cosmic ray primaries such as proton (p), helium (He), nitrogen (N), aluminum (Al), and iron (Fe) are simulated using CORSIKA version 7.6900 to generate extensive air showers at the GRAPES-3 location. Two combinations of hadronic interaction models are employed: (i) QGSJET-II-04 and FLUKA, and (ii) EPOS-LHC and FLUKA. The secondary particles from these extensive air showers are tracked until their energies fall below 1 MeV, 1 MeV, 10 MeV, and 50 MeV for γ -rays, electrons, muons, and hadrons, respectively, or until they reach the GRAPES-3 observational level. Extensive air showers are generated for energies ranging from 1 TeV to 10 PeV per particle and a zenith angle from 0° to 45° . The azimuthal direction is uniformly distributed between 0° and 360° . The energy range is divided into 20 equal logarithmic bins with a width of 0.2. Showers are generated for each primary, assuming their spectra follow a power law with a spectral index of -2.5 in each energy bin. CORSIKA produces several output files, among which the binary file is crucial. It contains details about the CORSIKA run, observational level, and primary cosmic rays, including particle ID, energy spectrum, and zenith and azimuth angle ranges. The data file captures information about each secondary particle reaching the observational level, including particle ID, spatial coordinates (x, y, z), momentum components (p_x, p_y, p_z), and the time of flight from the initial interaction (t). The binary file contents are converted and stored in ROOT format to facilitate efficient data storage and access.

Further analysis uses an in-house developed framework, including a comprehensive simulation of the GEANT4 (Geometry and Tracking 4) response of EAS secondary particles in the scintillator detector. This framework encompasses cal-

6.1 CORSIKA simulation

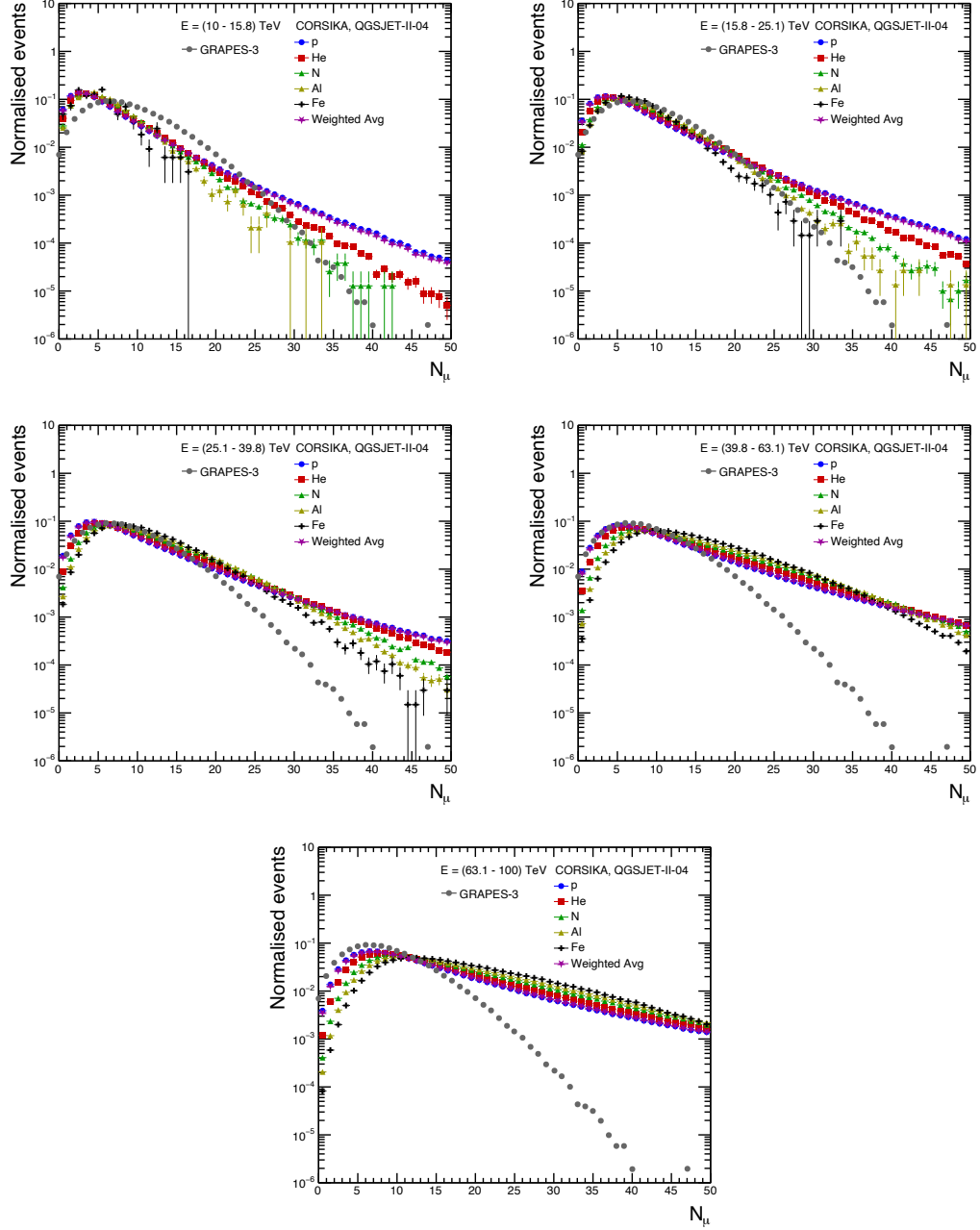


Figure 6.1: A comparison of the observed muon multiplicity distribution for shower size $10^{4.6}$ – $10^{4.8}$ with simulations for p, He, N, Al, and Fe for QGSJET-II-04.

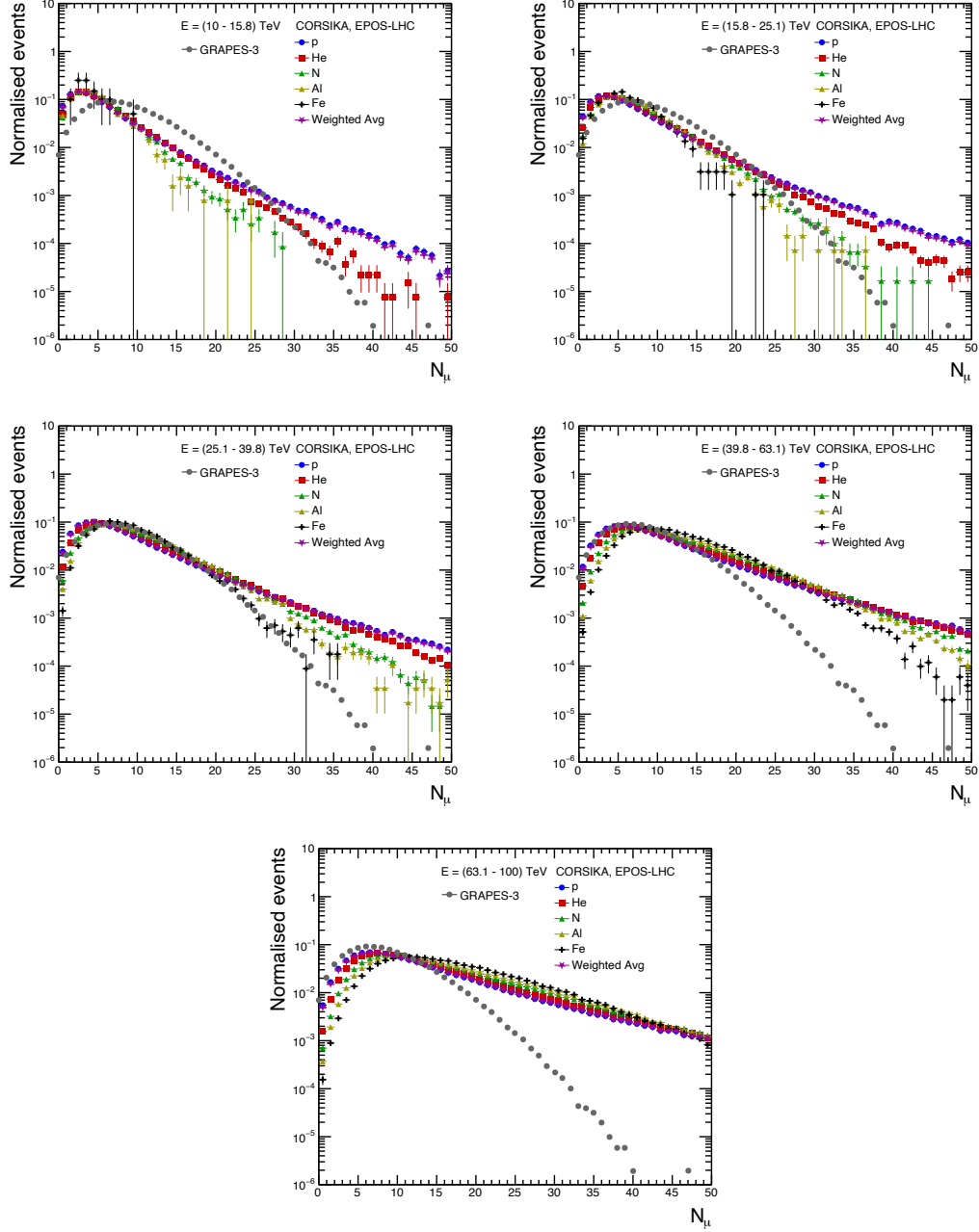


Figure 6.2: A comparison of the observed muon multiplicity distribution for shower size $10^{4.6}$ – $10^{4.8}$ with simulations for p, He, N, Al, and Fe for EPOS-LHC.

ibrating deposited energy to generate particle density recorded by the scintillator detector (ρ) and EAS trigger generation. Each EAS is processed ten times, with

6.1 CORSIKA simulation

the core location randomly selected within a circular area of radius 150 m from the center of the EAS array (-13.85 m, 6.29 m), referred to as dataset-1. Due to the steeply declining cosmic ray flux, this dataset has limited statistics at higher energies. Thus, another dataset (dataset-2) is generated for energies from 100 TeV to 10 PeV to enhance statistics at higher energies. In this dataset, each EAS is randomly positioned ten times within a circular area radius 60 m from the array's center. This choice considers an EAS core selection area of 50 m from the array's center, providing an excellent angular resolution of nearly 4 m at 100 TeV and better than 1 m above 1 PeV. Each EAS secondary particle's spatial and temporal coordinates are translated to the GRAPES-3 coordinate system, considering the randomized EAS core position.

For each EAS secondary particle incident, the effective area of a scintillator detector and the energy deposited in the detector volume is determined using a pre-simulated GEANT4 database. This database contains the response of EAS secondary particles, including muons, electrons, gamma rays, protons, neutrons, and pions, for each scintillator detector configuration. The response of each particle type is simulated over an energy range from 1 MeV to 100 GeV and a zenith angle range from 0° to 60° . The energy range is divided into 101 logarithmic bins, and the zenith range is divided into 21 $\sec(\theta)$ bins with a bin width of 0.05. The deposited energy is recorded as an integral probability distribution with 800 bins for each particle type for given energy and zenith angle bins. The energy deposited by EAS secondary particles in the scintillator detector is computed based on their energy and zenith angle values and the type and thickness of the plastic scintillator block. Similarly, the energy deposited by a single muon is simulated using GEANT4 and utilized for calibration. The total energy deposited by EAS secondary particles in a given scintillator detector is converted into ρ using muon calibration. A discriminator threshold of 0.5 minimum ionizing particles is applied. The ρ and information for each triggered detector are used to validate the trigger conditions in the simulation. To calculate the true shower size N_e^{true} ,

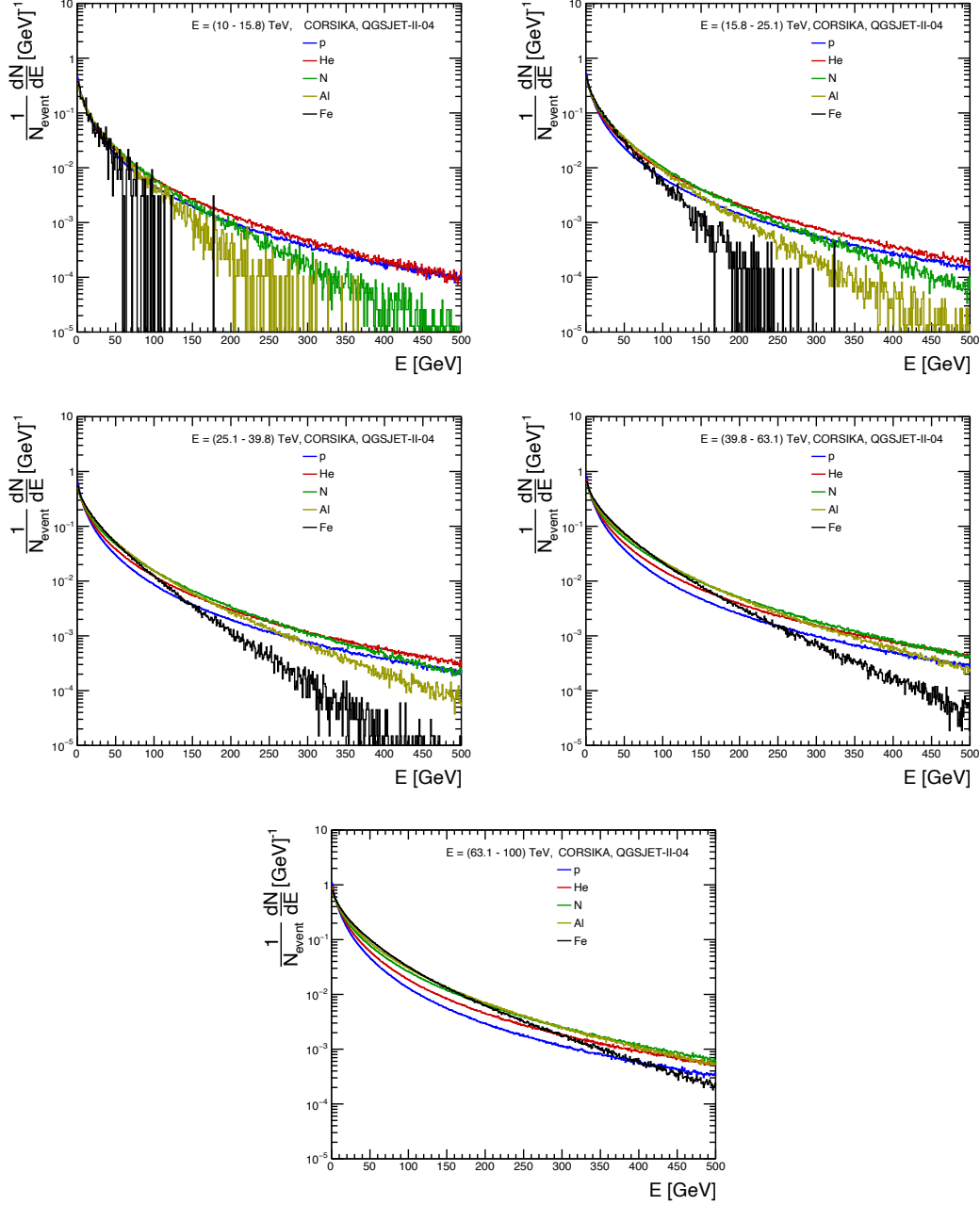


Figure 6.3: Muon energy spectra with simulations for primary cosmic rays (p, He, N, Al, Fe) using the QGSJET-II-04 model.

a virtual $1000 \text{ m} \times 1000 \text{ m}$ continuous grid of scintillator detectors, each with an area of 1 m^2 , is assumed to be layered on the observational level, centered

6.1 CORSIKA simulation

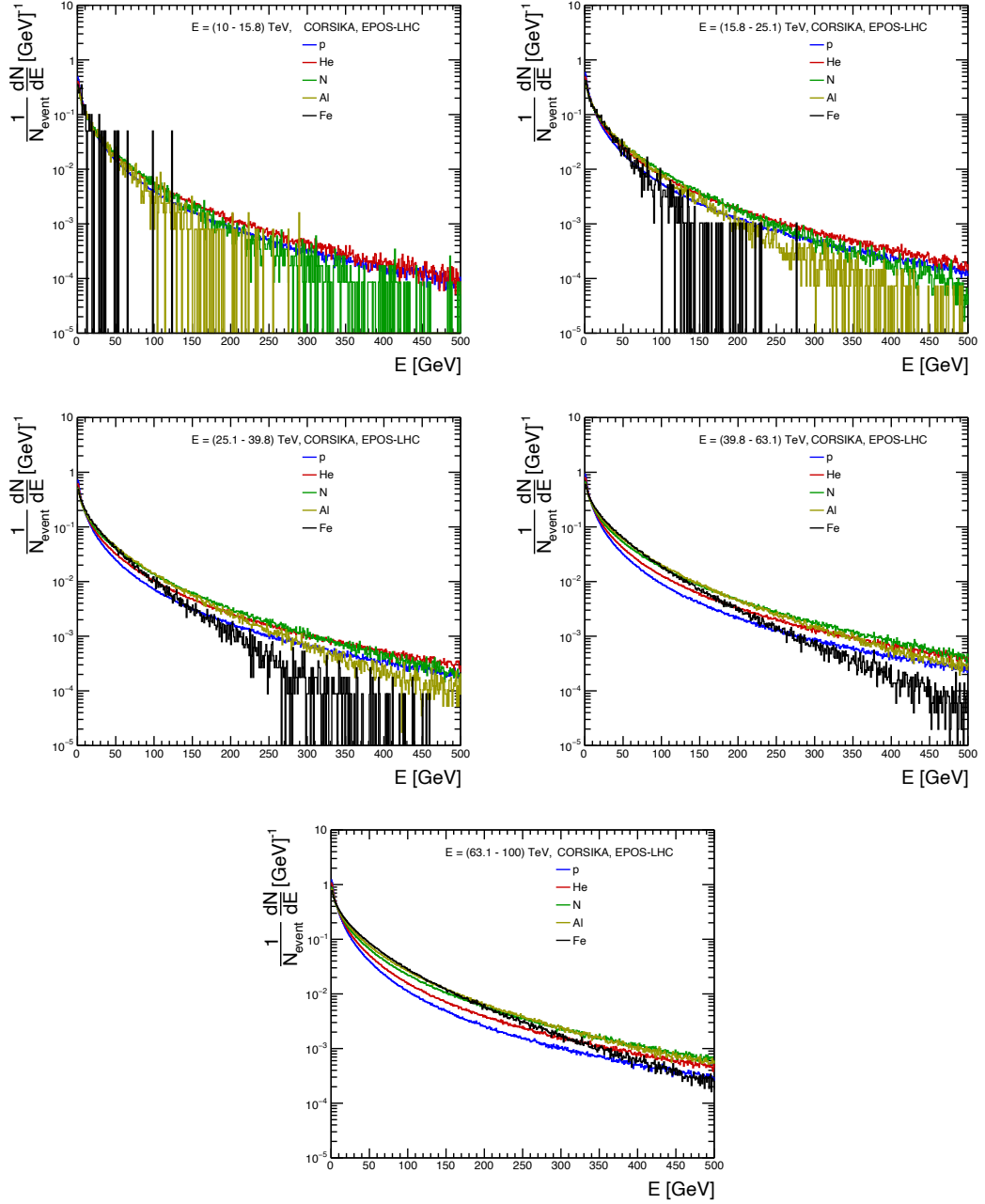


Figure 6.4: Muon energy spectra with simulations for primary cosmic rays (p, He, N, Al, Fe) using the EPOS-LHC model.

on the shower axis. The observational area beyond the grid is considered a giant scintillator detector. The grid configuration is selected randomly. The

deposited energy by each EAS secondary particle is calculated using the GEANT4 database and converted into ρ using muon calibration. The N_e^{true} is calculated by summing the ρ measured by all scintillator detectors within the grid and the giant scintillator detector outside the grid. The N_e^{true} is used to estimate the shower size resolution, σ_{N_e} , of the GRAPES-3 EAS array.

This thorough simulation procedure provides important insight into the muon puzzle and improves our knowledge of cosmic ray physics by precisely modeling the energy distribution and behavior of secondary particles in EAS.

6.2 Results and Discussion

This section compares the simulation results from the hadronic interaction models like the QGSJET-II-04 and the EPOS-LHC for different primary particles, mainly composed of the cosmic ray flux, with GRAPES-3 experimental data for muon multiplicity distributions. We also show the simulated energy spectra and zenith angle distributions of various primary particles in cosmic ray air showers for two hadronic interaction models such as QGSJET-II-04 and EPOS-LHC. This analysis could help us understand the underlying physics behind particle interaction in very high-energy and enhance our knowledge of cosmic ray physics in a much-improved way.

6.2.1 Muon multiplicity distribution

Understanding the dynamics of particle interactions and the formation of extensive air showers (EAS) in Earth's atmosphere can be gained by examining the muon multiplicity distributions in cosmic-ray events. Figures 6.1 and 6.2 show simulated distributions of muon multiplicity distribution using the QGSJET-II-04 and EPOS-LHC models for various primary particles. These distributions show the number of muons detected within air showers initiated by primary cos-

6.2 Results and Discussion

mic rays such as proton(p), helium (He), nitrogen (N), aluminum (Al), and iron (Fe). The central motivation for studying these distributions lies in addressing the longstanding muon puzzle, which revolves around observed discrepancies between predicted and actual muon multiplicities in cosmic ray showers. We have studied the muon multiplicity for various primary particles between (10 - 100) TeV and divided them into five equal logarithmic energy bins with a width of 0.2. In each energy bin, we studied the muon multiplicity and took a weighted average of each primary to calculate the weighted average spectra. As we know, cosmic rays are composed of atomic nuclei; among these nuclei, over 87% are protons (p), 12% are helium (He) nuclei and the remaining 1% are other heavy nuclei (such as N, Al, Fe). Keeping this in mind, we have taken the weighted average of the spectra and plotted it along with all the primary particles. By comparing simulated results with experimental data, mainly we have shown for air showers within the $10^{4.6}$ to $10^{4.8}$ size range, we aim to validate the predictive power of the QGSJET-II-04 and EPOS-LHC models. Likewise, air showers of different sizes can also be analyzed. However, we have presented here a single shower size. These analyses are required to refine our cosmic ray interactions and composition models and discover new fundamental physics phenomena that govern the cosmic ray sources. The comparison of simulation data with experimental data suggests the precision measurement of our existing models and our understanding of the hadronic interaction models. It seeks a need for modification in these models to understand the reason behind this discrepancy in muon multiplicity that might improve our knowledge and knowledge.

Hence, the multiplicity spectra of muon serve as an essential observable in cosmic ray physics to decode the composition and propagation of particles in cosmic ray extensive air showers, suggesting there is a requirement for a more in-depth understanding of the nature of particle interactions and sources of these particles at the highest energies.

6.2.2 Muon energy spectra

The investigation of the energy spectra of muons resulting from interactions of primary cosmic rays, such as protons and heavier nuclei like helium (He), nitrogen (N), aluminum (Al), and iron (Fe), with Earth's atmosphere is important for understanding the complexities of the high-energy phenomena observed. The energy distribution of these muons not only provides essential information on the composition but also the behavior of primary cosmic rays and serves as a necessary measurement for validating the theoretical models that predict these interactions. Post-LHC hadronic interaction models like QGSJET-II-04 and EPOS-LHC play a central role in simulating the complex hadronic interactions governing air shower development in the Earth's atmosphere.

Figures 6.3 and 6.4 show the energy spectra of muons simulated for different primary cosmic rays particles such as p, He, N, Al, and Fe using the QGSJET-II-04 and EPOS-LHC models, respectively. These models, differing in their treatments of high-energy hadronic interactions and particle fragmentation processes, predict distinct muon energy spectra. Generally, muon spectra show a power-law distribution with fewer high-energy muons at higher energies due to increased interactions or decay processes. Lighter primaries like proton and helium yield steeper spectra with fewer high-energy muons, while heavier primaries like nitrogen, aluminum, and iron produce flatter spectra with more high-energy muons. Although these comparisons are based solely on simulations, they provide valuable insights into particle production mechanisms in cosmic ray showers, advancing our knowledge of cosmic ray astroparticle physics and fundamental particle interactions. By comparing simulated muon spectra with experimental data, researchers can pinpoint discrepancies that may signify areas for model refinement and improve our understanding of particle production mechanisms in cosmic ray showers. This ongoing effort advances our knowledge of cosmic ray astrophysics and broader explorations into fundamental particle interactions and astrophysi-

6.2 Results and Discussion

cal phenomena. Future endeavors should prioritize refining hadronic interaction models, validating simulations against experimental data, and probing anomalies that could reveal new insights into the universe's most energetic processes.

6.2.3 Muon zenith angle distributions

One of the key observables in solving the muon puzzle in cosmic ray physics is the analysis of the muon zenith angle distribution. It helps us to understand how they interact and propagate in the Earth's atmosphere. The interaction of the primary cosmic rays in the Earth's atmosphere produces a cascade of particles called EAS and the produced secondaries, like muons, that could penetrate deep into the atmosphere and reach the surface of the Earth.

Figures 6.5 and 6.6 show the zenith angle distributions of muons simulated for different primary cosmic rays (p, He, N, Al, and Fe) using the QGSJET-II-04 and EPOS-LHC models, respectively. We have divided the zenith angle from 0 to 45 ° into four bins from 1 to 1.4 with a bin width of 0.1. We observe that the observed muon peaks at the smaller zenith angles (near vertical) and decreases towards higher zenith angles (horizon). This is due to the fact that the muons that travel through a longer atmospheric path are more likely to decay or be absorbed. Interestingly, we observed that, as we move towards higher zenith angle bins, the muon number increases for heavier primaries. This is because of more extensive air showers produced by heavier primary nuclei, which result in a more significant number of secondary particles. However, even at higher zenith angles, we observed higher muon numbers for proton primary. For lighter primaries like proton and helium, the produced distributions are narrower, with fewer secondary particles in the EAS. In contrast, heavier primaries such as nitrogen, aluminum, and iron create broader distributions as the higher mass and energy of these heavier primaries result in a higher probability of producing muons that can penetrate through the atmosphere at larger angles.

These results are consistent across both the QGSJET-II-04 and EPOS-LHC models and provide a significant understanding of the behavior of different primary cosmic rays and the performance of these hadronic interaction models. We can refine our models and improve our predictions by understanding these distributions. This lays the groundwork for future comparisons with experimental data, which will help further investigate this direction, validate these models, and find discrepancies that suggest areas where our understanding of particle interactions could be improved.

6.3 Summary

The muon puzzle in cosmic ray-induced air showers presents a complicated challenge demanding advances in experimental techniques and theoretical models. Addressing discrepancies in muon multiplicity requires refining the existing post-LHC hadronic interaction models using data from forward-direction collider experiments like the LHCb. This interdisciplinary approach integrates enhanced experimental capabilities, refined theoretical frameworks, and potential insights into new physics phenomena.

- Ongoing improvements, presented by experiments like NEVOD-DECOR, are crucial for enhancing muon measurements and air shower simulations.
- Models like QGSJET-II-04 and EPOS-LHC highlight that heavier primaries (e.g., nitrogen, aluminum, iron) generate more number of muons than lighter ones (e.g., proton, helium). This variation significantly impacts predicted muon counts in the extensive air shower (EAS).
- Primary composition affects muon energy distribution, with lighter primaries yielding steeper spectra and heavier ones producing flatter spectra with more high-energy muons.

6.3 Summary

- Observations show heavier nuclei have higher muon multiplicities, especially at larger zenith angles, influencing extensive air shower characteristics.
- Comparing simulated data with experimental observations from GRAPES-3 and other detectors strengthens our better understanding of cosmic ray-induced air showers and their muonic components in EAS.

Through this comprehensive ongoing analysis, the study aims to contribute to the continuing efforts to resolve the muon puzzle and advance the field of cosmic ray and astroparticle physics. The insights gained will help refine theoretical models and improve our understanding of the fundamental processes governing high-energy cosmic phenomena.

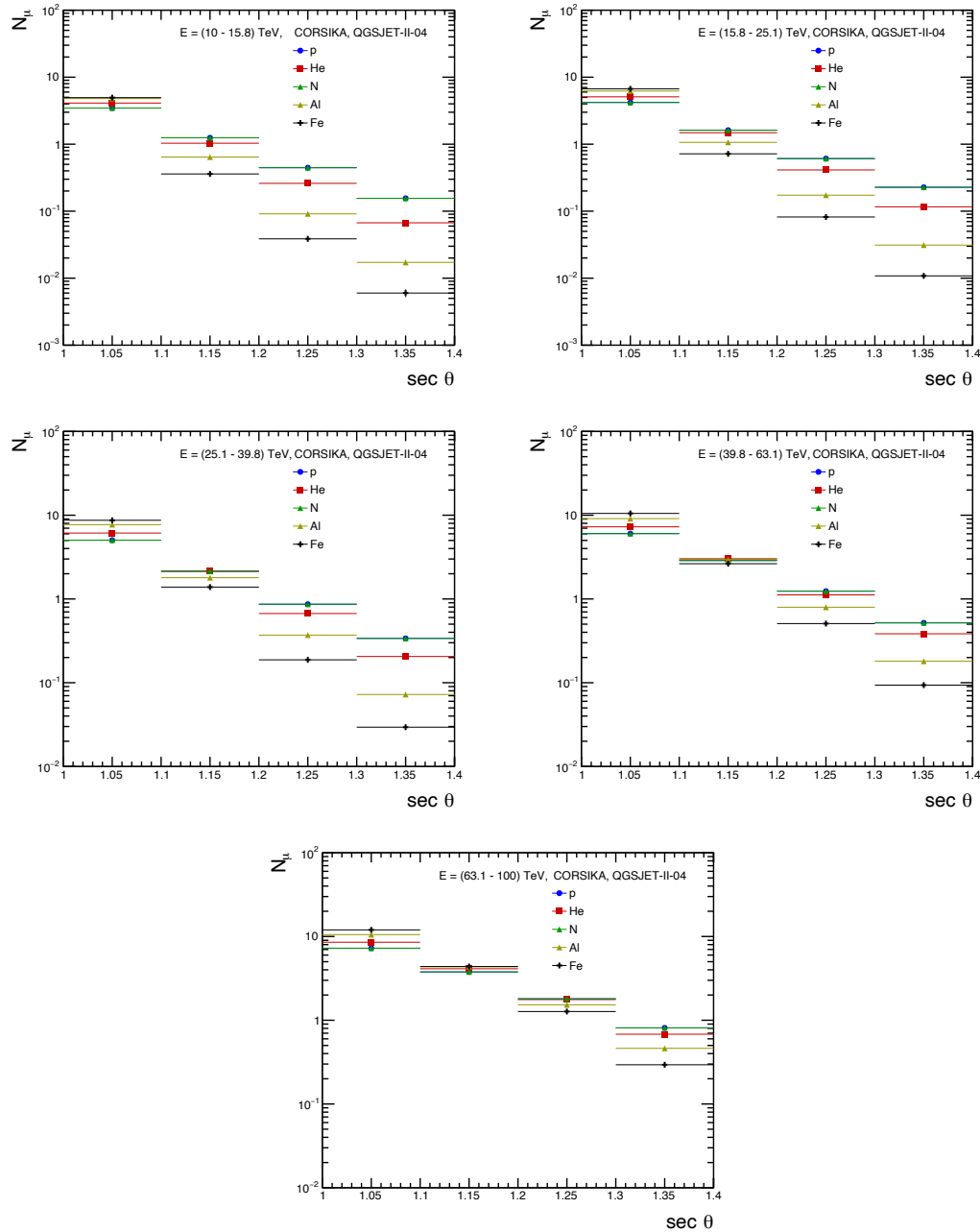


Figure 6.5: Simulated muon zenith angle distributions for different primary cosmic rays primaries (p, He, N, Al, Fe) using the QGSJET-II-04 model. This figure demonstrates the variation in muon count with the zenith angle, showing the effects of different primary particles on air showers and muon production characteristics.

6.3 Summary

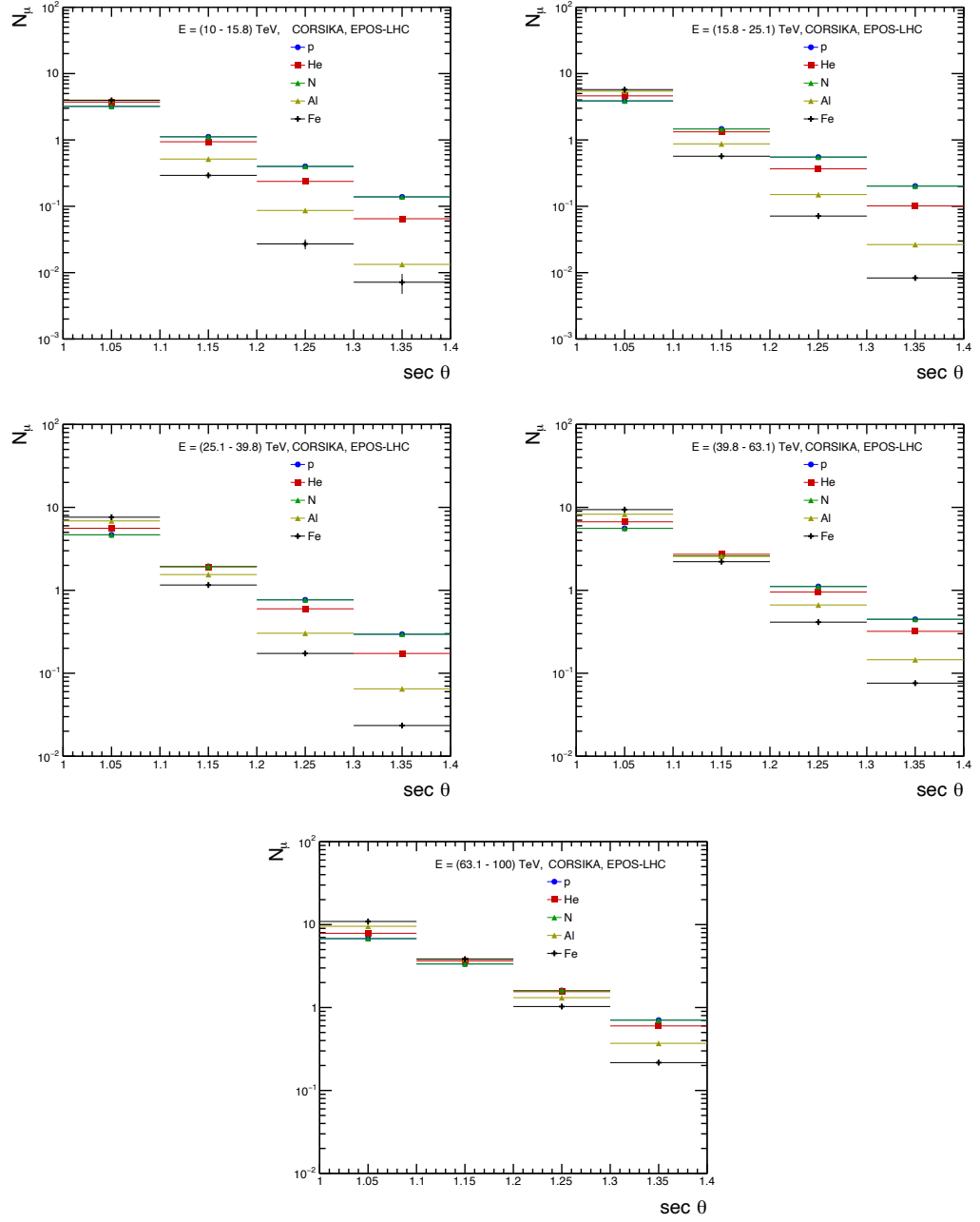


Figure 6.6: Simulated muon zenith angle distributions for different primary cosmic rays primaries (p, He, N, Al, Fe) using the EPOS-LHC model. This figure demonstrates the variation in muon count with the zenith angle, showing the effects of different primary particles on air showers and muon production characteristics.

Chapter 7

Summary and Outlook

In this thesis, we started with the motivation of characterizing the hadronic phase in relativistic heavy-ion collisions and studying the muon puzzle in cosmic ray events with the GRAPES-3 experiment. We briefly discuss the QCD phase diagram, possible phase transition, and some QGP signatures. Additionally, it explores cosmic rays' origin and energy spectra, followed by an overview of direct and indirect detection techniques. Chapter 2 examines the influence of nuclear deformation and hadron cascade time in Xe+Xe collisions, shedding light on how these factors shape particle ratios and flow patterns. Chapter 3 explores the impact of external magnetic fields and non-extensive statistics on hadron gas properties, providing insights into the interplay between magnetic effects and thermodynamic behavior in heavy-ion collisions. Chapter 4 discusses the role of chemical potential at kinetic freeze-out in pp collisions, offering an alternative perspective on freeze-out dynamics and its implications for particle production. Chapter 5 provides an overview of the GRAPES-3 detectors used for data analysis. Finally, Chapter 6 presents the study of the muon puzzle in cosmic ray events with the GRAPES-3 experiment. The essential findings of this thesis are summarized below:

- We observed a significant dependence of p_T -differential particle ratios for

ϕ/π and p/π on hadron cascade time (τ_{HC}), particularly at low p_{T} , with the ϕ/π ratio being more sensitive. A higher τ_{HC} shifts low p_{T} particles to intermediate and high p_{T} regions due to increased interactions, influencing the particle ratios.

- Considering the mass dependence on τ_{HC} , the ϕ/p p_{T} -differential particle ratio was examined. This ratio scales with τ_{HC} in the (50-60)% centrality class, but a notable dependence on τ_{HC} is seen at intermediate p_{T} for mid-central collisions.
- The p_{T} -differential charged particle elliptic flow is higher for $\tau_{\text{HC}} = 25 \text{ fm}/c$ compared to $5 \text{ fm}/c$ at both very low and high p_{T} . This suggests that increased anisotropy in the azimuthal distribution of charged particles may result from multiple scatterings in the hadronic phase with higher τ_{HC} .
- Consistent with experimental results at LHC energies, no scaling behavior was observed with the number of constituent quarks (n_{q}) on elliptic flow. The hadron cascade time does not affect the quark-participant scaling violation in elliptic flow, likely due to initial state effects rather than hadronic rescattering, which is a final state effect.
- To study the impact of hadronic cascade time on the bulk medium, p_{T} -integrated charged particle elliptic flow was estimated across different centrality classes. The p_{T} -integrated charged particle elliptic flow remains almost independent of hadronic cascade time, likely due to the compensation of anisotropy across various p_{T} regions.
- The impact of hadron cascade time was observed on p_{T} -differential identified particle ratios, p_{T} -differential, and p_{T} -integrated charged particle elliptic flow. This highlights the interplay of various hadronic phase effects on these observables, such as scattering cross-sections, hadronic phase lifetime, and momentum anisotropy inherited from the initial collision geometry.

-
- We observe the effect of hadron cascade time on p_T -differential identified particle ratios, p_T -differential, and p_T -integrated charged particle elliptic flow. This reveals the interplay of various hadronic phase effects, such as scattering cross-sections, hadronic phase lifetime, and momentum anisotropy inherited from the initial collision geometry, on these observables.
 - Higher collision energies generate stronger magnetic fields, with the LHC producing the strongest observed.
 - The influence of the non-extensive parameter, q , on thermodynamic properties was explored, showing that deviations from equilibrium increase energy density, pressure, and entropy density.
 - Under a strong magnetic field ($eB = 15m_\pi^2$), the system maintains positive magnetization across all q -values while deviating from equilibrium ($q = 1.15$), resulting in diamagnetic behavior under a weaker magnetic field ($eB = m_\pi^2$), transitioning to paramagnetic behavior as the magnetic field strength increases.
 - A transition from diamagnetic to paramagnetic behavior in non-central heavy-ion collisions was identified as collision energy increases from RHIC to LHC levels, a phenomenon that requires further investigation.
 - The squared speed of sound (c_s^2) of the hadron gas in the presence of a magnetic field was examined, showing adherence to the Stefan-Boltzmann limit of $1/3$ while decreasing asymptotically with increasing magnetic field strength, indicating increased interactivity within the system.
 - The analysis provides insights into the complex interplay between non-extensive statistics, magnetic fields, and thermodynamic properties in heavy-ion collisions, emphasizing further research to understand these phenomena

fully.

- The transverse momentum spectra of various particle species in pp collisions at $\sqrt{s} = 7$ TeV and 13 TeV were analyzed using the Tsallis non-extensive statistical model. Experimental data were fitted for different particle species, including non-strange, strange, and multi-strange particles, illustrating good agreement between the model and data.
- Parameters such as the non-extensive parameter (q), temperature parameter (T_0), and radius parameter (R_0) were determined at zero chemical potential ($\mu = 0$) using the Tsallis distribution.
- The non-extensive parameter (q) was found to be largely independent of the system's chemical potential (μ), suggesting that T_0 and R_0 account for the contribution of μ in the system.
- The value of q exhibited a decreasing trend with increasing charged-particle multiplicity, indicating that the system approaches thermal equilibrium at higher multiplicities, except for pions, which showed an increasing trend due to contributions from resonance decay.
- Temperature (T_0) showed a mass-ordering trend, with heavier particles exhibiting higher temperatures across all charged-particle multiplicities, suggesting a mass-dependent differential freeze-out scenario.
- Temperature (T) at non-zero chemical potential increased monotonically with charged-particle multiplicity, indicating the absence of chemical equilibrium and a weak particle species dependency.
- The system's radius (R) increases with increasing charged-particle multiplicity, suggesting larger system sizes associated with higher multiplicities and particle species dependency in low and high-multiplicity regions.

-
- Chemical potential (μ) exhibited particle species dependency and varied considerably, transitioning from positive to negative values for heavier particles as charged-particle multiplicity increased.
 - The χ^2/ndf analysis confirmed the goodness of fit, with values consistently less than one, indicating the robustness of the Tsallis distribution in describing the experimental data at the LHC.
 - Ongoing improvements, exemplified by experiments like NEVOD-DECOR, are crucial for enhancing muon measurements and air shower simulations.
 - Models like QGSJET-II-04 and EPOS-LHC highlight that heavier primaries (e.g., nitrogen, aluminum, iron) generate more muons than lighter ones (e.g., hydrogen, helium). This variation significantly impacts predicted muon counts.
 - Primary composition affects muon energy distribution, with lighter primaries yielding steeper spectra and heavier ones producing flatter spectra with more high-energy muons.
 - Observations show heavier nuclei have higher muon multiplicities, especially at larger zenith angles, influencing extensive air shower characteristics.
 - Comparing simulated data with experimental observations from GRAPES-3 and other detectors strengthens our better understanding of cosmic ray-induced air showers and their muonic components in EAS.

The findings presented in this thesis provide a comprehensive understanding of the complex interplay between nuclear deformation, hadron cascade time, magnetic fields, and non-extensive statistics in the context of relativistic heavy-ion collisions and the study of the muon puzzle in cosmic ray events. The significant dependence of particle ratios and elliptic flow on hadron cascade time highlights

the importance of hadronic phase interactions in shaping observables, while the effects of magnetic fields and non-equilibrium statistics on hadron gas properties offer new insights into the thermodynamic behavior of these systems. Furthermore, the detailed analysis of pp collision data using the Tsallis non-extensive statistical model underscores the robustness of this approach in describing experimental results across different particle species and multiplicities. The GRAPES-3 experiment's contributions to our understanding of cosmic rays through the precise detection and analysis of muon data emphasize the need for ongoing improvements in experimental techniques and theoretical models. Overall, this thesis advances our knowledge of both heavy-ion collisions and cosmic ray physics, paving the way for future research to explore the underlying mechanisms and potential new physics in these fascinating domains.

Bibliography

- [1] J. J. Thomson, *Phil. Mag. Ser. 5* **44**, 293 (1897).
- [2] E. Rutherford, *Phil. Mag. Ser. 6* **21**, 669 (1911).
- [3] E. Rutherford, *Phil. Mag. Ser. 6* **37**, 581 (1919).
- [4] J. Chadwick, *Nature* **129**, 312 (1932).
- [5] S. H. Neddermeyer and C. D. Anderson, *Phys. Rev.* **51**, 884 (1937).
- [6] J. C. Street and E. C. Stevenson, *Phys. Rev.* **52**, 1003 (1937).
- [7] C. M. G. Lattes, H. Muirhead, G. P. S. Occhialini and C. F. Powell, *Nature* **159**, 694 (1947).
- [8] G. D. Rochester and C. C. Butler, *Nature* **160**, 855 (1947).
- [9] B. Degrange, G. Fontaine, and P. Fleury, Tracking Louis Leprince-Ringuet's contributions to cosmic-ray physics, *Physics Today* **66** 8 (2013).
- [10] V. D. Hopper and S. Biswas *Phys. Rev.* **80**, 1099 (1950).
- [11] O. Chamberlain, E. Segre, C. Wiegand and T. Ypsilantis, *Phys. Rev.* **100**, 947 (1955).
- [12] F. Reines and C. L. Cowan, *Nature* **178**, 446 (1956).
- [13] G. Danby, J. M. Gaillard, K. A. Goulianos, L. M. Lederman, N. B. Mistry, M. Schwartz and J. Steinberger, *Phys. Rev. Lett.* **9**, 36 (1962).

- [14] V. E. Barnes, P. L. Connolly, D. J. Crennell, B. B. Culwick, W. C. Delaney, W. B. Fowler, P. E. Hagerty, E. L. Hart, N. Horwitz and P. V. C. Hough, *et al.* Phys. Rev. Lett. **12**, 204 (1964).
- [15] D. J. Griffiths, Introduction to Elementary Particles, Wiley (1987).
- [16] https://upload.wikimedia.org/wikipedia/commons/thumb/0/00/Standard_Model_of_Elementary_Particles.svg/1254px-Standard_Model_of_Elementary_Particles.svg.png?20240130105357.
- [17] H. Perkins, Introduction to High Energy Physics, Cambridge University Press (2012).
- [18] P. A. Zyla *et al.* [Particle Data Group], PTEP **2020**, 083C01 (2020).
- [19] R. C. Hwa and X. N. Wang, Quark-gluon plasma 3, World Scientific (2004).
- [20] A. Bazavov *et al.* [HotQCD Collaboration], Phys. Rev. D **90**, 094503 (2014).
- [21] J. Adams *et al.* [STAR Collaboration], Nucl. Phys. A **757**, 102 (2005).
- [22] R. Sahoo and T. K. Nayak, Curr. Sci. **121**, 1403 (2021).
- [23] N. Cabibbo and G. Parisi, Phys. Lett. B **59**, 67 (1975).
- [24] E. Annala, T. Gorda, A. Kurkela, J. Nättilä and A. Vuorinen, Nature Phys. **16**, 907 (2020).
- [25] M. G. Alford, K. Rajagopal and F. Wilczek, Phys. Lett. B **422**, 247 (1998).
- [26] O. Philipsen, Prog. Part. Nucl. Phys. **70**, 55 (2013).
- [27] M. A. Stephanov, Prog. Theor. Phys. Suppl. **153**, 139 (2004).
- [28] J. Rafelski, Melting Hadrons, Boiling Quarks - From Hagedorn Temperature to Ultra-Relativistic Heavy-Ion Collisions at CERN, Springer, 2016, ISBN 978-3-319-17544-7.

BIBLIOGRAPHY

- [29] J. Rafelski, Eur. Phys. J. A **51**, 114 (2015).
- [30] S. A. Chin, Phys. Lett. B **78**, 552 (1978).
- [31] J. D. Bjorken, Phys. Rev. D **27**, 140-151 (1983).
- [32] CERN, New state of matter created at CERN, Jan 2023, <https://home.web.cern.ch/news/press-release/cern/new-state-matter-created-cern>.
- [33] I. Arsene *et al.* [BRAHMS Collaboration], Nucl. Phys. A **757**, 1 (2005).
- [34] B. B. Back *et al.* [PHOBOS Collaboration], Nucl. Phys. A **757**, 28 (2005).
- [35] K. Adcox *et al.* [PHENIX Collaboration], Nucl. Phys. A **757**, 184 (2005).
- [36] R. Snellings, J. Phys. G **41**, 124007 (2014).
- [37] R. Schotter, Precision measurements in the multi-strange baryon sector at the LHC with the ALICE experiment, tel-04519825.
- [38] <https://particlesandfriends.wordpress.com/2016/10/14/evolution-of-collisions-and-qgp/>.
- [39] <http://indico.oris.mephi.ru/event/181/session/2/contribution/9/material/slides/0.pdf>.
- [40] A. M. Poskanzer and S. A. Voloshin, Phys. Rev. C **58**, 1671 (1998).
- [41] A. Bilandzic, R. Snellings and S. Voloshin, Phys. Rev. C **83**, 044913 (2011).
- [42] K. Aamodt *et al.* [ALICE Collaboration], Phys. Rev. Lett. **105**, 252302 (2010).
- [43] R. Pasechnik and M. Šumbera, Universe **3**, 7 (2017).
- [44] J. Rafelski and B. Muller, Phys. Rev. Lett. **48**, 1066 (1982).

- [45] P. Koch, B. Muller and J. Rafelski, Phys. Rept. **142**, 167 (1986).
- [46] J. Adam *et al.* [ALICE Collaboration], Nature Phys. **13**, 535 (2017).
- [47] S. Acharya *et al.* [ALICE Collaboration], Eur. Phys. J. C **80**, 693 (2020).
- [48] S. S. Adler *et al.* [PHENIX Collaboration], Phys. Rev. Lett. **91**, 072301 (2003).
- [49] B. B. Back *et al.* [PHOBOS Collaboration], Phys. Rev. Lett. **91**, 072302 (2003).
- [50] V. Khachatryan *et al.* [CMS Collaboration], JHEP **04**, 039 (2017).
- [51] T. Matsui and H. Satz, Phys. Lett. B **178**, 416 (1986).
- [52] B. Abelev *et al.* [ALICE Collaboration], Phys. Rev. Lett. **109**, 072301 (2012).
- [53] R. Arnaldi *et al.* [NA60 Collaboration], Nucl. Phys. A **783**, 261 (2007).
- [54] A. Adare *et al.* [PHENIX Collaboration], Phys. Rev. Lett. **98**, 232301 (2007).
- [55] A. Adare *et al.* [PHENIX Collaboration], Phys. Rev. C **84**, 054912 (2011).
- [56] V. F. Hess, Phys. Z. **13**, 1084 (1912).
- [57] W. Kolhörster, Phys. Zeitsch, **14**, 1153 (1913).
- [58] W. Kolhörster, Verhandlungen der Deutschen Physikalischen Gesellschaft **16**, 719 (1914).
- [59] P. Király, J. Phys. Conf. Ser. **409**, 012001 (2013).
- [60] M. S. Longair, High Energy Astrophysics (3rd ed.), Cambridge University Press (2011).
- [61] W. Baade and F. Zwicky, Proc. Nat. Acad. Sci. **20**, 254 (1934).

BIBLIOGRAPHY

- [62] W. Baade and F. Zwicky, Proc. Nat. Acad. Sci. **20**, 259 (1934).
- [63] E. Waxman, Phys. Rev. Lett. **75**, 386 (1995).
- [64] S. D. Wick, C. D. Dermer and A. Atoyan, Astropart. Phys. **21**, 125 (2004).
- [65] R. J. Protheroe and A. P. Szabo, Phys. Rev. Lett. **69**, 2885 (1992).
- [66] E. G. Berezhko, Astrophys. J. Lett. **684**, L69 (2008).
- [67] <https://web.physics.utah.edu/~whanlon/spectrum.html>.
- [68] G. Kulikov and G. Kristiansen, Sov. Phys. J. Exp. Theor. Phys. 35, 441 (1959).
- [69] E. G. Berezhko and L. T. Ksenofontov, J. Exp. Theor. Phys. **89**, 391 (1999).
- [70] K. Kobayakawa, Y. Sato and T. Samura, Phys. Rev. D **66**, 083004 (2002).
- [71] L. G. Sveshnikova, Astron. Astrophys. **409**, 799 (2003).
- [72] A. A. Lagutin, Y. A. Nikulin and V. V. Uchaikin, Nucl. Phys. B Proc. Suppl. **97**, 267 (2001).
- [73] J. Candia, E. Roulet and L. N. Epele, JHEP **12**, 033 (2002).
- [74] A. D. Erlykin and A. W. Wolfendale, J. Phys. G **23**, 979 (1997).
- [75] T. K. Gaisser, R. Engel, and E. Resconi, Cosmic Rays and Particle Physics, Cambridge University Press (2016).
- [76] R. L. Workman *et al.* [Particle Data Group], PTEP **2022**, 083C01 (2022).
- [77] R. U. Abbasi *et al.* [Telescope Array Collaboration], Astropart. Phys. **80**, 131 (2016).
- [78] A. Aab *et al.* [Pierre Auger Collaboration], Phys. Rev. D **102**, 062005 (2020).

- [79] A. Aab *et al.* [Pierre Auger Collaboration], Phys. Rev. Lett. **125**, 121106 (2020).
- [80] K. Greisen, Phys. Rev. Lett. **16**, 748 (1966).
- [81] G. T. Zatsepin and V. A. Kuzmin, JETP Lett. **4**, 78 (1966).
- [82] https://en.wikipedia.org/wiki/Greisen%E2%80%93Zatsepin%E2%80%93Kuzmin_limit
- [83] R. U. Abbasi *et al.* [HiRes Collaboration], Phys. Rev. Lett. **100**, 101101 (2008).
- [84] J. Abraham *et al.* [Pierre Auger Collaboration], Phys. Rev. Lett. **101**, 061101 (2008).
- [85] T. Abu-Zayyad *et al.* [Telescope Array Collaboration], Astrophys. J. Lett. **768**, L1 (2013).
- [86] H. Tanaka *et al.* [GRAPES-3 Collaboration], J. Phys. G **39**, 025201 (2012).
- [87] F. Varsi *et al.* [GRAPES-3 Collaboration], Phys. Rev. Lett. **132**, 051002 (2024).
- [88] T. Antoni *et al.* [KASCADE Collaboration], Astropart. Phys. **24**, 1 (2005).
- [89] M. G. Aartsen *et al.* [IceCube Collaboration], Phys. Rev. D **100**, 082002 (2019).
- [90] R. U. Abbasi *et al.* [Telescope Array Collaboration], Astropart. Phys. **64**, 49 (2015).
- [91] A. Aab *et al.* [Pierre Auger Collaboration], Phys. Rev. D **96**, 122003 (2017).
- [92] M. Aguilar *et al.* [AMS Collaboration], Phys. Rev. Lett. **114**, 171103 (2015).
- [93] M. Aguilar *et al.* [AMS Collaboration], Phys. Rev. Lett. **115**, 211101 (2015).

BIBLIOGRAPHY

- [94] O. Adriani *et al.* [PAMELA Collaboration], *Science* **332**, 69 (2011).
- [95] M. J. Christ, S. Dake, J. H. Derrickson, W. F. Fountain, M. Fuki, J. C. Gregory, T. Hayashi, R. Holynski, J. Iwai and A. Iyono, *et al.* *Astrophys. J.* **502**, 278 (1998).
- [96] V. A. Derbina *et al.* [RUNJOB Collaboration], *Astrophys. J. Lett.* **628**, L41 (2005).
- [97] Y. S. Yoon, T. Anderson, A. Barrau, N. B. Conklin, S. Coutu, L. Derome, J. H. Han, J. A. Jeon, K. C. Kim and M. H. Kim, *et al.* *Astrophys. J.* **839**, 5 (2017).
- [98] Q. An *et al.* [DAMPE Collaboration], *Sci. Adv.* **5**, eaax3793 (2019).
- [99] <https://www.mpi-hd.mpg.de/hfm/CosmicRay/Showers.html>.
- [100] W. Heitler, *The Quantum Theory of Radiation*, (3rd ed.), Oxford University Press, London (1954).
- [101] R. Snellings, *New J. Phys.* **13**, 055008 (2011).
- [102] B. I. Abelev *et al.* [STAR Collaboration], *Phys. Rev. C* **75**, 054906 (2007).
- [103] A. Adare *et al.* [PHENIX Collaboration], *Phys. Rev. Lett.* **98**, 162301 (2007).
- [104] Z. Feng, G. M. Huang and F. Liu, *Chin. Phys. C* **41**, 024001 (2017).
- [105] S. Acharya *et al.* [ALICE Collaboration], *Phys. Lett. B* **784**, 82 (2018).
- [106] S. Tripathy, S. De, M. Younus and R. Sahoo, *Phys. Rev. C* **98**, 064904 (2018).
- [107] B. Kim [ALICE Collaboration], *Nucl. Phys. A* **982**, 279 (2019).

- [108] S. Singha, B. Mohanty and Z. W. Lin, *Int. J. Mod. Phys. E* **24**, 1550041 (2015).
- [109] R. Rath, S. Tripathy, R. Sahoo, S. De and M. Younus, *Phys. Rev. C* **99**, 064903 (2019).
- [110] B. Abelev *et al.* [ALICE Collaboration], *Phys. Rev. C* **88**, 044910 (2013).
- [111] P. Bozek and I. Wyskiel-Piekarska, *Phys. Rev. C* **85**, 064915 (2012).
- [112] Z. w. Lin and C. M. Ko, *Phys. Rev. C* **65**, 034904 (2002).
- [113] Z. W. Lin, C. M. Ko, B. A. Li, B. Zhang and S. Pal, *Phys. Rev. C* **72**, 064901 (2005).
- [114] L. W. Chen, V. Greco, C. M. Ko and P. F. Kolb, *Phys. Lett. B* **605**, 95 (2005).
- [115] X. N. Wang and M. Gyulassy, *Phys. Rev. D* **44**, 3501 (1991).
- [116] C. Loizides, J. Kamin and D. d'Enterria, *Phys. Rev. C* **97**, 054910 (2018).
- [117] H. Masui, B. Mohanty and N. Xu, *Phys. Lett. B* **679**, 440 (2009).
- [118] P. Dasgupta, R. Chatterjee and D. K. Srivastava, *Phys. Rev. C* **95**, 064907 (2017).
- [119] A. Singh, P. K. Srivastava, O. S. K. Chaturvedi, S. Ahmad and B. K. Singh, *Eur. Phys. J. C* **78**, 419 (2018).
- [120] R. Hofstadter, Nobel Lecture, December 11, 1961.
- [121] R. D. Woods and D. S. Saxon, *Phys. Rev.* **95**, 577 (1954).
- [122] D. L. Hendrie, N. K. Glendenning, B. G. Harvey, O. N. Jarvis, H. H. Duhm, J. Saudinos and J. Mahoney, *Phys. Lett. B* **26**, 127 (1968).

BIBLIOGRAPHY

- [123] P. Moller, J. R. Nix, W. D. Myers and W. J. Swiatecki, *Atom. Data Nucl. Data Tabl.* **59**, 185 (1995).
- [124] G. Giacalone, J. Noronha-Hostler, M. Luzum and J. Y. Ollitrault, *Phys. Rev. C* **97**, 034904 (2018).
- [125] D. A. Varshalovich, A. N. Moskalev, and V. K. Khersonskii, *Quantum Theory of Angular Momentum* (World Scientific, Singapore, 1988), Chap. 5.
- [126] B. Schenke, P. Tribedy and R. Venugopalan, *Phys. Rev. C* **89**, 064908 (2014).
- [127] C. Nepali, G. I. Fai and D. Keane, *Phys. Rev. C* **76**, 051902 (2007).
- [128] B. Zhang, *Comput. Phys. Commun.* **109**, 193 (1998).
- [129] V. Greco, C. M. Ko and P. Levai, *Phys. Rev. Lett.* **90**, 202302 (2003).
- [130] R. J. Fries, B. Muller, C. Nonaka and S. A. Bass, *Phys. Rev. Lett.* **90**, 202303 (2003).
- [131] B. A. Li and C. M. Ko, *Phys. Rev. C* **52**, 2037 (1995).
- [132] B. Li, A. T. Sustich, B. Zhang and C. M. Ko, *Int. J. Mod. Phys. E* **10**, 267 (2001).
- [133] S. Acharya *et al.* [ALICE Collaboration], *Phys. Lett. B* **802**, 135225 (2020).
- [134] D. Sahu, S. Tripathy, G. S. Pradhan and R. Sahoo, *Phys. Rev. C* **101**, 014902 (2020).
- [135] G. S. Pradhan, R. Rath, R. Scaria and R. Sahoo, *Phys. Rev. C* **105**, 054905 (2022).
- [136] N. Mallick, R. Sahoo, S. Tripathy and A. Ortiz, *J. Phys. G* **48**, 045104 (2021).

- [137] S. Acharya *et al.* [ALICE Collaboration], JHEP **10**, 152 (2021).
- [138] S. Acharya *et al.* [ALICE Collaboration], JHEP **09**, 006 (2018).
- [139] H. J. Warringa, Phys. Rev. D **86**, 085029 (2012).
- [140] K. Fukushima, D. E. Kharzeev and H. J. Warringa, Phys. Rev. Lett. **104**, 212001 (2010).
- [141] D. E. Kharzeev, L. D. McLerran and H. J. Warringa, Nucl. Phys. A **803**, 227 (2008).
- [142] A. Bzdak and V. Skokov, Phys. Lett. B **710**, 171 (2012).
- [143] W. T. Deng and X. G. Huang, Phys. Rev. C **85**, 044907 (2012).
- [144] V. Skokov, A. Y. Illarionov and V. Toneev, Int. J. Mod. Phys. A **24**, 5925 (2009).
- [145] R. C. Duncan and C. Thompson, Astrophys. J. Lett. **392**, L9 (1992).
- [146] P. Dey, A. Bhattacharyya and D. Bandyopadhyay, J. Phys. G **28**, 2179 (2002).
- [147] T. Vachaspati, Phys. Lett. B **265**, 258 (1991).
- [148] J. R. Bhatt and A. K. Pandey, Phys. Rev. D **94**, 043536 (2016).
- [149] S. Konar, J. Astrophys. Astron. **38**, 47 (2017).
- [150] A. Reisenegger, [arXiv:1305.2542 [astro-ph.SR]].
- [151] V. Vovchenko, Int. J. Mod. Phys. E **29**, 05, 2040002 (2020).
- [152] C. Ratti, R. Bellwied, The Deconfinement Transition of QCD: Theory Meets Experiment, Lecture Notes in Physics, vol 981, Springer, Cham, (2021), https://link.springer.com/chapter/10.1007/978-3-030-67235-5_6.

BIBLIOGRAPHY

- [153] G. S. Pradhan, D. Sahu, S. Deb and R. Sahoo, *J. Phys. G* **50**, 055104 (2023).
- [154] G. Kadam, S. Pal and A. Bhattacharyya, *J. Phys. G* **47**, 125106 (2020).
- [155] G. Endrödi, *JHEP* **04**, 023 (2013).
- [156] D. P. Menezes, M. Benghi Pinto, S. S. Avancini, A. Perez Martinez and C. Providencia, *Phys. Rev. C* **79**, 035807 (2009).
- [157] A. N. Tawfik, A. M. Diab, N. Ezzelarab and A. G. Shalaby, *Adv. High Energy Phys.* **2016**, 1381479 (2016).
- [158] L. Landau and E. Lifshits, *Quantum mechanics: non-relativistic theory, Course of theoretical physics, Volume 3*, Pergamon Press, U.K. (1977).
- [159] G. S. Bali, F. Bruckmann, G. Endrödi, S. D. Katz and A. Schäfer, *JHEP* **08**, 177 (2014).
- [160] E. S. Fraga and A. J. Mizher, *Phys. Rev. D* **78**, 025016 (2008).
- [161] S. Chakrabarty, *Phys. Rev. D* **54**, 1306 (1996).
- [162] **Particle Data Group** Collaboration, J. Beringer *et al.*, *Review of Particle Physics (RPP)*, *Phys.Rev.* **D86** 010001 (2012).
- [163] B. I. Abelev *et al.* [STAR Collaboration], *Phys. Rev. C* **75**, 064901 (2007).
- [164] A. Adare *et al.* [PHENIX Collaboration], *Phys. Rev. C* **83**, 064903 (2011).
- [165] K. Aamodt *et al.* [ALICE Collaboration], *Eur. Phys. J. C* **71**, 1655 (2011).
- [166] B. Abelev *et al.* [ALICE Collaboration], *Phys. Lett. B* **717**, 162 (2012).
- [167] B. Abelev *et al.* [ALICE Collaboration], *Phys. Lett. B* **712**, 309 (2012).
- [168] S. Chatrchyan *et al.* [CMS Collaboration], *Eur. Phys. J. C* **72**, 2164 (2012).

- [169] T. Bhattacharyya, J. Cleymans, A. Khuntia, P. Pareek and R. Sahoo, Eur. Phys. J. A **52**, 30 (2016).
- [170] K. Aamodt *et al.* [ALICE Collaboration], Eur. Phys. J. C **71**, 1655 (2011)
- [171] S. Deb, G. Sarwar, R. Sahoo and J. e. Alam, Eur. Phys. J. A **57**, 195 (2021).
- [172] S. Deb, D. Sahu, R. Sahoo and A. K. Pradhan, Eur. Phys. J. A **57**,158 (2021).
- [173] D. Sahu, S. Tripathy, R. Sahoo and A. R. Dash, Eur. Phys. J. A **56**,187 (2020).
- [174] C. Beck, Eur. Phys. J. A **40**, 267 (2009).
- [175] C. Tsallis, J. Statist. Phys. **52**, 479 (1988).
- [176] C. Tsallis, R. S. Mendes and A. R. Plastino, Physica A **261**, 534 (1998).
- [177] J. Cleymans and D. Worku, J. Phys. G **39**, 025006 (2012).
- [178] J. Cleymans and D. Worku, Eur. Phys. J. A **48**, 160 (2012).
- [179] M. D. Azmi and J. Cleymans, Eur. Phys. J. C **75**, 430 (2015).
- [180] S. R. de Groot, W. A. van Leeuwen, C. G. van Weert, Relativistic Kinetic Theory (North Holland, 1980).
- [181] M. Peskin and D. Schroeder, An introduction to quantum field theory, Westview Press, U.S.A. (1995).
- [182] P. Ramond, Field Theory: A Modern Primer, Westview Press, (2001).
- [183] E. Elizalde, An asymptotic expansion for the first derivative of the generalized Riemann zeta function, UBFT-FP-4-85, <https://inspirehep.net/literature?sort=mostrecent&size=25&page=1&>

BIBLIOGRAPHY

- [q=E.~Elizalde%2C%20An%20asymptotic%20expansion%20for%20the%20first%20derivative%20of%20the%20generalized%20Riemann%20zeta%20function%2C%20UBFT-FP-4-85&ui-citation-summary=true.](#)
- [184] Digital Library of Mathematical Functions, release date 2012-03-23. National Institute of Standards and Technology, <http://dlmf.nist.gov/>.
- [185] J. S. Schwinger, Phys. Rev. **82**, 664 (1951).
- [186] P. Elmfors, D. Persson and B. S. Skagerstam, Astropart. Phys. **2**, 299 (1994).
- [187] J. O. Andersen and R. Khan, Phys. Rev. D **85**, 065026 (2012).
- [188] L. D. Landau, E. M. Lifshitz, Fluid Mechanics, Pergamon Press, Third Edition (1966).
- [189] J. Cleymans and D. Worku, Mod. Phys. Lett. A **26**, 1197-1209 (2011).
- [190] D. Prorok and L. Turko, [arXiv:hep-ph/0101220 [hep-ph]].
- [191] M. Gyulassy and L. McLerran, Nucl. Phys. A **750**, 30 (2005).
- [192] P. Braun-Munzinger and J. Stachel, Nature **448**, 302 (2007).
- [193] B. V. Jacak and B. Muller, Science **337**, 310 (2012).
- [194] J. Cleymans and K. Redlich, Phys. Rev. C **60**, 054908 (1999).
- [195] W. Florkowski and W. Broniowski, Phys. Lett. B **477**, 73 (2000).
- [196] A. Andronic, P. Braun-Munzinger, K. Redlich and J. Stachel, Nature **561**, 321 (2018).
- [197] J. Sollfrank, P. Koch and U. W. Heinz, Phys. Lett. B **252**, 256 (1990).

- [198] Z. Tang, Y. Xu, L. Ruan, G. van Buren, F. Wang and Z. Xu, Phys. Rev. C **79**, 051901 (2009).
- [199] S. Chatterjee, B. Mohanty and R. Singh, Phys. Rev. C **92**, 024917 (2015).
- [200] S. Chatterjee, S. Das, L. Kumar, D. Mishra, B. Mohanty, R. Sahoo and N. Sharma, Adv. High Energy Phys. **2015**, 349013 (2015).
- [201] D. Thakur, S. Tripathy, P. Garg, R. Sahoo and J. Cleymans, Adv. High Energy Phys. **2016**, 4149352 (2016).
- [202] S. Chatterjee and B. Mohanty, Phys. Rev. C **90**, 034908 (2014).
- [203] M. Waqas and F. H. Liu, Indian J. Phys. **96**, 1217 (2022).
- [204] M. Waqas, G. X. Peng, F. H. Liu and Z. Wazir, Sci. Rep. **11**, 20252 (2021).
- [205] M. Waqas, G. X. Peng and F. H. Liu, J. Phys. G **48**, 075108 (2021).
- [206] A. Adare *et al.* [PHENIX Collaboration], Phys. Rev. D **83**, 052004 (2011).
- [207] A. Adare *et al.* [PHENIX Collaboration], Phys. Rev. C **83**, 064903 (2011).
- [208] V. Khachatryan *et al.* [CMS Collaboration], JHEP **02**, 041 (2010).
- [209] V. Khachatryan *et al.* [CMS Collaboration], Phys. Rev. Lett. **105**, 022002 (2010).
- [210] G. Aad *et al.* [ATLAS Collaboration], New J. Phys. **13**, 053033 (2011).
- [211] V. Khachatryan *et al.* [CMS Collaboration], Phys. Rev. Lett. **116**, 172302 (2016).
- [212] G. S. Pradhan, D. Sahu, R. Rath, R. Sahoo and J. Cleymans, Eur. Phys. J. A **60**, 3, 52 (2024).
- [213] G. Wilk and Z. Włodarczyk, Phys. Rev. Lett. **84**, 2770 (2000).

BIBLIOGRAPHY

- [214] T. S. Biro and A. Jakovac, Phys. Rev. Lett. **94**, 132302 (2005).
- [215] G. Wilk and Z. Wlodarczyk, Phys. Rev. C **79**, 054903 (2009).
- [216] G. Wilk and Z. Wlodarczyk, Eur. Phys. J. A **40**, 299 (2009).
- [217] T. S. Biro, G. G. Barnaföldi and P. Van, Physica A **417**, 215 (2015).
- [218] T. Bhattacharyya, P. Garg, R. Sahoo and P. Samantray, Eur. Phys. J. A **52**, 283 (2016).
- [219] A. Deppman, J. Phys. G **41**, 055108 (2014).
- [220] A. Deppman, Phys. Rev. D **93**, 054001 (2016).
- [221] A. Deppman, E. Megias and D. P. Menezes, Phys. Rev. D **101**, no.3, 034019 (2020).
- [222] A. Deppman, E. Megias, D. P. Menezes and T. Frederico, Entropy **20**, 633 (2018).
- [223] G. Cook, R. H. Dickerson, American Journal of Physics **63**, 737 (1995).
- [224] C. R. Allton, S. Ejiri, S. J. Hands, O. Kaczmarek, F. Karsch, E. Laermann, C. Schmidt and L. Scorzato, Phys. Rev. D **66**, 074507 (2002).
- [225] C. R. Allton, S. Ejiri, S. J. Hands, O. Kaczmarek, F. Karsch, E. Laermann and C. Schmidt, Phys. Rev. D **68**, 014507 (2003).
- [226] R. V. Gavai and S. Gupta, Phys. Rev. D **68**, 034506 (2003).
- [227] C. R. Allton, M. Doring, S. Ejiri, S. J. Hands, O. Kaczmarek, F. Karsch, E. Laermann and K. Redlich, Phys. Rev. D **71**, 054508 (2005).
- [228] A. Bazavov, H. T. Ding, P. Hegde, O. Kaczmarek, F. Karsch, E. Laermann, Y. Maezawa, S. Mukherjee, H. Ohno and P. Petreczky, *et al.* Phys. Rev. D **95**, 054504 (2017).

- [229] K. Rajagopal and F. Wilczek, in *At the Frontier of Particle Physics: Handbook of QCD* ed. M. Shifman, p. 2061 (World Scientific, Singapore) (2001).
- [230] J. Cleymans, G. I. Lykasov, A. S. Parvan, A. S. Sorin, O. V. Teryaev and D. Worku, *Phys. Lett. B* **723**, 351 (2013).
- [231] J. Cleymans and M. Wellington Paradza, *MDPI Physics* **2**, 654 (2020).
- [232] J. Cleymans and M. W. Paradza, [arXiv:2010.05565 [hep-ph]].
- [233] M. Rybczynski and Z. Wlodarczyk, *Eur. Phys. J. C* **74**, 2785 (2014).
- [234] V. A. Okorokov, *Adv. High Energy Phys.* **2015**, 790646 (2015).
- [235] V. A. Okorokov, *Adv. High Energy Phys.* **2016**, 5972709 (2016).
- [236] K. Aamodt *et al.* [ALICE Collaboration], *Phys. Rev. D* **82**, 052001 (2010).
- [237] M. M. Aggarwal *et al.* [STAR Collaboration], *Phys. Rev. C* **83**, 064905 (2011).
- [238] K. Aamodt *et al.* [ALICE Collaboration], *Phys. Rev. D* **84**, 112004 (2011).
- [239] S. Acharya *et al.* [ALICE Collaboration], *Phys. Rev. C* **99**, 024906 (2019).
- [240] S. Acharya *et al.* [ALICE Collaboration], *Phys. Lett. B* **807**, 135501 (2020).
- [241] S. Acharya *et al.* [ALICE Collaboration], *Eur. Phys. J. C* **80**, 167 (2020).
- [242] Version: 6.26/06, CERN ROOT: <http://root.cern.ch>.
- [243] A. Khuntia, H. Sharma, S. Kumar Tiwari, R. Sahoo and J. Cleymans, *Eur. Phys. J. A* **55**, 3 (2019).
- [244] Z. Bai and Y. X. Liu, *Phys. Rev. D* **108**, 014018 (2023).
- [245] <https://www.tifr.res.in/grapes3/science.html>

BIBLIOGRAPHY

- [246] S. K. Gupta *et al.* [GRAPES-3 Collaboration], Nucl. Instrum. Meth. A **540**, 311 (2005).
- [247] P. K. Mohanty *et al.* [GRAPES-3 Collaboration], Astropart. Phys. **31**, 24 (2009).
- [248] P. K. Mohanty, S. R. Dugad and S. K. Gupta, Rev. Sci. Instrum. **83**, 043301 (2012).
- [249] Y. Hayashi *et al.* [GRAPES-3 Collaboration], Nucl. Instrum. Meth. A **545**, 643 (2005).
- [250] G. H. Choi, E. S. Seo, S. Aggarwal, Y. Amare, D. Angelaszek, D. P. Bowman, Y. C. Chen, M. Copley, L. Derome and L. Eraud, *et al.* Astrophys. J. **940**, 107 (2022).
- [251] N. Gorbunov, V. Grebenyuk, D. Karmanov, I. Kovalev, I. Kudryashov, A. Kurganov, A. Panov, D. Podorozhny, S. Porokhovoy and L. Sveshnikova, *et al.* Adv. Space Res. **64**, 2546 (2019).
- [252] B. Hariharan *et al.* [GRAPES-3 Collaboration], Phys. Rev. Lett. **122**, 105101 (2019).
- [253] P. K. Mohanty *et al.* [GRAPES-3 Collaboration], Phys. Rev. Lett. **117**, 171101 (2016).
- [254] P. K. Mohanty *et al.* [GRAPES-3 Collaboration], Phys. Rev. D **97**, 082001 (2018).
- [255] Fahim Varsi, [Thesis GRAPES-3 Collaboration], “Measurement of the energy spectrum and composition of cosmic rays by the GRAPES-3 experiment,” (2023)

- [256] Pravata Kumar Mohanty, [Thesis GRAPES-3 Collaboration], “An investigation of the sun-induced diurnal anisotropy in cosmic rays measured with the GRAPES-3 experiment,” (2014)
- [257] W. L. Leo, Techniques for Nuclear and Particle Physics Experiments, (Narosa Publishing, New Delhi, 1995).
- [258] J. A. Bellido, R. W. Clay, N. N. Kalmykov, I. S. Karpikov, G. I. Rubtsov, S. V. Troitsky and J. Ulrichs, Phys. Rev. D **98**, 023014 (2018).
- [259] H. P. Dembinski *et al.* [EAS-MSU, IceCube, KASCADE-Grande, NEVOD-DECOR, Pierre Auger, SUGAR, Telescope Array and Yakutsk EAS Array], EPJ Web Conf. **210**, 02004 (2019).
- [260] A. G. Bogdanov, R. P. Kokoulin, G. Mannocchi, A. A. Petrukhin, O. Saavedra, V. V. Shutenko, G. Trinchero and I. I. Yashin, Astropart. Phys. **98**, 13 (2018).
- [261] J. Albrecht, L. Cazon, H. Dembinski, A. Fedynitch, K. H. Kampert, T. Pierog, W. Rhode, D. Soldin, B. Spaan and R. Ulrich, *et al.* Astrophys. Space Sci. **367**, 27 (2022).
- [262] C. Grupen, N. O. Hashim, B. Jost, F. Maciuc, S. Luitz, A. Mailov, A. S. Muller, A. Putzer, B. Rensch and H. G. Sander, *et al.* Nucl. Phys. B Proc. Suppl. **175**, 286 (2008).
- [263] J. Abdallah *et al.* [DELPHI Collaboration], Astropart. Phys. **28**, 273 (2007).
- [264] A. A. Petrukhin, Nucl. Instrum. Meth. A **742**, 228 (2014).
- [265] O. Saavedra, M. B. Amelchakov, N. S. Barbashina, A. G. Bogdanov, D. V. Chernov, A. Chiavassa, L. I. Dushkin, S. S. Khokhlov, V. A. Khomyakov and V. V. Kindin, *et al.* J. Phys. Conf. Ser. **409**, 012009 (2013).

BIBLIOGRAPHY

- [266] D. Heck, J. Knapp, J. N. Capdevielle, G. Schatz and T. Thouw, FZKA-6019.
- [267] H. Fesefeldt, PITHA-85-02, RWTH Aachen, **647** 27, (1985).
- [268] G. Battistoni, T. Boehlen, F. Cerutti, P. W. Chin, L. S. Esposito, A. Fassò, A. Ferrari, A. Lechner, A. Empl and A. Mairani, *et al.* *Annals Nucl. Energy* **82**, 10 (2015).
- [269] S. A. Bass, M. Belkacem, M. Bleicher, M. Brandstetter, L. Bravina, C. Ernst, L. Gerland, M. Hofmann, S. Hofmann and J. Konopka, *et al.* *Prog. Part. Nucl. Phys.* **41**, 255 (1998).
- [270] J. Ranft, *Phys. Rev. D* **51**, 64 (1995).
- [271] T. Pierog, I. Karpenko, J. M. Katzy, E. Yatsenko and K. Werner, *Phys. Rev. C* **92**, 034906 (2015).
- [272] H. J. Drescher, M. Hladik, S. Ostapchenko, T. Pierog and K. Werner, *Phys. Rept.* **350**, 93 (2001).
- [273] N. N. Kalmykov, S. S. Ostapchenko and A. I. Pavlov, *Nucl. Phys. B Proc. Suppl.* **52**, 17 (1997).
- [274] S. Ostapchenko, *Phys. Rev. D* **83**, 014018 (2011).
- [275] E. J. Ahn, R. Engel, T. K. Gaisser, P. Lipari and T. Stanev, *Phys. Rev. D* **80**, 094003 (2009).
- [276] W. R. Nelson, H. Hirayama, and D. W. O. Rogers, *Strings*, EGS4 code system, Technical report, Stanford Linear Accelerator Center, Menlo Park, CA (USA), (1985).
- [277] K. Kamata and J. Nishimura, *Prog. Theor. Phys. Suppl.* **6**, 93 (1958).
- [278] K. Greisen, *Ann. Rev. Nucl. Part. Sci.* **10**, 63 (1960).